Improving Surface Characteristics of Mold Steel using Electric Discharge Alloying

A Thesis

Submitted in Partial Fulfilment of the Requirements for the Degree of

Doctor of Philosophy

By

Ngangkham Devarani

(Roll No. 136103036)

Department of Mechanical Engineering

Indian Institute of Technology Guwahati

Guwahati, Assam, India

2022

TH-2735_136103036

Indian Institute of Technology Guwahati

Department of Mechanical Engineering

Guwahati – 781039

STATEMENT

The present thesis entitled, **"Improving Surface Characteristics of Mold Steel using Electric Discharge Alloying"** has been carried out by me under the supervision of Prof. Shrikrishna N. Joshi, Department of Mechanical Engineering, Indian Institute of Technology Guwahati. This work has not been submitted elsewhere for the award of any degree.

Ng. Devarani

Date: 22/11/2021

Ngangkham Devarani

Roll. No. 136103036

Department of Mechanical Engineering,

Indian Institute of Technology Guwahati,

Guwahati – 781039, India

TH-2735_136103036

Indian Institute of Technology Guwahati

Department of Mechanical Engineering

Guwahati – 781039

CERTIFICATE

It is certified that the work described in this thesis, entitled, **"Improving Surface Characteristics of Mold Steel using Electric Discharge Alloying"** done by **Ms. Ngangkham Devarani (Roll No. 136103036),** a Ph.D. student in the Department of Mechanical Engineering, Indian Institute of Technology Guwahati, for the award of degree of **Doctor of Philosophy** has been carried out under my supervision. This work has not been submitted elsewhere for the award of any degree.

Date: 24 November 2021

Prof. Shrikrishna N. Joshi

Professor

Department of Mechanical Engineering

Indian Institute of Technology Guwahati,

Guwahati – 781039, India

TH-2735_136103036

Dedicated to

My family

TH-2735_136103036

ABSTRACT

Electric discharge alloying (EDA) is one of the evolving and promising techniques in the field of surface alloying. In EDA, deliberate transfer of tool material over the workpiece surface along with decomposed dielectric is anticipated to form a hard alloyed layer over the workpiece. The process mechanism of EDA lies in the basic concept of re-solidification of the melted tool and workpiece material which is resulted from electric discharge generated between them. This process could find its application in industrially important material, namely AISI P20 – DIN 1.2311 – SCM4, a low-alloy tool steel which is widely used as thermoplastic molds, extrusion dies, injection molds, and die-casting dies. It is essential to improve the surface characteristics of the dies and molds in terms of its hardness, wear, and corrosion resistance as it suffers from mechanical wear, corrosive environment during the casting process. Considering these aspects, electric discharge alloying is found to be economical and less time-consuming for surface modification, as the same set-up will be used for both the fabrication and repair of the molds.

The main focus of the present work is to enhance the surface characteristics of AISI P20 mold steel in terms of its hardness, corrosion resistance, and wear resistance by using the electrical discharge alloying process. It was envisaged to achieve this by alloying titanium, aluminium, and nitrogen over AISI P20 mold steel by using a green compact powder metallurgy tool with a composition of 50 % titanium and 50 % aluminium compacted at a compaction pressure of 443 MPa. Three types of dielectric media, namely hydrocarbon oil, deionized water, and urea mixed deionized water, were considered. The present work investigates the EDA process both experimentally and numerically. The study was carried out to investigate the influence of the EDA processing conditions viz. discharge current, discharge duration, and the type of dielectric medium onto the alloyed layer thickness, material deposition rate, surface roughness, elemental distribution, hardness, wear-resistance, and corrosion resistance. Further, an integrated FEM-ANN model has been developed for quick and accurate computation of the alloyed layer thickness in EDA of AISI P20 mold steel using different dielectric media viz. hydrocarbon oil, deionized water, and urea mixed deionized water.

In the initial part of the work, experimental investigations were successfully carried out to alloy titanium and aluminium with AISI P20 steel by using hydrocarbon oil as the dielectric medium. The alloyed workpieces were characterized by using energy-

TH-2735_136103036

dispersive X-ray spectroscopy (EDS), and results showed that up to a maximum of 18 % Ti and 18.7 % Al could be observed over the alloyed workpiece surface. Further, elemental mapping of the alloyed surface over the top surface, as well as the cross-sectioned region, indicated that the tool elements present are uniformly distributed in the alloyed region. Apart from the elemental transfer, the formation of Fe_3C and TiAl at the alloyed region was confirmed from the X-ray diffraction pattern. The thickness of the alloyed layer formed was observed to be dependent on the discharge current and pulse on-time, and a uniform layer of up to 70 µm could be achieved. The alloyed layer showed improvement in hardness of four times more than that of the parent material, i.e., 300 $HV_{0.3}$ to 1125 $HV_{0.3,}$ and this ascertains the usefulness of the EDA process in improving the surface characteristics of the parent material. Further, it was observed that the material deposition rate and surface roughness is dependent on the EDA processing conditions. An increase in the discharge current and pulse on-time resulted in a higher material deposition rate, and the surface roughness of the alloyed workpieces exhibit a roughness value in the range of 4.5 to 8.5 µm.

The work has been extended to study the alloying process in water-based dielectric medium, i.e., by using deionized (DI) water and urea mixed deionized water. It was observed that a maximum of 16.5 % Ti with 12 % Al, 35.02 % oxygen and 4 % nitrogen could be observed for the workpiece processed in urea mixed deionized water, while for that of the workpiece processed in deionized water, a maximum of 27.2 % Ti with 7.6 % Al and 40.3 % oxygen was observed. Formation of an alloyed layer composed of TiAl, $Fe_3O_{4,}$ and Ti_4AlN_3 has been observed for the workpiece processed using urea mixed DI water, while for the workpiece processed in deionized water, the alloyed layer is composed of TiAl and Fe_3O_4. The study on the alloyed layer thickness indicated that the thickness is more for the workpieces processed using DI water as compared to that of the urea mixed. Alloyed layer of 60.19 µm thickness could be observed for the workpiece processed using DI water, while that for urea mixed deionized water was 53.25 µm. The difference in the hardness value of the alloyed layer was observed to be marginal for the workpiece processed in the two dielectric media. While using deionized water, the hardness of the alloyed layer was obtained to be 579.83 $HV_{0.3}$, while for that of urea mixed deionized water, the value was 604.35 $HV_{0.3}$. The material deposition rate is mainly affected by the discharge current. An increase in discharge current results in a higher deposition rate for both deionized water and urea mixed deionized water. The surface

TH-2735_136103036

roughness extends a range of 5.94 µm to 12.45 µm for the workpiece processed in deionized water, while that of urea mixed deionized water, the range is 5.98 µm to 12.54 µm showing that the addition of urea does not have a significant difference in the roughness value.

A comparative study in terms of wear and corrosion resistance for the workpieces alloyed in the three different types of dielectric media has been made. Results indicated that there is minimal wear for the workpieces processed in hydrocarbon oil, followed by workpieces processed in urea mixed deionized water, unprocessed workpiece, and workpiece processed in deionized water. Further, the mass loss after the wear test for the workpiece processed in hydrocarbon oil was significantly reduced by 46 % from that of the unprocessed workpiece. The change in mass loss is quite marginal for the unprocessed workpiece and the workpieces processed in the water-based dielectric. In addition to the wear test, an electrochemical corrosion test was conducted for the workpieces processed in different dielectric media, and results showed that that the impedance modulus and the maximum phase angle are the highest for the workpiece processed in hydrocarbon oil, indicating the highest polarization resistance. The corrosion resistance value for the workpiece processed using hydrocarbon oil was almost double the corrosion resistance of the unprocessed workpiece. There was a 110 % enhancement in the corrosion resistance for the workpiece processed in hydrocarbon oil from that of the unprocessed workpiece.

Further, an integrated FEM-ANN model was used to compute the alloyed layer thickness by considering accurate values for fraction of energy distributed to the workpiece, F_A. These values were computed by using the inverse estimation method and the ANN-based model. The neural network of 3-10-1 architecture was found to be the optimum network. The developed methodology suggests that the fraction of energy F_A varies from 0.129 to 0.215. This can be employed in the thermal analysis of the electric discharge-based manufacturing processes. The performance of the developed FEM-ANN was verified by carrying out the experiments. It was found acceptable with an average prediction deviation of 6.55 %. Overall, the present work facilitates a simple and quick methodology for accurate computation of the alloyed layer thickness for complex manufacturing processes such as EDA. This provides an efficient and economical alternative to the costly, tedious, and time-consuming experimental work.

TH-2735_136103036

TH-2735_136103036

Acknowledgements

It has been a wonderful experience for me during the entire span of my research work. Many people have inspired, motivated, and helped me during the entire course of this work, and it is my heartfelt desire to acknowledge their immense goodwill and valuable support.

I wish to express my sincere and deep appreciation to my supervisor, Prof. Shrikrishna N. Joshi, for his encouragement, insightful guidance, all patience, support, and enthusiastic support throughout my studies, including the writing of this dissertation. I am especially thankful to him for critically reviewing the reports and research papers despite his busy schedule of academic and other administrative works. I owe him a lot for the valuable advice he has given me whenever I needed it.

I am highly thankful to my doctoral committee members, Prof. U. S. Dixit, Prof. Arbind K. Singh, and Dr. Sachin Gautam, for their continuous academic guidance and for checking my work progress and seminars during my Ph.D. Their valuable discussions and suggestions were truly encouraging for me.

I would like to express my sincere gratitude to Prof. K. S. R. Krishna Murthy, Prof. S. Senthilvelen, Prof. Santosha K. Dwivedy, Prof. Anoop K. Dass, and Prof. Pinakeswar Mahanta, present and former Heads, Department of Mechanical Engineering, Indian Institute of Technology Guwahati, for providing various laboratory facilities and sanctioning funds without which completion of the work would not have been possible. I am also grateful to all the faculty members of the Mechanical Engineering department.

I would also like to thank the Ministry of Human Resource and Development (MHRD), Government of India, and Science and Engineering Research Board (SERB), Government of India for providing financial support. I sincerely thank the Indian Institute of Technology Guwahati for providing all sorts of infrastructural facilities to carry out this doctoral research work. I would also like to acknowledge the Advanced Manufacturing Laboratory, Material Science Laboratory, Central Workshop, and Central Instruments Facility of Indian Institute of Technology Guwahati and all scientific officers and staff members for providing instruments and helping me to carry out the research work.

I deeply acknowledge the unabated support and counseling provided by my colleagues and friends, Dr. Ravikant, Dr. Borad M. Barkachary, Dr. Gururaj Bolar, Dr.

TH-2735_136103036

S. Sunderlal Singh, Ms. Sanghamitra Das, and Mrs. Upasana Sarma, throughout my studies. I also highly appreciate the technical cooperation given by Mr. Jiten Basumatary and Mr. Saiffuddin Ahmed.

I am also grateful to my friends Dr. Leichombam Sophia, Dr. Sanasam Vipej, Ms. Th. Debika, Ms. Ksh. Priyalakshmi, Dr. Diana Sagolsem, Dr. Pukhram Bhumita, Mr. Kh. Amit, Dr. Franco M., and Dr. T. Gishan for their constant support. I would also like to thank the family of the College of Agricultural Engineering and Post Harvest Technology (Central Agricultural University, Imphal), Ranipool, Sikkim for their immense support and encouragement.

My most sincere gratitude and appreciation go to my father, Dr. Ng. Ibotombi Singh, my mother, Mrs. Chirom Damayanti Devi, my elder sisters, Ms. Ng. Nirmala, Mrs. Ng. Lilabati, my brother-in-law Mr. Stanley Soibam, my younger brother Mr. Alva Ngangkham, and my niece Melvina Soibam for their patience, continuous encouragement, and moral support over the past difficult years. I am deeply indebted to all the other members of my family who gave me constant support and encouragement throughout my life.

There are many more persons who helped me in many more ways and whose names elude me at this moment of time. I extend my gratitude to them.

Last, but not the least, I shall always be grateful to God for providing me such an awesome aura for research work.

Ng. Devarani

Date: 12/04/2022 Ngangkham Devarani

TH-2735_136103036

Table of Contents

TH-2735_136103036

TH-2735_136103036

TH-2735_136103036

TH-2735_136103036

List of Figures

TH-2735_136103036

TH-2735_136103036

TH-2735_136103036

TH-2735_136103036

TH-2735_136103036

TH-2735_136103036

TH-2735_136103036

TH-2735_136103036

List of Tables

TH-2735_136103036

TH-2735_136103036

List of Abbreviations

Abbreviation	Description
ANFIS	Adaptive network based fuzzy interference system
BPNN	Back propagation neural network
CNC	Computer numerically control
CVD	Chemical vapour deposition
DI	Deionized
EDA	Electric discharge alloying
EDM	Electric discharge machine
EDS	Energy dispersive X-ray spectroscopy
EDSA	Electric discharge surface alloying
EIS	Electrochemical impedance spectroscopy
FDM	Finite difference method
FEM	Finite element method
FESEM	Field emission scanning electron microscope
GA	Genetic algorithm
HC	Hydrocarbon
JCPDS	Joint committee on powder diffraction standards
LVDT	Linear variable differential transformer
MDR	Material deposition rate
MLE	Multi-layer electrode
MSE	Mean square error
PM	Powder metallurgy
PVD	Physical vapour deposition
RBNN	Radial basis neural network
SCE	Saturated calomel electrode
UIT	Ultrasonic impact treatment
USM	Ultrasonic machining
XRD	X-ray diffraction

TH-2735_136103036

TH-2735_136103036

List of Symbols

Symbol	Description	Unit
ρ	Density of the workpiece	kg/m^3
ρ_d	Density of the dielectric medium	kg/m^3
μ	Dynamic viscosity of the dielectric medium	kg/ms
$[B]$	General geometric matrix.	-
$[C]$	Global heat capacity matrix	W/µm^2
C_p	Specific heat of the workpiece	J/kg K
C_{pd}	Specific heat of the dielectric medium	J/kg K
(C_{peff})	Effective heat capacity	J/kg K
d	Mean diagonal of the indent	mm^2
D_t	Thermal diffusivity	m^2/s
F	Load applied	gf
F_A	Fraction of energy distributed to the workpiece / anode	-
F_C	Fraction of energy distributed to the cathode	-
h	Convective heat transfer coefficient	W/m^{2}K
$HV_{0.3}$	Vickers hardness value at 300 gf load	-
I_d	Discharge current	A
k	Thermal conductivity of the workpiece	W/mK
k_d	Thermal conductivity of the dielectric medium	W/mK
$[K_T]$	Global conductivity matrix	W/mK
L_d	Thermal diffusion length	µm
L_H	Latent heat of melting of the workpiece	kJ/kg
n	Size of the testing dataset	-
$[N]$	Interpolation or shape function matrix	-
Nu_x	Nusselt number	-
Pr	Prandtl number	-
$\{Q\}$	Heat flux vector	W/µm^2
r	Radial coordinate (radial distance)	µm
R_e	Reynolds number	-
R_{pc}	Radius of the plasma channel	µm
t	Time	µs
t_{on}	Pulse on-time or pulse duration	µs

TH-2735_136103036

T	Surface Temperature	K
T_a	Ambient temperature	K
$\{T_e\}$	Element nodal temperature matrix	K
ΔT	Temperature difference	K
q_0	Maximum heat flux	W/µm^2
$q(r)$	Heat source	W/µm^2
v	Flow velocity	m/s
V	Discharge voltage	V
x	Characteristic length	m
X_0	Low predictive index	-
X	Desired percentage data greater than prescribed value	-
z	Axial coordinate (distance below the workpiece surface)	µm

TH-2735_136103036

CHAPTER 1

Introduction

The industrial tools and components such as dies and molds, tools, turbine blades, and parts of internal combustion engines operating in stringent environmental conditions undergo high surface degradation. This essentiality led to the increase in demand for advanced materials, viz., like nickel super alloys, aluminium/titanium alloys, and high-temperature steels. These possess high hardness, high toughness, high fatigue, corrosive resistance, and wear resistance. However, bulky work parts or components entirely made up of these materials are expensive. In view of this, improvement of surface characteristics of these components by alloying required elements can be an alternate cost-effective process.

1.1 Surface alloying and treatment of AISI P20 mold steel

AISI P20 – DIN 1.2311 – SCM4 belongs to low-alloy tool steel. It possesses excellent toughness and strength. It is widely used to manufacture thermoplastic molds, extrusion dies, injection molds, and die-casting dies. The plastic injection molds suffer mechanical wear due to the relative movements of the mold parts as well as due to the abrasive actions by the reinforced materials such as hard and abrasive fibers or whiskers (Öztürk et al. 2005). The acids and chlorides formed due to the decomposition of thermoplastics by overheating create a corrosive environment (Rosalbino et al. 2012). In addition to this, gas liberated from plastic materials at elevated temperatures during the injection molding process results in localized corrosion of the mold steel (Öztürk et al. 2005). Novák et al. (2006) worked on abrasive wear and corrosion test of tool steel and reported that the wear resistance is dependent on the surface hardness, roughness, microstructure, and phase composition. However, corrosion resistance is mainly affected by the presence of a compound layer. It is, thus, essential to improve the surface characteristics in terms of its hardness and improvement in wear resistance and corrosion resistance of the dies and molds.

Nitriding and carburizing are common techniques that are generally used to enhance the surface characteristics of mold steel. The process of nitriding can be carried out by gas nitriding wherein the part is heated at around 530 °C in a dry ammonia gas atmosphere, thereby resulting in diffusion of atomic nitrogen in the workpiece surface.

TH-2735_136103036

Plasma nitriding of steel, also known as ion nitriding, is carried out to introduce elemental nitrogen on the surface to enhance its hardness (Berg et al. 2000; Sirin and Kaluc 2012). In this process, high voltage electrical energy is used to generate plasma in a vacuum. During the discharge process, nitrogen gets diffused into the steel surface. In this process, nitrogen can also combine with other alloying elements such as chromium to form an alloy. In nitrocarburising, nitrogen and carbon are diffused on the surface by either plasma technologies or by the gas method (Pereloma et al. 2001). It is generally carried out in the temperature range of 560 to 580 °C for steels. The coated layer exhibits good tribological properties.

In physical vapour deposition (PVD), the material to be deposited undergo thermal evaporation in the form of atoms and molecules and thereafter gets condenses on the surface of the workpiece to be coated (Deng et al. 2020). In general, the coating thickness of about 2 to 5 µm can be obtained using this process. In chemical vapour deposition (CVD), the workpiece is exposed to a volatile medium that reacts with the work surface to achieve desired coatings. Though it produces a quality coating, it has environmental hazards in terms of residual gases released during the chemical reaction process. In general, PVD is widely used for coating of tools used in drilling, turning, and milling. Coating of TiN, TiAlN, AlTiN, and CrAlN using PVD technology has been successfully carried out to enhance the wear and friction properties by Aihua et al. (2012). Though PVD is widely employed for coating, the thin coated layers may not be sufficient in industrial applications. The thin layers may get ruptured during their operations (Su et al. 1998). To meet this challenge, Ibrahim et al. (2015) worked on multilayer TiAlN/CrN coatings on AISI P20 steel using the PVD technique and found that multilayer coating exhibits higher hardness and elastic modulus as compared to that of monolayer coatings.

Apart from coating of desired elements to attain superior surface properties, surface hardening is being carried out by laser surface engineering. It includes laser heating, melting, vaporization, and peening. Annealing and solid-state phase transformation hardening come under laser heating. Laser melting provides alloying, cladding, and grain refinement, while thin-film deposition, marking, and scribing come under laser vaporization. Shah and Dahotre (2002) deposited vanadium carbide by using a laser to extend the die life and achieved coating that could resist the unwanted chemical reaction caused by molten aluminium. Park et al. (2019) studied the wear and corrosion behavior of mold steel before and after laser heating and reported that the laser processed

TH-2735_136103036

parts showed significant enhancement in wear resistance. However, the effect of laser treatment on corrosion resistance was marginal due to microstructural homogenization. The combined effect of gas nitriding and laser surface treatment of P20 steel surface on the surface hardness, wear, and corrosion behavior was also studied by Yan et al. (2020). It was concluded that the surface hardness and the wear resistance could be enhanced; however, the corrosion resistance deteriorates.

Literature reports eminent research articles on repairing the molds and dies by laser welding (Borrego et al. 2009), three-dimensional micro-welding (Horii et al. 2008), and electron beam welding (Jhavar et al. 2013). However, these methods need highly skilled labor and an inert processing environment, which certainly limits their applicability (Vedani et al. 2007). In addition to this, worn-out molds and dies require added steps of regrinding and preparing the surface for proper adhesion of the material to be coated (Moro et al. 2004). These factors thereby increase the cost of production.

In view of enhancing the surface characteristics of steel, researchers have also investigated the electric discharge alloying (EDA) for surface modification. In EDA, an alloyed layer exhibiting superior surface characteristics could be achieved by deliberate transfer of desired elements. This can be achieved by changing the type of the tool material (Tyagi et al. 2018; Wang et al. 2002) or by mixing desired powders in the dielectric (Sharma et al. 2020). Electric discharge alloying was noted to be economical and less time-consuming for surface modification, as the same machine tool set-up, i.e., electric discharge machine, can be used for both the machining and surface modification of the molds. In view of the cost-effectiveness, simplicity, ease of operation, it was thought worthy to carry out extensive and systematic experimental and numerical investigations to reinforce the utility of EDA and to improve the surface characteristics of important P20 mold steel by alloying high-value elements such as Ti, Al, and N.

1.2 Process mechanism of electric discharge alloying

In electric discharge alloying, an electric discharge occurs at the inter-electrode gap or the spark gap. This results in a peak rise in temperature as high as 10000 ˚C at the spark location due to the formation of plasma (Ho and Newman 2003). This high-temperature plasma results in the melting and vaporization of both tool electrode and workpiece. During this short span of the electric discharge phenomenon, a melt pool is formed, which consists of both tool and workpiece material along with decomposed elements of the

TH-2735_136103036

dielectric medium (Murray et al. 2017). Upon solidification of the melt pool, an alloy is formed over the workpiece at the region where the discharge has occurred.

Surface alloying of work material occurs mainly due to the high-temperature electrical discharge occurring between the electrodes. Figure 1.1 shows the phenomenon of electrical discharge formation. In general, normal polarity is preferred for machining operations. Reverse polarity, i.e., tool as negative terminal and workpiece as positive terminal, is considered for the alloying process. When the tool electrode is made negative, higher heat distribution is attained at the tool terminal as compared to that of the workpiece terminal. This results in higher wear of tool electrode and thereby promoting deliberate transfer of the tool material onto the workpiece (Ho et al. 2007; Kumar and Batra 2012). For a discharge to occur between the electrodes, the tool and workpiece are submerged in a dielectric medium and are placed very close to each other at around 10 to 100 µm distance apart. Then, an open circuit voltage is applied across the electrodes. The breakdown of the dielectric is initiated when it reaches to its critical values that is called the breakdown voltage. The location of breakdown is generally the closest point between the electrodes. When a breakdown occurs, the voltage falls, and the current rises abruptly. In this stage, the dielectric gets ionized, and a plasma channel is created between the electrodes.

With the formation of the plasma channel, a discharge current is established due to the continuous movements of electrons. During this process, the fast-moving electrons collide with ions, and intense heat generates. This heat energy melts and vaporizes the tool and workpiece surfaces. The plasma channel expands with time. At the end of discharge, plasma implodes, and a vacuum is created. The surrounding dielectric gushed into the vacuum medium. Due to this, molten metal ejects and leaves a small crater (in the order of 1-500 µm diameters) at the electrodes. The molten material is then flushed out by the dielectric medium, and a fresh dielectric fills up the gap between the electrodes for the next discharge to occur.

TH-2735_136103036

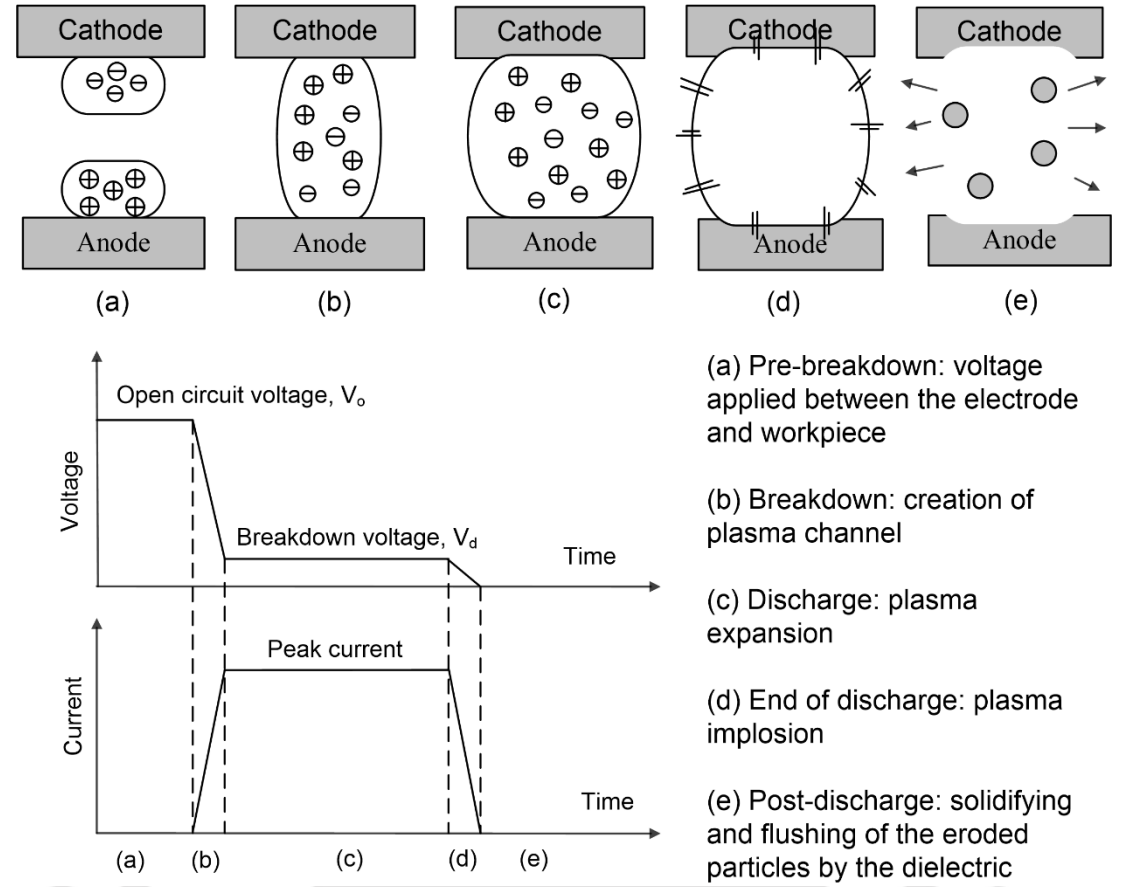

Figure 1.1 Principle of electric discharge in EDA

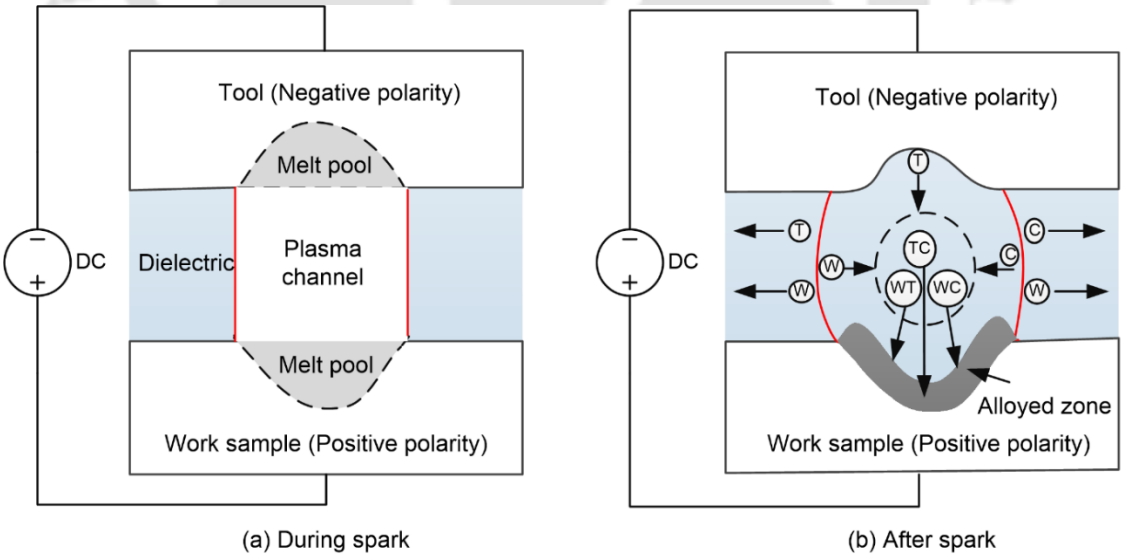

Figure 1.2 Schematic diagram for EDA phenomenon (a) During spark and (b) After a spark

TH-2735_136103036

The melting of both the tool and workpiece is shown in Figure 1.2(a). The elements released from the tool and workpiece are fused with the carbon generated from the hydrocarbon dielectric. Some of these solidified molten material deposits on the workpiece, and an alloyed layer is formed, as shown in Figure 1.2(b). In the figure, T signifies the tool material, W signifies the workpiece material, and C signifies the decomposed carbon from the dielectric. An alloy of possible combinations such as TW, TC, WC, or WTC can be formed by the EDA process.

1.3 Advantages and limitations

Electric discharge alloying has the following advantages.

- The process has the capability of alloying desired electrically conductive material.
- Alloying over complex surfaces and complicated contours can be performed.
- Surface characteristics such as wear resistance, corrosion resistance, hardness, etc., can be enhanced by using suitable operating conditions.
- The alloyed surface consists of craters due to the multiple sparking, and such a surface can be used for oil retention, which will help in lubrication.

In spite of the numerous advantages, EDA possesses certain limitations

- Only electrically conductive material can be alloyed.
- The processed surfaces may have microcracks at the alloyed region due to rapid quenching.
- Achieving a uniform alloyed layer thickness is a challenging task.

1.4 Motivation for the present research work

Electric discharge alloying is one of the evolving and promising techniques in the field of surface alloying. It is employed for alloying the workpiece surface to obtain specific functional characteristics such as improved hardness, resistance to wear, and corrosion. The process of EDA has evolved from the concept of converting the undesirable phenomenon of wearing of tool material and formation of the recast layer during electric discharge machining into the alloying process. Some initial research attempts on controlling or manipulating the process have been reported. The primary objective was to assess the possibility of applying the EDA to improve the properties of the electrically discharged surface (Yan et al. 2005). Deliberate transfer of the desired element onto the workpiece surface during the EDA operation could be achieved in various ways, such as

TH-2735_136103036

mixing desired powder particles in the dielectric (Kumar and Batra 2012), changing the tool material, or by changing the dielectric medium (Bai and Koo 2006). Out of these available techniques, changing tool material is quite a convenient process as alloying by powder mixed dielectric may lead to non-uniform distribution of the powder.

From the reported literature, it is learned that formation of a uniform alloyed layer by EDA is still a challenging task. This is attributed to the stochastic nature of the discharge phenomenon. A very scant work has been reported on surface alloying of AISI P20 mold steel. It is one of the industrially important materials used for fabrication of injection molds and is subjected to stringent environmental conditions. This has motivated to investigate the electric discharge alloying of mold steel as the same set-up can be used for fabrication as well as for enhancement of the surface characteristics.

Extensive research has been reported on the numerical modeling and simulation of the electric discharge machining process; however, a very scant work has been reported in modeling of EDA phenomenon. The magnitude and characteristics of the alloyed layer are dependent upon input parameters, namely discharge current, discharge voltage, pulse on-time, duty cycle, and dielectric medium. The energy distribution factor is also one of the key parameters which influence the EDA phenomenon. Therefore, there is a need to compute the energy distribution factor for a set of processing conditions in order to develop a thermal-based EDA model. Further, few works have been reported on the computation of alloyed layer thickness using artificial neural networks and hard computing methods together. This has motivated in developing an integrated FEM – ANN methodology to compute the alloyed layer thickness by using inverse computation of energy distribution among the electrodes.

1.5 Scope of the present research work

The present work is focused on alloying of Ti and Al over the surface of AISI P20 mold steel by using electric discharge based process. Deliberate transfer of tool material element is envisaged to form a hard alloyed layer over the workpiece. The influence of EDA processing conditions viz., pulse on-time, discharge current, and type of dielectric medium on the alloyed layer thickness, material deposition rate, and surface roughness are investigated. The types of dielectric media used are hydrocarbon oil, deionized water, and urea mixed deionized water. A comparative study on the hardness of the alloyed layer, wear resistance, and corrosion resistance of the workpieces alloyed in the different

TH-2735_136103036

dielectric media is made. Therefore, the main aim of this work is to form a uniform alloyed layer over the workpiece so as to enhance its characteristics.

In order to gain an insight into the process mechanism involved in electric discharge alloying and further to predict the output performance, a numerical model has been developed. In EDA, the thermal energy distribution factor is critical in deciding the alloyed layer thickness. In view of this, a soft computing based inverse, novel, and simple methodology has been developed in the present work to accurately predict the energy distribution factor and in turn the alloyed layer thickness. Also, the employment of soft computing techniques can aid in the development of a robust predictive model.

1.6 Organization of the thesis

The **first chapter** presents an overview of electric discharge surface alloying, its phenomenon, the advantages and limitations of the alloying process over other well-established alloying techniques. The motivation for carrying out the present work is presented. The **second chapter** deals with the review of the available literature for surface alloying by EDA is presented. Based on the review of the available literature, certain research gaps are realized, and the objective of the present work was derived. The **third chapter** presents the details about the experimental set-up, characterization tools used, and methodology followed. In the **fourth chapter**, the results of EDA alloying of titanium and aluminium with AISI P20 mold steel using hydrocarbon oil dielectric have been discussed. The experimental characterization in terms of material deposition rate, surface roughness, alloyed layer thickness, the hardness of the alloyed layer, and the distribution of the alloying elements along with the type of compound formed is discussed in detail. In the **fifth chapter**, the effect of dielectric media, namely deionized water and urea mixed deionized water in alloying of titanium and aluminium with AISI P20 mold steel has been discussed in detail. Detailed characterization of the alloy formed over the workpiece has been reported. The **sixth chapter** deals with the comparative study on the tribological behavior in terms of the wear and corrosion resistance for the workpieces processed in different dielectric media viz. hydrocarbon oil, deionized water, and urea mixed deionized water. In the **seventh chapter**, an integrated FEM-ANN model developed to compute the alloyed layer thickness by inverse computation of the energy distribution factor is presented. Finally, in the **eighth chapter**, the important conclusions drawn from the present study are provided. Also, the future scope of the work is included.

TH-2735_136103036

CHAPTER 2

Literature Review on Electric Discharge Alloying Process

2.0 Scope

This chapter presents the fundamentals of electric discharge alloying in terms of its process mechanism, process parameters, and performance measures. An extensive and critical review about the available literature has been presented. It includes papers related to various aspects of EDA, such as experimental studies on electric discharge alloying by using conventional tool electrode, powder metallurgy electrode, and different dielectric media. The chapter also presents the state of the art of research carried out on developing a thermal-based numerical model related to EDA. Use of experimental-based process modeling of EDA, such as soft computing technique has also been discussed.

2.1 Process characteristics of electric discharge alloying

Electric discharge alloying (EDA) is the process of alloying the workpiece surface as a result of the electric discharge generated between tool and workpiece submerged in a dielectric medium. During the discharge, high-temperature plasma is formed, resulting in melting and vaporization of tool and workpiece. This creates a melt pool over the workpiece. The melt pool thereby forms an alloyed layer upon solidification. The alloyed layer consists of elements from the tool, workpiece, and dielectric medium. Deliberate transfer of the tool elements onto the workpiece surface is anticipated by changing the type of the tool material or dielectric medium. Electric discharge alloying is carried out on all electrically conductive materials irrespective of their hardness, toughness, brittleness, or any other physical or mechanical properties. The important process parameters that govern the electric discharge alloying process are the discharge voltage, discharge current, pulse on-time, and pulse off-time.

Following sub-sections deals with the performance measures of EDA.

2.1.1 Formation of alloyed layer

During the discharge phenomenon, there is intense heating of the workpiece. This results in the formation of two main distinct regions or layers over the parent material. The regions are alloyed region and heat diffused region (shown in Figure 2.1). The alloyed region is formed from the unexpelled molten material. It is also termed as recast layer as

TH-2735_136103036

this layer is formed from solidified melt pool. Changes in the metallurgical and tribological properties in this layer are reported by various researchers as the layer is composed of elements from the tool, workpiece, and dielectric medium. Adjacent to the alloyed region is the heat diffused region. This is the region that has not been melted but has attained the recrystallization temperature. In this region, changes in the grain structures are observed. The thickness of the alloyed region and the heat diffused region generally depends on the processing parameters. There are no changes in the microstructures of the parent material as the heat of the discharge could not get penetrated.

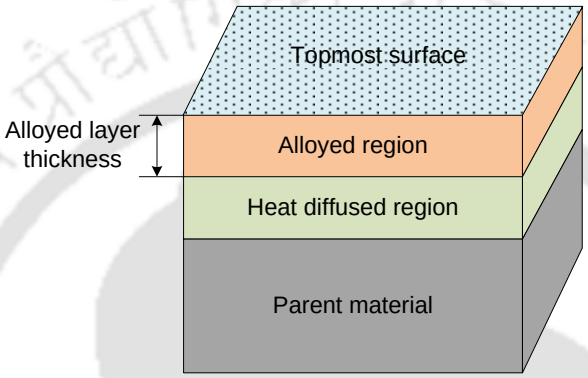

Figure 2.1 Schematic diagram showing the layers formed after EDA

2.1.2 Surface roughness

Surface roughness refers to the surface irregularities present in the workpiece after the EDA operation. Due to the multiple discharges occurring simultaneously at different locations of the tool and work interface, there is presence of peaks and valleys on the workpiece surface. The roughness of the surface is dependent on the EDA processing parameters namely pulse on-time, discharge current, and the type of dielectric medium. Depending on the requirement, the processing parameters are chosen.

2.1.3 Material deposition rate

In EDA, it is expected that the mass of the workpiece will be enhanced as a result of the transfer of the tool material over the workpiece. It is measured by the material deposition rate. During the EDA process, due to the high heat intensity, both the tool and workpiece undergo melting and evaporation. This results in deposition of the tool elements over the workpiece as well as erosion of the workpiece at the same time. The material deposition rate is calculated on the net weight gain of the workpiece after the EDA operation. It is the amount of material deposited onto the workpiece per unit time and is calculated by

TH-2735_136103036

considering the difference in mass of the workpiece before and after EDA operation during the total time taken for the alloying. It depends on the optimum setting of the machine input parameters such as discharge current, pulse duration, discharge voltage, and duty cycle.

2.1.4 Surface characteristics of the alloyed layer

The surface of the workpiece after the EDA operation is noted to have the presence of tool elements as well as decomposed dielectric medium. Depending on the EDA processing conditions along with tool, workpiece, and dielectric medium combinations, the alloyed surface can show different characteristics such as enhancement in hardness, wear-resistance, and corrosion resistance. For an EDA surface showing enhancement in the hardness and wear resistance, the same surface can show deterioration in the corrosion resistance or vice versa. In view of this, researchers have exploited the phenomenon of material transfer during EDA in order to obtain desired surface characteristics.

2.2 Experimental studies on electric discharge alloying

Numerous works have been reported in the field of electric discharge alloying by using different types of tool material, such as solid copper, graphite, titanium, and powder metallurgy electrodes such as tungsten carbide and copper, titanium and aluminium, etc. The process of EDA was also studied by varying the type of the dielectric medium. Some work has also been reported on mixing of powder particles such as Si, Al, Ti, etc., in the dielectric. A review of these works is presented in subsequent sub-sections.

2.2.1 Electric discharge alloying by using conventional tool electrode

Literature reports that solid tool electrodes made up of electrolytic copper (Yan et al. 2005), graphite electrode (Chang-Bin et al. 2011), multilayer electrode of graphite, and titanium (Hwang et al. 2010) have been tried. Barash and Kahlon (1964) observed the formation of hard layer was formed over the workpiece of mild steel by using cooper tool. Xia et al. (1996) used copper as tool (anode) and workpiece (cathode) material to study the difference in material removal from the anode and cathode surface. Low material removal from the anode surface was noted due to the formation of carbon coating. Carbon coating on the anode surface was observed due to the pyrolysis effect of dielectric medium. Therefore, polarity of the tool electrode plays an important role. In electric discharge alloying, negligible or low material removal with significant material

TH-2735_136103036

deposition over the workpiece surface is desirable. This condition can be attained when the workpiece is made anode, and the tool is made the cathode. Numerous works have been reported in this direction in which significant deposition is achieved by employing tool as cathode (Kunieda and Yoshida 1997). The schematic diagram of surface modification using conventional solid electrode is as shown in Figure 2.2. There is intense heating of the tool and workpiece due to the plasma formation (Figure 2.2 (a)). Due to the formation of the plasma, a melt pool is created and upon solidification of this melt pool, an alloyed layer is formed over the workpiece (Figure 2.2 (b)).

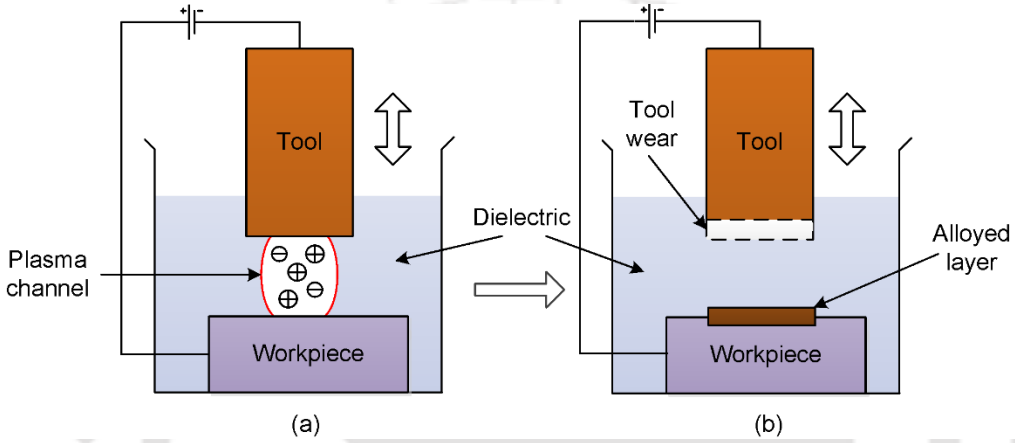

Figure 2.2 Schematic diagram for EDA using conventional solid electrode (a) Plasma channel formation and (b) Formation of alloyed layer

Soni and Chakraverti (1996) observed that deposition of significant copper-tungsten tool materials transferred onto the workpiece surface. It was also observed that the hardness of the workpiece surface was enhanced significantly. Mohri et al. (2000) demonstrated that EDM could be used for both machining and additive processes. In their work, thin wires of tungsten, brass, and copper of 125 µm diameter were used as electrodes for drilling of AISI – 1049 steel workpiece and reported that under the same operating conditions, holes were successfully drilled on using copper and brass. However, deposition of tungsten was observed with the use of tungsten electrodes.

Chang-bin et al. (2011) worked on surface alloying of titanium alloy using different dielectric, namely air, nitrogen gas, and silicone oil using graphite tool electrode. The surface hardness of the workpiece alloyed in silicone oil was maximum (3.5 times the hardness of the parent material), followed by nitrogen gas and air. During an experimental investigation performed by Stambekova at al. (2012) for surface modification of 5083 Al alloy using a Si-Fe alloy, the hardness of the deposited layer was

TH-2735_136103036

noted to be improved as compared to that of the parent material. The alloyed surface also showed enhancement in corrosion resistance.

Hwang et al. (2010) used multilayer electrode (MLE) for surface alloying of Ni work surface. The MLE is comprised of graphite and Ti layers stacked alternately. The results indicated that the graphite layer of the MLE enhances the concentration of carbon elements in a localized workpiece surface as compared to the bulk electrode made up of Ti. The high concentration of C leads to the formation of TiC, which was found to influence the surface hardness of coated layer.

Mordyuk et al. (2016, 2017) reported a hybrid process of ultrasonic impact treatment (UIT) and electric discharge surface alloying (EDSA) by using chromium and molybdenum as an anode on low-carbon steel 20GL. It was noted that with the use of chromium as an anode in the combined sequential process of UIT + EDSA + UIT, the fatigue strength was increased by 30 % from that of the untreated workpiece (Mordyuk et al. 2016). Further, with the use of molybdenum as an anode in the combined sequential process of EDSA + UIT treatment, the surface properties such as anti-corrosion property, wear resistance, and the fatigue strength were enhanced by 85 %, 43 %, and 5 %, respectively, as compared to that of the untreated workpiece (Mordyuk et al. 2017).

2.2.2 Electric discharge alloying by using powder metallurgy electrode

In this alloying process, powder metallurgy (PM) based tool electrodes are prepared by compaction of required powdered particles composition at certain compaction pressure. The compacted PM electrode without any heat treatment is referred to as green compact electrode. In general, green compact electrodes and sintered (heat-treated) PM electrodes are commonly used. The properties of PM tool electrode, such as thermal, electrical, and mechanical properties, can effectively be controlled by changing the compaction pressure, sintering temperature, and composition (Gangadhar et al. 1991; Simão et al. 2002).

Compaction pressure is an important parameter that influences the hardness and the electrical conductivity of the PM tool electrode. At low compaction pressure, the powder particles are loosely bonded. However, the hardness of the PM tool electrode increases with increase in compacting pressure as the particles get strain hardened. Apart from hardness, electrical conductivity of the PM tool also increases with increase in compaction pressure due to a stronger bond between the particles. In addition to

TH-2735_136103036

compaction pressure, sintering temperature also influences the electrical conductivity of the PM tool. Increase in sintering temperature increases the electrical conductivity of the PM tool due to solid bonding between the particles, while electrodes sintered at lower temperatures erode faster due to weak bonding between the particles. Therefore, to obtain more electrical conductivity, the compacting pressure and sintering temperature should be high during the preparation of the PM electrode. One of the major advantages of PM processed electrodes from the manufacturing point of view is that in the pre-sintering condition, these can be easily machined to the required shape with an acceptable level of accuracy. Further, the use of PM tool is economical as a large number of tool electrodes can be made from a single die and punch assembly (Samuel and Philip 1997).

From the above discussion, it can be summarized that the properties of the PM tool can be easily manipulated and controlled. With the use of PM tool electrode in electric discharge alloying, deliberate transfer of desired elements over the workpiece surface can be easily made by changing the composition of the tool. Further, the material deposition rate can be controlled by varying compaction pressure and sintering temperature. Figure 2.3 shows the schematic diagram for EDA using the PM tool electrode. The formation of plasma between the tool and workpiece (Figure 2.3 (a)) melts and erodes the powder metallurgy electrode (Figure 2.3 (b)). This eroded material from the tool gets deposited over the workpiece, thereby forming an alloyed layer (Figure 2.3 (c)).

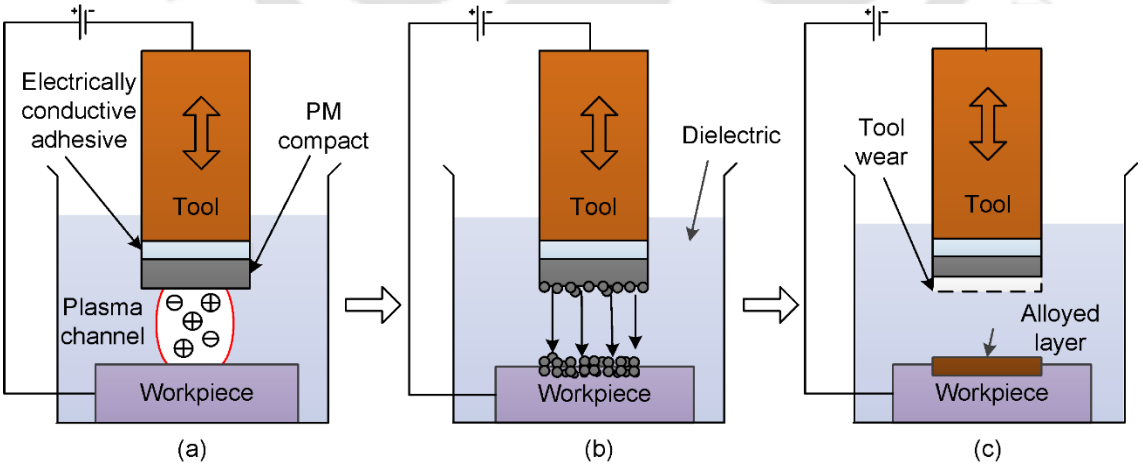

Figure 2.3 Schematic diagram for EDA using PM tool electrode (a) Plasma channel formation; (b) PM tool breakdown and (c) Formation of alloyed layer

Works have been reported to compare the alloying process by using conventional and powder metallurgy electrode. Gangadhar et al. (1991) compared the mild steel workpiece

TH-2735_136103036

surface after processing with a solid copper electrode and bronze compact and concluded that the use of powder compact electrode results in an easier transfer of the tool material. Samuel and Philip (1997) used an electrolytic copper compact electrode to modify the surface of hardened steel at various levels of current and pulse duration and found that the use of powder compact electrode is more sensitive to discharge current and pulse on-time when compared with a conventional electrode. Ho et al. (2007) worked on surface modification of Ti6Al4V by using a solid electrode and Cu powder metallurgical tool. In their work, glow discharge optical emission spectroscopy-based analysis showed that the percentage of copper transferred from the solid electrodes to the workpiece was about 29 %, while from the powder compact electrodes, the level was nearly 78 % at the workpiece surface.

Mohri et al. (1993) applied a green compact tool of WC/Co and copper electrode, and obtained a hard layer of WC with 60 µm thickness over the workpiece of carbon steel. The authors studied the alloying process by using aluminium compact electrodes as well as titanium compact electrodes. The alloyed layer showed higher corrosion resistance and wear resistance. Shunmugam et al. (1994) worked on alloying of HSS tools with the employment of PM tool of WC/Fe electrode and observed an enhancement in resistance to the wear of the alloyed surface by 25 % to 60 % under the same working condition of pressure and temperature present during metal cutting operation. Lee et al. (2004) worked on Ti alloy with WC/Co as PM tool material and achieved a considerable reduction in the coefficient of friction (nearly 50 %) with alloyed electrical discharge surface as compared to that of surface machined with standard graphite electrodes under similar process conditions. Patowari et al. (2011) worked on C-40 grade steel by using a PM tool of W/Cu, and obtained an alloyed layer thickness of up to 785 µm with improved hardness from 9.81 to 12.75 GPa. Simao et al. (2002) performed EDA of tungsten and titanium on AISI D2 steel and reported the enhancement of EDA layer hardness ranging from 620 HK to 1350 HK. Tsai et al. (2003) employed Cr/Cu electrodes to enhance the corrosion resistance of AISI 1045 medium carbon steel.

Chen et al. (2008) observed that by using semi-sintered electrodes made of Cu-W powders, the alloyed surface showed two distinctive results. When the no-load voltage and peak current were set high, material removal was observed. In contrast, a deposit was formed on the workpiece surface when the no-load voltage and peak current were set to a low level. The deposited layer could be regarded as an alloyed layer with improved

TH-2735_136103036

machined surface performance. Further, it was concluded that the surface modification through EDA using semi-sintered electrodes was a promising process that could deposit an adequate layer thickness (approximately 180 to 210 μm) in a very short elapsed working time (approximately 600 μs). Moreover, the modified alloyed layer could be regulated by varying the composition of the semi-sintered powders.

Numerous works have been reported with the use of PM tool electrode made up of tungsten, tungsten carbide, copper, and cobalt. However, less work have been reported in using Ti powder metallurgy electrode. Tsunekawa et al. (1994) have worked in alloying of pure aluminium plate. In their work, an alloyed TiC layer of 100 μm thick was successfully obtained and the surface hardness was improved from 3.5 to 10.5 GPa. Wang et al. (2002) worked on alloying carbon steel by using Ti powder green compact electrode and reported that a hard ceramic layer of TiC was coated on the surface. TiC concentration was as high as 51 % at a discharge current of 2 to 10 A and pulse duration of 2 to 12 μs. Results found that the hardness of the ceramic layer is three times higher than that of the parent material. Moro et al. (2004) compared the performance of a cutting tool alloyed with PM-based EDA process and PVD coating technology. It was observed that the tool life of the EDA alloyed workpiece processed by semi-sintered TiC electrode increased in comparison to that of the PVD - TiN coated workpiece.

Observations

Composition, compaction pressure, and sintering temperature of the powder metallurgy tool electrode played a major role in an efficient deposition. EDA input parameters such as electrode polarity, voltage, and current significantly affect the deposition quality. Attempts have been carried out to improve functional surface characteristics such as wear and corrosion resistance using varying PM tools such as Ti, WC/Co, WC/Fe, TiC/WC/Co, Cr/Cu, WC/Cu, semi sintered TiC, etc. Further, it is observed that powder metallurgical tool electrode is more favorable than conventional electrode due to ease in control of material transfer. This is due to the fact that the electrical conductivity and the bonding strength of the particle in the PM tool can be controlled by varying the sintering temperature, compaction pressure, and powder composition.

2.2.3 Electric discharge alloying by using different dielectric medium

The basic principle of EDA evolves from the transfer of material components comprising of the tool elements and the composition of the dielectric medium during the electrical

TH-2735_136103036

discharge process. Therefore, it necessitates the investigation of the study of the effect of various dielectric media on the workpiece surface after the electric discharge phenomenon. Ekmekci et al. (2005) employed commercial kerosene and deionized (DI) water as the dielectric media with copper and graphite as tool material to study the surface integrity of AISI P20 mold steel after EDA and reported that cementite was formed for the workpieces processed with kerosene and also the white layer thickness was highest for workpieces processed at longest pulse duration.

Yan et al. (2005) also worked on the surface modification of titanium by mixing white crystalline granular urea in distilled water to impart better wear resistance of pure titanium by using electrolytic copper as a tool electrode. Characterization of the alloyed surface showed that TiN was synthesized on the workpiece surface by a chemical reaction that involved elements obtained from the workpiece and urea mixed dielectric. Santos et al. (2017) studied the influence of varying concentrations of urea mixed with DI water for nitriding the surface of AISI 4041 steel. Results indicated that with the addition of urea, the dielectric strength reduces, and a noticeable change in the formation of the plasma channel was observed. Also, the use of urea concentration higher than 10 g/L was not recommended as the plasma formation was not stable. Further, no significant morphological changes, nitride layer thickness, types of nitrides formed, and hardness was observed. Da Silva et al. (2020) investigated the formation of nitride layer on the surface of annealed AISI H13 steel by using urea mixed DI water with copper as tool electrode and showed that iron nitride was formed, and as a result of this, the hardness of the processed workpiece was increased by three times as compared with the unprocessed workpiece.

Xiao et al. (2014) used smelted titanium electrode and ethanolamine aqueous solution as dielectric and reported that titanium carbonitride (TiCN) was successfully alloyed over carbon steel substrate by using EDA. TiCN layer of 15 µm thick with few micro-cracks was obtained when the current and pulse duration of 20 A and 390 µs was applied. The authors compared the bonding strength of the TiCN alloyed workpiece with the workpiece coated with TiN by using magnetron sputtering technique. Results indicated that the bonding strength of EDA alloyed workpiece is four times higher than that of workpiece coated with magnetron sputtering. Zhang et al. (2014a) compared the influence of five different dielectrics viz. air, oxygen, kerosene, DI water, sand water-in-oil emulsion on the material removal characteristics by EDM and found that there is a

TH-2735_136103036

difference in the shape of the crater formed for the different dielectric media. The use of liquid dielectric gives a higher removal efficiency than the gaseous dielectric. Sadagopan and Mouliprasanth (2017) showed that a dielectric medium with high viscosity increases the material removal rate, which is attributed due to higher energy density as a result of a reduction in the plasma channel. Biodiesel, transformer oil, and kerosene were the different dielectric media used in their study. Niamat et al. (2019) used kerosene and distilled water for processing of aluminium 6061 using EDA. The results indicated that the material removal rate is higher in distilled water than in kerosene which is due to the formation of carbide layer in the latter case.

Mixing powders in the dielectric medium is another way of achieving an alloyed surface by EDA. For this, powders particles such as Si, Ti, Al, Cu, Cr, etc. (Kansal and Kumar 2007; Syed and Palaniyandi 2012) are mixed in the dielectric medium. These powder particles are suspended in the gap between the tool and workpiece as shown in Figure 2.4 (a). Suspension of powder particles facilitates faster ignition by creating a higher discharge probability and lowering the breakdown strength of the insulating dielectric medium. This results in an improvement in spark efficiency (Wong et al. 1998). With a high generation of electrical discharge between the electrodes, atoms got diffused and entered the crack and void areas, thereby generating an alloyed surface with less micro-cracks (Figure 2.4 (b) and (c)). This technique is also used for depositing hard layers such as WC, TiC, etc. (Janmanee and Muttamara 2012). Use of conductive powders such as graphite and aluminium mixed in dielectric results in a fine surface finish of the workpiece with a roughness value (R_a) less than 1 µm. This is due to stable electrical discharges owing to the uniform dispersion of the powder particles (Wong et al. 1998).

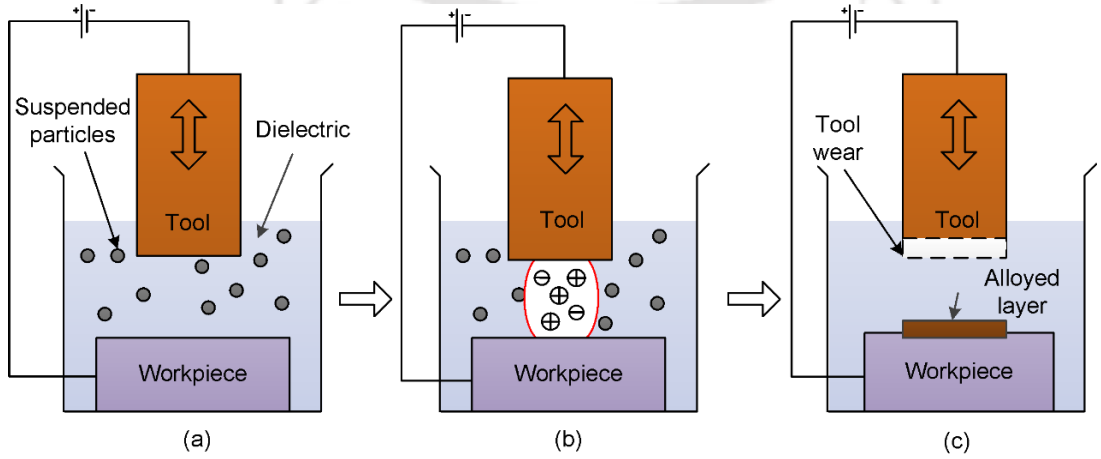

Figure 2.4 Schematic diagram for EDA using powder mixed dielectric (a) Suspension of powder particles; (b) Plasma channel formation and (c) Formation of alloyed layer

TH-2735_136103036

Kumar and Batra (2012) worked on alloying the surface of H13 die steel using suspended tungsten powder in the dielectric medium of commercial-grade kerosene. It was possible to achieve a maximum amount of 3.25 % tungsten on the machined surface. Favorable machining conditions for material transfer by EDM were found to be low discharge current (less than 5 A), shorter pulse on-time (less than 10 µs), longer pulse off-time (more than 50 µs), and negative tool polarity. Further, peak current was found to be the most significant factor for the phenomenon of surface modification. Janmanee and Muttamara (2012) studied the surface modification of tungsten carbide using titanium powder suspended hydrocarbon dielectric by EDM. Suspended Ti powder and carbon from decomposed dielectric lead to the formation of TiC layer, which thereby enhanced the surface hardness of the coated layer to 1750 HV. Varying current and duty cycles resulted in the change of titanium-coated layer thickness. Authors concluded that Ti powder suspension increases the hardness and reduces the micro-cracks of the WC work surface.

Electrical discharge machining (EDM) combined with ultrasonic machining (USM) was used to investigate the surface modification of Al–Zn–Mg alloy using Cu rod and by mixing TiC particles in the dielectric by Chen and Lin (2009). The experimental results showed an improvement in surface roughness as compared to that of the conventional EDM process. Further, a combination of EDM with USM yielded an alloyed layer that improved the hardness and wear resistance as compared to that of the conventional EDM process.

Observations

From the referred literature, it is observed that electric discharge alloying can be achieved by mixing suitable materials such as urea, TiC particles, and conductive powders like Si, Ti, Al, Cu, Cr, graphite, etc., in a suitable liquid dielectric medium. It is reported that a fine surface finish with R_a of less than 1 µm and a high hardness value of 1750 HV can be achieved by mixing desired powder particles in the dielectric medium. Therefore, surface modification by using powder mixed dielectric is beneficial in enhancing the surface property like improving in hardness and better surface roughness. In this aspect, surface modification of die steel material can be explored in EDA by varying the suspended powder particles like Ti, Al, urea, etc., and their percentage composition in the liquid dielectric medium.

TH-2735_136103036

2.3 Process modeling and simulation of electric discharge alloying

The fundamental principle of electric discharge alloying is similar to that of the electric discharge machining process. Both EDA and EDM occur as a result of electric discharge generated between the tool and the workpiece, which are submerged in a dielectric medium. In EDA, an alloyed layer is formed as a result of re-solidification of the melted tool and workpiece material over the workpiece, while in EDM, craters are formed due to melting and vaporization of the workpiece. The basic difference is that EDA deals with alloying of material while EDM deals with material removal. In EDA, deliberate transfer of the elements onto the workpiece is achieved by making the tool as cathode and the workpiece as the anode (discussed in Section 2.2.1). Limited works have been reported in modeling and simulation of electric discharge alloying; however, numerous models have been reported to establish the relationship between the input and output parameters in electric discharge machining. The models include dimensional analysis (Jeswani 1979), response surface methodology model (Puri and Bhattacharyya 2005), multiple statistical regression model (Petropoulos et al. 2004), partial differential equation model (Puri and Bhattacharyya 2003), artificial neural network model (Tsai and Wang 2001a) and thermal model (Rajurkar and Wang 1993; Salonitis et al. 2009). Following subsection deals with the relevant works that have been reported to model the process of EDA.

2.3.1 Dimensional analysis

Dimensional analysis is a mathematical approach for solving several engineering problems by correlating the variables involved in a physical process. It works by the systematic arrangement of the involved variables and combining them to form non-dimensional parameters. The variables are expressed in terms of the primary dimensions, namely mass, length, time, temperature. Then, the variables are correlated to establish an empirical relationship between them. Jeswani (1979) used dimensional analysis to establish an empirical relationship by correlating the pulse energy, evaporation temperature, specific heat, thermal conductivity, density, and latent heat of vaporization to determine the volume of material removed by using Buckingham's pi theorem. The results were compared for a variety of tool materials and observed that the established correlation showed a good fit for different types of tool material. Wang and Tsai (2001) developed a semi-empirical model to determine the material removal, tool wear, and surface roughness (Tsai and Wang 2001c) by using dimensional analysis. The prediction

TH-2735_136103036

showed a good agreement with the experimental results with an error of less than 10 % for surface finish and 20 % for material removal rate. The process parameters considered were peak current, polarity, pulse duration, and material properties such as density, specific heat, thermal conductivity, melting temperature, etc. Yahya and Manning (2004) also worked in determining the material removal rate by employing dimensional analysis. In their work, mass, length, time, and current were the primary dimensions considered. The process parameters considered were pulse on-time, discharge voltage, sparking frequency, and material property factor. The predicted result using the developed model compared well with the experimentally determined material removal rate.

2.3.2 Thermo-physical modeling of EDA

In this section, relevant literature on thermal modeling of the electric discharge phenomenon has been discussed. The fundamental working principle of EDA and EDM are similar in nature. The process of EDA evolved from EDM. Therefore, to develop a thermo-physical model of EDA, there is a need to understand the process modeling of EDM. In thermo-physical modeling of EDM, the main effect of electric discharge on the workpiece is considered as heat flux. The resultant temperature distribution of the workpiece after considering the governing equation and thermal boundary conditions has been studied. The reported literature on process modeling of electric discharge phenomenon have been categorized into analytical and numerical model depending on the approach and are summarized.

A. Analytical modeling

To understand the mechanism of electric discharge in EDA, there is a need to study and explore the models developed for EDM. Researchers worldwide have made various attempts since the early seventies to study the EDM phenomenon. Due to its stochastic and complex nature, modeling electric discharge in EDM has never been easy. The analysis was carried out by considering the concepts of electro-thermal and electro-mechanical of the electric discharge. Singh and Ghosh (1999) reported that the material removal in EDM at pulse durations less than 5 µs is due to the electrostatic forces. However, for long pulse durations, melting phenomenon dominates, and in such a case, the concept of electro-thermal is considered to be the mechanism for material removal.

The use of the electro-thermal model is widely accepted in modeling the EDM phenomenon. In this regard, thermal-based models have been developed by using the

TH-2735_136103036

mathematical equations of different modes of heat transfer. The heat conduction in solids without heat generation is given as

$$\frac{\partial^2 T}{\partial r^2}+\frac{1}{r}\frac{\partial T}{\partial r}+\frac{\partial^2 T}{\partial z^2}=\frac{1}{\alpha}\frac{\partial T}{\partial t} \tag{2.1}$$

where r and z are the radial and vertical distance in m, T is the temperature in K, t is time in s, and α is thermal diffusivity in m^2/s.

The thermal diffusivity α is given by

$$\alpha=\frac{k}{\rho C_p} \tag{2.2}$$

where ρ is the density of the material in kg/m^3, k is the thermal conductivity in W/mK and C_p is the specific heat in J/kg K.

Jilani and Pandey (1982) considered the effect of latent heat of melting as

$$\alpha'=\frac{k}{\rho\left(C_p+\frac{L_H}{T_m}\right)} \tag{2.3}$$

where L_H is the latent heat of melting J/kg and T_m is the melting temperature in K.

Researchers used various types of heat flux such as point heat source (Dibitonto et al. 1989; Patel et al. 1989), disc heat source (Beck 1981; Jilani and Pandey 1982).

For a point heat source, the heat flux equation considered as

$$q=\frac{F_A V I_d}{2\pi r} \tag{2.4}$$

For a disc heat source, the heat flux equation considered as

$$q=\frac{F_A V I_d}{2\pi R_{pc}^2} \tag{2.5}$$

where F_A is the fraction of the total energy transferred to the anode, V is the discharge voltage in V, I_d is the discharge current in A, r is the radial distance in m, R_{pc} is the radius of the heat source in m and q is the heat flux in W/m^2.

In the work of DiBitonto et al. (1989), the cathode erosion model and anode erosion model (Patel et al. 1989) were developed by considering point heat sources in a

TH-2735_136103036

spherical coordinate system. In the study, the fraction of energy transferred to the cathode (F_C) was considered to be 18.3 %, and that for the anode (F_A) was 8 %. These fraction of energy values were considered to be constant for all the theoretical computations. The material removal rate determined from the analytical results was compared with that of the experimental results for iron as a cathode and copper as an anode.

Beck (1981) considered a semi-infinite cylinder as the workpiece with a heat input of a disc heat source. In the model, transient temperature distribution was obtained from the approximation of an exact series solution consisting of only a few terms. Similarly, Jilani and Pandey (1982) applied a disc shape heat source with a cylindrical workpiece incorporating latent heat of melting. The computation time was found to be improved in their model. Pandey and Jilani (1986) computed the plasma channel growth considering the workpiece as a semi-infinite body with a disk-shaped heat source. The model predicted the re-solidified layer thickness, and the results were in good agreement with the published experimental results.

B. Numerical modeling of EDA

In order to understand the numerical modeling of EDA, there is a need to investigate the development of numerical modeling pertaining to the effects of electrical discharge phenomenon. In this regard, researchers have attempted different approaches for numerical modeling of EDM. The finite difference method (FDM) and finite element method (FEM) are the two numerical methods that are widely used in modeling of EDM. In these methods, thermal based model consisting of the transient nonlinear partial differential equation is being solved. In FDM, the solution approach is based on the Taylors series expansion, but FEM is based on integral minimization. FDM uses pointwise approximations to the governing equations, while FEM uses piecewise or regional approximations. In a comparison of the two approaches, FEM is more flexible as it can handle highly nonlinear equations such as complex geometry.

Thermal based numerical model of EDM is based on the determination of temperature distribution, surface roughness, maximum temperature, and also material removal rate. Salah et al. (2006) used FDM to predict the surface roughness and the removal rate of the workpiece and compared with the experimental data obtained during electrical discharge machining of SS316L. The experimental results were compared with the simulated results by considering two cases, viz., using constant thermal conductivity

TH-2735_136103036

and varying thermal conductivity. Results indicated that the use of temperature-dependent thermal conductivity gives a better result as compared to that of constant thermal conductivity. Izquierdo et al. (2009) modeled multiple discharges in EDM by employing FDM to predict the surface roughness and material removal rate from temperature distribution data. The model showed a 6 % error in the predicted result as compared with the experimental results.

Works have also been reported with the use of the finite element method to model the electric discharge phenomenon. Shankar et al. (1997) studied the profile of the spark generated during the discharge phenomenon. It was concluded that the middle section of the spark has a smaller cross-section and is non-cylindrical. Also, the spark radius at the anode surface is smaller than that at the cathode surface. Authors also analyzed the amount of total energy distributed to the cathode, anode, and inter-electrode gap for different currents, pulse duration, and inter-electrode distance values. The predicted material removal rate and the relative electrode wear rate were compared with the experimental results and found that they agreed well. In the work of Das et al. (2003), FEM based model was developed to predict the phase transformation and residual stresses developed due to the electric discharge phenomenon by studying the transient temperature distribution at all nodes of the work domain. Kansal et al. (2008) also used FEM to develop a model of powder mixed electric discharge machining by using an axisymmetric two-dimensional work domain. In their model, the heat source was considered to be Gaussian distribution. The effect of input process parameters, such as current, pulse on-time, pulse off-time and the fraction of energy distributed to workpiece, on to the material removal rate were studied.

Literature reports various works to determine the fraction of energy transferred to the work domain by using both FDM and FEM. This factor is one of the important parameters in modeling electric discharge phenomenon. Gostimirovic et al. (2012) reported that discharge energy plays a significant role in the machining characteristics in the EDM process. With the increase in discharge energy, the material removal rate increases up to an optimal value. The surface roughness and also the white layer thickness depends on the discharge energy. This discharge energy is basically a function of the fraction of energy distributed to the workpiece. Numerous works have been carried out to determine the F_A (fraction of energy transferred to the anode) or F_C (Fraction of energy transferred to cathode) value for the EDM process by inverse computation of the heat

TH-2735_136103036

conduction problem. Chiou et al. (2011) evaluated the input power and thermal conductivity of the workpiece by inverse estimation. Temperature measurements at various levels of discharge duration and at different locations were recorded, and the results were compared with the numerical solutions. On a similar front, Zhang et al. (2014b) worked on determining the F_A and F_C value and the plasma diameter during the EDM process by comparing the experimentally determined crater diameter with that of the numerical result. The work was carried out for both positive and negative polarity and also by using different dielectric media, viz. deionized water, kerosene, oil, and water in oil emulsion. Results indicated that the fraction of energy distribution is more in positive polarity regardless of the dielectric medium used. Further, in the work of Ming et al. (2017), the fraction of energy distributed for different workpieces was compared. It was reported that the fraction of energy value varied from material to material, i.e., 0.079 to 0.12 for Al 6061, 0.028 to 0.034 for Inconel 718 and 0.029 to 0.037 % for SKD 11.

In the case of the electric discharge alloying process, reverse polarity is generally preferred (Gangadhar et al. 1991), and hence, it becomes important to determine the fraction of energy (F_A) transferred to the workpiece which is made anode or the positive polarity. The fraction of energy transferred to the anode as determined by Patel et al. (1989) is a fixed value of 0.08. Shabgard et al. (2013) found out that the range of energy transferred to the anode was within 0.0413 to 0.364, and it was dependent on pulse duration and input discharge current. Algodi et al. (2018) computed the fraction of energy going to the workpiece during electrical discharge coating by comparing the experimentally determined crater radii with that of the numerically simulated results and concluded that the F_A varies from 0.07 to 0.53.

2.3.3 Soft computing based process modeling

Artificial neural network (ANN) is a soft computing technique used to develop a network that establishes a nonlinear relationship between the input process parameters and the desired outputs. It has the capability of functional mapping even from incomplete and noisy data. Researchers have employed ANN in EDA as it is very difficult to develop an analytical model due to the stochastic nature of the electric discharge phenomenon. Tsai and Wang compared various types of the neural network model to predict the surface finish (Tsai and Wang 2001b) and material removal rate (Tsai and Wang 2001a) in electric discharge machining and found that the adaptive network-based fuzzy interference system (ANFIS) is best suited for both cases. Panda and Bhoi (2005) used

TH-2735_136103036

feed-forward back propagation neural network using the Levenberg Marquardt technique to predict the material removal rate.

The concept of using a hybrid model of artificial neural network (ANN) and genetic algorithm (GA) for optimization of EDM process parameters has also been reported in numerous works. Mohana et al. (2009) used a hybrid model of ANN and GA to optimize the surface roughness. The model considered average current, average voltage, and machining time as the input parameters to develop the ANN model, and surface roughness is the output parameter. The developed model is optimized using GA by adjusting the weight of the network. In a similar manner, Ming et al. (2016) developed a backpropagation neural network (BPNN) and radial basis neural network (RBNN) to predict the material removal rate and surface roughness separately in the machining of SiC/Al composite by using EDM. The mean prediction error of the optimal network using BPNN was reported to be 10.61 %, while that using RBNN was 12.77 %. The network was further optimized by using GA.

Apart from developing a neural network to predict a single objective, Joshi and Pande (2011) developed an integrated FEM-ANN-GA model to train a network having multiple output parameters. The developed model was used to determine the optimum process conditions which would give the optimum performance of the EDM process in terms of material removal rate, tool wear rate, and crater depth. A backpropagation neural network with a scaled conjugate gradient algorithm was employed.

Scant work has been reported in developing of neural network in the field of electric discharge alloying. Patowari et al. (2010) developed a feed-forward back propagation neural network to predict the material deposition rate and average alloyed layer thickness in the electric discharge alloying process. In their work, the input parameters considered were compaction pressure, sintering temperature, peak current, pulse on-time, and pulse off-time and observed that for both the material deposition rate and alloyed layer thickness, the optimum network was attained with five number of neurons in the hidden layer.

Observations

Numerous mathematical models, both analytical and theoretical, have been developed to study the phenomenon of spark generated by EDM. Analytical methods give an exact solution, while numerical methods give an approximate solution to the mathematical

TH-2735_136103036

problem based on a trial and error procedure. Analytical methods can be time-consuming due to the complex functions involved or due to the large data size. In such cases, numerical methods are used since they are generally iterative techniques that use simple arithmetic operations to generate numerical solutions.

Extensive work has been carried out to predict the material removal rate, surface roughness, plasma flushing efficiency, residual stresses, and also the white layer thickness by thermal analysis in the electric discharge machining process. Researchers noted that the fraction of energy distributed to the work domain was the most important factor. Some attempts have been noted on the use of inverse estimation method in computation of input parameters. In spite of the extensive works carried out in modeling of EDM, scant work has been reported in the field of alloying or coating by EDM. Algodi et al. (2018) worked in modeling single spark interactions during electrical discharge coating. In their work, the experimentally determined alloyed layer thickness was compared with the numerically determined crater depth of the melted region, and the results were found to be satisfactory. Works have also been reported in the use of soft computing techniques like ANN to develop a network that can predict the material removal rate, surface roughness, etc. Use of hybrid models such as FEM-ANN-GA has also been reported.

2.4 Research gaps

In the field of electric discharge alloying, various experimental works have been reported. Deliberate transfer of materials or alloying is quite possible with the use of EDA. If the process of alloying by EDA could be well established, then it will play a vital role in the manufacturing industry due to its flexibility and is economical as compared to other available coting techniques such as PVD, CVD, magnetron sputtering, etc. These techniques require a specific vacuum chamber for its fabrication, thereby increasing the cost of production. The coating thickness is also limited to around 5 µm. Though CVD produces a quality coating, it has environmental hazards in terms of residual gases released during the chemical reaction process. Therefore, there is a need to come up with some efficient techniques to replace this coating technique. In view of this, electrical discharge alloying can be a highly promising technique. However, it limits its application in the industry due to the lack of information about the characteristics of the alloyed layer in terms of its hardness, wear resistance, corrosion resistance, and also thickness of the alloyed layer. Hence it has become an important area of research to be explored for

TH-2735_136103036

understanding the underlying mechanism by experimental investigations as well as by development of physics-based predictive model.

Works have been reported with the use of different types of tool material viz. solid tool electrode of electrolytic copper (Yan et al. 2005), graphite electrode (Chang-Bin et al. 2011), multilayer electrode of graphite and titanium (Hwang et al. 2010), etc. for alloying the workpiece to enhance its surface properties. Apart from the solid electrode, powder metallurgy tools have also been used for alloying as it has the flexibility to control the binding energy of the molecules by varying the compaction pressure, elemental composition and also sintering temperatures (Suzuki and Kobayashi 2013). Attempts have been carried out to improve functional surface characteristics such as wear and corrosion resistance by using varying PM tools such as Ti green compact, WC/Co, WC/Fe, TiC/WC/Co, Cr/Cu, WC/Cu, semi sintered TiC, etc. However, scant work has been reported in the alloying of titanium, aluminium, and nitrogen with AISI P20 mold steel by using EDA.

Other than the transfer of tool material over the workpiece by varying the tool material, alloying by EDA has also been done by using different dielectric such as urea mixed dielectric (Santos et al. 2017), mixing of different powder in the dielectric such as silicon powder (Kansal and Kumar 2007), titanium powder (Janmanee and Muttamara 2012), aluminum powder (Syed and Palaniyandi 2012), etc. for different purposes. From the reported literature, it is also observed that dielectric media plays a vital role in EDA. In this field, less work has been reported in surface alloying of mold steel by varying the dielectric media. Therefore, investigations can be made to study the effects of different dielectric media in EDA of mold steel. An extensive study can be made to study the influence of the input process parameters onto the alloyed layer thickness, hardness of the alloyed layer, material deposition rate, surface roughness, elemental transfer, hardness, wear and corrosion resistance behavior.

Apart from the experimental works reported to study the phenomenon of electric discharge alloying, researchers have also worked on modeling the EDA process. In spite of the fact that there is an abundant amount of literature available to model the discharge phenomenon in EDM to predict the material removal rate, surface roughness, tool wear rate, etc., limited work has been reported in the field of modeling the EDA phenomenon. A very scant work has been reported on the computation of alloyed layer thickness on the workpiece by employing accurate values of energy distribution factor. Further, it is

TH-2735_136103036

learned that less work is reported on the prediction of alloyed layer thickness using artificial neural networks and hard computing methods together. There is a need to develop a simple, efficient method to compute the alloyed layer thickness by using inverse computation of energy distribution among the electrodes.

2.5 Objectives of the present work

The main objective of the present work is to enhance the surface characteristics of AISI P20 mold steel viz. hardness, wear resistance, and corrosion resistance by using the electrical discharge alloying process. It was envisaged to achieve this by alloying titanium, aluminium, and nitrogen over AISI P20 mold steel. The sub-objectives of the present work are listed below.

- To deposit a layer of titanium and aluminium over AISI P20 mold steel by using the EDA process and powder metallurgy technology-based green tool electrodes.
- To critically analyze the deposition of desired elements with three types of dielectric media viz. hydrocarbon oil, deionized water, and urea mixed deionized water.
- To examine and measure the surface characteristics in terms of hardness, wear resistance, and corrosion resistance.
- To study the influence of the process parameters viz. discharge current, discharge duration, and type of dielectric medium on the alloyed layer thickness, material deposition rate, surface roughness, elemental distribution, hardness, wear-resistance, and corrosion resistance.
- To develop an integrated FEM – ANN methodology to compute the alloyed layer thickness by using inverse computation of energy distribution among the electrodes.

To achieve the mentioned objective, the present work has been planned in five stages, as shown in Figure 2.5.

Stage 1: In the first stage, a thorough literature survey has been carried out on the relevant research works that have been reported. Later, the works reported in the field of modeling were thoroughly studied. Thereafter, the research gaps were realized, and the objectives were derived, then the present work has been planned. In the present work, the alloying phenomenon of AISI P20 mold steel has been studied experimentally and numerically.

Stage 2: Alloying of AISI P20 mold steel with the use of powder metallurgy electrodes of titanium and aluminium has been carried out in a hydrocarbon oil dielectric medium.

TH-2735_136103036

The transfer of the tool elements and the decomposed hydrocarbon oil has been analyzed using EDS, and also the compounds formed were also studied using XRD analysis. Apart from this, the thickness of the alloyed layer and its hardness were determined, and the effect of input parameters was studied.

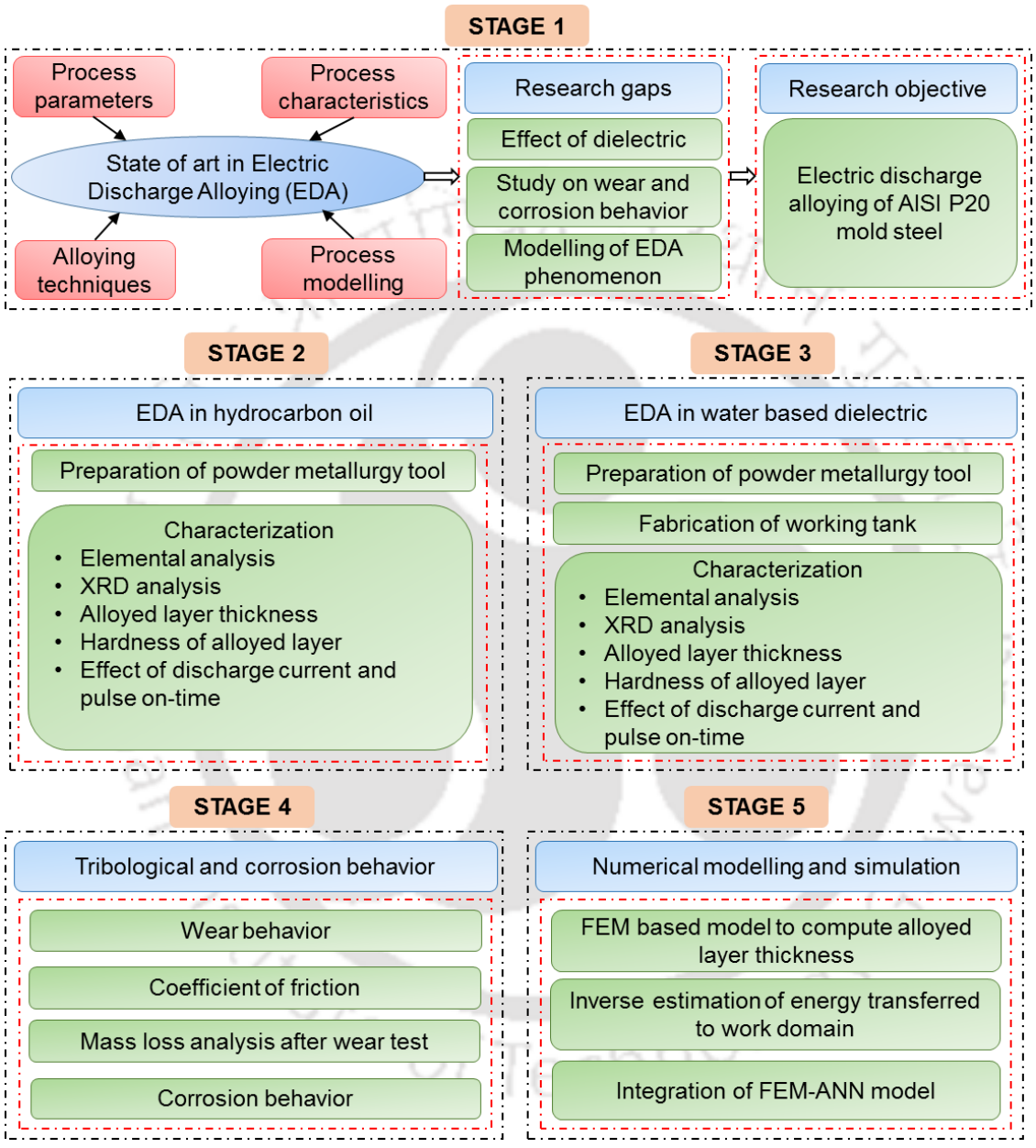

Figure 2.5 Overview of the present research work

Stage 3: In continuation with the electric discharge alloying of Ti and Al on AISI P20 mold steel using hydrocarbon oil, works have also been carried out in deionized water and urea mixed deionized water to study the effect of dielectric medium on the alloying phenomenon. Similar to the work carried out in stage 2, the elemental distribution, type

TH-2735_136103036

of compounds formed, alloyed layer thickness, and also the hardness of the alloyed layer were also determined.

Stage 4: A comparative study of the wear and corrosion behavior for the workpieces processed in the three different dielectric media viz. hydrocarbon oil, deionized water, and urea mixed deionized water was carried out.

Stage 5: A physics-based numerical model has been developed to predict the alloyed layer thickness. The alloyed layer thickness was computed by considering accurate values of the fraction of energy distributed to the workpiece. This fraction of energy distribution was determined by the inverse estimation method. Thereafter, the developed model has been integrated with ANN to develop a robust predictive model.

The details of the work are presented in the subsequent chapters.

TH-2735_136103036

TH-2735_136103036

CHAPTER 3

Experimental: Equipment, Materials, and Methodology

3.0 Scope

This chapter presents the details of the equipment used, materials, and the experimental methodology followed in the present work on the electrical discharge alloying of titanium and aluminium on the AISI P20 mold steel. The experimental setup, its components, range of parameters, and the working conditions are presented. Description and utility of various characterization tools adopted for the characterization of alloyed workpieces are presented. Various materials used and the procedures to prepare the tool and the workpiece are presented.

3.1 Equipment

This section discusses the equipment used in the present study, namely electric discharge machine, precision balance, hydraulic press, profilometer, sample molding press, optical microscope, micro-hardness tester, field emission scanning electron microscope (FESEM), energy-dispersive X-ray spectroscopy (EDS), X-ray diffraction (XRD), pin-on-disc setup and reference 600 galvanostat.

3.1.1 Experimental setup for electric discharge alloying

In the present study, electric discharge alloying has been carried out by using an electric discharge machine with facilities such as changing the tool polarity, dielectric medium, and using powder metallurgy tool. For this, a separate working tank has been fabricated. In electric discharge alloying, both the tool and workpiece are submerged in a dielectric medium, and the shape of the alloyed surface is complementary to the tool geometry. Figure 3.1 shows the schematic diagram of the experimental setup. The typical components are tool holder, work table, DC power supply, servo control unit, working tank, flushing unit, dielectric reservoir, filter pressure gauge, and high-pressure pump. For the present study, all the experimental works were performed by using ZNC/ENC35 die-sinking EDM (Made by: Sparkonix). It is shown in Figure 3.2. Pulsed power was supplied to the tool and workpiece electrodes from the DC power supply unit. In electric discharge alloying, the tool, workpiece, and the type of dielectric media play a very important role in the type of alloy formed over the workpiece after the EDA operation.

TH-2735_136103036

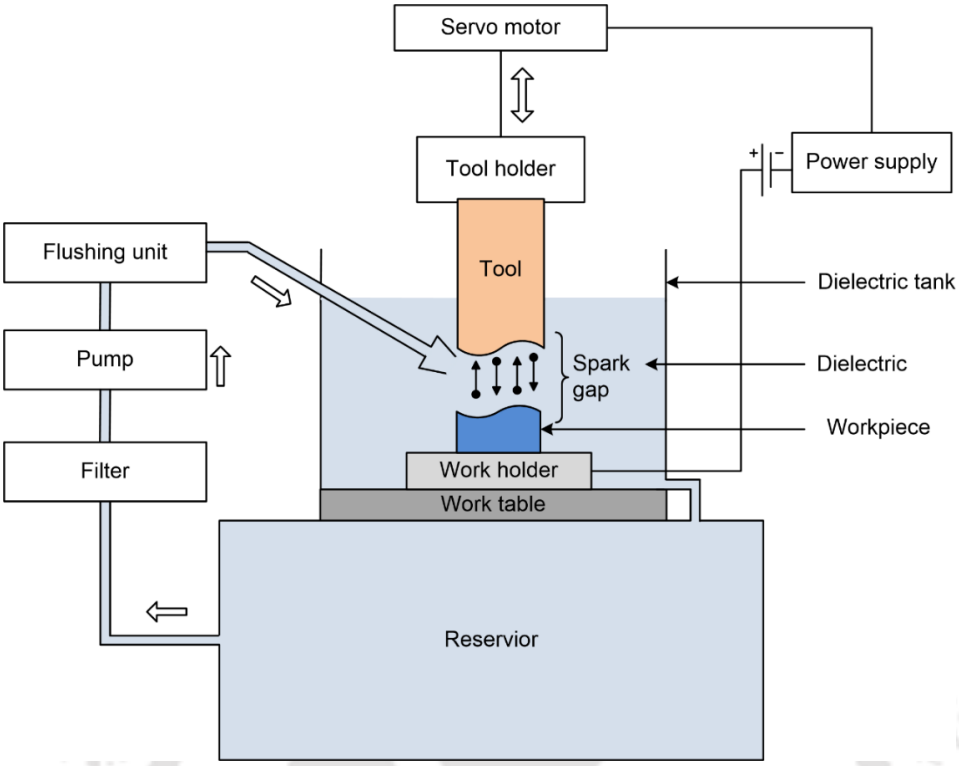

Figure 3.1 Schematic diagram of the experimental setup

Figure 3.2 Die sinking electric discharge machine used for EDA

TH-2735_136103036

A good tool electrode should have properties such as good thermal and electrical conductivity, machinability, should be readily available and inexpensive. In the present study, powder metallurgy tool electrode of Ti and Al has been used for alloying of AISI P20 mold steel. The tool electrode is fed along the Z-axis direction (vertical) into the workpiece by using a servo control feeding arrangement. The tool servo-mechanism is used to maintain a pre-determined working gap between the tool and the workpiece by sensing the gap voltage. Once the gap voltage sensor senses that the gap between the tool and the workpiece is bridged, a signal will be sent to the servo motor, and the tool will reverse its direction. This up and down motion of the tool ensures proper flushing of the unwanted debris, thereby resulting in a uniform sparking phenomenon. To ensure proper flushing, the dielectric fluid is flushed through the spark gap to remove gaseous and solid debris during the alloying process. The dielectric fluid should have high dielectric strength. The types of dielectric media used for the present study are hydrocarbon oil, deionized water, and urea mixed deionized water. Effective filtration of the dielectric fluid is essential.

Figure 3.3 shows the working tank used to perform the electric discharge alloying (EDA) in hydrocarbon oil. It consists of a tool electrode and the workpiece immersed in a dielectric with a provision for flushing the debris particles from the inter-electrode gap. The flushing pressure is being monitored by a pressure gauge. The dielectric stored in the reservoir is recirculated during the operation with the help of a high-pressure pump after filtration.

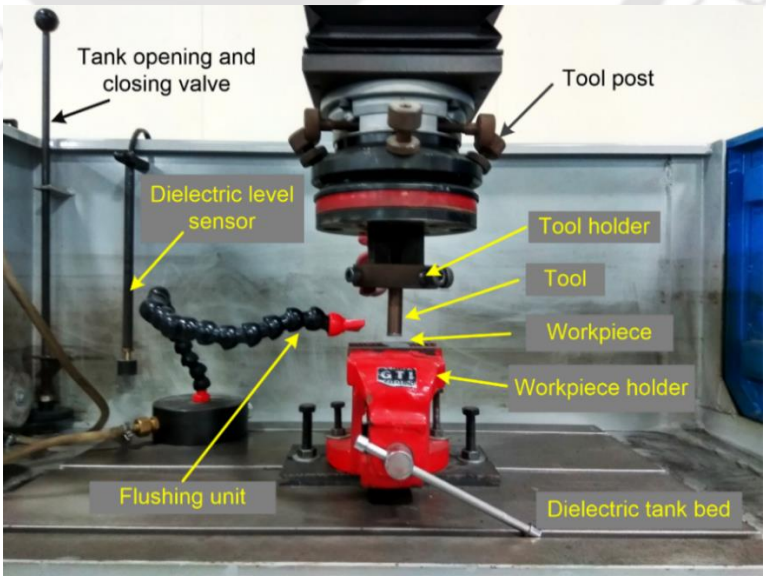

Figure 3.3 Working tank for using hydrocarbon oil as dielectric

TH-2735_136103036

To investigate the EDA phenomenon in the water-based dielectric, i.e., deionized water or urea mixed deionized water, a separate tank has been fabricated. The EDM machine has an oil level interlock. A minimum level of oil of 10 cm has to be provided to keep the machine running, the height of the tank is maintained in such a way that the oil level interlock is open, and the hydrocarbon oil should not enter and mix with the dielectric liquid in the fabricated tank. Figure 3.4 shows the tool and workpiece arrangement with the fabricated tank. The fabricated tank is of dimension 400 × 350 mm with a height of 230 mm. It is of capacity to hold 30 L of liquid and is made from a tin sheet of 2 mm thick. To prevent the leakage, the joints were sealed at the outer cover. The tank is fitted onto the machine bed. The working fluid is poured into the tank only after ensuring that the tank is leak-proof. During the EDA operation, debris in the inter-electrode gap needs to be removed as the debris can cause arcing during the EDA operation. For this purpose, a pump is provided in the tank to ensure effective flushing of the debris.

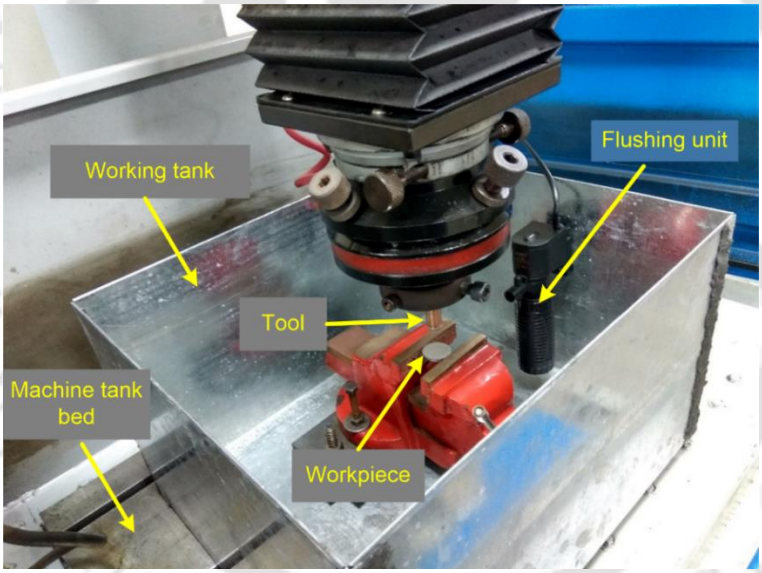

Figure 3.4 Fabricated working tank arrangement for using water-based dielectric

The controllable input machine parameters of EDA are discharge current, discharge voltage, pulse on-time and off-time, duty cycle, flushing pressure, and polarity. The available ranges of the input parameters are as tabulated in Table 3.1. These parameters have their impact on output parameters such as tool wear, material deposition, hardness of the alloyed surface, surface finish, dimensional accuracy, and overall surface integrity.

TH-2735_136103036

Table 3.1 Machine parameters and their available ranges

Sl. no	Parameter	Minimum value	Maximum value	In steps of
1.	Discharge current, (A)	0	49	1
2.	Pulse on – time, (μs)	0.5	1050	1 to 99
3.	Duty cycle (%)	1 (10%)	9 (90%)	1
4.	Discharge voltage, (V)	10	99	1
5.	Flushing pressure ($lb/inch^2$)	0	30	1
6.	Polarity	Normal (Tool as positive terminal) Reverse (Tool as negative terminal)		

The main input parameters considered in the present study are discussed below.

A. Discharge current

This is the amount of current available during the discharge phenomenon. It is one of the main input parameters which controls the output performance. A higher amount of discharge currents results in higher material removal but at the cost of surface roughness. Low discharge currents are generally used to get a fine surface finish. The experimental setup used has maximum discharge current settings of up to 49 A, and it can be changed in steps of one.

B. Discharge voltage

It is the reference voltage set between the tool and the workpiece, and it determines the width of the spark gap. Higher voltage settings increase the gap, which improves the flushing conditions and helps to stabilize the machining performance. The available range in the present setup is 10 to 99 V, and it can be changed in steps of 1.

C. Pulse on-time and pulse off-time

The electric discharge phenomenon occurs in a cyclic manner, usually in units of microseconds. Each cycle is constituted of pulse on-time and pulse off-time. The effective discharge phenomenon occurs during the pulse on-time wherein there will be a flow of current. Right after the occurrence of the discharge, the dielectric behaves like an insulator until the next discharge. This duration is termed pulse off-time. The output performance

TH-2735_136103036

of EDA, such as material deposition rate, alloyed layer thickness, surface roughness, etc., is dependent on the amount of energy applied during the pulse on-time. The pulse on-time can be set as per requirement in the range of 0.5 to 1050 µs. In the present setup, the pulse off-time cannot be set, but the duty cycle can be set, and it is discussed in the next sub-section.

D. Duty cycle

Duty cycle is the ratio of the pulse on-time to the total cycle time (pulse on-time + pulse off-time). It is one of the important input parameters as the inappropriate setting of the duty cycle can result in ineffective flushing of the unwanted debris formed during the discharge phenomenon. It is denoted by τ , and the expression is given by

$$\text{Duty cycle, } \tau = \frac{t_{on}}{t_{on} + t_{off}} \tag{3.1}$$

where t_{on} is the pulse on-time in µs and t_{off} is the pulse off-time in µs.

The duty cycle is expressed in percentage, and the available range of the duty cycle in the present setup is from 10 % to 90 %. The machine takes the value of duty cycle in the range of 1 to 9, wherein 1 indicates 10 % and 9 indicates 90 %. The value can be varied in steps of 1, i.e., by 10 %.

E. Polarity

Normal and reverse are the two polarity setting available in the machine. In normal polarity, the tool is connected to the positive terminal and the workpiece to the negative terminal, while in reverse polarity, the tool is connected to the negative terminal and the workpiece to the positive terminal. In general, normal polarity is preferred for machining operation, while reverse polarity is considered for the alloying process. Higher energy distribution is attained at the negative terminal as compared with the positive terminal. In EDA, higher erosion of the tool is anticipated for deliberate transfer of the tool material over the workpiece. Therefore, for the present study, negative tool polarity is considered.

3.1.2 Precision electronic balance

Precision electronic balance (Made by: Citizon) available at Advanced Manufacturing Laboratory, IIT Guwahati, has been used for measuring the weight of powders, weight of

TH-2735_136103036

the workpiece before and after EDA operation. Based on these values, the material deposition rate. This balance has a measuring accuracy of up to four decimal places.

3.1.3 Hydraulic press

Hydraulic press (Made by: AMT machine and tools) available at Advanced Manufacturing Laboratory, IIT Guwahati was used to prepare powder metallurgy compacts or pellets. Figure 3.5 shows the hydraulic machine used. The press has a loading capacity of up to 60 tons in steps of 2. The powder to be compacted is taken in a die set and kept in between the plates of the press. The load is gradually applied using the lever via the hydraulic oil.

Figure 3.5 Hydraulic press

3.1.4 Profilometer

Contact stylus profilometer (Made by: Mitutoyo) available at Advanced Manufacturing Laboratory, IIT Guwahati has been used for measuring the surface roughness of the EDA surface. The stylus of the profilometer moves over the workpiece for the predefined length, and the roughness was measured for that specific path. After scanning the surface for its peaks and valleys, the profilometer calculates the surface roughness in terms of R_a

TH-2735_136103036

(average roughness) and R_z (difference between tallest peak and deepest valley), and the results were displayed. The roughness values were given in µm. For the present study, the surface roughness was measured for a length of 3 mm, and R_a was considered. The roughness measurement was taken at five different scan paths, and the average value was considered for the analysis.

3.1.5 Sample molding press

Sample molding press (Made by: Buehler) available at Material Science Laboratory, IIT Guwahati has been used to prepare molds for the characterization of workpieces after EDA operation. It is shown in Figure 3.6. It is used for the hot mounting of the workpiece that is to be polished. For preparing the mold, the workpiece was placed inside the mold cavity and was filled with the molding powder. Later, with the help of an electric heater, the mold was heated up, and the molding powder was compacted by applying pressure with the help of the lever. Thereafter, the heater was removed, and the mold was cooled down for around 20 mins, and the mounted workpiece was removed from the mold cavity.

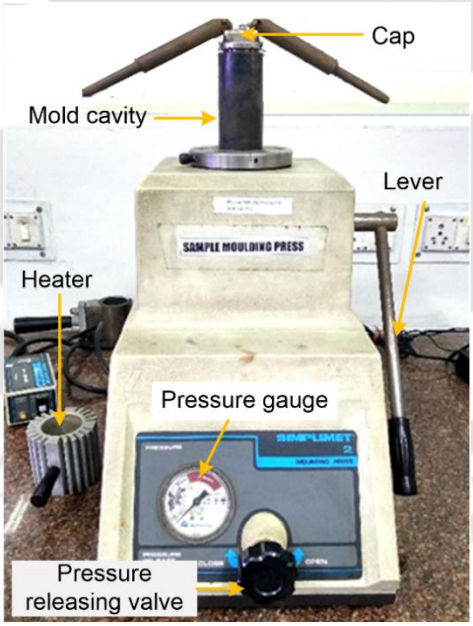

Figure 3.6 Sample molding press

3.1.6 Single disc polishing machine

Single disc polishing machine (Made by: Metco and Model: Bainpol) available at Material Science Laboratory, IIT Guwahati has been used for polishing of mounted workpieces. It consists of an 8” aluminium rotating disc, and the rotational speed of the

TH-2735_136103036

disc can be adjusted in the range of 50 to 1000 rpm. Figure 3.7 shows the single-disc polishing machine.

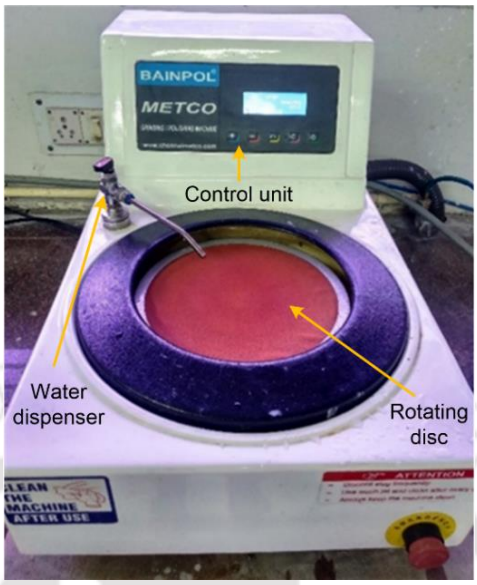

Figure 3.7 Single disc polishing machine

3.1.7 Optical microscope

An optical microscope (Made by: Carl ZEISS), available at Material Science Laboratory, IIT Guwahati with magnification up to 200× was used to measure the alloyed layer thickness, indention size and to capture the morphology of the workpiece. It is shown in Figure 3.8.

Figure 3.8 Optical microscope

TH-2735_136103036

3.1.8 Microhardness tester

Vickers microhardness tester (Made by: Omni Tech) was used to measure the hardness of the alloyed region. Its loading capacity ranges from 1 to 2000 gf, and the size of the indenter is 0.5 µm. It is equipped with a magnifying lens of 10 ×. The pictorial image of the instrument is shown in Figure 3.9 and is available at Material Science Laboratory, IIT Guwahati.

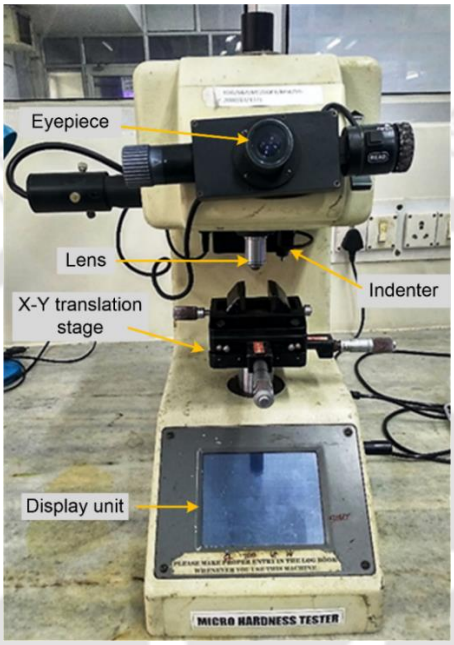

Figure 3.9 Microhardness tester

3.1.9 Field emission scanning electron microscope (FESEM) integrated with energy dispersive X-ray spectroscopy (EDS)

Field emission scanning electron microscope (Made by: Zeiss sigma) integrated with energy dispersive X-ray spectroscopy (EDS) available Central Instrumentation Facility, IIT Guwahati has been utilized for elemental analysis of the workpiece. The FESEM has magnification up to 15,000 × and it was used to study the morphology of the alloyed surface.

3.1.10 X-ray diffractometer (XRD)

The XRD diffractometer (Made by: Xpert) available at Advanced Manufacturing Laboratory, IIT Guwahati has been used to perform the XRD analysis of the EDA surface. For the present study, the XRD was used with filtered Cu-Kα1 radiation ($\lambda = 0.154056$Å) at 40 kV and 20 mA. The diffraction angle ranges from 0˚ to 90˚.

TH-2735_136103036

3.1.11 Pin-on-disc

The pin-on-disc machine (Made by: Ducom) available at Tribology laboratory, IIT Guwahati, was used for sliding of the alloyed surface. The machine consists of a rotating disc made up of steel with 100 mm diameter, which can be rotated at varying speeds. A strain gauge-based load cell with 0.1 N accuracy and a linear variable differential transformer (LVDT) sensor with an accuracy of 0.1µm is attached with the machine to determine the frictional force and wear, respectively. Figure 3.10 (a) shows a pictorial view of the setup, and Figure 3.10 (b) shows the schematic of pin-on-disc setup.

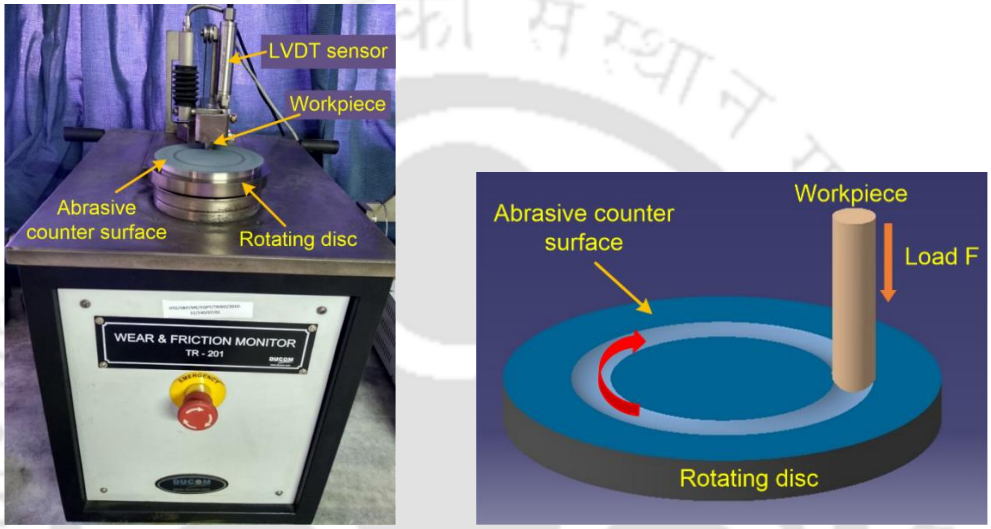

(a) (b)

Figure 3.10 (a) Pin-on-disc machine; (b) Schematic diagram of the working of pin-on-disc

3.1.12 Reference 600 galvanostat

The corrosion tests were carried out by using Reference 600 galvanostat (Made by: Gamry instruments) available at Centre for Nanotechnology, IIT Guwahati. Three-electrode electrochemical corrosion test setup was used. The three-electrode is comprised of a test workpiece as working electrode, saturated calomel electrode (SCE) as reference electrode, and a Platinum wire as the counter electrode.

The following section deals with the materials employed for the present study. The composition of the workpiece and the tool materials used have been discussed in detail.

3.2 Materials

The workpiece used for the present study was AISI P20 mold steel. Energy-dispersive X-ray spectroscopy (EDS) analysis was carried out to determine the composition of the

TH-2735_136103036

elements present in the workpiece before the alloying operation. The composition of the was found to be 2.1 wt. % Cr, 0.5 wt. % Si, 97.2 wt. % Fe and traces of Mn, P, C, and S. The EDS spectra is shown in Figure 3.11.

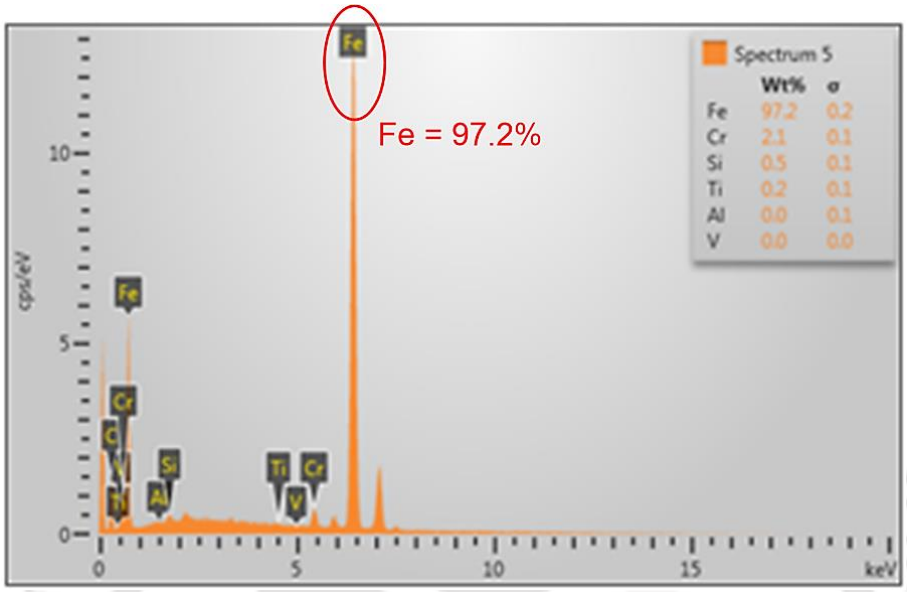

Figure 3.11 EDS spectra showing the composition of the parent material P20 mold steel

The tool electrode material employed for the present study was a green compact powder metallurgy tool made of titanium and aluminium. For this study, 99 % pure titanium and aluminium powders with particle sizes of 300 µm and 40 µm respectively have been used. The preparation procedure for the workpiece and powder metallurgy tool has been discussed in detail in the following section.

3.3 Experimental methodology

This section presents the methodology adopted for the experimental investigation during alloying Ti and Al onto the surface of AISI P20 mold steel using EDA. The overview of the experimental work is shown in Figure 3.12. The first step for the electric discharge alloying was the preparation of the workpiece and the tool electrode. Thereafter, experiments were performed at varying processing conditions. In the present study, the alloying process was carried out in three different types of dielectric media, viz. hydrocarbon oil, deionized water, and urea mixed deionized water. After successful experimentation, a parametric study was performed to study the effect of pulse on-time and discharge current onto the alloyed layer thickness, material deposition rate, and the surface roughness of the workpiece after EDA operation. Characterization of the alloyed surfaces was carried out to study the presence of elements of tool material decomposed

TH-2735_136103036

dielectric material element and their compounds onto the workpiece. Further, the hardness of the alloyed layer, the wear, and the corrosion behavior of the alloyed surfaces were also examined.

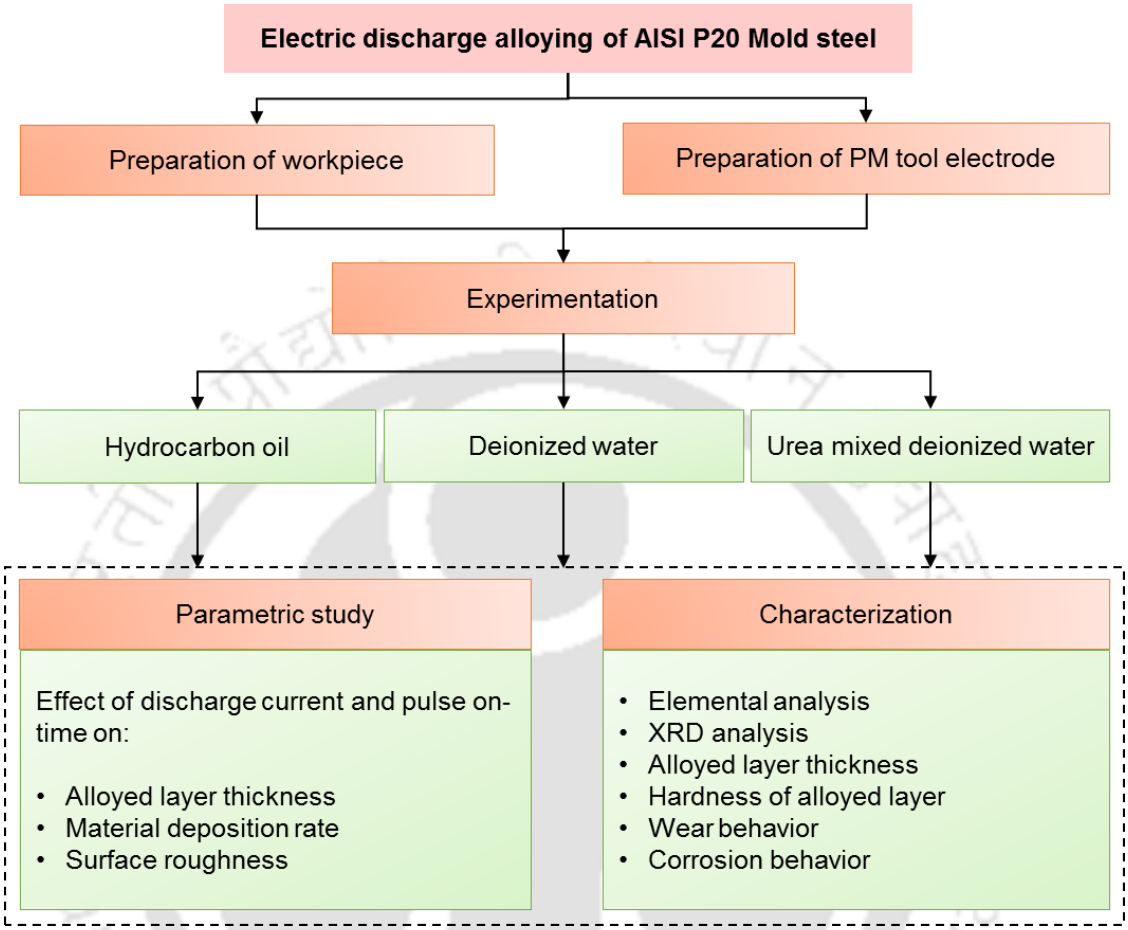

Figure 3.12 Overview of the experimental work

Following sub-section deals with the step-by-step procedure for workpiece and tool preparation in detail.

3.3.1 Workpiece preparation

The workpiece used for the present study was AISI P20 mold steel. The workpiece was having 24 mm diameter and 2.5 mm thickness (Figure 3.13). Before conducting the experiments, unwanted materials were removed by polishing the surface with emery sheets of grit numbers 400 - 2000. Once the surface is clean enough, it was washed with acetone and made ready for EDA.

TH-2735_136103036

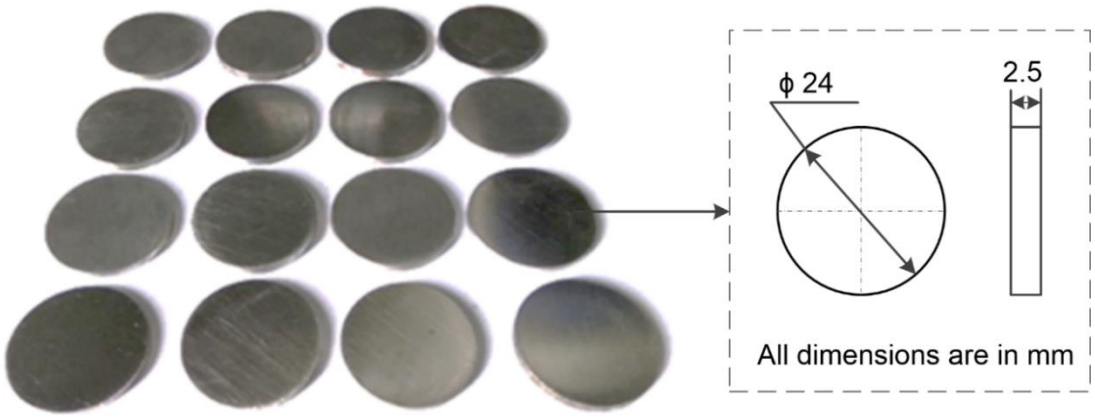

Figure 3.13 Camera image of the workpieces prepared for EDA

3.3.2 Powder metallurgy tool preparation

The procedure followed for the preparation of the powder metallurgy tool of titanium and aluminium is depicted in Figure 3.14.

The steps followed were:

- **Step 1** - Accurate weights of the powders to be mixed were measured using an electronic precision balance.
- **Step 2** - The powders with the required composition were mixed thoroughly using mortar and pestle.
- **Step 3** - The mixed powders were then transferred to a die cavity. The die set used for this study is of 13 mm diameter.
- **Step 4** – The mixed powders were then compacted using a hydraulic press at the desired pressure, and the compacted powder was then removed from the die set in the form of a pellet.
- **Step 5** - The pellet was then pasted over a copper rod with the help of an electrically conductive silver-loaded epoxy adhesive. The copper rod acts as a tool holder, and hence the PM tool is ready for EDA.

TH-2735_136103036

Figure 3.14 Preparation of powder metallurgy tool for EDA

TH-2735_136103036

3.3.3 Experimental details

After the preparation of the workpieces and the PM tools, experiments were planned. Before conducting the experiments, preliminary experiments were performed to explore the effect of the available input ranges of the process parameters by analyzing the sparking behavior. Several trials have been done, and the results of some of the trials are given in Table 3.2.

Table 3.2 Preliminary experimental results

Sl. No.	Discharge current, A	Pulse on-time, µs	Tool composition		Compaction pressure, MPa	Remarks
			Ti	Al		
1.	8	546	100 %	-	443	Arcing
2.	8	546	75 %	25 %	443	Arcing
3.	8	546	50 %	50 %	296	Tool breakage
4.	8	546	50 %	50 %	443	Uniform sparking
5.	8	546	50 %	50 %	591	Uniform sparking
6.	4	546	50 %	50 %	443	Non-uniform sparking
7.	6	546	50 %	50 %	443	Uniform sparking
8.	14	546	50 %	50 %	443	Rough surface
9.	6	396	50 %	50 %	443	Non-uniform sparking
10.	6	1166	50 %	50 %	443	Arcing

During the trial, arcing was observed that at 100 % and 75 % titanium composition (Sl. No. 1 and 2). This is because, Ti has very low electrical conductivity as compared to that of Al. This resulted in inconsistent sparking or arcing. Further, with a tool composition of 50 % Ti and 50 % Al compacted at a low compaction pressure of 296 MPa (Sl. No. 3), tool breakage occurred due to weak binding. With higher compaction pressure of 443 MPa and 591 MPa (Sl. No. 4 and 5) and tool composition of 50 % Ti and 50 % Al, the compacted pellet possesses sufficient strength and resulted in uniform sparking during the operation. However, for the present study, tool composition of 50 % Ti and 50 % Al

TH-2735_136103036

compacted at 443 MPa was considered, as lesser compaction pressure gives lesser strength and higher erosion.

Further, to set the range of discharge current and pulse on-time, extensive experiments were conducted at various combinations as listed in Table 3.2. From the study, it was observed that at the low current of 4 A, inefficient sparking was observed, and at a high current of 14 A, the sparking was very rigorous, thereby resulting in very rough surfaces. Also, at a low pulse on-time of 396 µs, there was non-uniform sparking, and at a high pulse on-time of 1166 µs, arcing was observed. Therefore, the range of the discharge current used was 6 A to 12 A, and the pulse on-time was in the range of 546 µs to 1006 µs. To perform the detailed study, four levels of discharge current and pulse on-time were considered. For this study, full factorial experiments were carried out. Experiments were conducted separately by using three dielectric media viz. hydrocarbon oil, deionized water, and urea mixed deionized water. To check the repeatability, each experiment was repeated three times. The experimental process conditions considered for the study are listed in Table 3.3.

Table 3.3 Experimental process conditions

Parameters	Conditions / Values
Dielectric medium	1. Hydrocarbon oil
	2. Deionized water
	3. Urea mixed deionized water (10 g/L concentration)
Pulse on-time, t_{on} (µs)	546, 706, 856 and 1006
Discharge current, I_d (A)	6, 8, 10, 12
Discharge voltage (V)	40
Duty cycle	50 %
Workpiece material	AISI P20 mold steel
Tool material	13 mm diameter PM tool of 50 % Ti and 50 % Al
Polarity	Tool electrode (Negative terminal)
Processing time	5 min

3.3.4 Characterization procedure

To characterize the alloyed workpiece for its alloyed layer thickness, layer hardness, wear resistance, and corrosion resistance, the following procedures have been followed.

TH-2735_136103036

A. Alloyed layer thickness

To study the alloyed layer thickness, the workpieces were prepared by using computer numerically controlled (CNC) wire cut EDM. The cross-sectioned workpieces were mounted using a sample molding press (Section 3.1.5). Then, they were polished to obtain a mirror finish using a single disc polishing machine (Section 3.1.6). Emery sheets of various grit numbers 400, 600, 800, 1000, 1200, 1500, and 2000 were used in sequence to obtain a finely polished surface. The workpieces were then polished using velvet cloth with Al_2O_3 powder suspension to further polish the workpiece. After achieving the mirror finish surface, the workpieces were etched with 10 % nital solution to make the interface of the alloyed layer with the parent material visible. Thereafter, the thickness of the alloyed layer was measured by using the optical microscope.

B. Hardness of the alloyed layer

To determine the hardness of the alloyed layer, the Vickers microhardness test was carried out with 300 gf load along the transverse section of the polished alloyed workpiece. The indentation size was measured with the help of an optical microscope, and the Vickers hardness value was calculated by using the expression

$$HV_{0.3} = 0.0018 \times \frac{F}{d^2} \tag{3.2}$$

where F is load in gf and d is the mean diagonal of the indent formed in mm^2.

C. Wear test

The wear test of both the unprocessed workpiece and EDA processed workpieces were performed separately. The processing conditions for the EDA workpieces considered for the wear test are pulse on-time of 546 µs and discharge current of 10 A with three different dielectric media of hydrocarbon oil, deionized water, and urea mixed deionized water. The workpiece specimen used for the wear test was of diameter 10 mm and height of 50 mm. Powder metallurgy tool electrode of Ti and Al with 13 mm diameter was used. To check the repeatability, the wear test was performed three times. The results are presented in the subsequent chapters. In the present study, an abrasive wear test has been conducted by using silicon carbide abrasive sheet of 1000 grit size. For this, an abrasive sheet was placed on the steel disc. The abrasive sheet was changed for every test so that the initial testing conditions were same for all the test. A wear track diameter of 60 mm with a rotational speed of 160 rpm was considered for the study. The sliding speed employed

TH-2735_136103036

was 0.5 m/s. The wear test experiments were conducted for 30 min by applying a load of 5 N.

D. Corrosion test

Electrochemical corrosion test was conducted to check the corrosion resistance of both the unprocessed workpiece and EDA processed workpiece separately. The test was conducted in 3.5 % NaCl electrolyte solution which was maintained at 25 °C temperature. Before the corrosion test, the cylindrical surface of the workpiece specimen was insulated by painting, and the end surface were not painted. This made the chemical reaction occur only at the exposed end surface only. The exposed end surface area was of 0.78 cm^2.

3.4 Summary

This chapter presents details of the equipment used, materials and methodology followed for the present study. The characterization procedure along with the results of preliminary experimental observation have also been discussed. From the observations, the working range of the input parameters and the fixed parameters were derived.

- For the present study, AISI P20 mold steel was used as the workpiece material, and powder metallurgy green compact of Ti and Al was employed as the tool material.
- Three types of dielectric media viz. hydrocarbon oil, deionized water, and urea mixed deionized water have been considered. A separate tank has been fabricated for using a water-based dielectric, and the details are presented.
- From the preliminary experimental results, tool composition of 50 % Ti and 50 % Al compacted at a compaction pressure of 443 MPa was considered to be the suitable parameters for further comprehensive investigation.
- The range of the discharge current setting was fixed in the range of 6 A to 12 A, and the pulse on-time setting was fixed in the range of 546 µs to 1006 µs.

The subsequent chapters present the comprehensive experimental and numerical investigations into the EDA of Ti and Al over the P20 mold steel.

TH-2735_136103036

TH-2735_136103036

CHAPTER 4

Experimental Investigations into Electric Discharge Alloying of Ti and Al on P20 Mold Steel with Hydrocarbon Oil Dielectric Medium

4.0 Scope

This chapter presents the research findings of the experimental work carried out on the electrical discharge alloying (EDA) of Ti and Al on AISI P20 mold steel in hydrocarbon oil dielectric by using titanium and aluminium powder compact electrode. The investigation into the elemental transfer onto the workpiece using energy dispersive X-ray spectroscopy (EDS) analysis and the formation of different phases using XRD analysis are presented. The effects of EDA process conditions on the alloyed layer thickness, material deposition rate, and surface roughness are also presented. Apart from these, hardness analysis of the deposited layer was carried out, and the results have been presented. Finally, the summary of the chapter has been presented.

4.1 Motivation

AISI P20 mold steel is an industrially important material commonly used in the manufacture of dies and molds. It is subjected to high wear and corrosive conditions in harsh shop floor conditions. It is thus essential to enhance its surface characteristics such as hardness, wear resistance, and corrosion resistance. In this work, it is envisaged that the powder metallurgical (PM) based tool electrode may help in the deposition of a significant amount of the desired element on the work part during the electric discharge alloying (EDA). Therefore, it was decided to perform a detailed material characterization of the alloyed portion of the workpiece to examine the efficacy of the EDA process. To carry out the proposed work, powder metallurgy compact was used as the tool material without any heat treatment or sintering process. The compact prepared without any heat treatment process is generally termed as green compact. For the present study, Ti and Al based powder metallurgy green compact electrode was used as the tool for EDA of AISI P20 mold steel, and the dielectric medium used was hydrocarbon oil.

4.2 Electric discharge alloying of AISI P20 mold steel in hydrocarbon oil

This section deals with the experimental results obtained after conducting a set of 16 experiments by varying the discharge current: 6, 8, 10, and 12 A, and pulse on-time: 546,

TH-2735_136103036

706, 856, and 1006 µs. Other parameters, namely, duty factor, tool composition, and polarity, were kept constant. The list of chosen parameters is presented in Table 3.3 of Chapter 3, Page No. 49. Each experiment was repeated thrice. The top surface of the tool and workpiece processed at pulse on-time (t_{on}) of 706 µs and discharge current (I_d) of 8 A is shown in Figure 4.1 (a) and (b), respectively. From Figure 4.1 (b), it can be observed that a circular region different from the parent material is formed after the EDA operation. This can be inferred from the difference in surface morphology of the parent and EDA processed region. The red dashed circle shown in Figure 4.1 (b) indicates the demarcation between the EDA processed region and the parent AISI P20 mold steel. The figure depicts that uniform sparking has taken place all over the sparking area in between the tool and the workpiece since the diameter of the circular region was noted to be 13 mm, which is the same as that of the tool diameter (Figure 4.1 (a)).

Figure 4.1 Top surface of (a) Tool and (b) Workpiece after EDA at t_{on} of 706 µs and I_d of 8 A

To analyze the EDA surface morphology, optical microscope and FESEM images were taken. Figure 4.2(a) displays the optical micrograph at 5×, and Figure 4.2(b) shows the FESEM micrograph at 1000× for the workpiece processed at t_{on} of 706 µs and I_d of 8 A. From Figure 4.2(a) it is observed that thermal effect such as melting of the workpiece has taken place. To analyze the presence of cracks or blowholes, the FESEM image was taken at 1000× for the same workpiece. Only a few micro-cracks and blowholes are observed at the top surface (Figure 4.2b). The presence of a few micro-cracks and blowholes can be attributed to the filling up of the surface by alloying of the tool material onto the workpiece. This presence of micro-cracks at the EDA surface is due to the difference in the thermal properties of the alloying tool and workpiece.

TH-2735_136103036

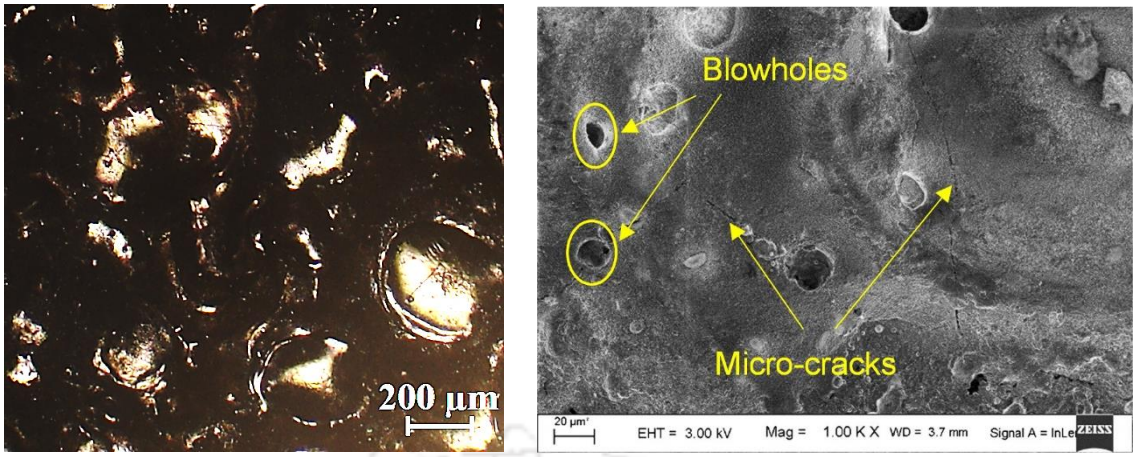

(a) (b)

Figure 4.2 (a) Optical micrograph at 5× and (b) FESEM micrograph at 1000× for EDA workpiece processed at t_{on} of 706 µs and I_d of 8 A

Figures 4.3(a) and 4.3(b) display the FESEM images of the cross-sectioned EDA workpiece at the edge and the middle section of the EDA workpiece, respectively. The interface between the alloyed region and the parent material can be observed. It can be inferred that a distinct layer has been deposited on the workpiece by the EDA process.

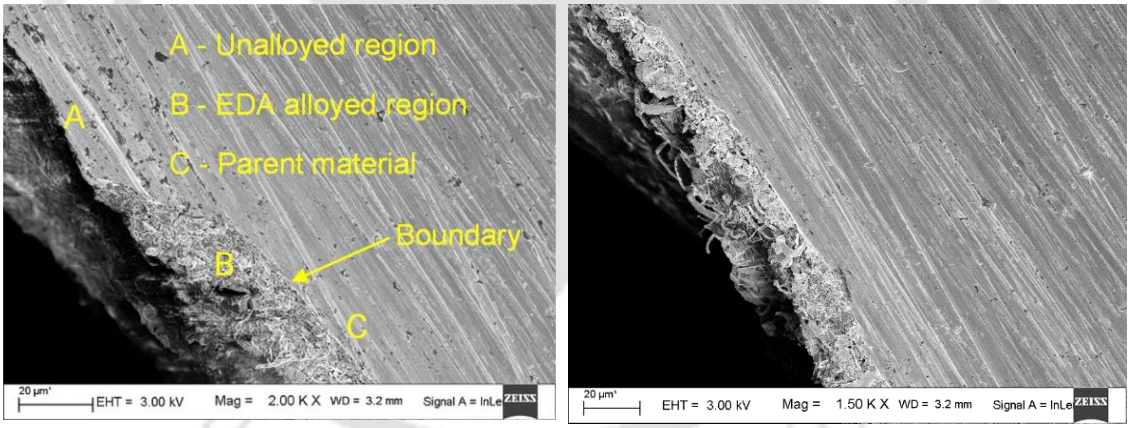

(a) (b)

Figure 4.3 FESEM micrographs showing the cross-sectioned of workpieces at magnifications of (a) 2000× at the edge and (b) 1500× at the middle section (The process conditions employed were: t_{on} of 706 µs and I_d of 8 A)

To further analyze the presence of the different elements, elemental analysis has been carried out using EDS, and the results are discussed in the following sub-section.

TH-2735_136103036

4.2.1 Elemental Analysis

To determine the percentage transfer of tool elements over the alloyed workpiece processed at t_{on} of 546 µs and I_d of 10 A, EDS analysis was performed. Area scan was carried out at various regions on the top surface of the workpiece. Figure 4.4 represents the micrograph and the composition of elements in spectrums 10, 11, 12, 13, 14, and 15, along with the EDS spectra. It can be observed from the EDS spectra that there is a transfer of tool element viz. Ti and Al over the surface of the workpiece. A maximum of 18 % Ti with 11.8 % Al could be observed in spectrum 12, and a maximum of 18.7 % Al with 10.9 % Ti could be observed in spectrum 15. AISI P20 mold steel being the parent material, composition of Fe in the alloyed region is in the range of 17 - 33 %, which is fairly reduced from a value of 97 % in comparison to that of parent material shown in Chapter 3, Figure 3.11, Page No 44.

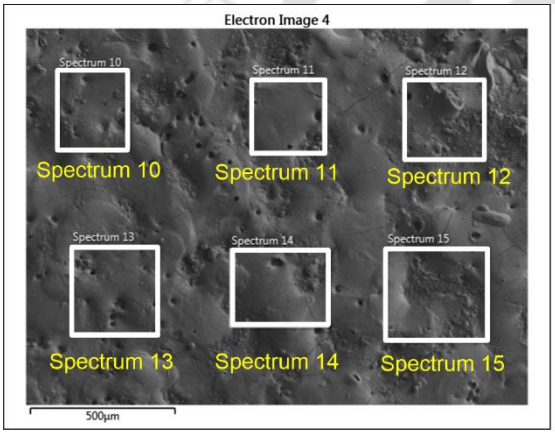

Elemental composition (wt. %)					
Spectrum	Ti	Al	Fe	O	C
10	12.9	16.1	26.7	16.5	26.8
11	13.0	18.2	32.6	14.0	21.1
12	18.0	11.8	17.0	23.1	26.5
13	19.0	14.4	23.8	19.2	23.0
14	12.0	16.9	28.6	15.1	26.3
15	10.9	18.7	26.8	14.4	28.3

(a)

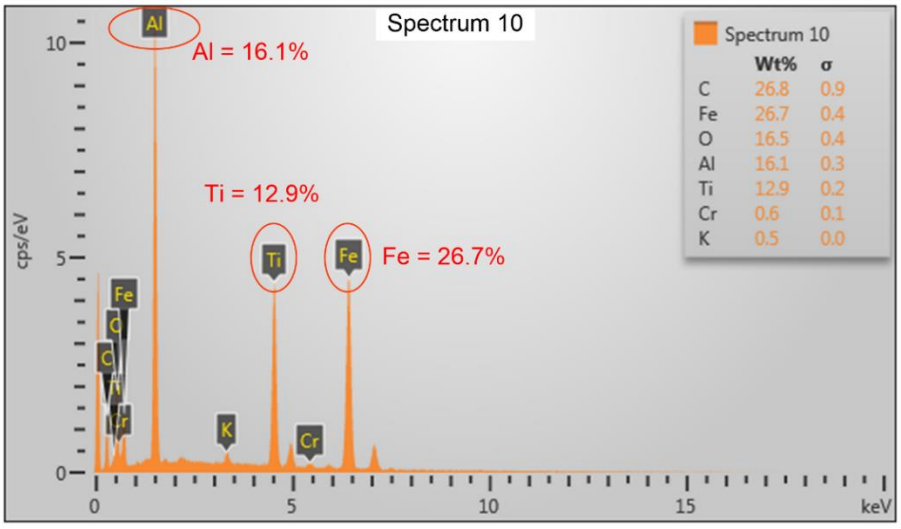

(b) Spectrum 10

TH-2735_136103036

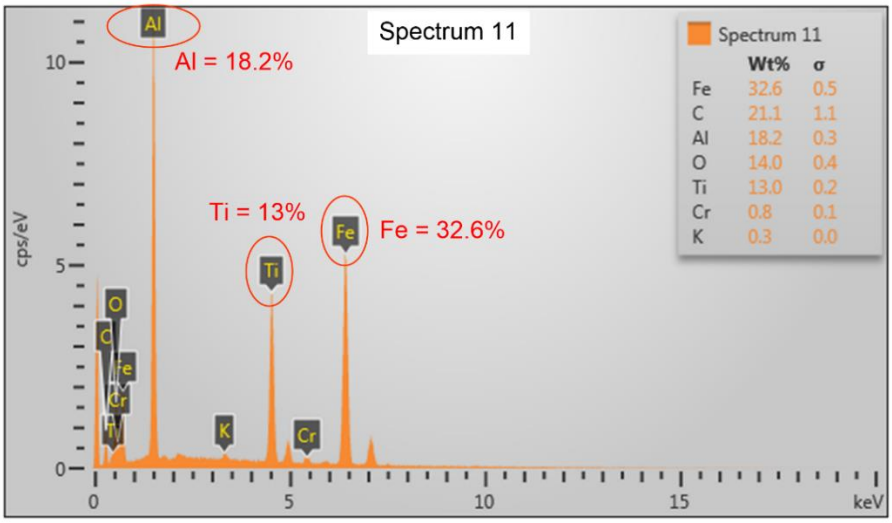

(c) Spectrum 11

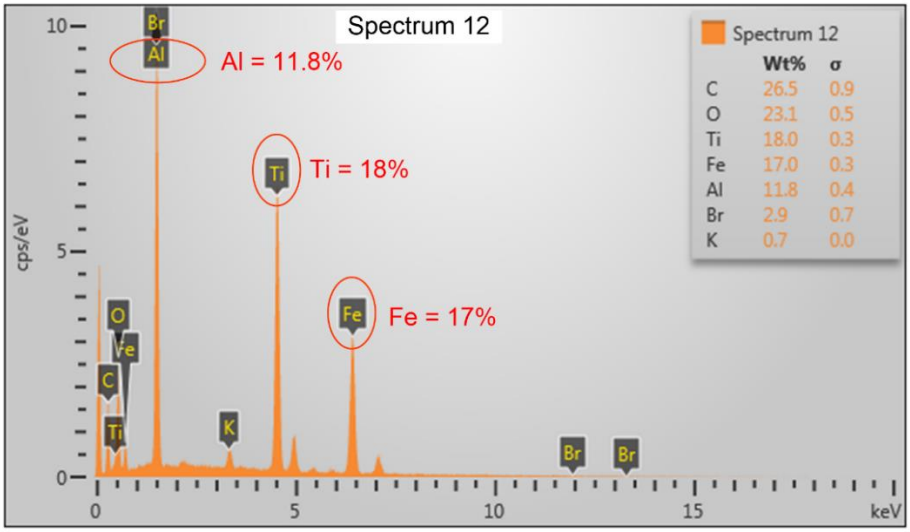

(d) Spectrum 12

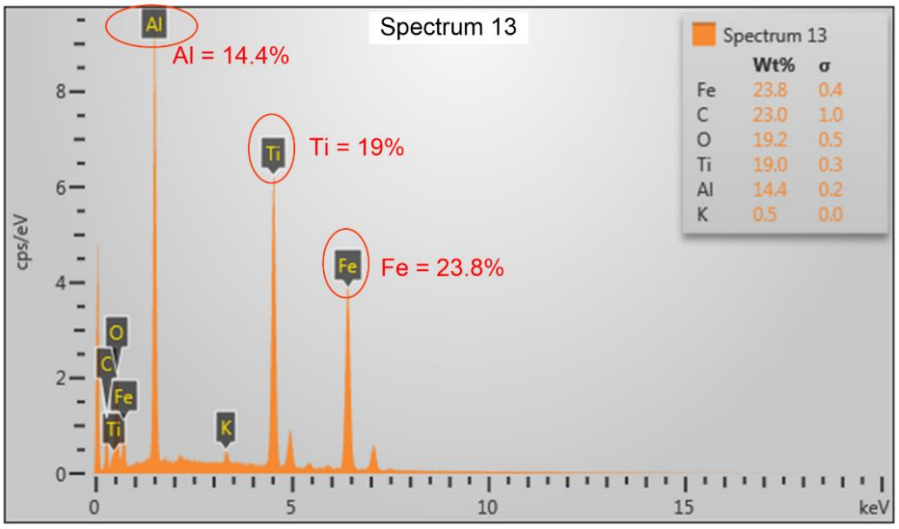

(e) Spectrum 13

TH-2735_136103036

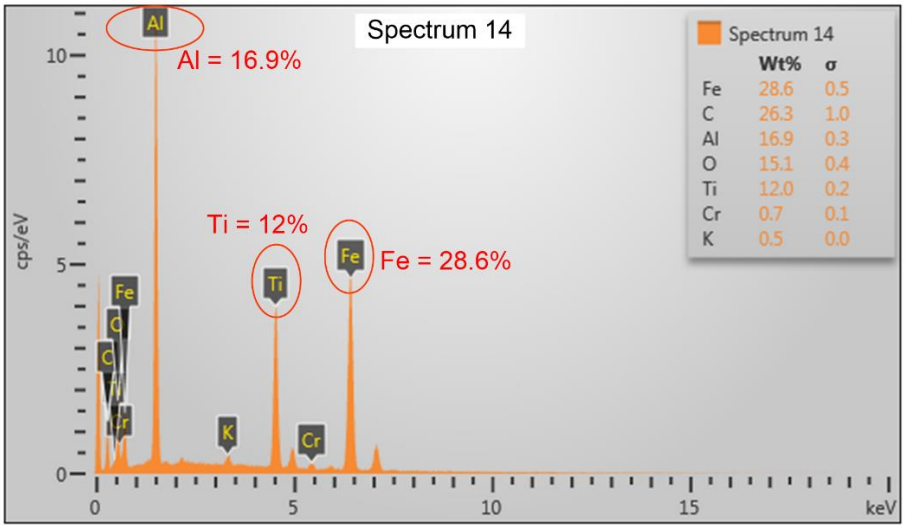

(f) Spectrum 14

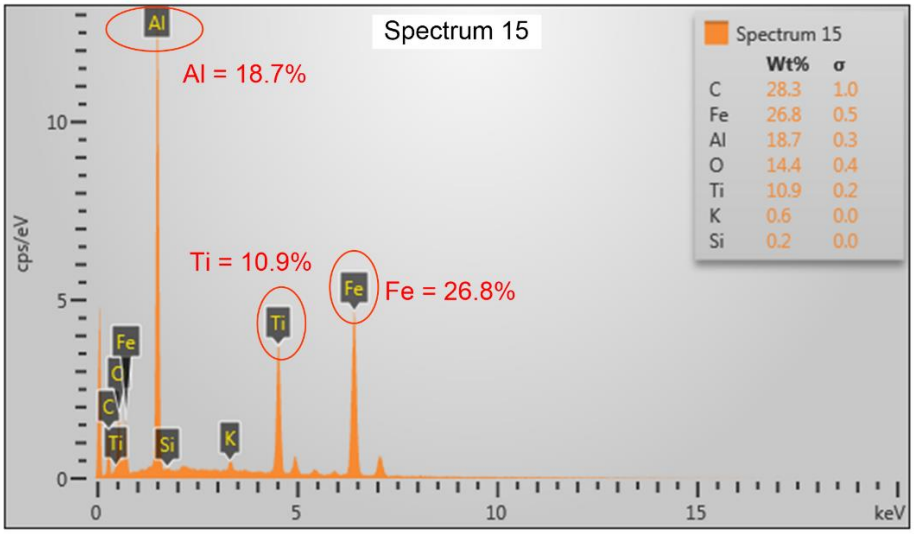

(g) Spectrum 15

Figure 4.4 (a) Micrographs and elemental compositions and EDS spectra for (b) Spectrum 10; (c) Spectrum 11; (d) Spectrum 12; (e) Spectrum 13; (f) Spectrum 14; (g) Spectrum 15 for EDA workpiece processed at t_{on} of 546 µs and I_d of 10 A

From Figure 4.4, it is clear that the transfer of the tool material onto the workpiece is successful; however, the distribution of the elements is not yet clear. To study the distribution of the elements transferred, elemental mapping has been done. Figure 4.5 shows the elemental mapping at the surface of the EDA workpiece. From the figure, it is observed that the distribution of the elements presents viz. Al, Ti, Fe, and C are uniform throughout the surface. The entire surface shown in Figure 4.5(a) is a region that is fully alloyed using EDA. The EDS layered image is shown in Figure 4.5(b). It depicts the uniform distribution of the elements present in the alloy. The distribution of Al and Ti can be observed in Figure 4.5(c) and Figure 4.5(d), respectively. Fe being the parent

TH-2735_136103036

material, its presence is noted in Figure 4.5(e); also, the presence of C dissociated from the decomposed hydrocarbon can also be observed in Figure 4.5(f).

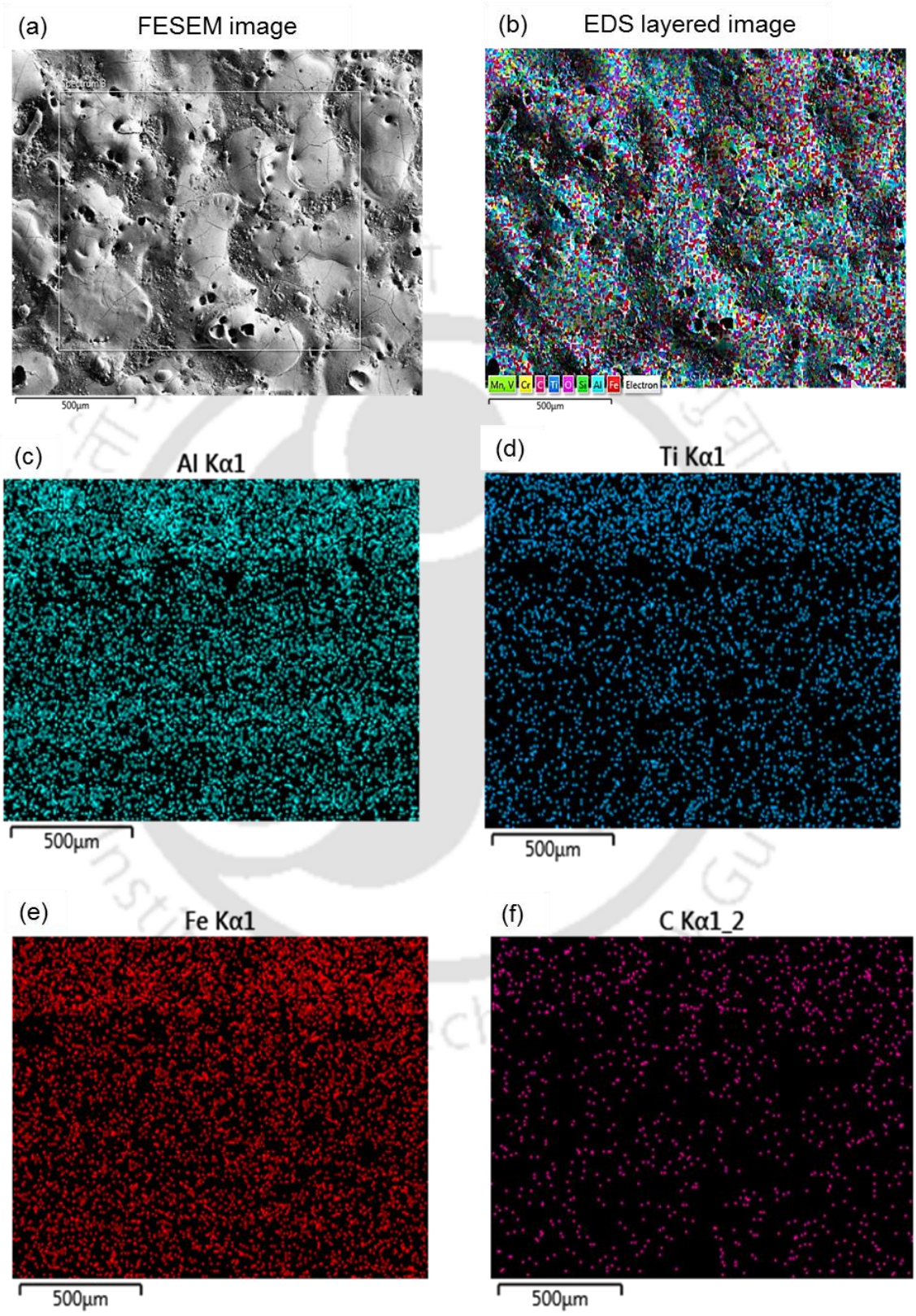

Figure 4.5 Elemental mapping of EDA alloyed surface at the top surface for the workpiece processed at t_{on} of 546 µs and I_d of 10 A

TH-2735_136103036

To further analyze the transfer of the elements along the depth of the alloyed layer, line scanning was performed along the cross-sectioned surface. Figure 4.6(a) shows the micrograph of the workpiece at which the line scan was performed. The scanning was performed from the top surface towards the depth of the workpiece as indicated in the figure from location "A" to "B". The elements present along the yellow line AB have been scanned, and Figure 4.6 (b) shows the presence of the elements along the line AB. From Figure 4.6 (b), the presence of Ti, Al, Fe, and a few other elements was observed up to a distance of around 45 µm. However, beyond the distance of 45 µm, the presence of Ti and Al is not found. This indicates that the tool materials are successfully transferred up to a certain thickness over the workpiece.

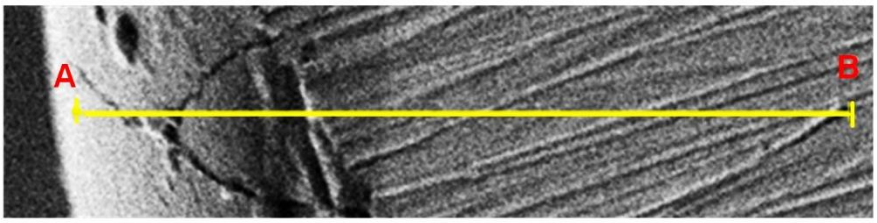

Scanning from top surface towards the depth of the work sample

(a)

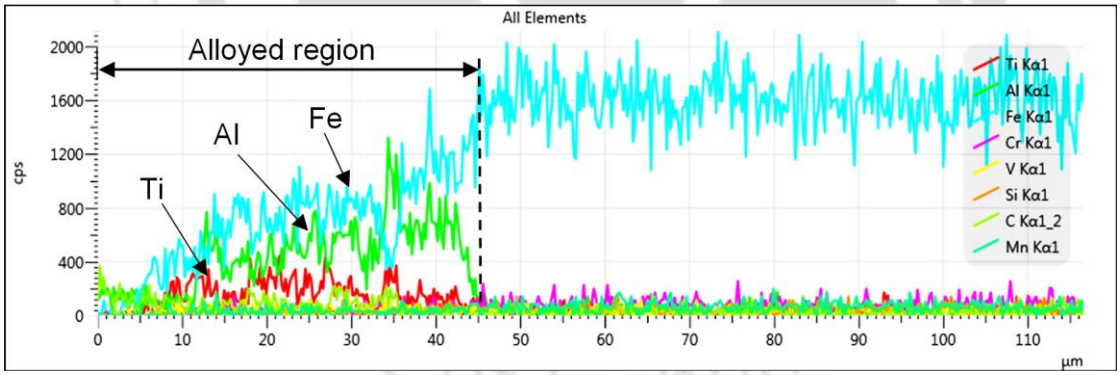

(b)

Figure 4.6 EDS line scan at cross-sectioned workpiece showing (a) Micrograph and (b) Elemental spectrum for the EDA workpiece processed at t_{on} of 546 µs and I_d of 10 A

The distribution of the elements along the thickness of the alloyed layer is depicted in Figure 4.7 by performing an elemental mapping over the cross-sectioned image. The distribution of Ti, Al, Fe, and C can be noticed. The EDS layered image, as shown in Figure 4.7(b), indicated that the distribution of Fe over the alloyed layer is fairly reduced in comparison with that of the parent material, which is indicated by the red color. Further,

TH-2735_136103036

the distribution of Al and Ti is observed to be more in the alloyed region in comparison with that of the parent material, as depicted in Figure 4.7(c) and Figure 4.7(d), respectively.

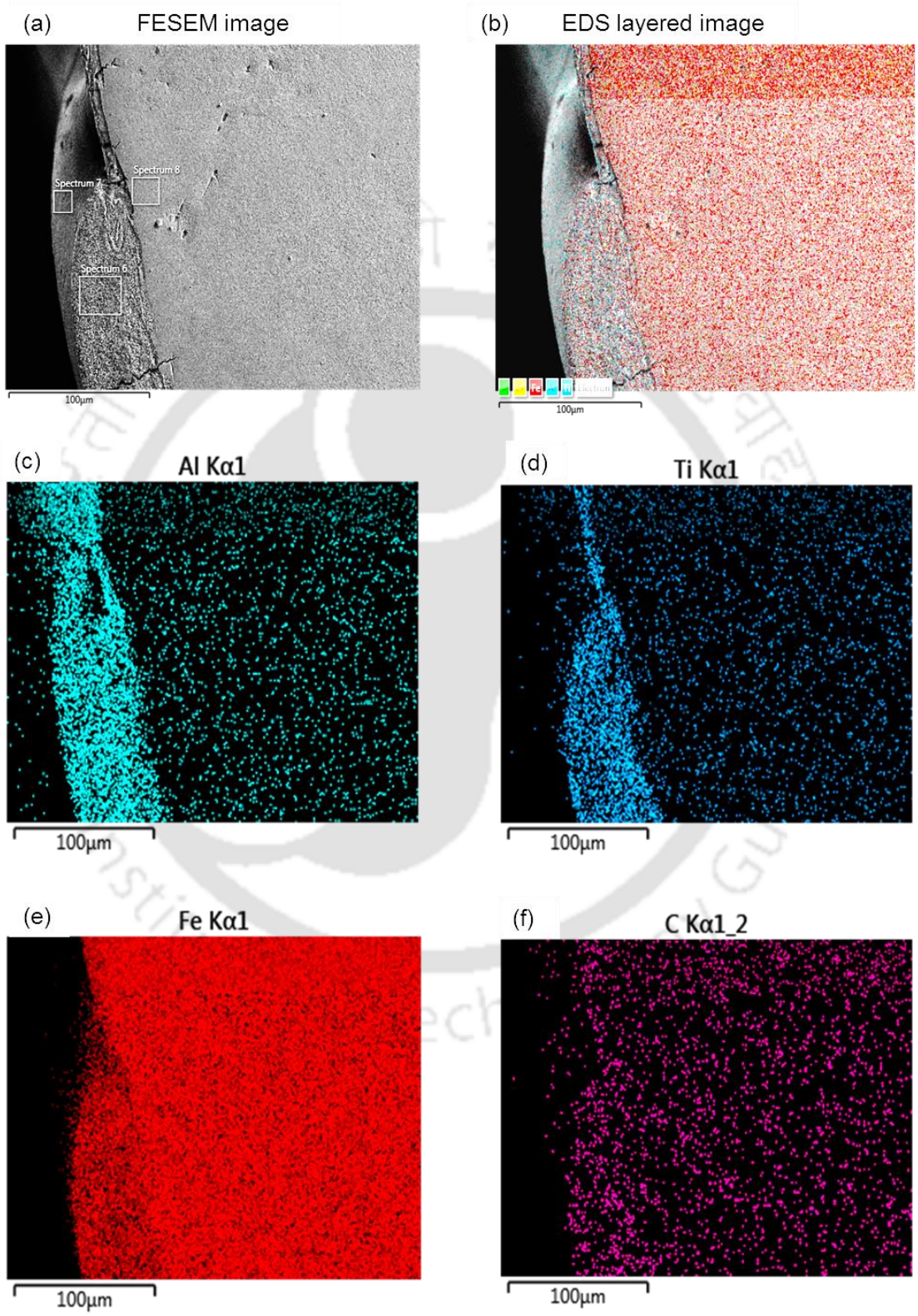

Figure 4.7 Elemental mapping of EDA alloyed surface at the cross-section for the workpiece processed at t_{on} of 546 µs and I_d of 10 A

TH-2735_136103036

The percentage contribution of the elements at the tool surface after the EDA operation was also analyzed. Figure 4.8 shows the EDS spectrum for the tool surface after EDA at processing condition of 546 µs pulse on-time and 10 A discharge current. As mentioned in the previous sections, the percentage composition of Ti and Al was 50 % Ti and 50 %, respectively, was found to be reduced to 36.2 % and 43.9 %, respectively (Figure 4.8). Moreover, two elements, viz. carbon, and iron, were found with 13.8 % and 6.1 %, respectively. Thus, it can be inferred that there has been deposition of carbon particles from decomposed hydrocarbon and Fe from the workpiece material. This revealed that there is a deposition of elements released from the hydrocarbon and workpiece material on the tool electrode as well.

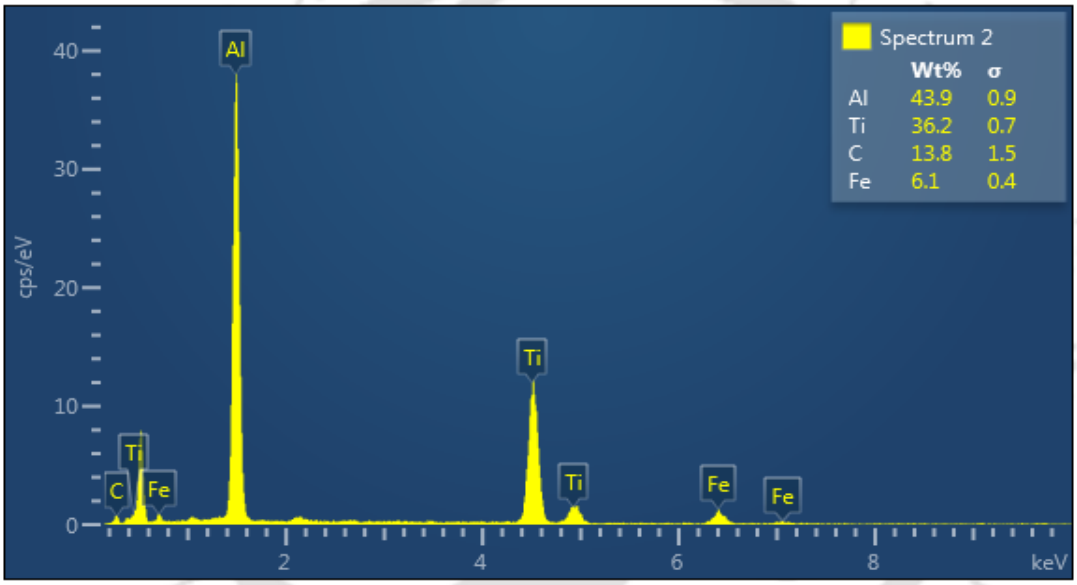

Figure 4.8 EDS spectrum for the tool surface after EDA at processing condition of 546 µs t_{on} and 10 A I_d

The elemental distribution at the tool surface was further analyzed. Figure 4.9 shows the distribution of Al, Ti, Fe, and C on the tool surface which was used for alloying at processing condition of 546 µs pulse on-time and 10A discharge current. From the figure, it is observed that the elements present are uniformly distributed. From the elemental analysis, it was observed that there was a successful transfer of particles released from the tool onto the workpiece surface.

TH-2735_136103036

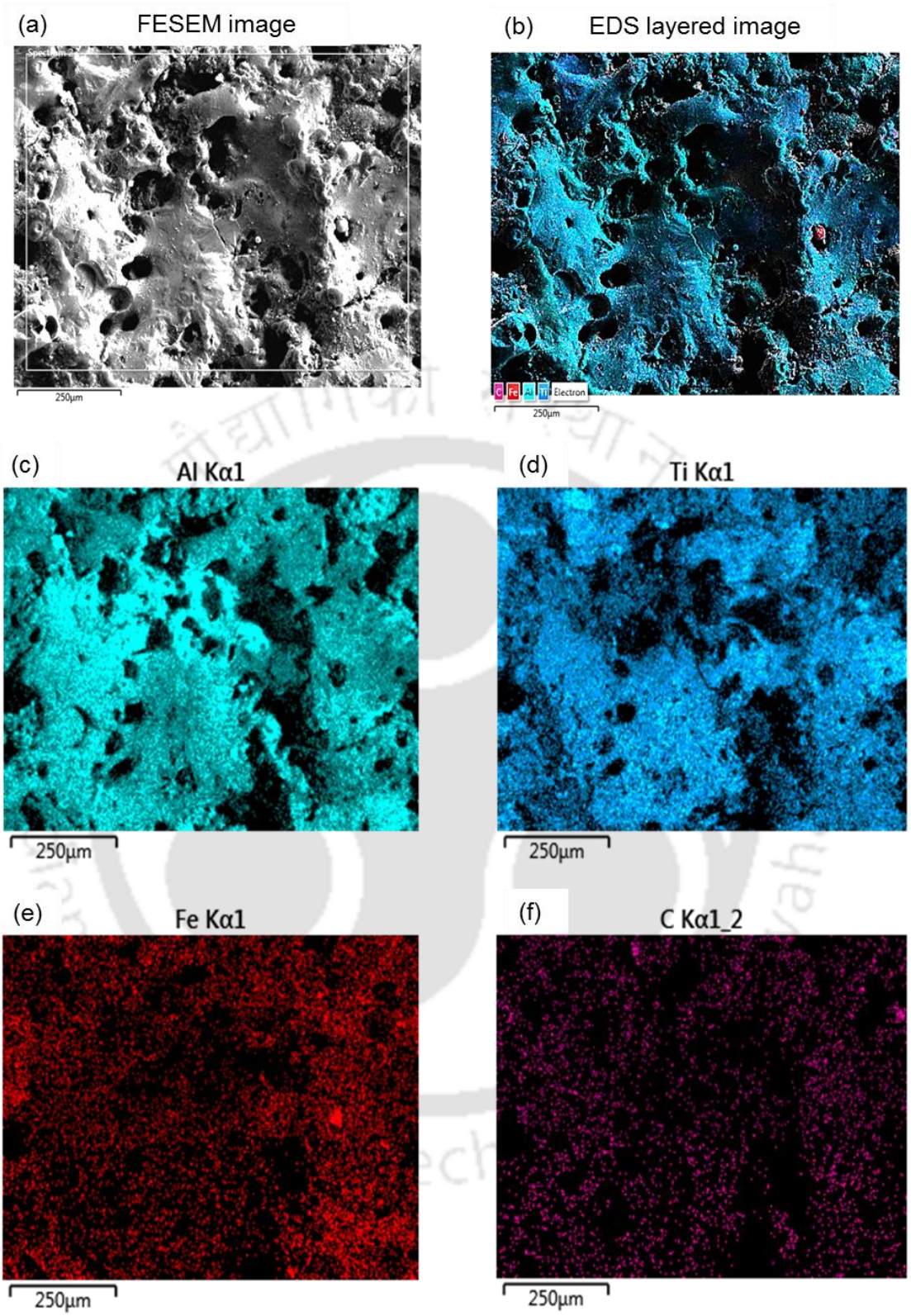

Figure 4.9 Elemental mapping of tool surface after EDA at processing condition of 546 µs t_{on} and 10 A I_d

To further check the type of the compounds formed, XRD analysis was carried out, and the results are reported in the following sub-section.

TH-2735_136103036

4.2.2 X-ray diffraction analysis

To determine the different phases present over the alloyed surface, X-ray diffraction analysis was carried out for the workpiece processed at t_{on} of 546 µs and I_d of 10 A. The diffraction pattern is shown in Figure 4.10. The presence of Fe_3C and TiAl has been noted from the peaks attained at the corresponding values of diffraction angles when compared with the already existing joint committee on powder diffraction standards (JCPDS) database bearing entry cards number 96-901-2189 for Fe_3C and 96-153-2770 for TiAl. It is noted that Fe_3C phase is orthorhombic and that for TiAl is tetragonal. The presence of Fe_3C and TiAl phases confirms that surface alloying has been successfully done using EDA.

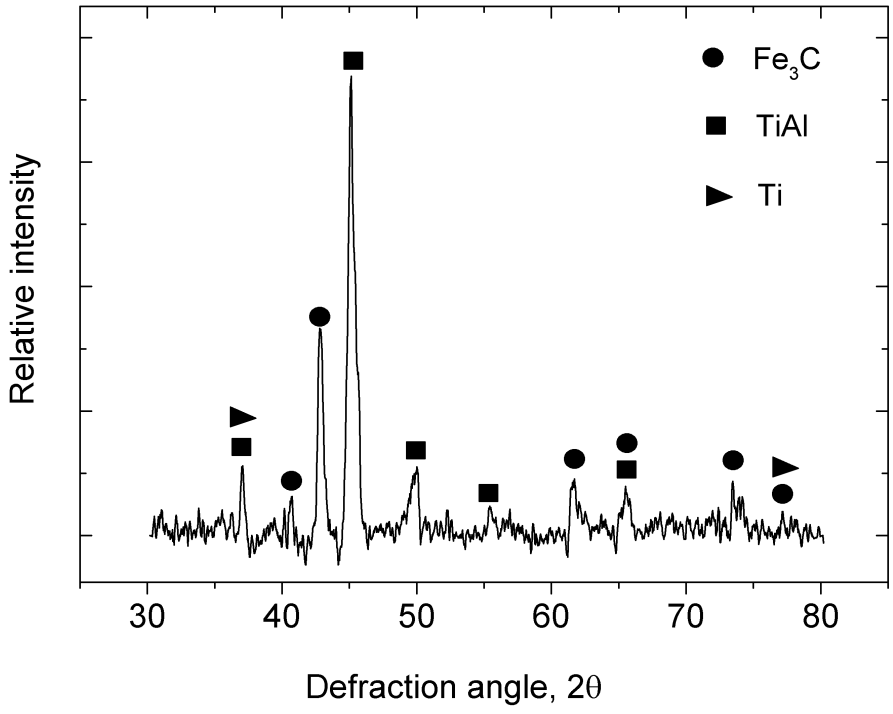

Figure 4.10 X-ray diffraction pattern for EDA surface for the workpiece processed at t_{on} of 546 µs and I_d of 10 A

After a thorough analysis of the elements present, their distribution, and the type of the compounds formed on the alloyed surface, the work is further extended to determine the thickness of the alloyed layer. The following sub-section reports the effect of discharge current and pulse on-time onto the alloyed layer thickness.

TH-2735_136103036

4.2.3 Alloyed layer thickness

To study the thickness of the alloyed layer, the polished cross-sectioned EDA workpieces were analyzed under an optical microscope. A distinct layer with a certain thickness of the alloyed region over the parent material could be observed after proper etching of the workpieces. Figure 4.11 shows a uniform layer of the alloyed region over the parent material, along with a schematic illustration.

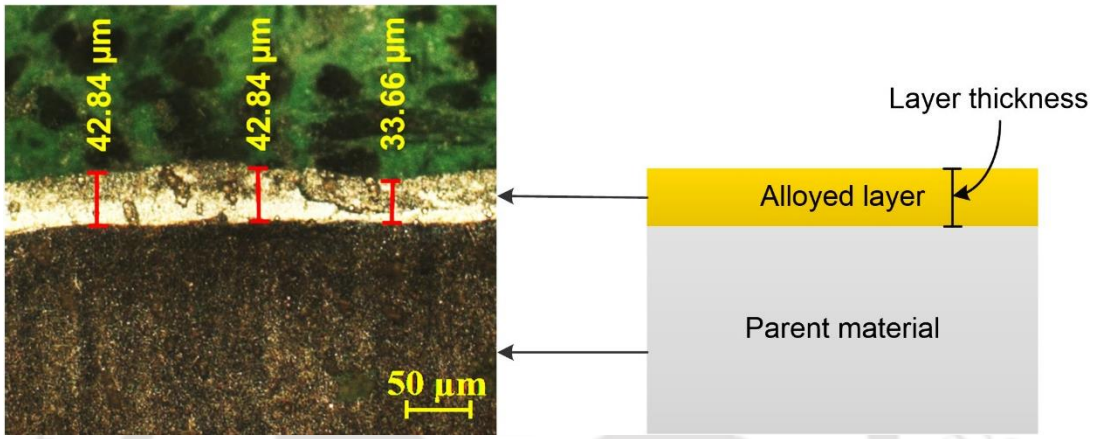

Figure 4.11 Optical micrograph at 20× showing uniform alloyed layer at a t_{on} of 546 µs and I_d of 6 A

The alloyed layer thickness measurements were taken from the top surface to the interface of the alloyed region and the parent material. The measurements were taken at 9 different locations with an approximate equal interval. An average value of the 9 readings was considered as the average alloyed layer thickness. To investigate the effect of discharge current and pulse on-time onto the alloyed layer thickness, the measurements were taken for all the 16 experiments, i.e., with a varying t_{on} and I_d combination as stated above. Figure 4.12 shows the alloyed layer with a varying t_{on} and I_d. From the figure, it is observed that the alloyed layer is uniform and continuous. There is no formation of large cracks that propagate and penetrate onto the parent material as it is not affected by the intense heat generated during sparking. It is also observed that at certain discharge current and pulse on-time combinations, the alloyed layers exhibit waviness. This is due to the overlapping of the electrical discharges/sparks. This formation of waviness can be explained in Figure 4.13. During the EDA phenomenon, when the first spark/discharge occurs, there is a melting of both the tool and workpiece. This creates a melt pool and a region of the heat-diffused region over the workpiece, as illustrated in Figure 4.13(a). The melt pool thereby forms the alloyed layer upon solidification. The next probable spark will occur at the least inter-electrode gap distance. If it is perceived that the next spark

TH-2735_136103036

occurs at the location just adjacent to the first spark location, as indicated in Figure 4.13(b), there will be the formation of a new melt pool that will overlap the melt pool region formed in the previous spark. This overlapping of the sparks results in the wavy nature of the alloyed layer formed, as shown in Figure 4.13(c).

भारतीय प्रौद्योगिकी संस्थान गुवाहाटी • Indian Institute of Technology Guwahati •

TH-2735_136103036

Pulse on-time (t_{on})	Discharge current (I_d)			
	6A	8A	10A	12A
546 µs	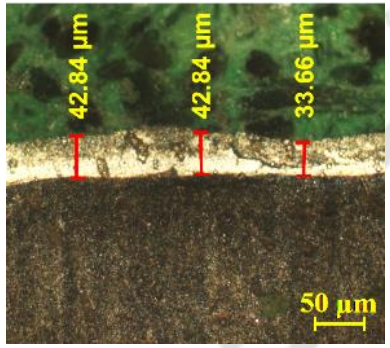	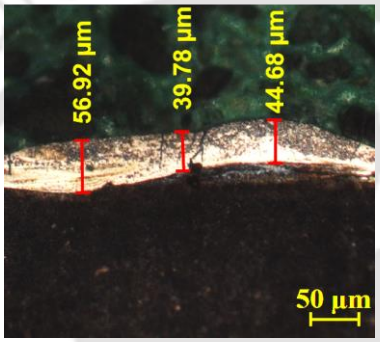	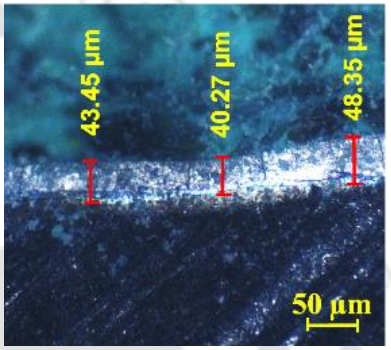	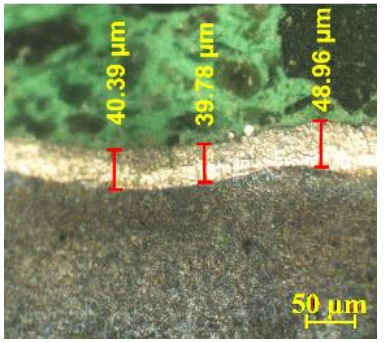
706 µs	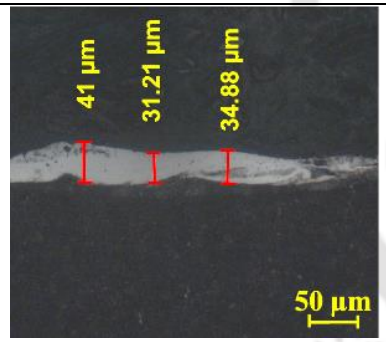	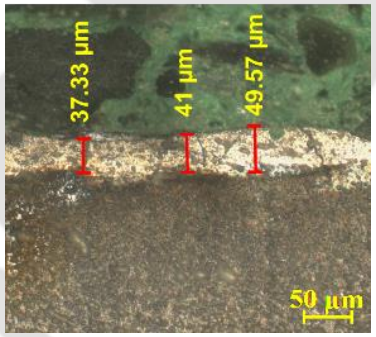	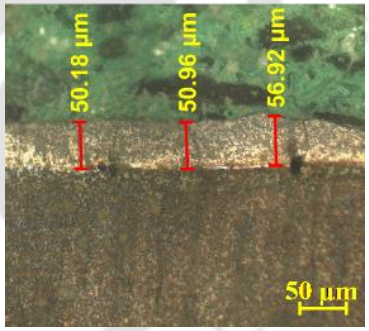	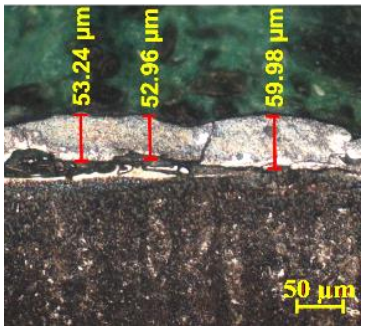

TH-2735_136103036

Pulse on-time (t_{on})	Discharge current (I_d)			
	6A	8A	10A	12A
856 µs	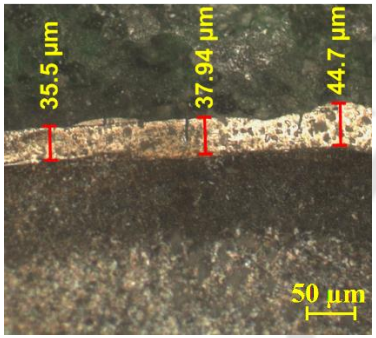	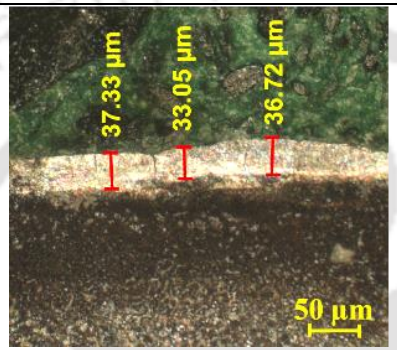	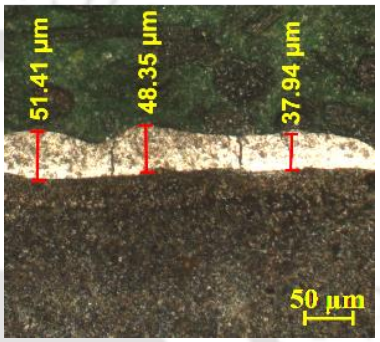	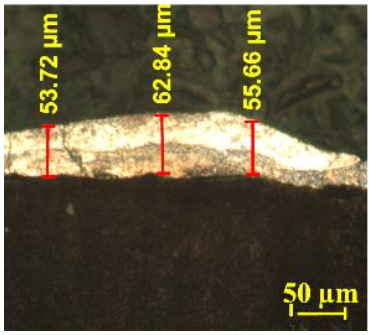
1006 µs	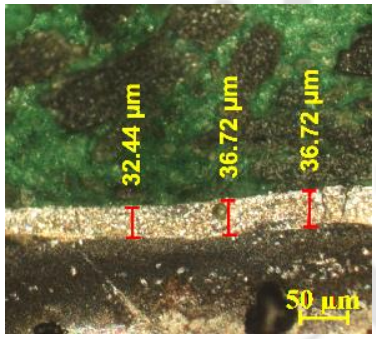	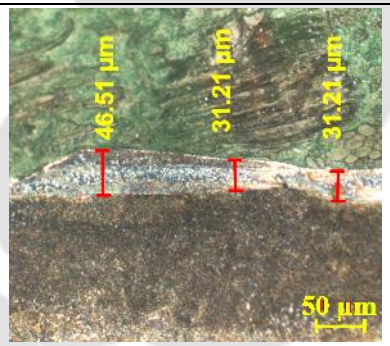	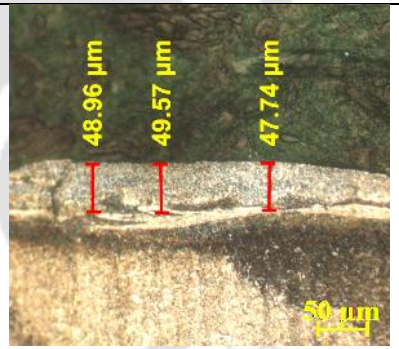	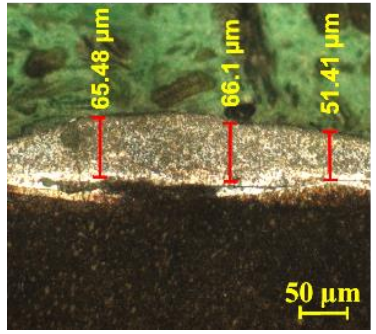

Figure 4.12 Optical micrographs at 20× showing uniform alloyed layer at varying t_{on} and I_d

TH-2735_136103036

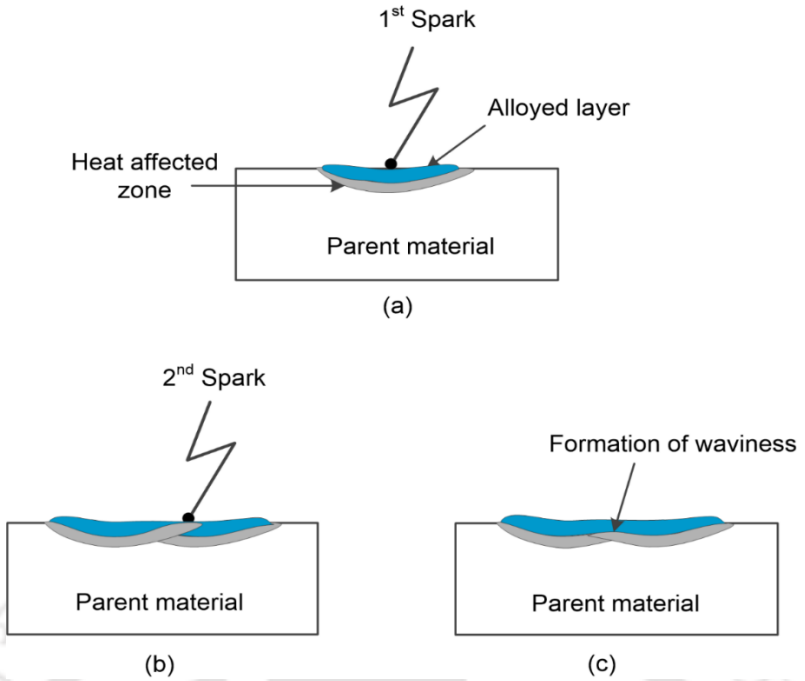

Figure 4.13 Schematic diagram illustrating the formation of waviness in the alloyed layer

Table 4.1 Experimental results for average alloyed layer thickness

Expt. no.	t_{on} (µs)	I_d (A)	Alloyed layer thickness (µm)				Coefficient of variation %
			Expt. 1	Expt. 2	Expt. 3	Average	
1.	546	6	38.22	36.27	39.11	37.87	3.84
2.	706	6	40.37	36.28	38.22	38.54	4.40
3.	856	6	34.68	39.37	36.02	35.18	2.07
4.	1006	6	33.82	37.02	34.43	32.33	6.04
5.	546	8	42.19	40.21	39.96	41.34	2.47
6.	706	8	42.61	40.21	41.82	41.55	2.94
7.	856	8	37.14	34.85	36.99	37.83	3.52
8.	1006	8	35.46	33.05	33.75	34.98	4.54
9.	546	10	46.58	46.58	49.75	47.64	3.84
10.	706	10	50.59	51.51	49.03	49.98	1.66
11.	856	10	48.37	52.23	50.46	47.11	8.75
12.	1006	10	46.92	42.51	46.31	45.88	3.15
13.	546	12	53.48	50.31	53.49	52.83	2.15
14.	706	12	53.49	48.48	51.66	52.46	1.78
15.	856	12	55.33	46.5	51.61	51.81	6.62
16.	1006	12	59.83	65.21	70.00	65.01	7.82

TH-2735_136103036

The experimental results for the average alloyed layer thickness of the three sets of experiments for each process condition along with the coefficient of variation, are tabulated in Table 4.1. The coefficient of variation for the alloyed layer thickness ranges from 1.66 % to 8.75 %. To investigate the effect of discharge current and pulse on-time on the average alloyed layer thickness, a line graph has been plotted as shown in Figure 4.14. It is noted that the average thickness of the alloyed layer ranges from 33 to 70 µm. Moreover, it was observed that for constant pulse on-time, the alloyed layer thickness increases with the increase in discharge current. This indicates alloying of more elements with the parent material due to higher discharge energy. However, for a fixed discharge current value, as the pulse on-time increases, the alloyed layer thickness is noted to be decreasing. This decreasing trend can be explained from the input heat intensity equation considered generally in the modeling of the EDM phenomenon. The effect of discharge current and pulse on-time onto the energy intensity can be understood by the expression given in Equation 4.1 (Joshi and Pande 2010). From equation (4.1), it is clear that the heat input is directly proportional to the discharge current and voltage; however, it is inversely proportional to the square of the radius of the plasma channel. The radius of the plasma channel is directly proportional to the pulse on-time (Equation (4.2)). Therefore, the energy intensity increases with an increase in discharge current but decreases with an increase in pulse on time. However, the decreasing trend of alloyed layer thickness with an increase in pulse on-time is not observed in case of pulse on-time of 1006 µs. This is due to the instability in the discharge phenomenon at a high value of discharge current and pulse on-time combination.

$$q_0 = \frac{4.57 F_A V I_d}{\pi R_{pc}^2} e^{\left\{-4.5\left(\frac{r}{R_{pc}}\right)^2\right\}} \tag{4.1}$$

$$R_{pc} = (2.04\times10^{-3}) I_d^{0.43} t_{on}^{0.44} \tag{4.2}$$

where $q(r)$ is the heat intensity following the Gaussian heat source model, F_A is the fraction of total EDM spark intensity distributed to the workpiece, I_d is the discharge current (A), V is the discharge voltage (V), t_{on} is the pulse on-time (µs), and R_{pc} is spark radius at the work surface (µm).

TH-2735_136103036

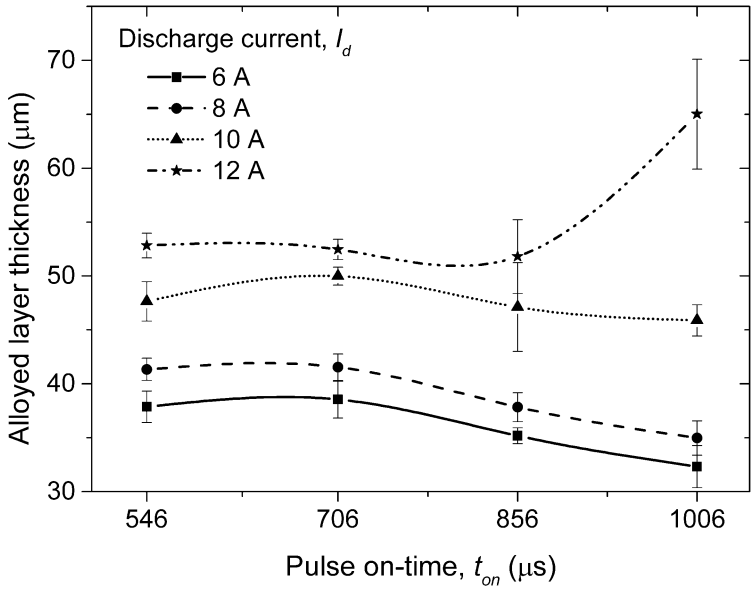

Figure 4.14 Line graph showing the effect of t_{on} and I_d on the alloyed layer thickness

From this section, it was observed that the alloyed layer thickness is dependent on the processing conditions, viz. discharge current and pulse on-time. Following sub-section deals with the hardness of the alloyed layer formed.

4.2.4 Hardness analysis

The hardness of the alloyed layer was determined along the cross-section of the alloyed workpiece. Figure 4.15 shows the indentation marks along the cross-section of the alloyed workpiece for the workpiece processed at t_{on} of 546 μs and I_d of 6 A. From the figure, it is observed that the size of the indentation is small in the alloyed region in comparison to that of the parent substrate material. The smaller the indentation size, the larger is the hardness value. The hardness value is calculated by using equation (4.3), and it has an inverse relation to the square of the mean of the diagonals of the indentation.

$$HV_{0.3} = 0.0018 \times \frac{F}{d^2} \tag{4.3}$$

where F is load in gf and d is the mean diagonal of the indent formed in mm^2 .

TH-2735_136103036

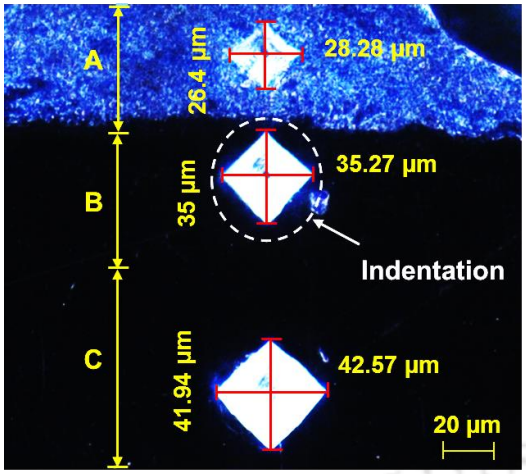

Figure 4.15 Optical micrograph at 40× showing the difference in the indentation size at different regions for EDA workpiece processed at t_{on} of 546 µs and I_d of 6 A

The hardness values for all 16 experiments were determined. The recorded measurements are shown in Table 4.2. The notation D1 and D2 in the table signifies the length of the diagonals of the indentation. From the measurements, the hardness of the alloyed region (1125 $HV_{0.3}$) was noted to be significantly higher than that of the interface and parent material region (300 $HV_{0.3}$). An increase in the hardness was noted to be approximately four times of the parent material, i.e., 307.98 % increase in the hardness value. From this section, it was observed that there is an enhancement in the hardness of the alloyed layer due to the formation of the compounds and the need to study the amount of material deposited per unit time thus arises. Figure 4.16 shows the indentation marks at the alloyed region and the parent material region for workpieces processed at varying levels of discharge current and pulse on-time. The following sub-section presents the results pertaining to the influence of discharge current and pulse on-time on the material deposition rate.

TH-2735_136103036

Table 4.2 Experimental results for the hardness of alloyed layer and parent material

Expt. No.	t_{on} (µs)	I_d (A)	Alloyed layer			Parent material			% Increase in $HV_{0.3}$
			D1 (µm)	D2 (µm)	$HV_{0.3}$	D1 (µm)	D2 (µm)	$HV_{0.3}$	
1.	546	6	28.28	26.40	744.26	42.57	41.94	311.58	138.87
2.	706	6	31.77	29.23	598.03	43.53	43.21	295.76	102.19
3.	856	6	29.86	29.55	630.47	42.89	42.89	302.42	108.47
4.	1006	6	27.32	25.42	800.03	42.67	40.98	318.02	151.56
5.	546	8	26.05	26.37	809.82	41.94	41.94	316.28	156.05
6.	706	8	22.64	22.03	1115.20	30.5	30.82	591.81	88.44
7.	856	8	30.18	28.28	651.13	44.16	43.84	287.35	126.59
8.	1006	8	31.04	28.59	625.83	43.84	43.53	291.51	114.68
9.	546	10	29.23	29.55	644.06	44.16	43.84	287.35	124.13
10.	706	10	27.01	27.01	762.56	38.44	38.13	379.55	100.91
11.	856	10	27.32	25.42	800.03	42.67	40.89	318.70	151.02
12.	1006	10	23.83	23.83	979.66	36.54	37.17	409.57	139.19
13.	546	12	27.96	27.96	711.62	44.16	43.53	289.39	145.90
14.	706	12	22.24	22.24	1124.75	43.45	46.39	275.69	307.98
15.	856	12	23.19	24.46	980.07	42.89	42.26	306.91	219.33
16.	1006	12	24.15	24.78	929.47	40.98	40.67	333.79	178.46

TH-2735_136103036

Pulse on-time (t_{on})	Discharge current (I_d)			
	6A	8A	10A	12A
546 µs	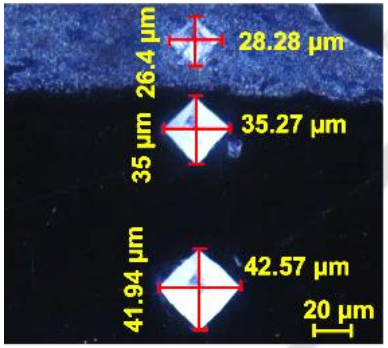	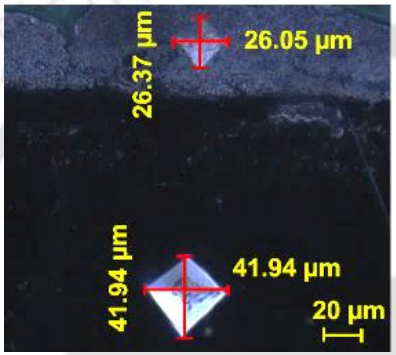	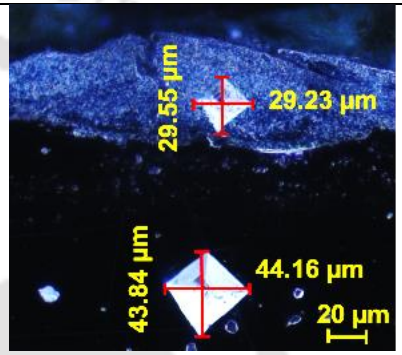	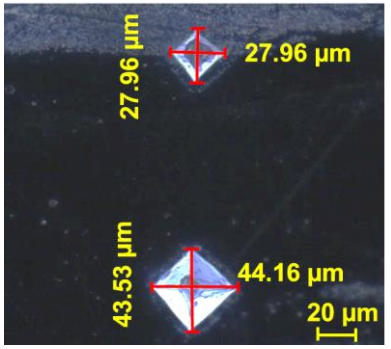
706 µs	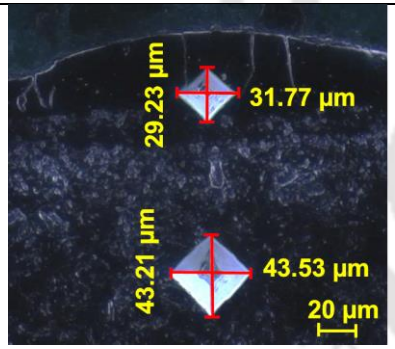	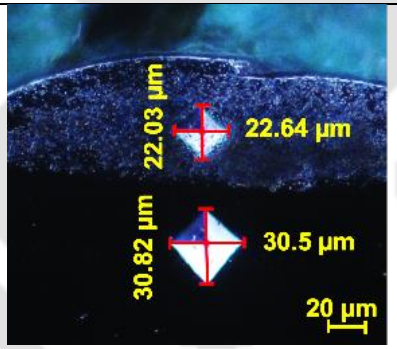	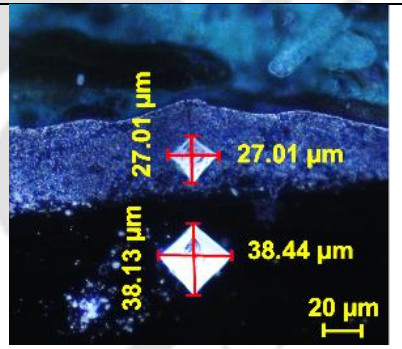	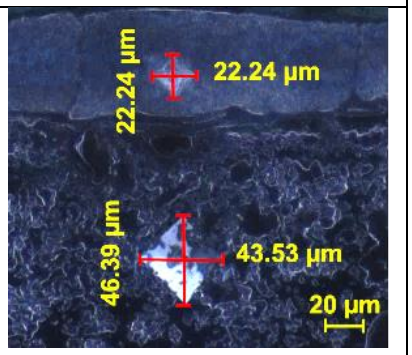

TH-2735_136103036

Pulse on-time (t_{on})	Discharge current (I_d)			
	6A	8A	10A	12A
856 µs	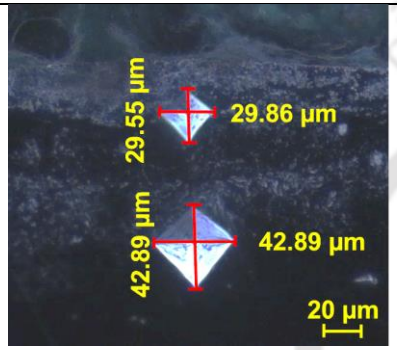	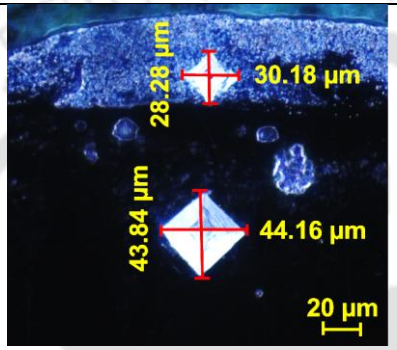	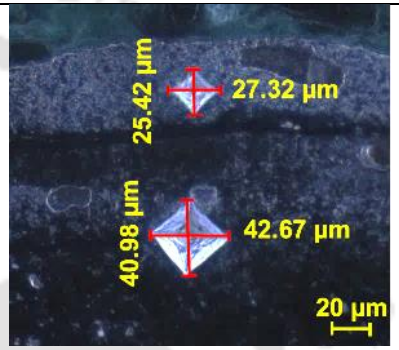	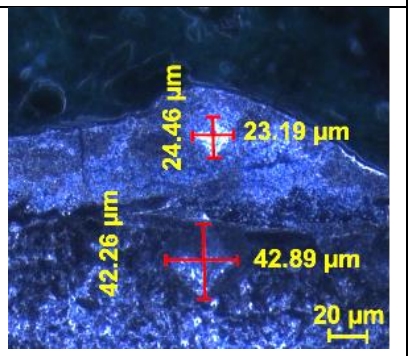
1006 µs	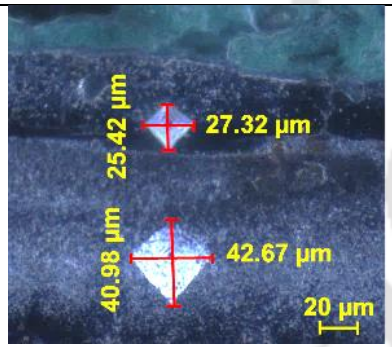	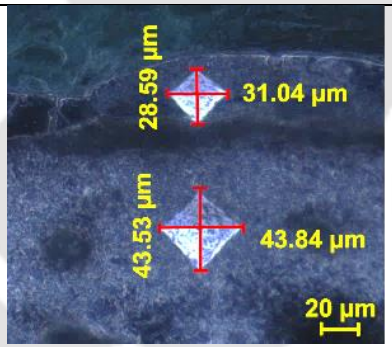	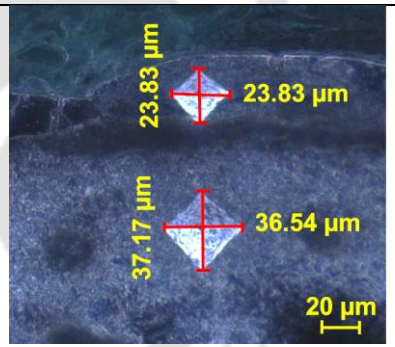	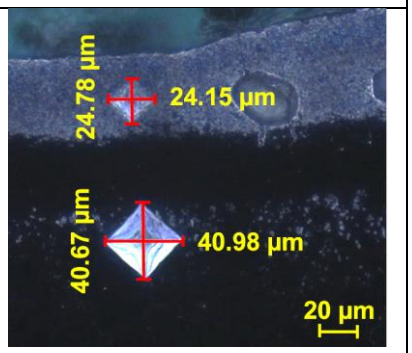

Figure 4.16 Optical micrograph at 40× showing the variation in the indentation size at a different location with varying t_{on} and I_d

TH-2735_136103036

4.2.5 Material deposition rate

In the present work, the material deposition rate was computed for all processed specimens by calculating the difference between the weights of the workpieces measured before and after electric discharge alloying. Figure 4.17 shows the line graph indicating the effect of discharge current and pulse on-time on the material deposition rate. From the graph, it is observed that for a fixed value of pulse on-time, the material deposition rate increases with the increase in discharge current. This is due to the high energy input that is being generated due to an increase in the discharge current. Further, for a fixed value of discharge current, the deposition rate was also found to be increased with the increase in pulse on-time. This is attributed to the application of more energy input due to a longer processing time.

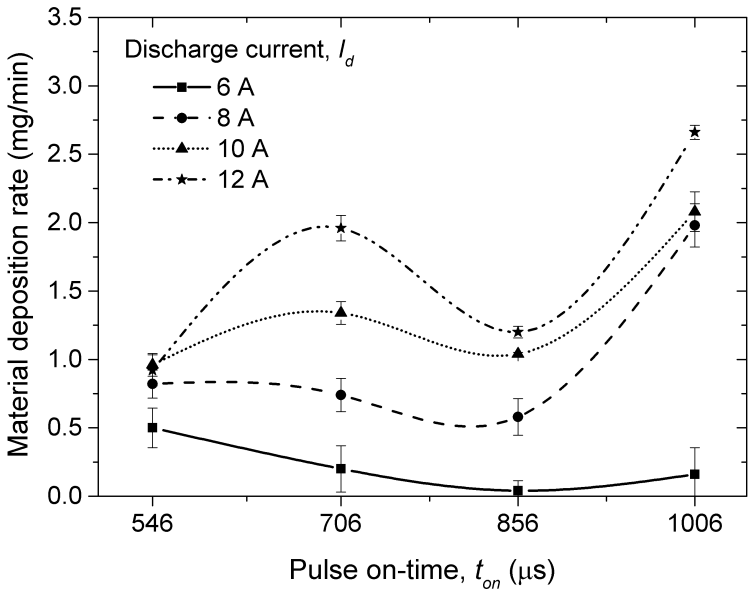

Figure 4.17 Effect of discharge current and pulse on-time on the material deposition rate

To study the surface morphology of the alloyed workpiece surface, the surface roughness was determined, and the results are reported in the following sub-section.

4.2.6 Surface roughness

The surface roughness of the alloyed workpieces was measured by using a contact stylus profilometer discussed in Chapter 3, Section 3.1.4, Page No. 39. The measurement was taken for a scan length of 3 mm. To study the effect of pulse on-time and discharge current on the average surface roughness (R_a) of the workpiece after EDA with PM tool electrode,

TH-2735_136103036

the roughness readings were measured at 5 different locations, and the average value along with the coefficient of variation are listed in Table 4.3. The coefficient of variation for the surface roughness ranges from 4.26 % to 17.57 %. Figure 4.18 shows the plot of the average values surface roughness with varying levels of pulse on-time and discharge current. The increase in the current level results in more R_a value, indicating that the surface becomes rough when processing at a higher current value owing to higher energy input. From the surface roughness plot shown in the figure, it is realized that the surface roughness varies between R_a value of 4.5 to 8.5 µm within the scope of the present work.

Table 4.3 Experimental results for the surface roughness

Expt. No.	t_{on} (µs)	I_d (A)	Surface roughness, R_a (µm)						Coefficient of variation %
			R1	R2	R3	R4	R5	Average	
1.	546	6	6.11	6.21	5.46	5.90	4.81	5.69	10.07
2.	706	6	5.25	5.87	5.74	5.26	5.07	5.44	6.37
3.	856	6	5.67	4.29	5.56	4.72	5.37	5.12	11.58
4.	1006	6	4.09	4.33	5.28	4.30	6.09	4.82	17.57
5.	546	8	6.00	7.74	6.50	6.79	5.9	6.57	11.27
6.	706	8	4.34	6.24	6.92	5.45	5.87	5.76	16.68
7.	856	8	7.98	6.00	7.14	6.10	6.00	6.31	14.07
8.	1006	8	5.84	6.09	6.44	5.97	5.80	6.03	4.26
9.	546	10	6.23	5.60	7.00	7.62	7.68	7.12	12.65
10.	706	10	7.82	6.19	8.29	7.27	7.70	7.45	10.65
11.	856	10	6.43	7.00	8.10	7.69	6.11	7.72	10.79
12.	1006	10	6.00	7.00	6.95	7.79	7.84	7.74	9.72
13.	546	12	6.47	7.58	7.58	7.58	8.19	7.72	8.07
14.	706	12	8.39	8.50	8.15	6.76	8.6	8.43	8.97
15.	856	12	7.19	7.85	7.01	8.00	6.38	7.51	8.76
16.	1006	12	6.66	7.00	6.47	7.44	8.19	7.72	8.91

TH-2735_136103036

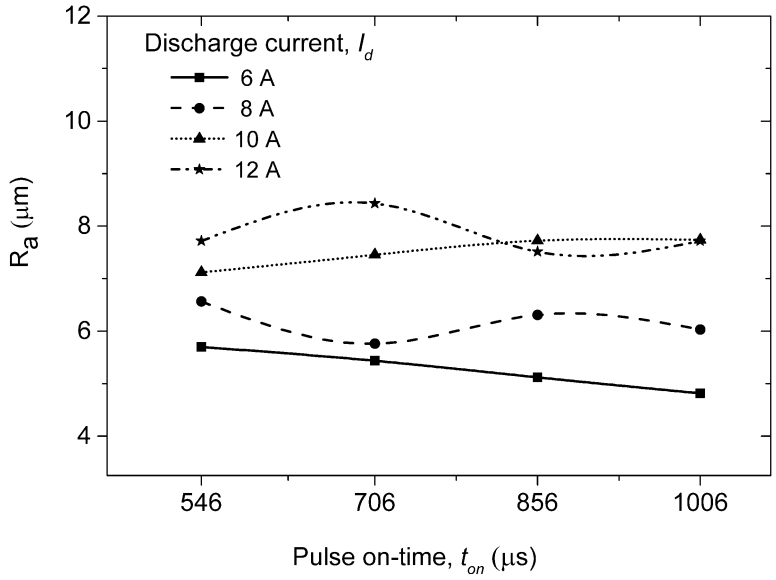

Figure 4.18 Effect of discharge current and pulse on-time on R_a

4.3 Summary

The chapter presents the experimental results on the electric alloying of titanium and aluminium onto the surface of AISI P20 mold steel workpieces in the presence of hydrocarbon oil dielectric medium. For efficient deposition of Ti and Al elements, powder metallurgy-based tool electrodes were specially designed and prepared. Systematic experiments were performed, and the findings were recorded. Based on these results, the influence of the working parameters such as pulse on-time and discharge current on alloyed layer thickness, material deposition rate, and surface roughness was thoroughly studied. The alloyed layer was characterized for its layer thickness, hardness, and type of the alloy formed. The following conclusions can be drawn from the present study.

- The transfer of the tool elements over the workpiece surface has been successfully confirmed from the EDS result. Elemental mapping of the alloyed surface over the top surface, as well as the cross-sectioned region, indicated that the tool elements present are uniformly distributed in the alloyed region. Elemental composition up to a maximum of 18 % Ti and 18.7 % Al could be observed over the alloyed workpiece surface.

TH-2735_136103036

- X-ray diffraction pattern indicated the formation of Fe_3C and TiAl at the alloyed region. Therefore, it can be concluded that the electric discharge surface alloying of Ti and Al with AISI P20 mold steel has been successfully achieved.
- A uniform layer of 33 to 70 µm thickness can easily be alloyed on the substrate material using powder metallurgy-based green compact tool electrode with the composition of 50 % Ti and 50 % Al.
- The hardness of the alloyed region was found to be four times more than that of the parent material, i.e., 300 $HV_{0.3}$ to 1125 $HV_{0.3}$. That ascertains the usefulness of the EDA process in improving the surface properties of the parent material.
- The material deposition rate was affected by the change in discharge current and pulse on-time. The increase in the discharge current and pulse on-time resulted in a higher material deposition rate.
- The surface roughness of the alloyed workpieces exhibited a roughness value in the range of 4.5 to 8.5 µm.

TH-2735_136103036

TH-2735_136103036

CHAPTER 5

Experimental Investigations into Electric Discharge Alloying of Ti and Al on P20 Mold Steel with Water-based Dielectric Medium

5.0 Scope

The present chapter deals with the experimental study of electric discharge alloying of Ti and Al on AISI P20 mold steel in deionized (DI) water and urea mixed deionized water. Experiments were planned and performed at varying combinations of process parameters such as pulse on-time, discharge current, and dielectric medium. The influence of these parameters on the alloyed layer thickness, hardness, material deposition rate, and surface roughness was thoroughly analyzed. A comparative analysis has been made between the results obtained with and without the addition of urea particles in the dielectric medium.

5.1 Motivation

In EDA, alloying of the workpiece can also be performed in the presence of various dielectric media. It was found interesting to study the influence of dielectric media on the performance parameters of the EDA process. It is envisaged that the physical and chemical properties of the dielectric medium formed by the particle mixed in the working medium affect the output performance of EDA. Water based dielectric medium has the advantage of low inflammability and is easily available at low cost. The electric discharge phenomenon can be manipulated and controlled by addition of organic compounds such as urea, and alcohol. With the addition of urea in deionized water, nitrogen can be alloyed over the workpiece which can enhance the surface characteristics. Therefore, the present chapter deals with the experimental investigations on surface alloying of P20 mold steel by using water based dielectric medium.

5.2 Electric discharge alloying of AISI P20 mold steel in DI water and urea mixed DI water

Literature reported that the electrical conductivity, viscosity, temperature, and thermal conductivity of the dielectric medium mainly influence the process performance in EDA. Santos et al. (2017) reported that the addition of urea in deionized water increases the electrical conductivity, i.e., reducing the resistivity of the medium. This results in early bridging and formation of discharge column as compared with that of the unmixed

TH-2735_136103036

dielectric medium. Therefore, the inter-electrode gap can be kept more for the urea mixed dielectric in comparison with that without urea. The shape and size of the plasma channel are affected by the addition of particles in the dielectric such as urea (Santos et al. 2017), Al, SiC, etc. (Chow et al. 2000). The plasma surface area interacting with the workpiece is smaller in urea mixed dielectric. The schematic diagram representing the increase in the inter-electrode gap and the shape of the plasma channel is depicted in Figure 5.1. The following sections and sub-sections deal with the influence of urea mixed dielectric medium on the output performance.

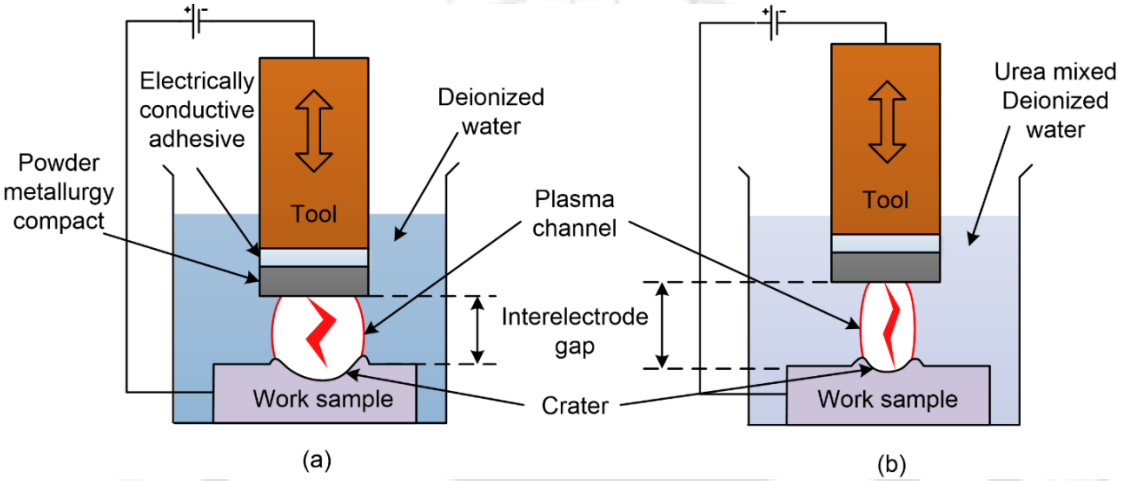

Figure 5.1 Schematic representation of plasma shape and size for (a) Deionized water and (b) Urea mixed deionized water

With all the possible combinations of pulse on-time and discharge current as listed in Chapter 3, Table 3.3. Page No. 49, a set of 16 experiments were conducted using deionized water and urea mixed deionized water separately. To assess the repeatability, each experiment was performed three times at the same processing condition. Figure 5.2 shows the images of the workpieces after the alloying process by using (a) deionized water and (b) urea mixed deionized water. The processing condition was 546 µs pulse on-time and 12 A discharge current. It is observed that for the workpiece processed in deionized water, there is uniform sparking. However, for the workpieces processed in urea mixed deionized water, it is observed that the surface is irregular and shows burnt patches. This indicates arcing occurred after the initiation of uniform sparking.

TH-2735_136103036

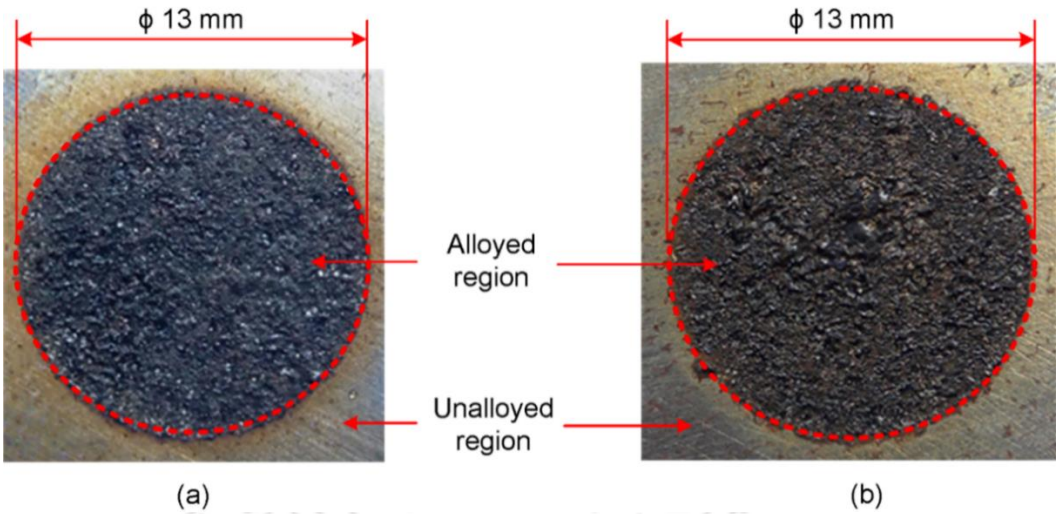

Figure 5.2 Pictorial image of workpiece top surface after EDA in (a) Deionized water and (b) Urea mixed deionized water (Both the workpieces were processed at 546 µs pulse on-time and 12 A discharge current)

The cross-sectioned microscopic image and FESEM image of the top surface for the workpiece alloyed using urea mixed DI water at t_{on} of 1006 µs, I_d of 6 A is shown in Figure 5.3. From the cross-sectioned image (Figure 5.3 (a)), it is observed that there is formation of three different distinct layers. The different layers are characterized by the difference in the microstructure. The first layer shows a distinctive feature of white color as observed from the optical microscope, and this layer is termed as the white layer in electric discharge machining; while in the case of EDA, it is termed as an alloyed layer which is characterized by the composition of different elemental composition with desirable surface properties. This layer experiences plasma-induced melting and vaporization. The melted tool and workpiece material get solidified in this layer, thereby forming an alloyed layer. Next to this layer is termed the diffusion layer. This layer is subjected to heat-induced by the plasma, which is formed during the electrical discharge phenomenon, but this layer has not been melted. The layer generally exhibits an increase in hardness due to the heat treatment as the layer experiences the heat induced by the plasma. Finally, the third layer observed is the parent material which exhibits a distinctive microstructure grain boundary. This layer has not been affected by the electrical discharge process, and hence the properties of the parent material are retained.

TH-2735_136103036

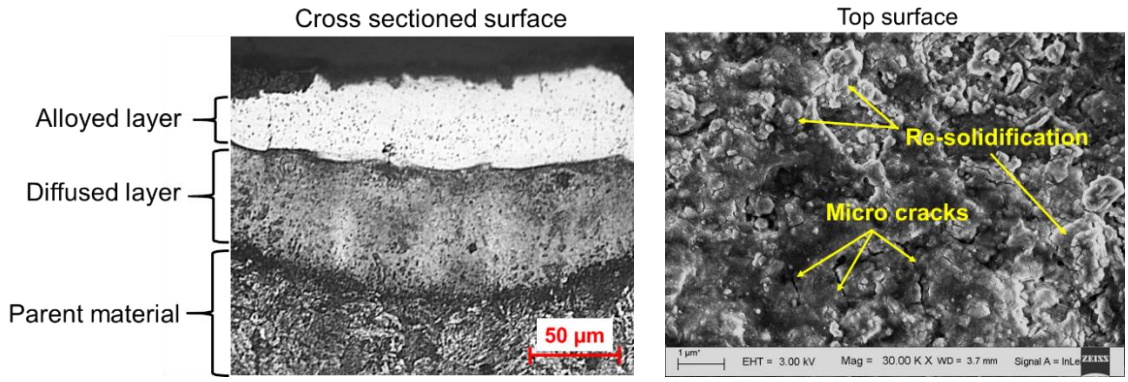

Figure 5.3 Microscopic image showing the cross-sectioned surface at 40× and (b) FESEM image showing the top surface of the EDA workpiece at 30,000× for the workpiece processed at t_{on} of 1006 µs and I_d of 6 A with urea mixed DI water dielectric medium

The FESEM micrograph showing the top surface of the alloyed workpiece is shown in Figure 5.3(b). From this figure, the re-solidification phenomenon could be observed as indicated by white globules. It is expected that these re-solidified regions consist of the tool and the workpiece materials. The presence of these elements can be analyzed by using EDS, and this has been reported in the following section. Further, from this FESEM image, there are few microcracks observed at the top surface. This is due to thermal stresses developed due to subsequent heating and quenching during the alloying process. Following sub-section deals with the study of the elements transferred onto the workpiece by EDS analysis.

5.2.1 Elemental analysis

This section presents the study on the transfer of the elements over the workpiece after electric discharge alloying in deionized water and urea mixed deionized water. The EDS spectrum and the related results are presented in the following sub-sections.

A. Elemental analysis for workpiece processed in DI water

To study the tool elements and decomposed dielectric transferred over the workpiece after alloying, EDS analysis was performed. Area scan of the workpiece was performed at the top surface. Figure 5.4 shows the micrograph and the composition of elements viz. Fe, Ti, Al, O, for the workpiece processed in DI water at pulse on-time of 856 µs and discharge current of 10 A. It is observed from the EDS spectra that Ti and Al elements

TH-2735_136103036

have been successfully transferred over the workpiece material. A maximum of 27.2 % titanium with 7.6 % aluminum and 40.3 % oxygen were observed.

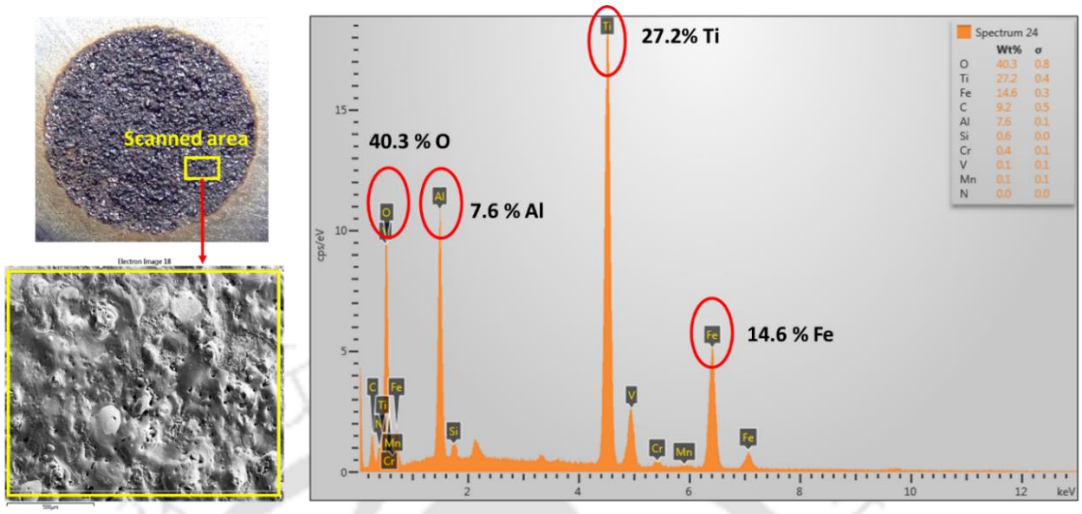

Figure 5.4 Pictorial image with micrograph and elemental spectra for EDA workpiece alloyed using DI water at t_{on} of 856 µs and I_d of 10A

The distribution of the elements present at the surface of EDA has been studied by elemental mapping for the workpiece processed using DI water at the processing condition of 856 µs pulse on-time and 10A discharge current. The FESEM image shown in Figure 5.5 (a) is depicting the interface region of the alloyed region and parent material indicated by the yellow curve. From the EDS layered image shown in Figure 5.5 (b), the difference in the color distribution at the alloyed and parent material is observed. The presence of Al and Ti over the alloyed region as compared to the parent material is noted in Figure 5.5 (c) and (d), respectively. Also, the concentration difference of Fe at the alloyed region and parent material shown in Figure 5.5 (e) indicates that the concentration of Fe has decreased at the alloyed region. It is also seen that oxygen is uniformly distributed throughout the entire surface in Figure 5.5 (f). This indicates the formation of oxide at both alloyed region and parent material. The formation of oxide is due to the use of DI water as the dielectric.

TH-2735_136103036

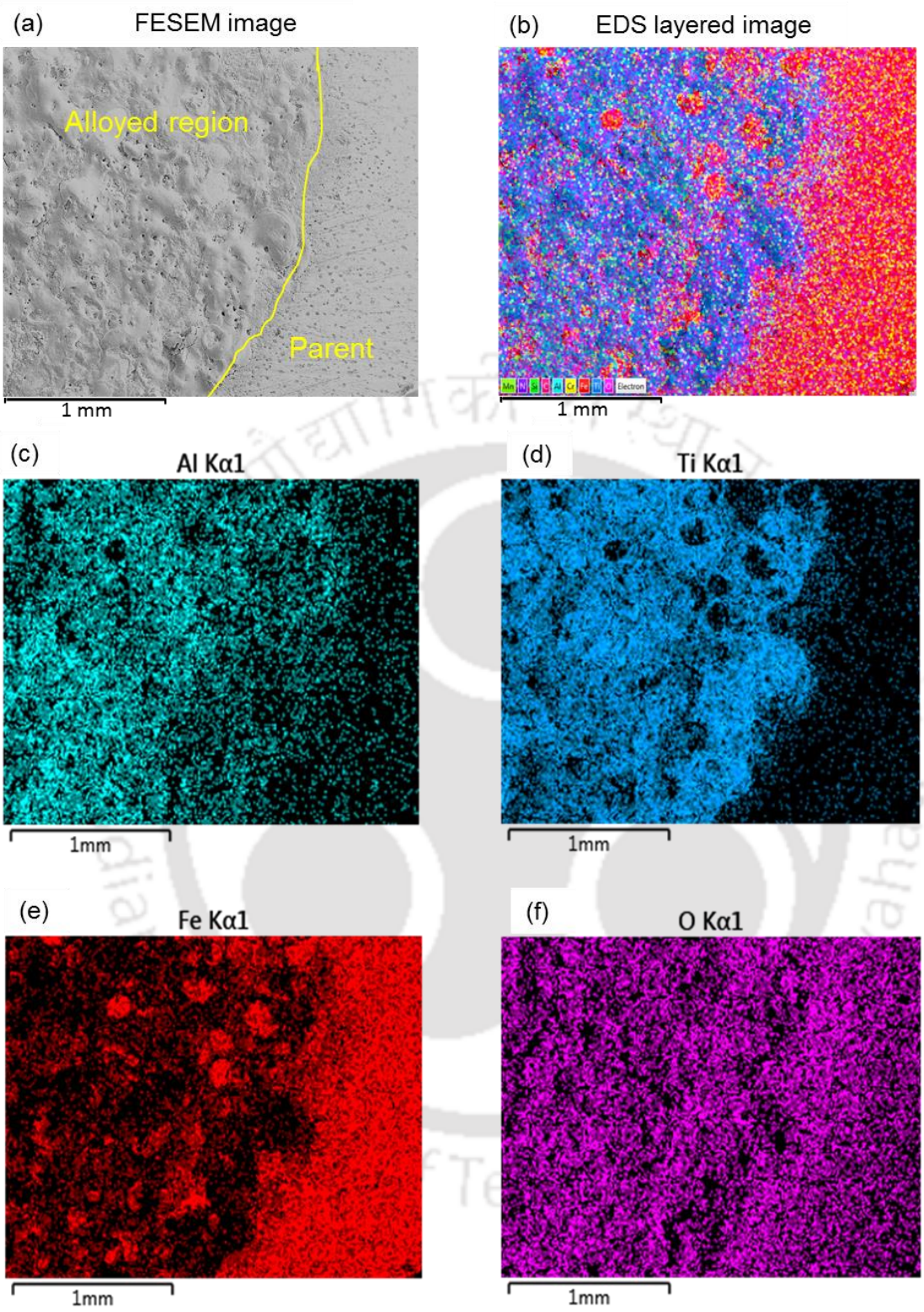

Figure 5.5 Micrographs showing the distribution of elements at the alloyed region and parent material for the workpiece alloyed in presence of DI water at t_{on} of 856 µs and I_d of 10A

The presence of the alloying elements along with the depth of the workpieces was assessed by using line scanning along the cross-sectioned surface. Figure 5.6 (a) shows

TH-2735_136103036

the line along which the scanning has been performed, and Figure 5.6 (b) shows the presence of the elements along with the depth as highlighted by different colors. From the figure, the presence of iron has been noted as indicated by the green curve. Further, the presence of Ti, Al, and oxygen at the alloyed region is noticed, as indicated by red, blue and magenta respectively. The presence of Ti, Al and nitrogen is seen to be more at the alloyed region. It is also observed that at the alloyed region, the presence of iron is reduced, as indicated by the green curve. This shows the fusion of the alloying elements at the alloyed region.

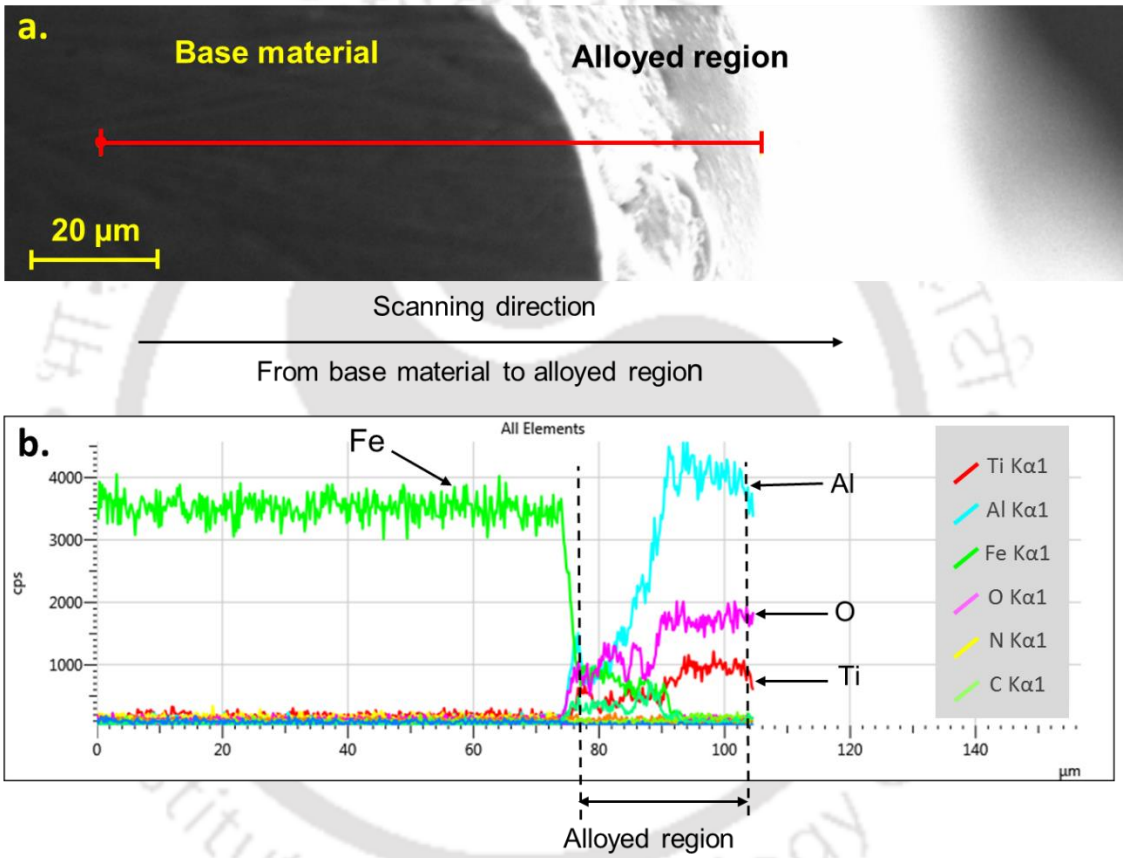

Figure 5.6 Distribution of elements along the cross-sectioned surface for workpiece alloyed using DI water at t_{on} of 856 µs and I_d of 10A

B. Elemental analysis for workpieces processed in urea mixed DI water

Figure 5.7 shows the micrograph and the elemental composition of elements viz. Fe, Ti, Al, O, and N for the workpiece processed in urea mixed DI water. It is observed from the EDS spectra that there is a transfer of tool element viz. Ti and Al over the work material along with nitrogen and oxygen from the urea mixed dielectric. Elemental concentration

TH-2735_136103036

up to a maximum of 16.5 % Ti with 12 % Al, 35.02 % oxygen, and 4 % nitrogen could be observed.

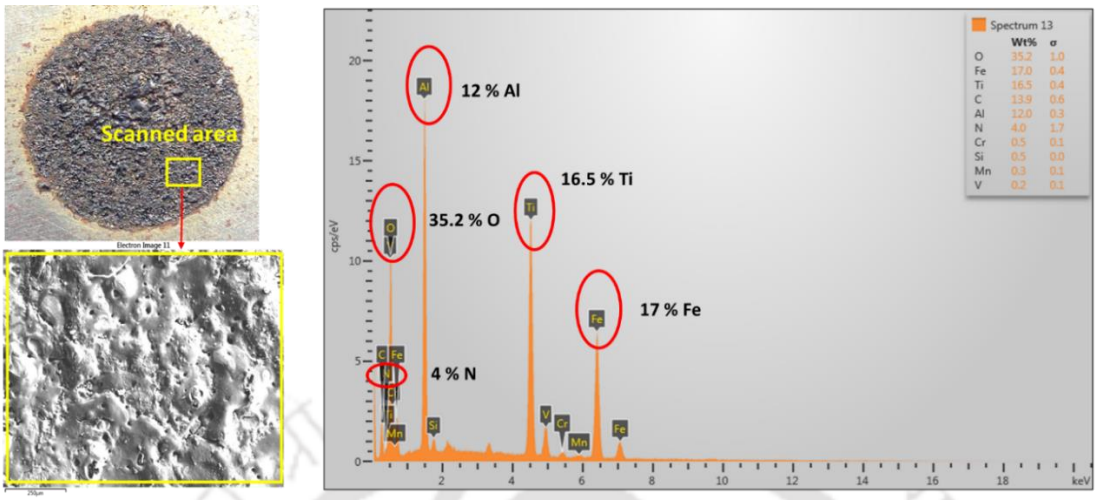

Figure 5.7 Micrograph and elemental spectra for EDA workpiece processed at t_{on} of 856 µs, and I_d of 10A using urea mixed DI water as dielectric

AISI P20 mold steel being the parent material, the composition of Fe in the alloyed region is in the range of 17 %, which is fairly reduced as compared to that of the parent material. The presence of Ti and Al is desirable for the present study and is attributed to material transfer from the tool material during the discharge phenomenon. The tool composition considered for the study is 50 % Ti and 50 % Al by weight. However, it is seen that the composition of Ti over the alloyed region is more as compared to that of Al in both cases. This is due to the higher density of Ti than that of Al. Some of the decomposed particles of Al from the tool might have been flushed away. Further, the presence of nitrogen and oxygen element was also noticed. These elements are perceived to be released from the decomposition of urea mixed DI water. It is clear from the spectra that for the workpiece processed in DI water, nitrogen is not detected; however, for workpiece processed with urea mixed DI water, nitrogen is detected. From this, it can be inferred that the workpiece has been successfully nitrided with the use of urea.

Figure 5.8 shows the distribution of elements over the alloyed workpiece. The FESEM image for the area of study is shown in Figure 5.8 (a), and the EDS layered image is shown in Figure 5.8 (b). From the figure, the distribution of Al, Ti, and nitrogen was observed in Figure 5.8 (c), (d), and (f), respectively. The presence of Fe, being the parent material, is depicted in Figure 5.8 (e).

TH-2735_136103036

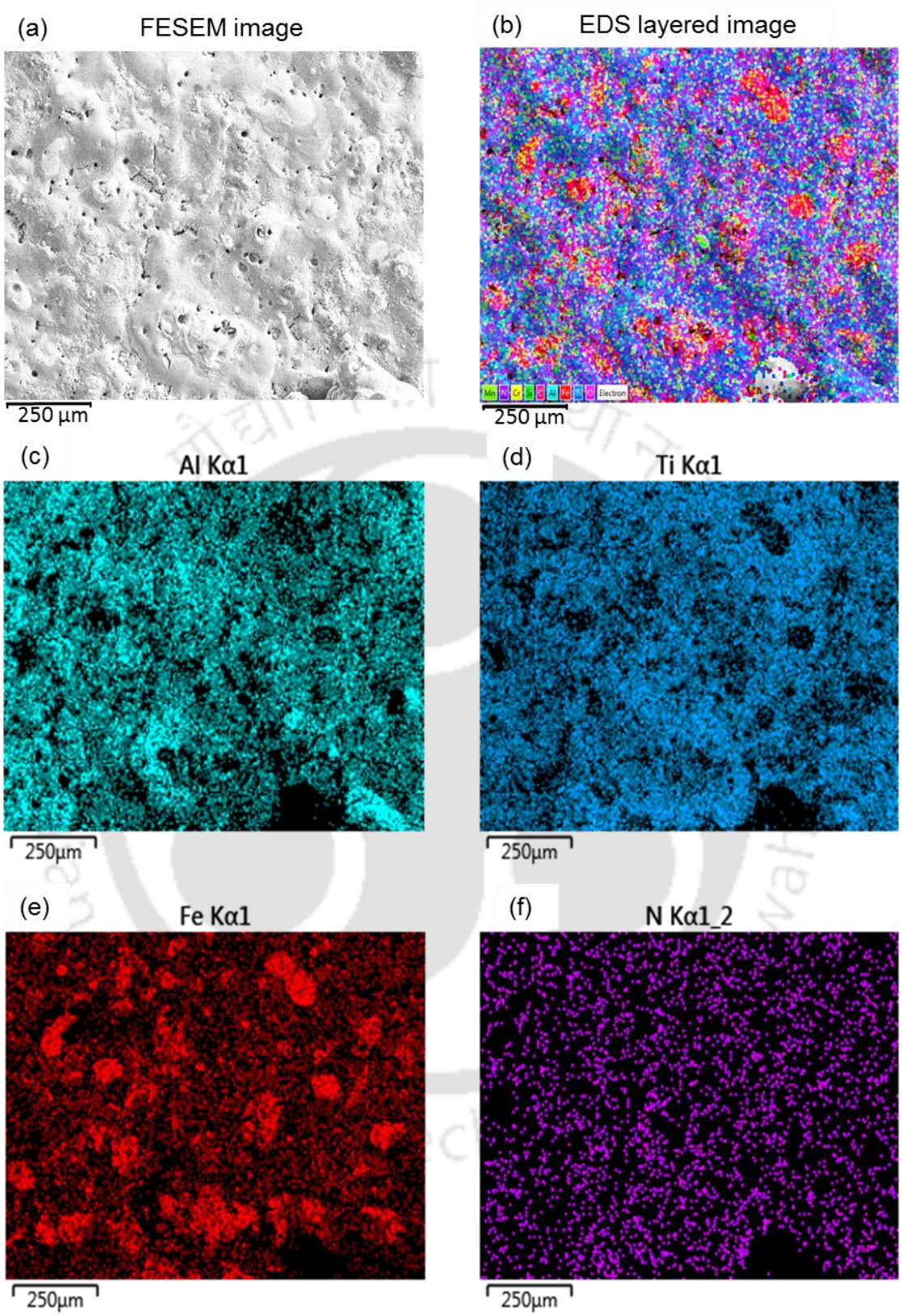

Figure 5.8 Micrographs showing the distribution of elements at the alloyed region for the workpiece alloyed using urea mixed DI water at t_{on} of 856 µs and I_d of 10A

TH-2735_136103036

5.2.2 X-ray diffraction analysis

X-ray diffraction analysis for the workpieces alloyed at t_{on} of 546 µs and I_d of 10 A with both the dielectric media, i.e., DI water and urea mixed DI water has been carried out to study the phases present in the alloyed surface. Figure 5.9 shows the comparison of the diffraction pattern for the workpieces processed in DI water and urea mixed DI water. From the figure, the presence of Ti_4AlN_3, Fe_3O_4, and TiAl has been observed for the workpiece processed using urea mixed DI water. The entry card number for these compounds in the existing JCPDS database are 96-152-6339 for Ti_4AlN_3, 96-900-2331 for Fe_3O_4, and 96-153-2770 for TiAl. Further, it is also noted that the peak corresponding to Ti_4AlN_3 is not observed for the workpiece processed in DI water. The presence of Ti_4AlN_3, Fe_3O_4, and TiAl confirms the formation of alloy as a result of electric discharge alloying. Also, the phases present are hexagonal for Ti_4AlN_3, cubic for Fe_3O_4, and tetragonal for TiAl.

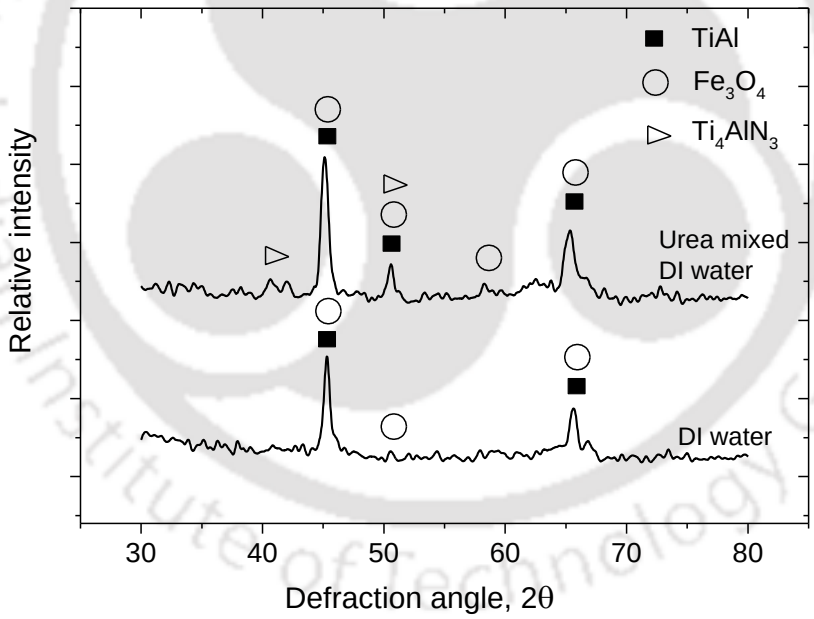

Figure 5.9 X-ray diffraction pattern for EDA surface for the workpiece alloyed using DI water and urea mixed DI water at t_{on} of 546 µs and I_d of 10 A

5.2.3 Alloyed layer thickness

To determine the alloyed layer thickness, the alloyed workpieces were cross-sectioned, polished, etched, and were observed under an optical microscope by following the procedure discussed in Chapter 3, Section 3.3.4, Page No. 50. Distinct layers of the

TH-2735_136103036

alloyed region, diffused region, and parent material were observed after the etching of the workpieces. To study the effect of discharge current and pulse on-time onto the alloyed layer thickness, the measurements were taken for all the 16 experiments, i.e., with a varying t_{on} and I_d combination as stated above for two different dielectrics viz., deionized water and urea mixed deionized water. Three sets of 16 experiments each were performed to check the repeatability. The following sub-sections present the experimental results of the alloyed layer thickness for the workpieces processed in two different dielectric media and finally making a comparison of the two.

A. Alloyed layer thickness for workpieces processed in DI water

The cross-section images of the workpieces processed in deionized water at four levels of pulse on-time (546 µs, 706 µs, 856 µs, and 1006 µs) and discharge current (6 A, 8 A, 10 A, and 12 A) are shown in Figure 5.10. The alloyed layer thickness is the distance from the top surface to the interface of the alloyed region and the diffused region, as shown in the figure. From the figure, it is observed that most of the alloyed layers exhibit a wavy nature. This is due to the overlapping of the electric discharge as discussed in Chapter 4, Figure 4.13, Page No. 69.

TH-2735_136103036

Pulse on-time	Dielectric medium – DI water			
	Discharge current			
	6A	8A	10A	12A
546 µs	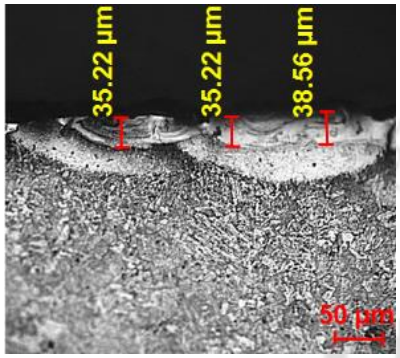	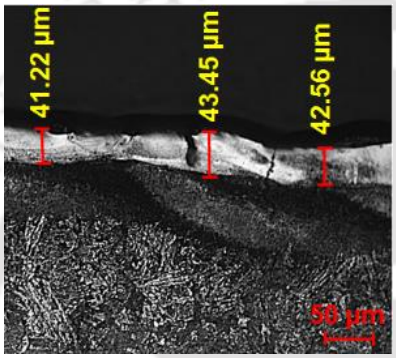	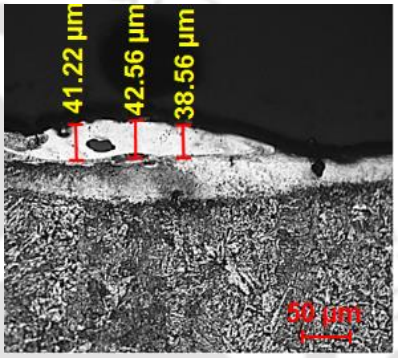	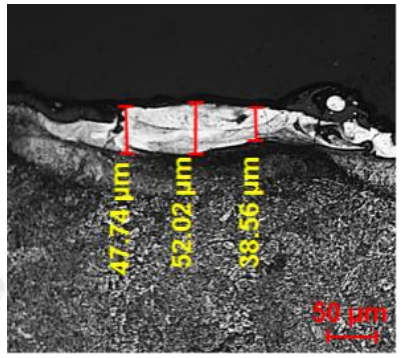
706 µs	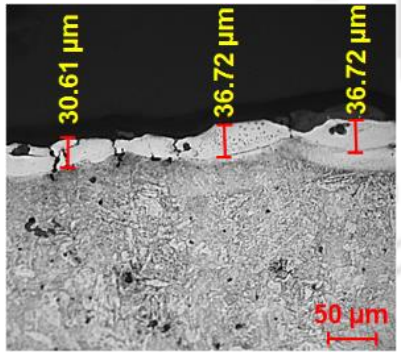	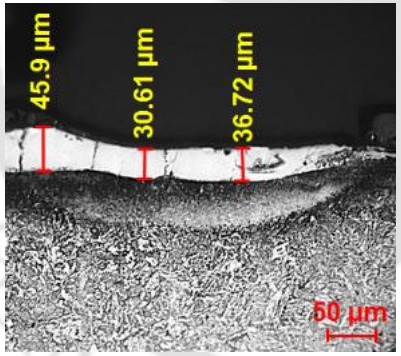	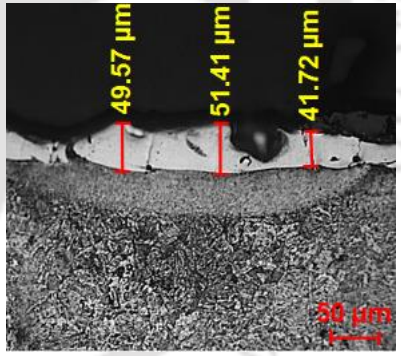	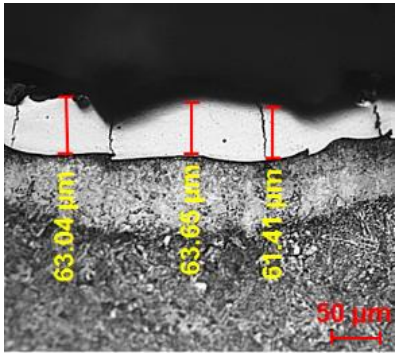

TH-2735_136103036

Pulse on-time	Dielectric medium – DI water			
	Discharge current			
	6A	8A	10A	12A
856 µs	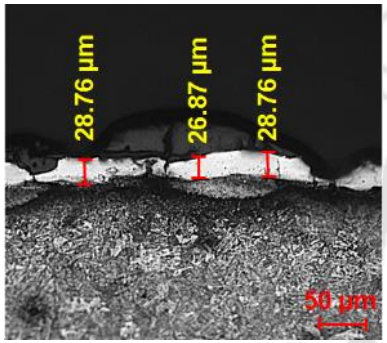	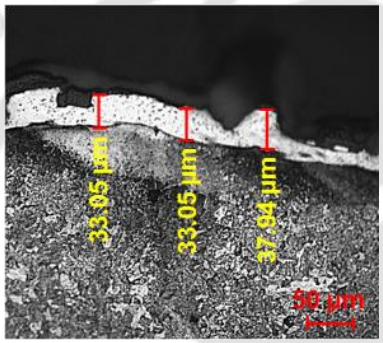	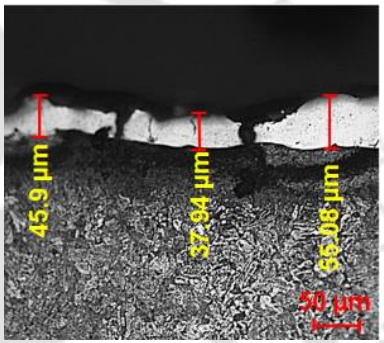	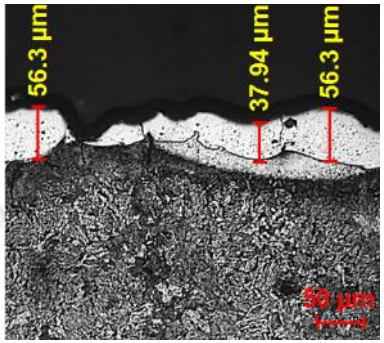
1006 µs	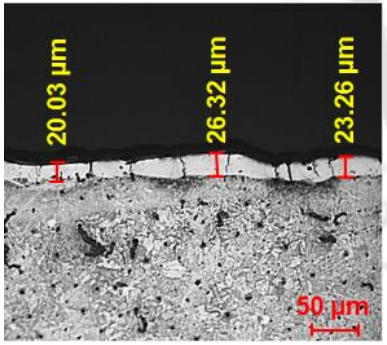	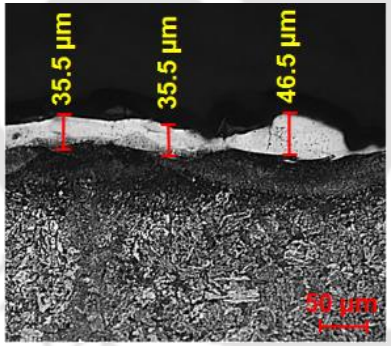	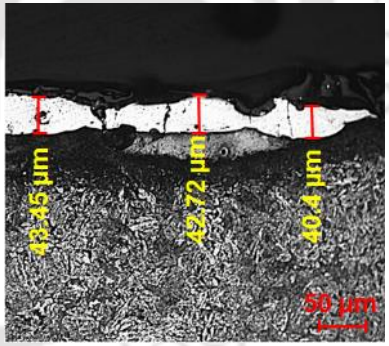	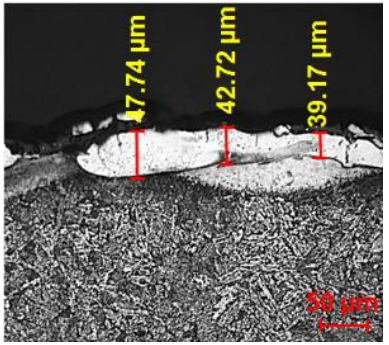

Figure 5.10 Optical micrographs at 20× showing uniform alloyed layer at varying on-time and discharge current processed with DI water as dielectric

TH-2735_136103036

The measurements of the alloyed layer thickness were taken at nine different locations with an approximate equal interval, and the average value of the nine readings was computed as the average alloyed layer thickness. For each set of processing condition, the experiment was repeated three times, and the average values were computed. These values are listed in Table 5.1. The alloyed layer thickness for the three repeated experiments are listed in column (iv), (v), and (vi), and the average of these three values are listed in column (vii). In column (viii), the coefficient of variation of the values is listed. It could be observed that the coefficient of variation is low which is in the range of 2.43 % to 9.58 %. A low coefficient of variation indicates that the measured data is good.

Table 5.1 Results pertaining to average alloyed layer thickness for workpiece processed in DI water

Expt. no.	t_{on} (µs)	I_d (A)	Alloyed layer thickness (µm)				Coefficient of variation %
			Expt. 1	Expt. 2	Expt. 3	Average	
(i)	(ii)	(iii)	(iv)	(v)	(vi)	(vii)	(viii)
1.	546	6	33.05	38.56	36.93	36.18	7.82
2.	706	6	35.45	30.61	34.21	33.42	7.52
3.	856	6	25.74	28.76	26.64	27.05	5.73
4.	1006	6	28.32	26.32	23.50	26.05	9.29
5.	546	8	41.33	42.23	40.23	41.26	2.43
6.	706	8	42.26	36.15	37.21	38.54	8.47
7.	856	8	35.63	40.20	36.12	37.32	6.72
8.	1006	8	33.21	37.94	36.29	35.81	6.70
9.	546	10	43.74	47.30	42.00	44.35	6.09
10.	706	10	41.33	49.57	48.35	46.41	9.58
11.	856	10	45.50	43.45	48.25	45.73	5.27
12.	1006	10	47.21	40.51	42.06	43.26	8.11
13.	546	12	45.33	52.02	47.00	48.12	7.23
14.	706	12	63.21	60.23	57.14	60.19	5.04
15.	856	12	50.21	50.50	43.39	48.03	8.37
16.	1006	12	56.34	47.74	55.26	53.11	8.82

Further, the effect of pulse on-time and discharge current onto the alloyed layer thickness has been studied. Figure 5.11 shows the variation of the thickness of the alloyed layer

TH-2735_136103036

when the discharge current and pulse on-time are varied. From the figure, it is observed that the alloyed layer thickness increases with an increase in discharge current for a fixed value of pulse-on time. This is due to the higher amount of energy input. However, for a fixed value of discharge current, the layer thickness tends to decrease with an increase in pulse on-time. This is because, with an increase in pulse on-time, the plasma radius increases, and hence the plasma intensity reduces (discussed in detail in Chapter 4, Section 4.2.3 Page No. 65). However, for the case of 12 A discharge current, the trend is not similar to the other three discharge current values. This is due to the instability of the discharge phenomenon at a high current. A similar observation was also made for the workpiece processed in hydrocarbon oil discussed in Chapter 4, Section 4.2.3, Page No. 65.

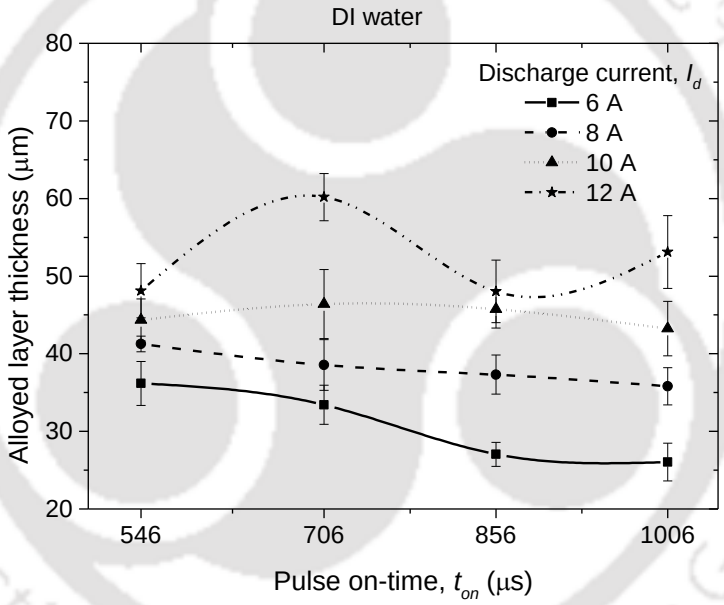

Figure 5.11 Effect of discharge current and pulse on-time on the alloyed layer thickness for workpieces processed using DI water

B. Alloyed layer thickness for workpieces processed using urea mixed deionized water

In a similar approach, alloying of AISI P20 mold steel was carried out in urea mixed deionized water with pulse on-time of 546 µs, 706 µs, 856 µs, and 1006 µs and discharge current of 6 A, 8 A, 10 A, and 12 A. The cross-section images of the alloyed workpieces are shown in Figure 5.12. From the figures, distinct layers of the alloyed region, diffused region, and the parent material are clearly observed. The nature of the alloyed layer

TH-2735_136103036

formed using urea mixed deionized water in terms of its uniformity and continuity was found to be similar to that of the workpieces processed with deionized water.

The thickness of the alloyed layer was measured in the same procedure as discussed for the case of workpieces processed in deionized water. The average values of the alloyed layer thickness measured are listed in Table 5.2. The alloyed layer thickness for the three repeated experiments are listed in column (iv), (v), and (vi), and the average of these three values are listed in column (vii). In column (viii), the coefficient of variation of the values is listed. It could be observed that the coefficient of variation ranges from 2.59 % to 15.46 %.

TH-2735_136103036

Pulse on-time, t_{on}	Dielectric medium – Urea mixed DI water			
	Discharge current, I_d			
	6A	8A	10A	12A
546 µs	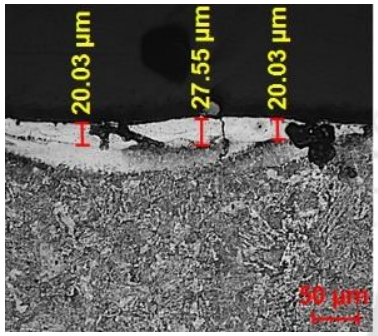	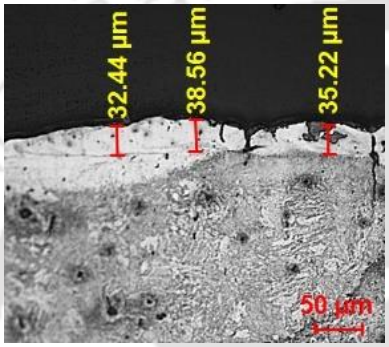	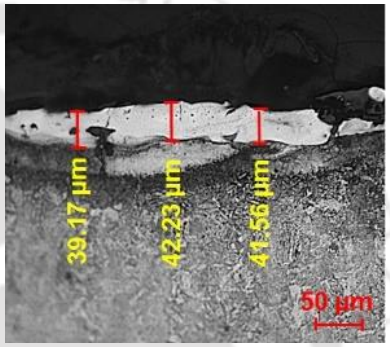	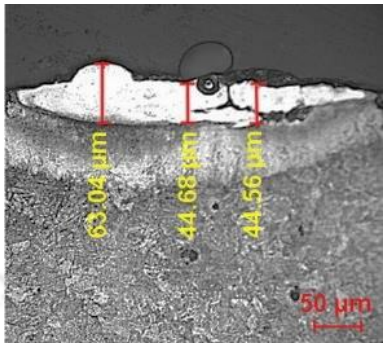
706 µs	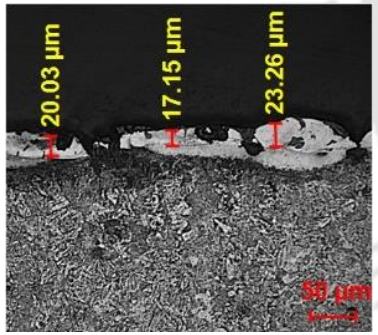	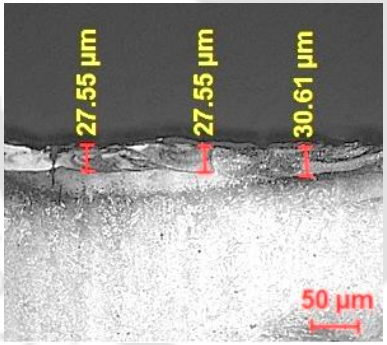	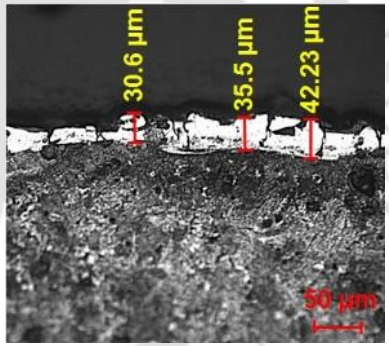	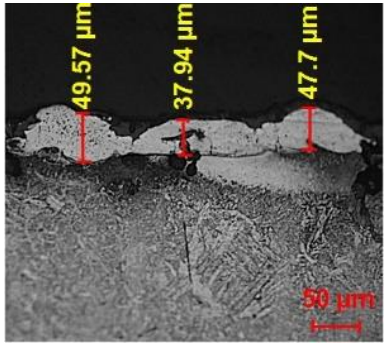

TH-2735_136103036

Pulse on-time, t_{on}	Dielectric medium – Urea mixed DI water			
	Discharge current, I_d			
	6A	8A	10A	12A
856 µs	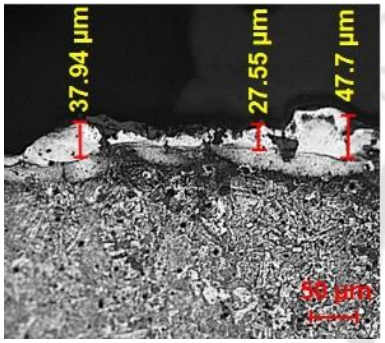	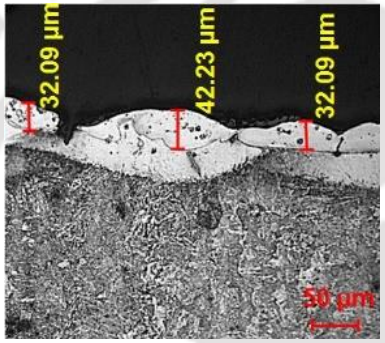	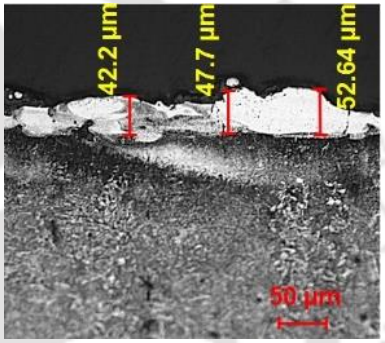	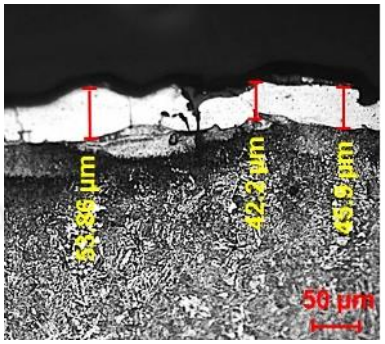
1006 µs	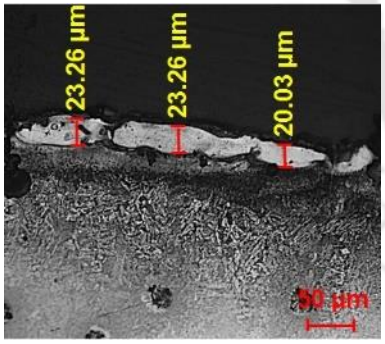	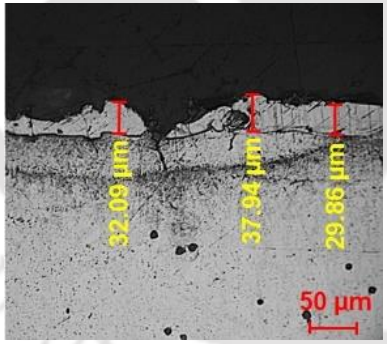	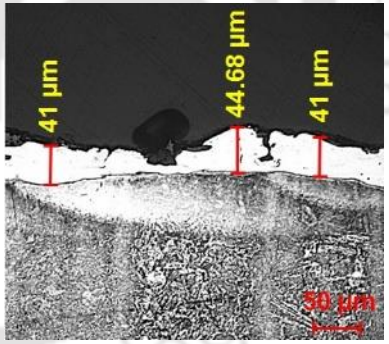	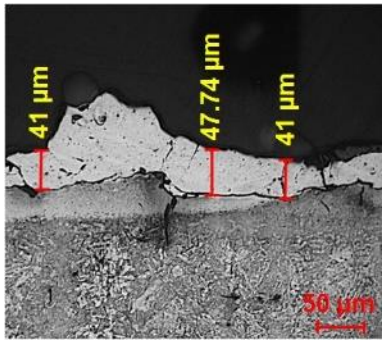

Figure 5.12 Optical micrographs at 20× showing uniform alloyed layer at varying on-time and discharge current processed with urea mixed DI water as dielectric

TH-2735_136103036

Table 5.2 Experimental results for average alloyed layer thickness for workpiece processed in urea mixed DI water

Expt. No.	t_{on} (µs)	I_d (A)	Alloyed layer thickness (µm)				Coefficient of variation %
			Expt. 1	Expt. 2	Expt. 3	Average	
(i)	(ii)	(iii)	(iv)	(v)	(vi)	(vii)	(viii)
1.	546	6	22.18	27.00	20.03	23.07	15.46
2.	706	6	22.54	20.65	20.03	21.07	6.19
3.	856	6	20.15	18.00	20.00	19.38	6.18
4.	1006	6	18.87	20.97	23.26	21.03	10.43
5.	546	8	35.41	32.00	32.44	33.28	5.57
6.	706	8	35.47	37.00	32.09	34.85	9.96
7.	856	8	33.29	32.09	35.00	33.46	4.37
8.	1006	8	28.57	27.00	30.00	28.52	7.44
9.	546	10	40.99	39.17	39.17	39.77	2.64
10.	706	10	36.11	35.50	42.00	37.87	9.48
11.	856	10	44.97	47.00	42.20	44.72	5.39
12.	1006	10	42.23	40.00	41.01	41.07	2.71
13.	546	12	50.76	52.00	57.00	53.25	6.20
14.	706	12	45.07	46.01	49.57	46.88	5.06
15.	856	12	47.32	53.00	53.85	51.39	6.91
16.	1006	12	45.58	47.01	48.00	46.86	2.59

To further assess the influence of discharge current and pulse on-time onto the alloyed layer thickness for the workpiece processed in urea mixed deionized water, a line graph has been plotted. Figure 5.13 shows the variation of the thickness of the alloyed layer when the discharge current and pulse on-time are varied. From the figure, it is observed that for a fixed value of pulse-on time, the alloyed layer thickness increases with an increase in discharge current owing to a higher amount of energy input. For the minimum discharge current of 6 A at varying pulse on-time, the alloyed layer thickness ranges from 19.38 µm to 23.07 µm, i.e., a difference of approximately 4 µm is observed, while for that of the maximum discharge current of 12 A, the thickness ranges from 46.86 µm to 53.25 µm, i.e., a difference of approximately 6 µm is seen. However, for a fixed value of minimum pulse on-time of 546 µs and at varying discharge current, the layer thickness ranges from 23.07 µm to 53.25 µm, i.e., a difference of approximately 30 µm, while for

TH-2735_136103036

that of the maximum pulse duration of 1006 µs, the layer thickness ranges from 21.03 µm to 46.86 µm, i.e., a difference of approximately 25 µm is observed. From this, it can be inferred that the discharge current has a significant influence on the alloyed layer thickness than the pulse on-time.

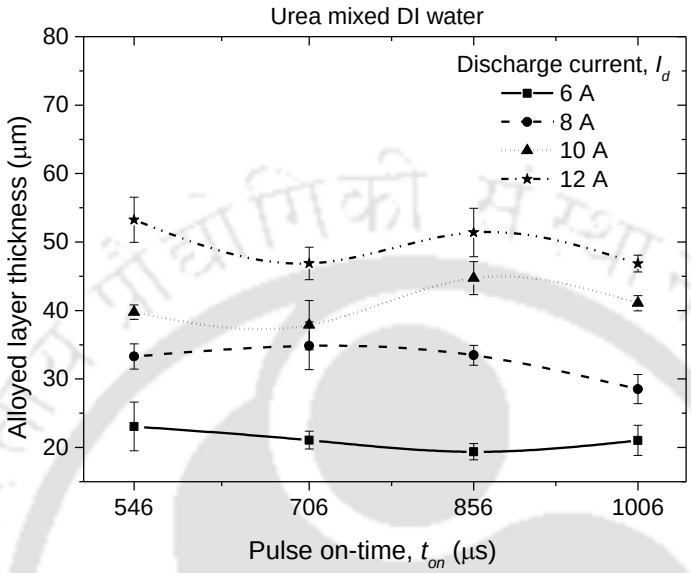

Figure 5.13 Effect of discharge current and pulse on-time on the alloyed layer thickness for workpieces processed using urea mixed DI water

C. Comparison of the alloyed layer thickness for workpieces processed in DI water and urea mixed DI water

The effect of pulse on-time and dielectric medium on the alloyed layer thickness for the workpieces processed at varying discharge current is as shown in Figure 5.14 with the help of a bar graph. From the figure, it is observed that with an increase in discharge current, the thickness of the alloyed layer increases for workpieces processed in both DI water and urea mixed DI water. This is due to higher energy intensity. It is also observed that with an increase in pulse on-time, the alloyed layer thickness decreases. This is because, with an increase in the pulse duration, the radius of the plasma channel formed during the sparking phenomena increases, thereby resulting in lower plasma intensity. This results in a low penetration depth of the heat induced by the plasma during the discharge phenomenon. Further, it is observed that the alloyed layer thickness is higher for the workpieces processed in DI water than the urea mixed DI water for discharge current of 6 A (Figure 5.14 (a)), 8 A (Figure 5.14 (b)), and 10 A (Figure 5.14 (c)). This is because, with the addition of urea in the DI water, the electrical conductivity increases,

TH-2735_136103036

and there is an early bridging of the discharge channel resulting in lower penetration of the heat, thereby resulting in the reduction of the melted depth of the workpiece (discussed in Section 5.2, Figure 5.1, Page No. 82). However, for the case of 12 A discharge current (Figure 5.14 (d)), the layer thickness for the workpiece processed in urea mixed DI water is higher than that of DI water at pulse on-time of 546 µs and 856 µs. This is due to the presence of unwanted debris leading to unstable discharge.

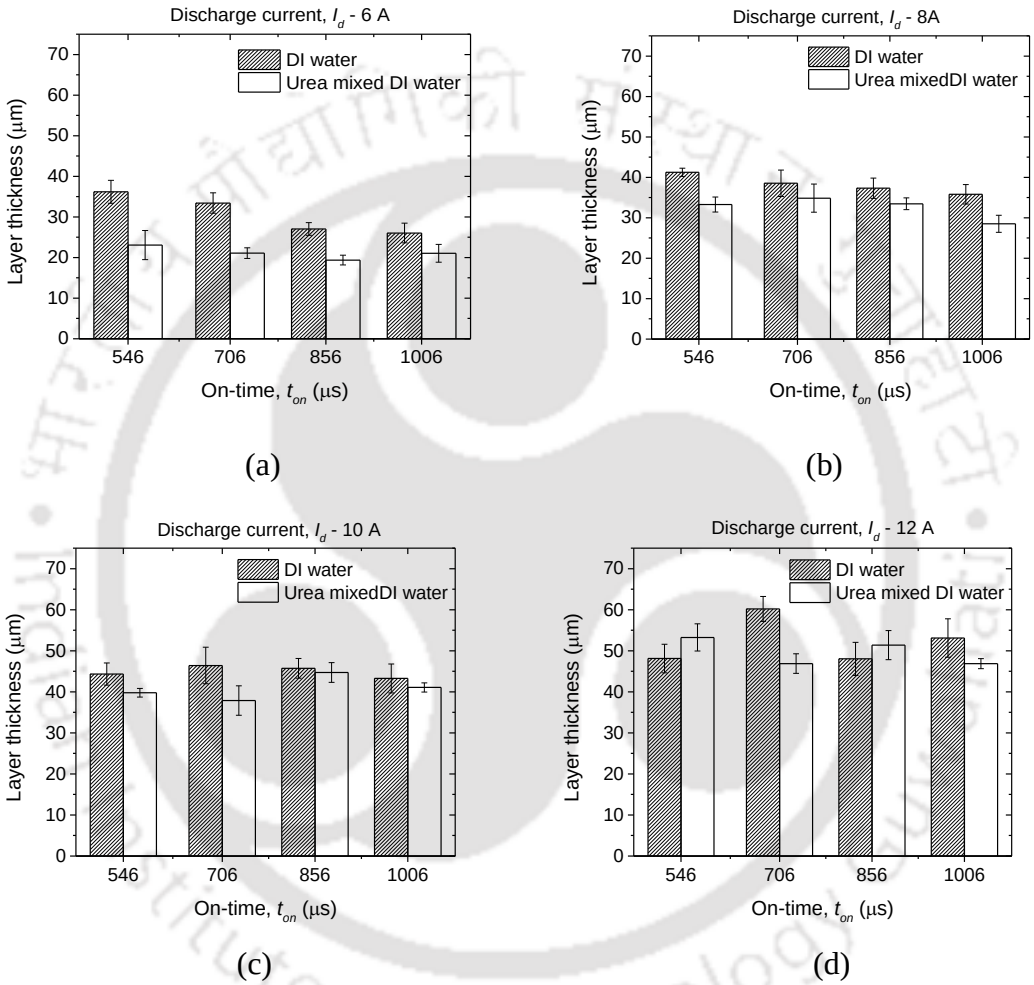

Figure 5.14 Bar graph showing the effect of t_{on} and the dielectric medium on the alloyed layer thickness for workpieces processed at varying discharge current

Following section deals with the hardness of the alloyed layer for the workpieces processed in the two different dielectric media.

5.2.4 Hardness analysis

The cross-sectioned workpieces shown in Figures 5.10 and 5.12 were further examined for the hardness in the alloyed region, diffused region, and parent material. Vickers hardness test was employed to determine the hardness values. Figure 5.15 shows the

TH-2735_136103036

comparison of the hardness value for the workpieces processed using different dielectric and at different regions. The hardness values were measured at the different layers formed after the alloying process. From the figure, it is observed that the hardness value at the alloyed region and diffused region is higher as compared with that of the parent material (approximately 300 $HV_{0.3}$). This increase in hardness at the alloyed region is due to the formation of TiAl and Ti_4AlN_3, as observed from the XRD analysis shown in Figure 5.9. Also, the enhancement in hardness of the diffused layer resulted due to heat treatment during the alloying process. For the alloyed layers, hardness of 579.83 $HV_{0.3}$ and 604.35 $HV_{0.3}$ were noted when processed using DI water, and urea mixed DI water, respectively. Higher hardness value observed in workpiece processed in urea mixed DI water is due to the formation of alloyed layer consisting of additional Ti_4AlN_3. The percentage increase in the hardness of the alloyed region for the workpiece processed in DI water was found to be enhanced by 87.04 % as compared to that of the parent material, while that for the workpiece processed in urea mixed deionized water was 101.45 %.

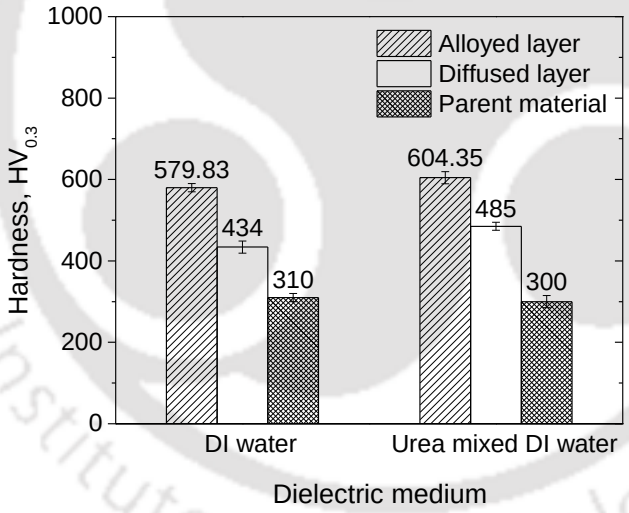

Figure 5.15 Hardness of the workpieces processed using different dielectric

The following sub-section deals with the material deposition rate for the two different processing conditions, and comparisons have also been made.

5.2.5 Material deposition rate

The material deposition rate (MDR) for the workpieces processed with both the dielectric medium was determined by following the similar approach as discussed in Chapter 4, Section 4.2.5, Page No. 76, for the workpiece processed in hydrocarbon oil. In this

TH-2735_136103036

section, a comparative study has been made and discussed in detail to study the effect of the pulse on-time and the discharge current with the use of deionized water and urea mixed deionized water as a dielectric medium.

The effects of pulse on-time, discharge current, and dielectric medium on the material deposition rate is shown in Figure 5.16. From the figure, it is observed that for fixed discharge currents of 6 A, 8 A, 10 A, and 12 A, the material deposition rate is found to be decreasing with increase in pulse on-time from 546 µs to 1006 µs for both the types of the dielectric medium. This is due to the decrease in energy density as a result of increasing the plasma channel radius. Similar observations were also made for the workpieces processed in hydrocarbon oil discussed in Chapter 4, Section 4.2.5, Page No. 76. However, for a fixed value of pulse on-time, the material deposition rate increases with an increase in discharge current in both cases. This is because, with an increase in discharge current, the power intensity increases, leading to higher wear of the PM tool and hence increasing the transfer of the material from the tool. It can be mentioned that during the EDA process, there is simultaneous erosion of both tool and workpiece material. But as the workpiece material is a solid material and the tool being the powder metallurgy compact, the erosion of tool material is higher, and hence its contribution onto the material deposition is more significant.

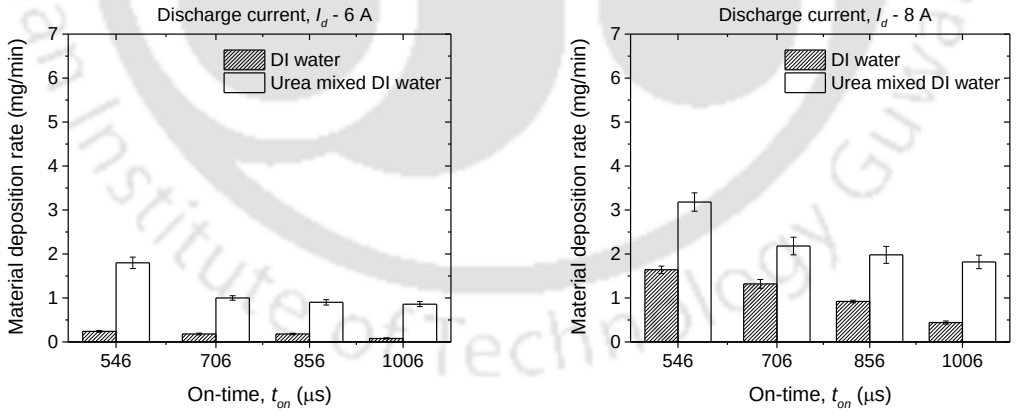

(a) (b)

TH-2735_136103036

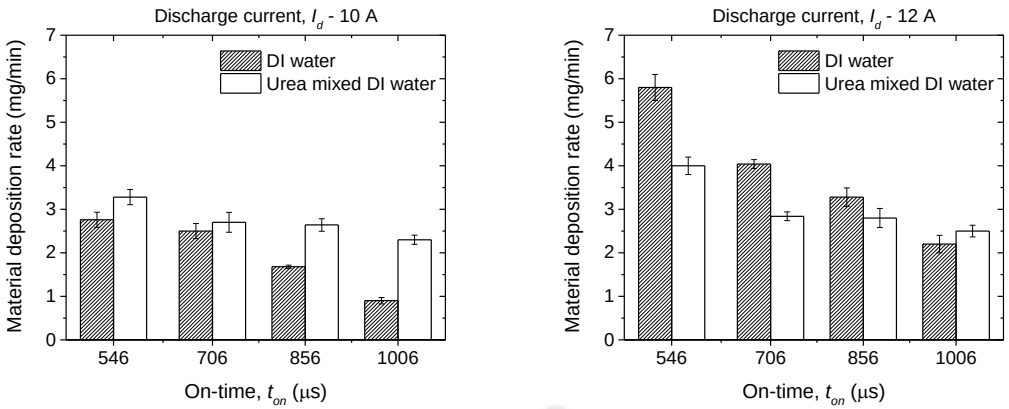

(c) (d)

Figure 5.16 Comparison of material deposition rate showing the effect of the pulse on-time, dielectric medium, and discharge current of (a) 6 A, (b) 8 A, (c) 10 A, and (d) 12 A

Further, on comparing the material deposition rate for the workpieces processed in the two dielectric media shown in Figure 5.16, it is observed that for the discharge current values of 6 A, 8 A, and 10 A, the MDR is higher for the workpieces processed in urea mixed deionized water for all the values of pulse on-time. This is because, with the addition of urea in the dielectric, the electrical conductivity of the medium increases, leading to early discharge. As a result, melting and erosion of the workpiece is reduced for the case of urea mixed deionized water, which is desirable for the alloying process. Therefore, a reduction in material removal from the workpiece results in an increase of material deposition rate in the case of urea mixed deionized water. However, for the case of the 12 A discharge current (Figure 5.16 (d)), the MDR is found to be lesser in the case of urea mixed deionized water as compared to DI water. This is because, at high current there is higher erosion of both workpiece and powder metallurgy tool. These eroded materials and presence of urea in the dielectric leads to the instability of the discharge phenomenon such as arcing and localized deposition.

In addition to the comparison made in the alloyed layer thickness (Figure 5.14) and material deposition rate (Figure 5.16) for the workpieces processed in DI water and urea mixed DI water separately, it has been observed that the addition of urea increases the material deposition rate in-spite of having lesser layer thickness. This is because of the difference in the density of the alloyed layer. The alloyed layer formed in the case of urea mixed dielectric comprises of Ti_4AlN_3 and TiAl (from XRD analysis). However, for the workpiece processed in deionized water, there is no formation of Ti_4AlN_3 (from XRD

TH-2735_136103036

analysis). Therefore, the presence of Ti_4AlN_3 resulted in the increase in material deposition rate for the workpiece processed in urea mixed DI water even though the layer thickness is lesser as compared to the workpieces processed in DI water.

Following sub-section deals with the surface roughness of the workpieces processed in the two different dielectric media at varying pulse on-time and discharge current.

5.2.6 Surface roughness

To study the surface roughness of the alloyed workpieces, the roughness measurements were taken for a scan length of 3 mm by using a contact stylus profilometer discussed in Chapter 3, Section 3.1.4, Page No. 39. The average surface roughness (R_a) of the workpieces after the alloying process are listed in Table 5.3 and Table 5.4 for workpieces processed in deionized water, and urea mixed deionized water, respectively.

Table 5.3 Experimental results for the surface roughness for the workpiece processed in deionized water

Expt. No.	t_{on} (µs)	I_d (A)	Surface roughness, R_a (µm)						Coefficient of variation %
			R1	R2	R3	R4	R5	Average	
1.	546	6	4.98	6.38	5.68	5.91	6.73	5.94	11.32
2.	706	6	6.71	5.91	5.68	6.91	7.32	6.51	10.61
3.	856	6	6.53	6.12	8.19	7.58	5.98	6.88	14.01
4.	1006	6	6.34	7.32	8.72	8.91	9.25	8.11	15.19
5.	546	8	5.54	7.89	7.26	8.31	8.12	7.42	15.15
6.	706	8	10.55	8.4	7.69	8.56	8.45	8.73	12.29
7.	856	8	10.39	8.78	10.25	9.21	10.19	9.76	7.39
8.	1006	8	10.56	11.57	11.67	9.21	9.05	10.41	12.01
9.	546	10	8.55	6.42	7.21	6.21	5.98	6.87	15.20
10.	706	10	8.36	8.25	7.88	9.25	9.51	8.65	8.04
11.	856	10	9.97	8.95	8.55	9.52	10.21	9.44	7.32
12.	1006	10	10.85	10.34	11.65	12.21	11.85	11.38	6.73
13.	546	12	10.25	9.35	9.55	8.16	8.54	9.17	9.06
14.	706	12	9.38	10.25	9.23	12.27	9.85	10.20	12.03
15.	856	12	9.05	9.66	11.72	12.15	10.55	10.63	12.39
16.	1006	12	13.7	11.55	11.15	12.21	13.65	12.45	9.47

TH-2735_136103036

Table 5.4 Experimental results for the surface roughness for the workpiece processed in urea mixed deionized water

Expt. No.	t_{on} (µs)	I_d (A)	Surface roughness, R_a (µm)						Coefficient of variation %
			R1	R2	R3	R4	R5	Average	
1.	546	6	7.98	7.32	7.12	6.05	7.32	7.16	9.77
2.	706	6	7.35	6.3	8.15	7.15	6.85	7.16	9.50
3.	856	6	5.35	5.15	7.55	6.55	5.32	5.98	17.34
4.	1006	6	10.15	9.55	7.95	8.55	10.05	9.25	10.42
5.	546	8	8.52	6.39	7.55	8.15	8.85	7.89	12.27
6.	706	8	9.35	7.85	8.21	9.15	7.50	8.41	9.61
7.	856	8	11.65	9.66	12.25	10.25	12.15	11.19	10.46
8.	1006	8	12.55	13.55	12.35	10.25	13.33	12.41	10.53
9.	546	10	8.95	9.22	7.35	9.15	7.44	8.42	11.20
10.	706	10	6.88	5.11	6.55	5.65	6.25	6.09	11.66
11.	856	10	7.65	7.11	8.65	8.52	8.32	8.05	8.09
12.	1006	10	9.36	10.22	9.65	11.74	10.72	10.34	9.12
13.	546	12	13.95	11.25	10.88	12.96	13.65	12.54	11.15
14.	706	12	10.95	13.15	10.77	12.72	13.75	12.27	10.91
15.	856	12	8.55	11.32	10.75	11.95	7.65	10.04	18.44
16.	1006	12	10.35	11.25	10.96	11.55	12.44	11.31	6.82

From the table, it is seen that the coefficient of variation for the surface roughness ranges from 6.73 % to 15.20 % for the workpieces processed in deionized water, while for that of urea mixed deionized water, the value ranges from 6.82 % to 18.44 %. The effect of discharge current and pulse on-time on the surface roughness is shown in Figure 5.17. From the figure, it is observed that for varying pulse on-time and fixed discharge current of 6 A, 8 A, 10 A, and 12 A, the surface roughness tends to increase with an increase in pulse on-time for the workpieces processed in deionized water. However, for the workpieces processed in urea mixed deionized water, a specific trend could not be observed. The surface roughness extends a range of 5.94 µm to 12.45 µm for the workpiece processed in deionized water while that of urea mixed deionized water, the range is 5.98 µm to 12.54 µm, which indicates that addition of urea does not have much impact on the surface roughness value.

TH-2735_136103036

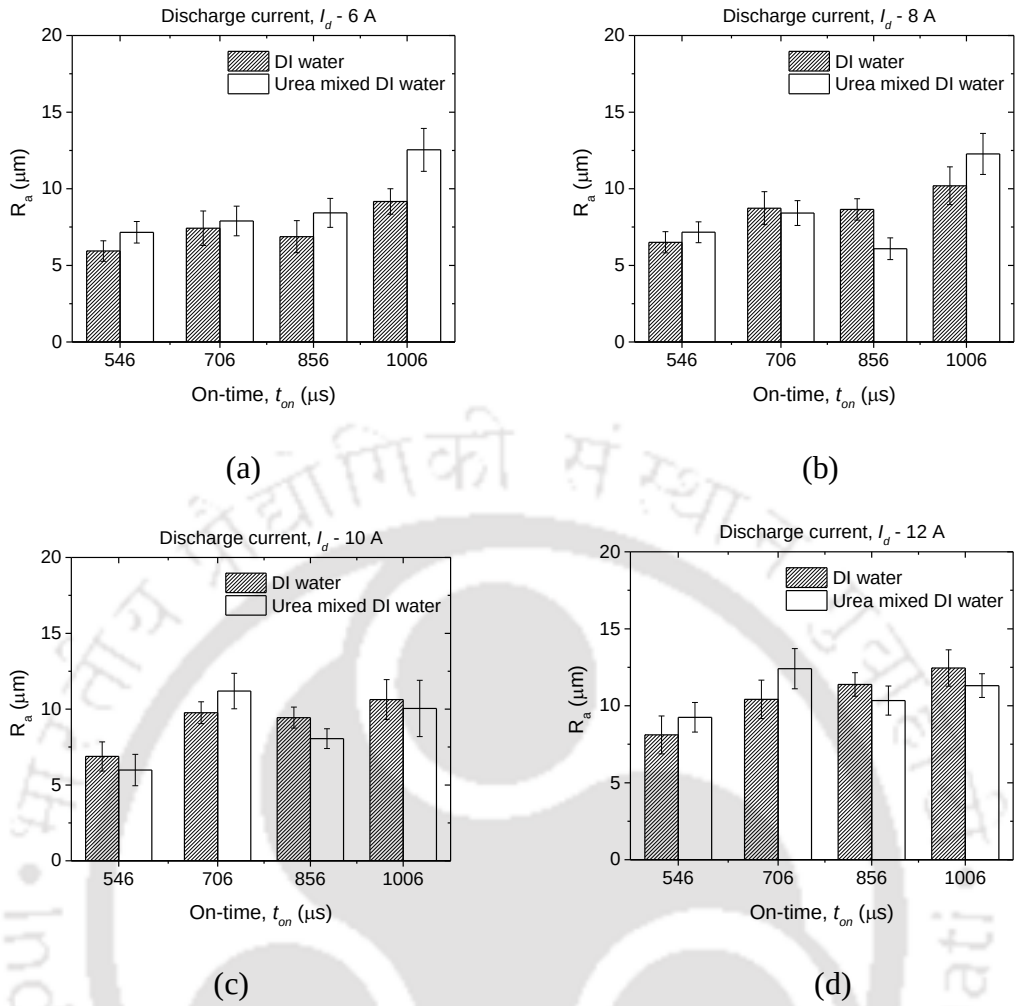

Figure 5.17 Surface roughness for workpieces processed in DI water and urea mixed DI water at varying pulse on-time and discharge current of (a) 6 A, (b) 8 A, (c) 10 A, and (d) 12 A

5.3 Summary

The effects of the dielectric medium on the electric discharge alloying of AISI P20 mold steel using powder metallurgy electrodes of titanium and aluminium have been investigated. Detailed investigations have been carried out to study the effect of pulse on-time discharge current and dielectric medium on the material transfer rate and alloyed layer thickness. The hardness of the alloyed layer has also been characterized.

- EDS results indicated that successful transfer of tool material along with decomposed elements from the dielectric has been successful, and their uniform distribution has also been analyzed from the elemental mapping. Elemental composition up to a maximum of 16.5 % Ti with 12 % Al, 35.02 % oxygen, and 4 % nitrogen could be observed for the workpiece processed in urea mixed deionized water, while for that

TH-2735_136103036

of the workpiece processed in deionized water, a maximum of 27.2 % titanium with 7.6 % aluminum and 40.3 % oxygen was observed.

- Formation of an alloyed layer composed of TiAl, Fe_3O_4, and Ti_4AlN_3 has been observed from the XRD analysis for the workpiece processed using urea mixed DI water, while for the workpiece processed in deionized water, the alloyed layer was composed of TiAl and Fe_3O_4. Therefore, successful alloying has been attained in the present study.
- The study on the alloyed layer thickness indicated that the thickness was more for the workpieces processed using DI water as compared to that of the urea mixed. On average, an alloyed layer of 60.19 µm thickness could be observed for the workpiece processed using DI water, while that for urea mixed deionized water was 53.25 µm.
- The difference in the hardness value of the alloyed layer was observed to be marginal for the workpiece processed in the two media. While using deionized water, the hardness of the alloyed layer was obtained to be 579.83 $HV_{0.3}$, while for that of urea mixed deionized water, the value was 604.35 $HV_{0.3}$. The percentage increase in the hardness of the alloyed region for the workpiece processed in DI water was found to be enhanced by 87.04 % as compared to that of the parent material, while that for the workpiece processed in urea mixed deionized water was 101.45 %.
- The material deposition rate was mainly affected by the discharge current. Increase in discharge current resulted in a higher deposition rate for both the type of dielectric medium.
- The surface roughness of the processed workpieces was found to be dependent upon the discharge current and pulse on-time; however, the addition of urea does not have a significant difference in the roughness value. The surface roughness was found to be in a range of 5.94 µm to 12.45 µm for the workpiece processed in deionized water while that of urea mixed deionized water, the range is 5.98 µm to 12.54 µm

TH-2735_136103036

CHAPTER 6

Wear and Corrosion Resistance Studies of Electric Discharge Alloyed Surfaces

6.0 Scope

This chapter presents findings pertaining to the wear and corrosion resistance characteristics of the electric discharge alloyed surfaces processed in different dielectric media. A comparative assessment of all three cases, viz. hydrocarbon oil, deionized water, and urea mixed deionized water, has also been carried out. The surface characteristics such as real-time wear behavior, friction behavior, and mass loss were studied by using the pin-on-disc technique. The corrosion resistance of the alloyed workpieces was assessed by using an electrochemical corrosion test.

6.1 Motivation

Previous chapters deal with the successful transfer of tool and dielectric material on the workpiece surface, which resulted in the formation of an alloyed layer. It was observed that the EDA processed workpieces exhibit improved surface behavior in terms of an increase in hardness value. To further investigate the important surface characteristics of the alloyed layer, a detailed investigation into the behavior of corrosion and wear resistance was thought to be essential. The findings obtained in this direction are presented in the subsequent sections.

6.2 Study of wear characteristics of the alloyed surface

To study the wear characteristics of the alloyed layer, the pin-on-disc instrument (Made by: Ducom) was used. The details of the equipment and procedure to use the instrument are presented in Chapter 3, Section 3.1.11 (Page No. 43) and Section 3.3.4 (Page No. 49) respectively. To perform the wear test for the alloyed surface, EDA was carried out using different dielectric media viz. hydrocarbon oil, deionized water, and urea mixed deionized water separately. The EDA processing parameters for the wear test workpiece and the wear test conditions are listed in detail in Table 6.1. Three repetitive experiments were conducted for the EDA process conditions listed in the table, and a wear test was performed for the alloyed workpieces separately. Figure 6.1 shows the workpieces

TH-2735_136103036

processed with EDA using dielectric media of hydrocarbon oil, deionized water, and urea mixed deionized water.

Table 6.1 EDA processing conditions and wear test conditions

EDA processing parameters for the wear test workpiece	
Dielectric medium	1. Hydrocarbon oil 2. Deionized water 3. Urea mixed deionized water (10 g/L concentration)
Pulse on-time, t_{on}	546 µs
Discharge current, I_d	10 A
Discharge voltage	40 V
Duty cycle	50 %
Workpiece material	AISI P20 mold steel of 10 mm diameter and 50 mm height
Tool material	13 mm diameter PM tool of 50 % Ti and 50 % Al
Polarity	Tool electrode (Negative terminal)
EDA processing duration	5 min
Wear test conditions	
Wear track diameter	60 mm
Rotational speed	160 rpm
Sliding speed	0.5 m/s
Load	5 N
Wear test duration	30 min

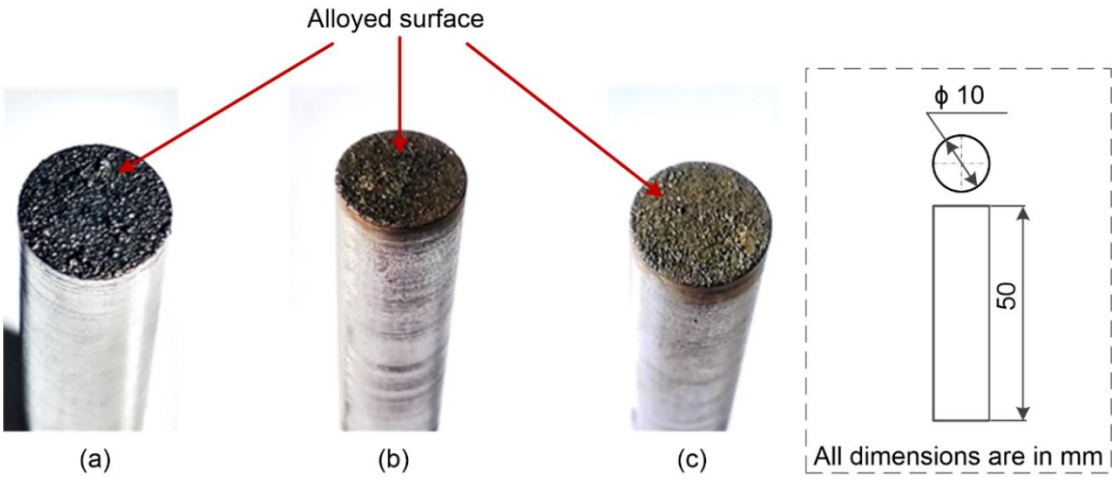

Figure 6.1 Wear test workpieces prepared using (a) Hydrocarbon oil (b) Deionized water and (c) Urea mixed deionized water

TH-2735_136103036

Following sub-sections discuss in detail about the wear test results for the workpieces alloyed in different dielectric media, and finally, a comparison has been made.

6.2.1 Wear behavior of EDA workpieces processed in hydrocarbon oil

To investigate the wear behavior, the alloyed workpieces were subjected to the wear test without any post-processing. The real-time wear data of the test has been recorded using a linear variable differential transformer (LVDT) sensor having 0.1 µm accuracy. The LVDT sensor gives the wear data in the form of deflection encountered by the workpiece at every instant of time. To study the wear behavior, a scatter plot of wear versus time was plotted, and a trend line has been generated for the plot. Figure 6.2 presents the wear versus time scatter plot for the workpiece processed in hydrocarbon oil. The red dotted line represents the trend line, and the regression equation for the trend line is also represented in the figure. For each of the wear tests, the regression equation for the trend line has been derived separately, and the corresponding values of wear with respect to the time have been plotted by using the obtained equation. The comparison of the wear behavior has been made by using the trend lines obtained for different wear test results.

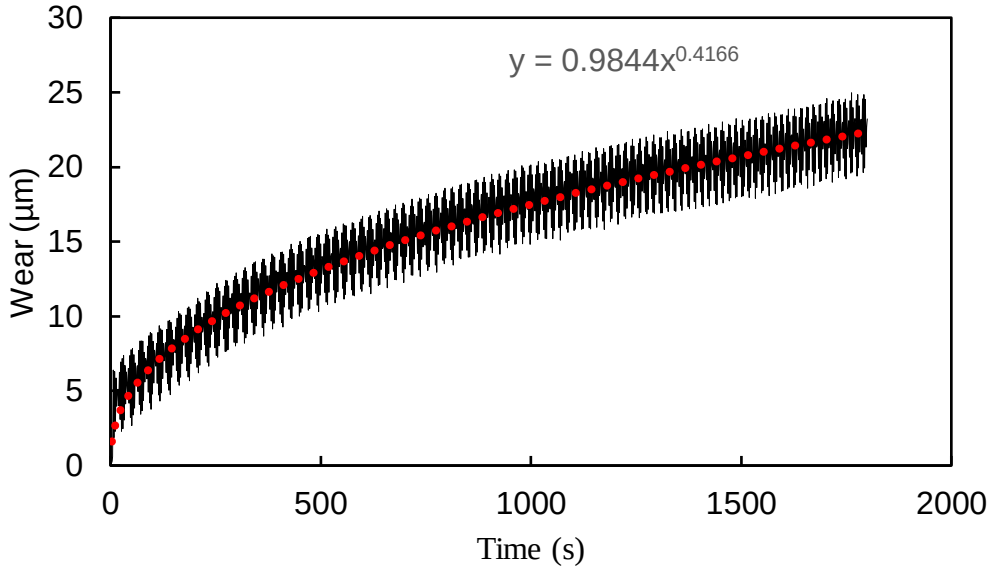

Figure 6.2 Scatter plot of wear behavior for EDA workpiece processed at pulse on-time of 546 µs and discharge current of 10 A using hydrocarbon oil

The wear behavior in terms of wear versus time plot of the alloyed workpieces for three repeated trails at the same EDA processing condition of 546 µs pulse on-time and current of 10 A in hydrocarbon oil are shown in Figure 6.3. From the figure, it is observed that in the initial duration of around 100 seconds, the wear increases rapidly for about 10 µm

TH-2735_136103036

(exponential rise in slope); however, with due course of time, there is a decrease in the slope. This trend is observed in all the repeated experiments. This increase in wear at the beginning of the wear test indicates the weak binding of the particles at the topmost surface of the alloyed region. This weak binding is due to the uneven and porous nature of the topmost layer, which can be inferred from the recorded surface roughness of the EDA processed workpieces. From the surface roughness plot shown in Chapter 4, Figure 4.18, Page No. 78, it was realized that the uneven surface extends a roughness (R_a) value of 4.5 to 8.5 µm. This roughness value is due to the presence of the uneven porous topmost layer, which thereby justifies the presence of rapid wear up to a depth of 10 µm. The low slope in the trend of the wear after a depth of about 10 µm signifies that there is a formation of a uniform hard alloyed region after a depth of 10 µm from the alloyed surface. This formation of a uniform hard layer region is also being supported by the friction coefficient curve shown in Figure 6.4. In the figure, the friction behavior of the alloyed surface for a period of 30 min is shown. From the figure, an exponentially decreasing trend of the friction coefficient is observed during the initial duration of about 100 s. This is because there is high wear of the non-uniform topmost layer consisting of loosely bonded alloying elements, which thereby increases the friction. However, with increase in time beyond 100 s, the uniform hard layer is reached. Therefore, the wear reduces, and hence there is a gradual decrease in the friction coefficient after 100 s.

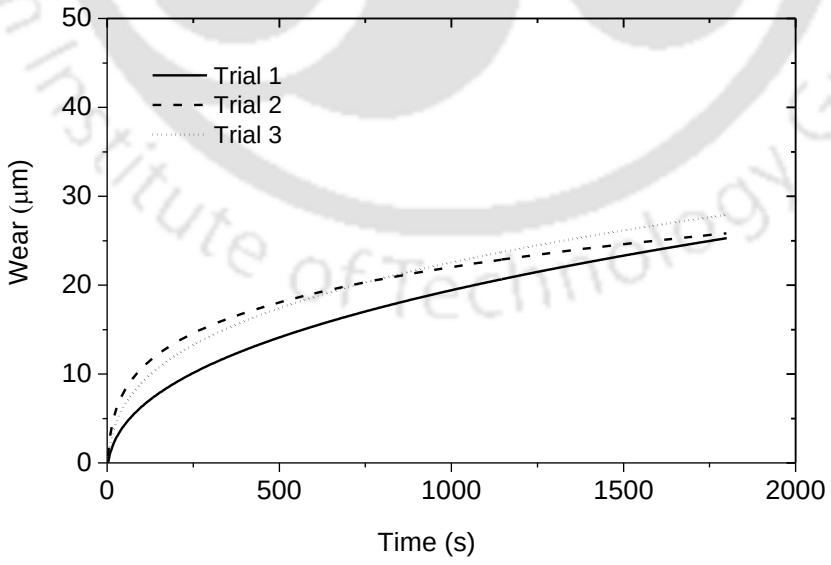

Figure 6.3 Wear behavior of EDA workpieces for three repeated trials at same EDA processing condition (t_{on} of 546 µs and I_d of 10 A in hydrocarbon oil)

TH-2735_136103036

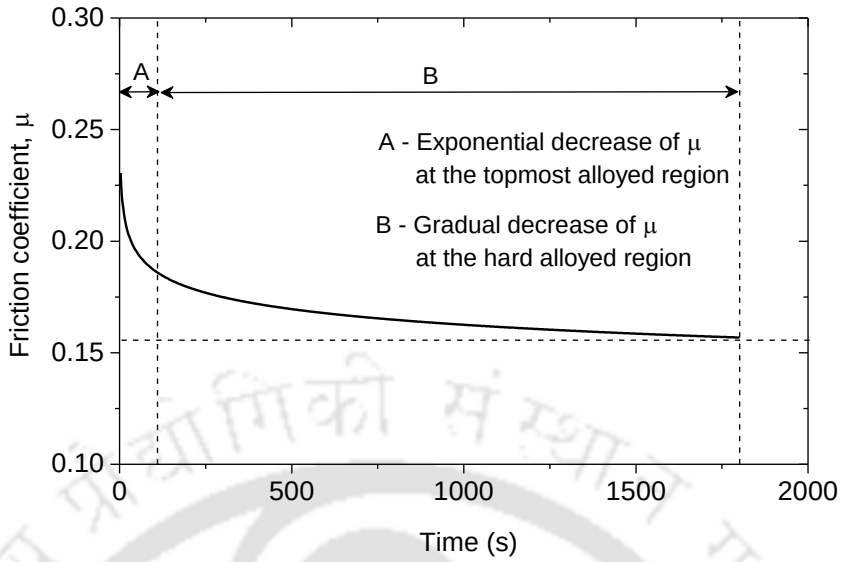

Figure 6.4 Friction behavior of the alloyed workpiece processed at t_{on} of 546 µs and I_d of 10 A in hydrocarbon oil

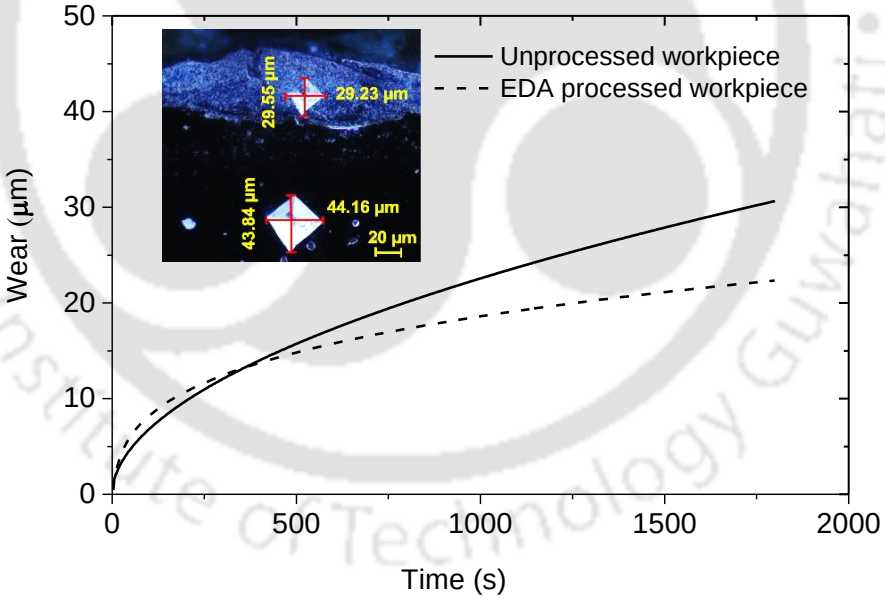

Figure 6.5 Comparison of wear behavior of unprocessed workpiece with that of EDA workpiece processed at t_{on} of 546 µs and I_d of 10 A in hydrocarbon oil

To compare the wear characteristic of the EDA processed workpiece with that of the unprocessed workpiece, the average value of wear for the three repeated experiments was considered. Figure 6.5 shows the comparison in wear behavior of the EDA processed workpiece with that of the unprocessed workpiece. The inset shows the variation in

TH-2735_136103036

indentation size along with the depth for the EDA processed workpiece. It shows that the hardness of the alloyed region is much more than the parent material since the indentation size observed is much smaller at the alloyed region in comparison to that of the parent material. This has already discussed in Chapter 4, Section 4.2.4, Page No. 71. From the line graph, it is observed that for the initial period of up to approximately 375 s, the wear of the alloyed workpiece is slightly higher than that of the unprocessed workpiece, and later, the wear for the unprocessed workpiece increases and at 375 s the wear value is about 13 µm. The increase in wear for the alloyed workpiece at the initial period is due to the presence of an uneven surface up to a height of about 10 µm, as indicated in the surface roughness plot shown in Chapter 4, Figure 4.18, Page No. 78. However, with due course of time, i.e., beyond 375 s, the wear increases for the unprocessed workpiece as compared with that of the alloyed workpiece. This indicates that the alloyed workpiece exhibited higher resistance to wear owing to higher hardness. From the figure, it is also observed that under the same wear testing condition, the maximum wear of the unprocessed workpiece is up to 30 µm while for the EDA processed workpiece is up to 15 µm indicating that the wear resistance is improved after the electric discharge based surface alloying. It can also be inferred that after 30 min of wear testing operation, the alloyed layer has not been fully worn out as the alloyed depth of 47.64 µm (Chapter 4, Section 4.2.3, Table 4.1, Page No. 69) was not reached.

The mass loss during the wear test operation was also determined by measuring the difference between the mass of the workpieces before and after the wear test. The mass loss analysis showed that the mass loss for the unprocessed workpiece was 9.43 mg, and that of the EDA processed workpiece was 5.10 mg for the experimental run of 30 min. The mass loss for the unprocessed workpiece is observed to be almost double times that of the alloyed workpiece. This certainly indicates that there is an enhancement in the wear resistance of the workpiece due to the electric discharge based alloying phenomenon.

By following similar approach, the wear characteristics of the workpiece processed in deionized water and urea mixed deionized water were also studied. The results are presented in the following sub-sections.

6.2.2 Wear behavior for EDA workpieces processed in deionized water

Figure 6.6 shows the comparison of the wear characteristics of the unprocessed workpiece with that of the EDA processed workpiece using deionized water as the dielectric. From

TH-2735_136103036

the figure, it is observed that the wear for the alloyed workpiece is marginally higher than that of the unprocessed workpiece. This is due to micropores and micro-cracks present in the alloyed region, which can be seen in Figure 6.7. The pores are noted to be in micron size and the density of the micropores present is high (Figure 6.7 (a)). From Figure 6.7 (b), it can be observed that along the cross-section of the alloyed workpiece, microcracks are present in the alloyed region. This thereby results in the high wear of the alloyed workpiece during the wear test.

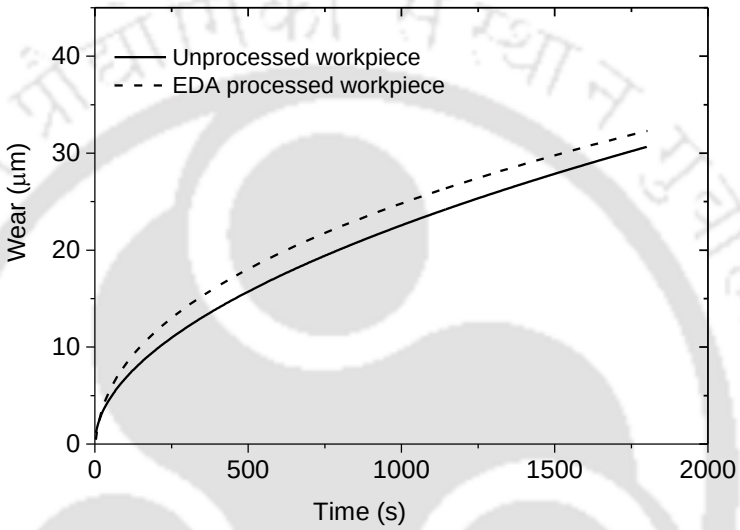

Figure 6.6 Comparison of wear behavior of unprocessed workpiece and EDA processed workpiece using deionized water dielectric

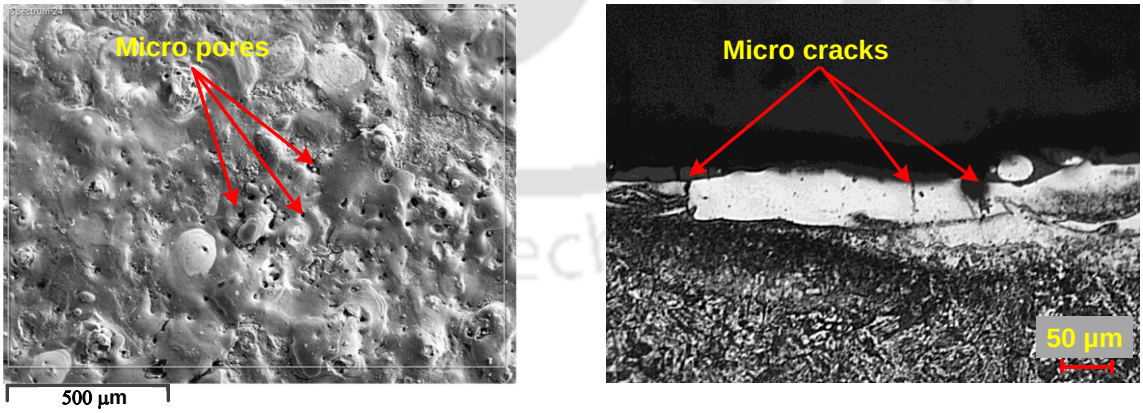

(a) (b)

Figure 6.7 (a) FESEM image showing the top surface at 100× and (b) Micrograph along the cross-section at 20× of the EDA workpiece processed at t_{on} of 1006 µs and I_d of 6A with DI water dielectric medium

In a similar approach to the previous section (Section 6.2.1), the friction behavior for the alloyed workpiece processed in deionized water is shown in Figure 6.8, and from the

TH-2735_136103036

figure, it is observed that for the initial few seconds of about 100 s, the friction coefficient increases exponentially and after some time there is a gradual increase. This is attributed to the wear of the weakly bound uppermost layer of the alloyed workpiece. Also, from the roughness plot discussed in Chapter 5, Table 5.3, Page No. 105. it was observed that for the process condition of 546 µs pulse on-time and 10 A discharge current, the roughness value was around 7 µm. This, therefore, justifies the exponential increase in friction coefficient at the beginning and the gradual increase thereafter.

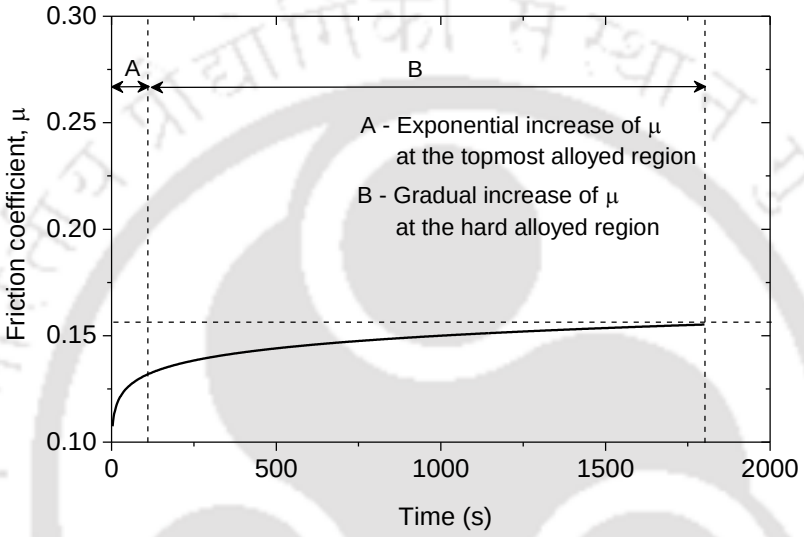

Figure 6.8 Friction behavior of the alloyed workpiece processed at t_{on} of 546 µs and I_d of 10 A in deionized water

Further, the mass loss analysis has also been carried out in a similar approach as discussed in the previous section (Section 6.2.1). Results indicated that the mass loss during the wear test for a run time of 30 min for the workpiece processed in deionized water was 9.26 mg which is approximately same as that of the unprocessed workpiece, i.e., 9.43 mg.

6.2.3 Wear behavior for EDA workpieces processed in urea mixed deionized water

Following the same methodology, as discussed in Section 6.2.1, the wear behavior of the unprocessed workpiece is also compared with the workpiece processed in urea mixed deionized water. Figure 6.9 shows the wear versus time graph for the unprocessed workpiece and EDA processed workpiece in urea mixed deionized water. From the figure, it is observed that the wear is higher in the case of the alloyed region as compared with the unprocessed workpiece initially for about 750 s, and thereafter, the wear of the unprocessed workpiece increases. The initial increase in the wear is due to the porous

TH-2735_136103036

nature and micro-cracks shown in Figure 6.10. However, the decrease in the wear of the alloyed workpiece as compared to the unprocessed workpiece after 750 s is due to the resistance offered by the uniform nitride alloyed region, which possesses higher hardness than the unprocessed workpiece. The presence of nitride layer was confirmed from the XRD result discussed in Chapter 5, Section 5.2.2, Page No. 90. Further, in regards to the friction behavior for the alloyed workpiece, processed in urea mixed deionized water, as shown in Figure 6.11, it is observed that a similar trend is followed for the workpiece processed in deionized water (Figure 6.8). There is an exponential increase in the friction coefficient at first 100 s and the increase is gradual after 100 s.

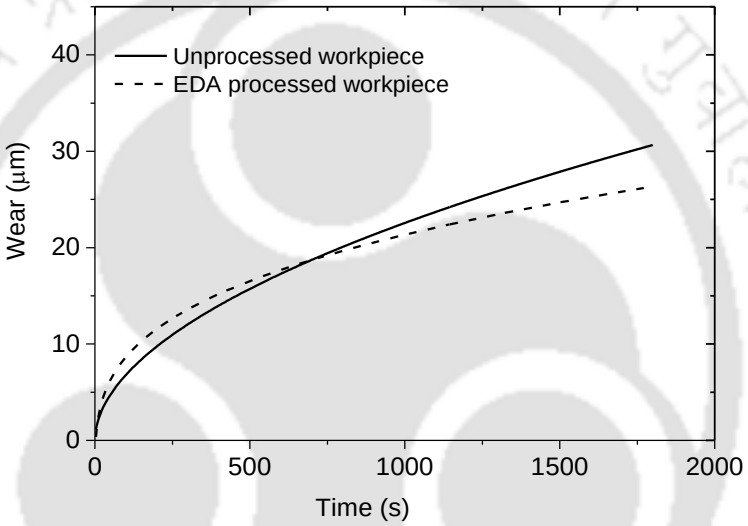

Figure 6.9 Comparison of wear behavior of the unprocessed workpiece and EDA processed workpiece processed using urea mixed deionized water at t_{on} of 546 µs and I_d of 10 A

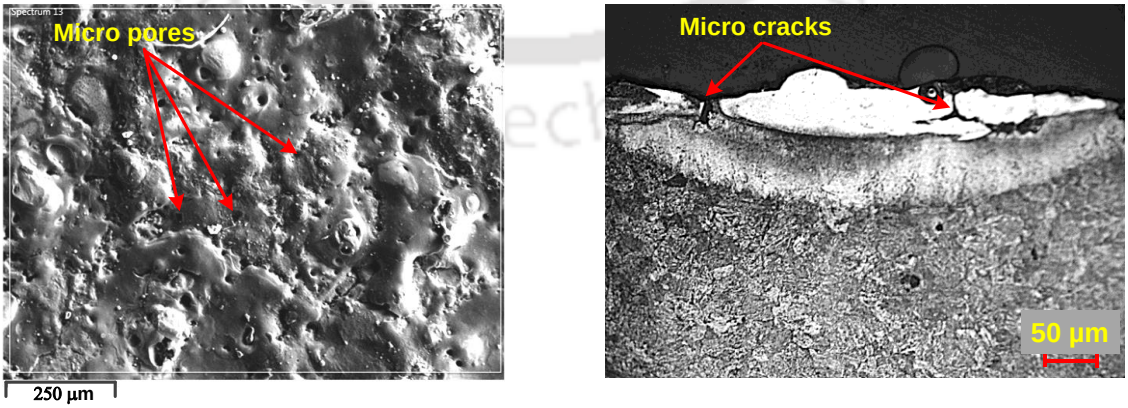

(a) (b)

Figure 6.10 (a) FESEM image showing the top surface at 125× and (b) Micrograph along the cross-section at 20× of the EDA workpiece processed at t_{on} of 1006 µs and I_d of 6 A with urea mixed DI water dielectric medium

TH-2735_136103036

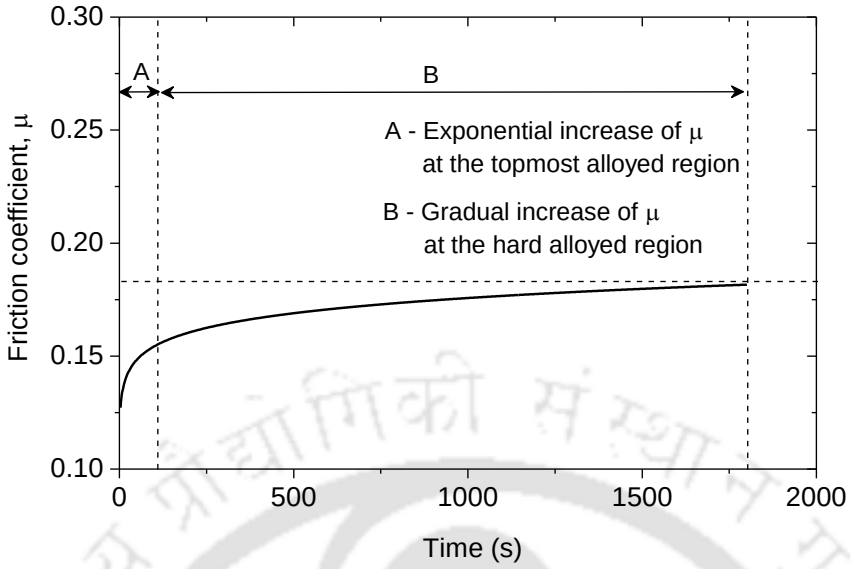

Figure 6.11 Friction behavior of the alloyed workpiece processed at t_{on} of 546 µs, and I_d of 10 A in urea mixed deionized water

In continuation, the mass loss during the wear test operation for 30 min was also determined for the workpiece processed in urea mixed deionized water. It was about 9.13 mg for the alloyed workpiece. The obtained mass loss value is slightly less than that of the unprocessed workpiece, which is 9.43 mg.

6.2.4 Comparison of wear, friction behavior, and mass loss of EDA workpieces processed in presence of various dielectric media

A comparative study has been made in the wear behavior of the EDA workpieces processed in presence of various dielectric media viz. hydrocarbon oil, deionized water, and urea mixed deionized water. The wear behavior of the three cases is shown in Figure 6.12. From the figure, it is observed that the wear is found to be minimal in the case of using hydrocarbon oil as the dielectric. This is because with the use of hydrocarbon oil, carbide layer is formed, having a high hardness of 1125 $HV_{0.3}$ (discussed in Chapter 4, Section 4.2.4, Page No. 71). However, for the workpieces processed in water-based dielectric viz., deionized water and urea mixed deionized water, there is a marginal difference in the wear of the alloyed workpieces and the unprocessed workpiece. This is due to the presence of microcracks and micropores, as discussed in Section 6.2.2 and Section 6.2.3. The improvement in the wear resistance for the workpieces processed in

TH-2735_136103036

hydrocarbon oil as compared with that of the workpieces processed in the water-based dielectric is due to a change in quenching medium.

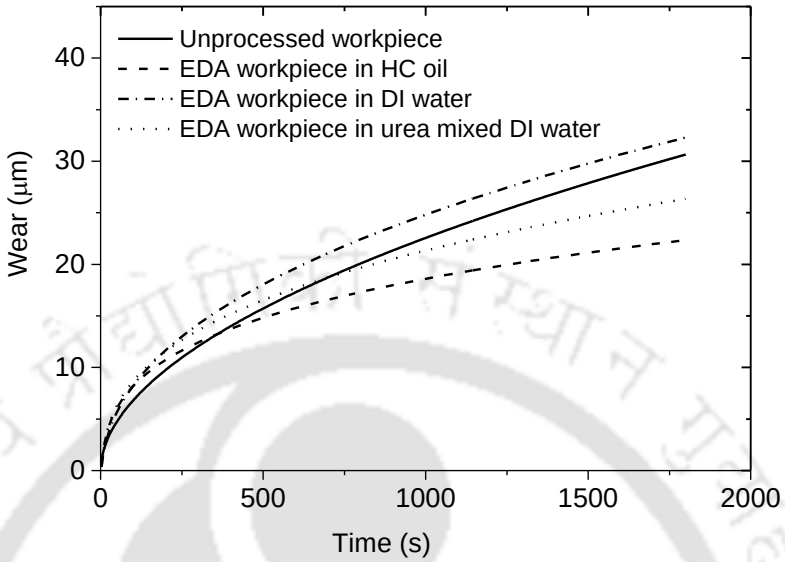

Figure 6.12 Comparison of wear behavior of EDA workpiece processed using different dielectric media

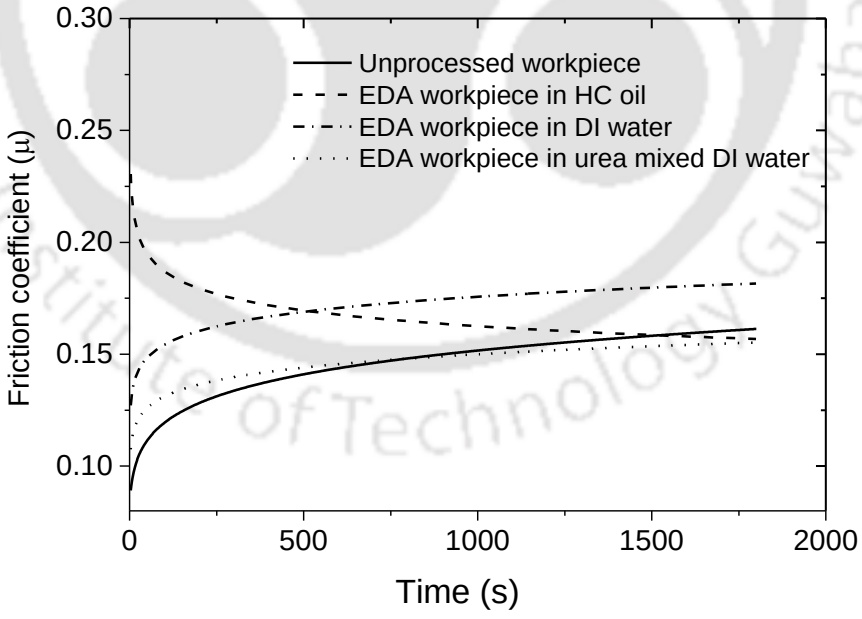

Figure 6.13 Comparison of friction behavior of EDA workpiece processed using different dielectric media

The friction behavior for the workpieces alloyed at different conditions is also calculated and compared, as shown in Figure 6.13. From the figure, it is observed that the friction

TH-2735_136103036

coefficient follows various trends with respect to time. For the workpieces processed in hydrocarbon oil, a decreasing trend is observed; however, for the workpieces processed in deionized water and urea mixed deionized water, the trend is increasing. This difference in trend is contributed by the surface roughness and amount of wear of the alloyed region. In the case of hydrocarbon, as the layer hardness is high, the worn-out material is less, and hence the friction coefficient keeps decreasing. However, in the case of the workpiece processed using deionized water and urea mixed deionized water, the amount of worn-out material is noted to be higher. This resulted in increase in friction coefficient increases.

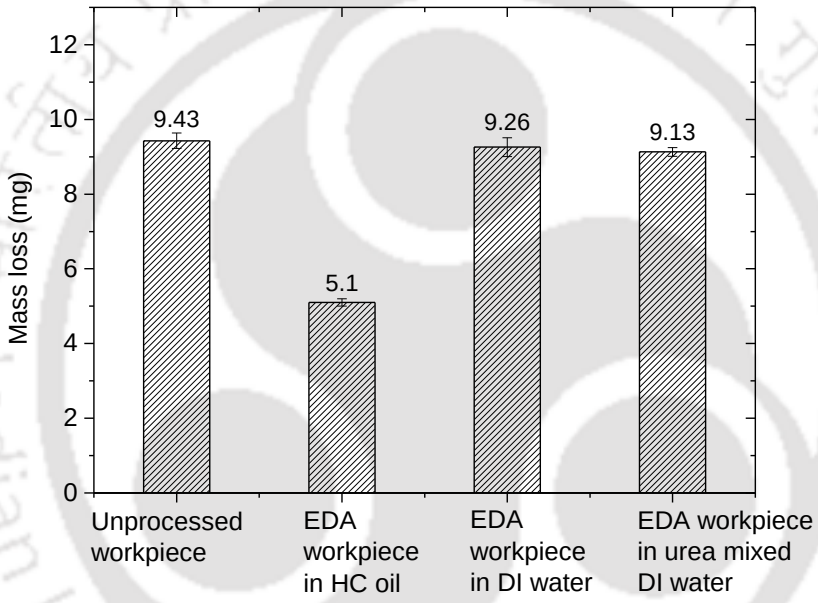

Figure 6.14 Comparison of mass loss occurred due to the wear of EDA workpieces processed using different dielectric media

Finally, the mass loss during the wear test has also been compared. Figure 6.14 shows the bar graph indicating the values of the mass losses for the unprocessed workpiece and the alloyed workpieces using different dielectric media. The figure depicts that the mass loss is least for the workpiece processed in hydrocarbon oil, i.e., the mass loss was significantly reduced by 46 % from that of the unprocessed workpiece. However, there is a marginal difference for the mass loss values for the unprocessed workpiece and alloyed workpieces processed in deionized water, and urea mixed deionized water.

From this section, it was observed that the wear behavior of the workpiece processed in hydrocarbon oil gives the best wear resistance behavior when compared with

TH-2735_136103036

that of the unprocessed workpiece and the ones processed in deionized water and urea mixed deionized water. The work was further extended to check the corrosion behavior of the alloyed workpieces. The following section presents the results of the corrosion resistance testing of the alloyed regions.

6.3 Corrosion behavior of EDA workpieces

For the corrosion test, EDA workpieces were processed in presence of varying dielectric media at the same operating condition, i.e., pulse on-time of 546 µs and discharge current of 10 A. The size of the workpieces used was 10 mm diameter and 50 mm height, and only the top surface was exposed for the test.

The corrosion behavior has been studied with the electrochemical impedance spectroscopy (EIS) technique by using reference 600 galvanostat (details are presented in Chapter 3, Section 3.1.12, Page No. 43). Electrochemical impedance gives the response of the electrochemical cell to an applied potential. The dependence of the chemical impedance with the frequency reveals the corrosion behavior of the workpiece. High impedance value indicates high corrosion resistance of the workpiece specimen. For the present study, the impedance data was acquired at a frequency range of 0.01 Hz to 0.1 MHz with 10 points per frequency decade. The amplitude of the sinusoidal signal considered was 10 mV, and the potentiodynamic readings were considered from 0.25 V below the open circuit potential till the anodic domain (0 V) at a scan rate of 0.5 mV/s. Figure 6.15 shows the images of the workpieces after the corrosion test for the unprocessed workpiece and the workpieces processed in different dielectric media viz. hydrocarbon oil, deionized water, and urea mixed deionized water. It can be observed that the corrosion has occurred in the exposed region only. The detailed results are discussed in the following sub-sections.

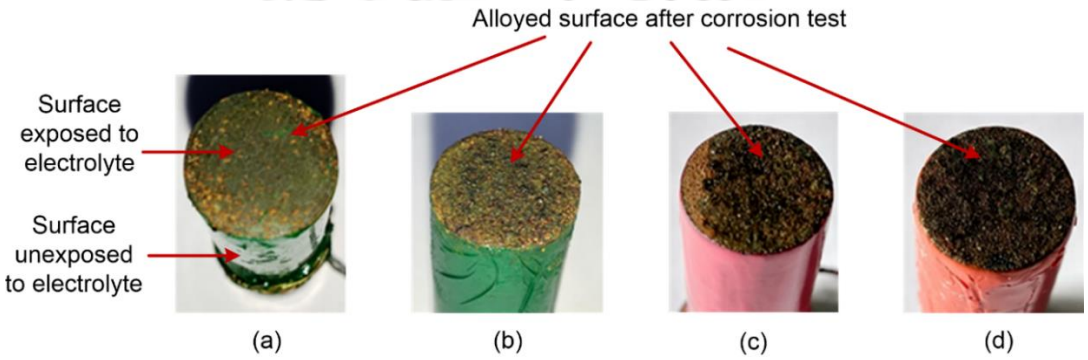

Figure 6.15 Camera images after corrosion test for (a) Unprocessed workpiece and workpieces alloyed in (b) Hydrocarbon oil (c) Deionized water and (d) Urea mixed deionized water

TH-2735_136103036

6.3.1 Corrosion behavior of the workpieces processed in hydrocarbon oil

The corrosion behavior was studied from the EIS spectra represented in the form of Bode diagram as shown in Figure 6.16 and Figure 6.17. From a Bode diagram, a high intercept value on the axis of the modulus of impedance, |Z| at low frequency (0.01 Hz) indicates better corrosion resistance. It was observed that the EDA processed workpiece possesses the higher value of impedance modulus (lZl), i.e., 1.35×10^3 Ωcm^2 , as compared to that of the unprocessed workpiece, i.e., 1.08×10^3 Ωcm^2. This indicates that the polarization resistance is higher for the EDA processed workpiece. Regarding the phase angle value (Figure 6.17), the EDA processed workpiece possesses a higher phase angle of -70° at a lower frequency while that for the unprocessed workpiece is -57°. This indicates that a protective layer has been formed over the EDA workpiece. Similar curves have been reported by Boztepe et al. (2018) during their study on the corrosion behavior of pre-hardened plastic mold steel (equivalent to AISI P20 mold steel).

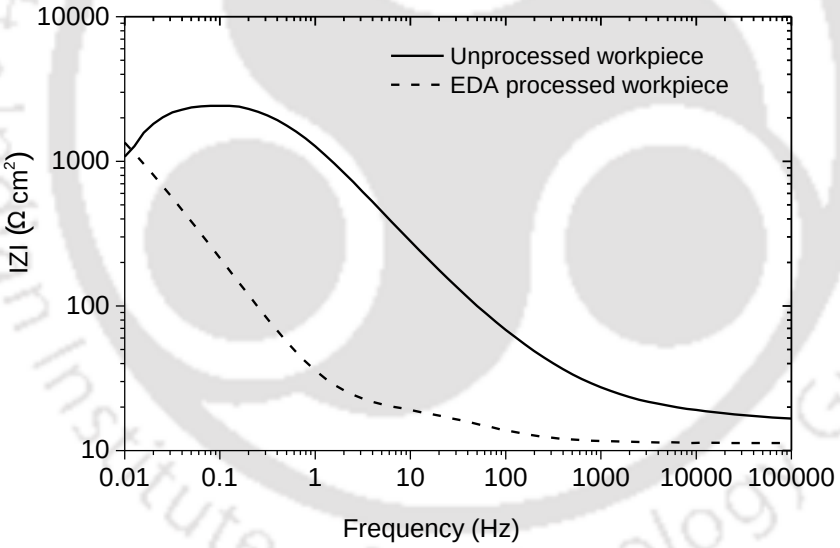

Figure 6.16 Bode diagram lZl for the unprocessed workpiece and EDA workpiece processed at t_{on} of 546 µs and I_d of 10 A in hydrocarbon oil

TH-2735_136103036

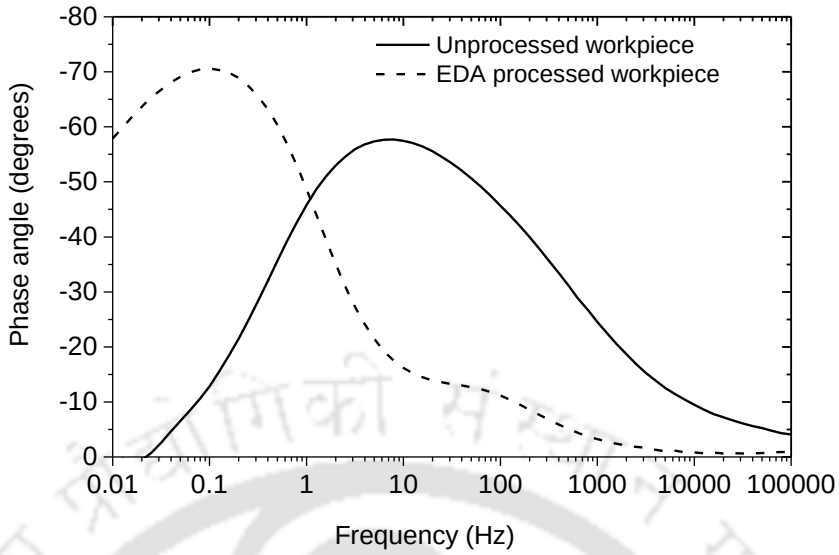

Figure 6.17 Bode diagram phase angle for the unprocessed workpiece and EDA workpiece processed at t_{on} of 546 µs and I_d of 10 A in hydrocarbon oil

The electrochemical equivalent circuit (EEC) used to fit the impedance spectra data is shown in Figure 6.18. Z-view software was used to fit the data. The components of the EEC are electrolyte resistance (R_E), corrosion resistance (R_C), porous layer resistance (R_{PL}), corrosion capacitance (C_C), and porous layer capacitance (C_{PL}). The EEC parameters generated from the EIS data are given in Table 6.2. From Table 6.2, it is observed that the corrosion resistance, R_C of the EDA processed workpiece is about double times higher than that of the unprocessed workpiece. This high corrosion resistance for the EDA processed workpieces is due to the carbide layer formed at the surface, as depicted in the XRD analysis (Chapter 4, Section 4.2.2, Page No 64). Further, the difference in the porous layer resistance R_{PL} is due to the surface morphology, i.e., the presence of micropores at the surface of the alloyed workpiece.

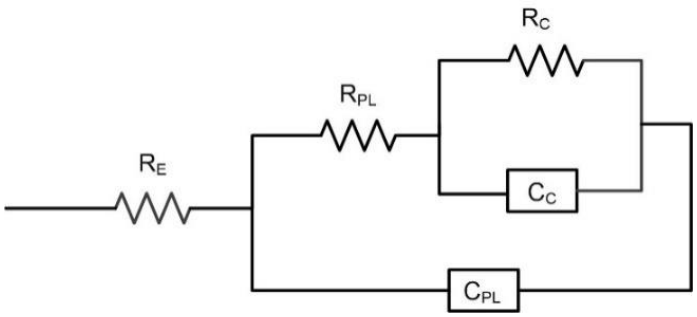

Figure 6.18 Electrochemical equivalent circuit used to fit the EIS data

TH-2735_136103036

Table 6.2 Equivalent circuit parameters obtained from EIS data for unprocessed workpiece and workpiece processed in hydrocarbon oil

Sl. No.	Parameter	Unprocessed workpiece	EDA workpiece in HC oil
1.	Corrosion resistance, R_C (Ω cm^2)	1.865×10^3	3.928×10^3
2.	Porous layer resistance, R_{PL} (Ω cm^2)	66.05	11.65
3.	Corrosion capacitance, C_C (F cm^{-2})	64.35×10^{-6}	5.027×10^{-3}
4.	Porous layer capacitance, C_{PL} (F cm^{-2})	60.53×10^{-6}	2.029×10^{-3}

6.3.2 Corrosion behavior of workpieces processed in deionized water

The Bode diagrams for the workpiece processed in deionized water are as shown in Figure 6.19 and Figure 6.20. From Figure 6.19, it is observed that the impedance for the alloyed workpiece is less than that of the unprocessed workpiece, i.e., at 0.01 Hz, the impedance modulus value for the alloyed workpiece is 0.16×10^3 Ωcm^2, while that for the unprocessed workpiece is 1.08×10^3 Ωcm^2. Also, from Figure 6.20, the maximum phase angle for the unprocessed workpiece is -57°, and that for the alloyed workpiece is $-44°$, i.e., the phase angle for the unprocessed workpiece is higher. From these two figures, it can be said that the polarization resistance is higher for the unprocessed workpiece when compared with the alloyed workpiece. This is due to the porous nature of the alloyed layer and also due to the formation of oxides as the working medium is deionized water. The formation of oxide is reported in the XRD analysis presented in Chapter 5, Section 5.2.2, Page No. 90. Further, on fitting the EIS data in the electrochemical circuit shown in Figure 6.18, the values of resistances and capacitances are determined and are listed in Table 6.3. It is seen that the corrosion resistance for the alloyed workpiece is 1.27×10^3 Ωcm^2 which is less than that of the unprocessed workpiece, i.e., 1.865×10^3 Ωcm^2 as listed in Table 6.2. Therefore, it can be said that the formation of the oxide layer in the alloyed workpiece results in decrease of the corrosion resistance.

TH-2735_136103036

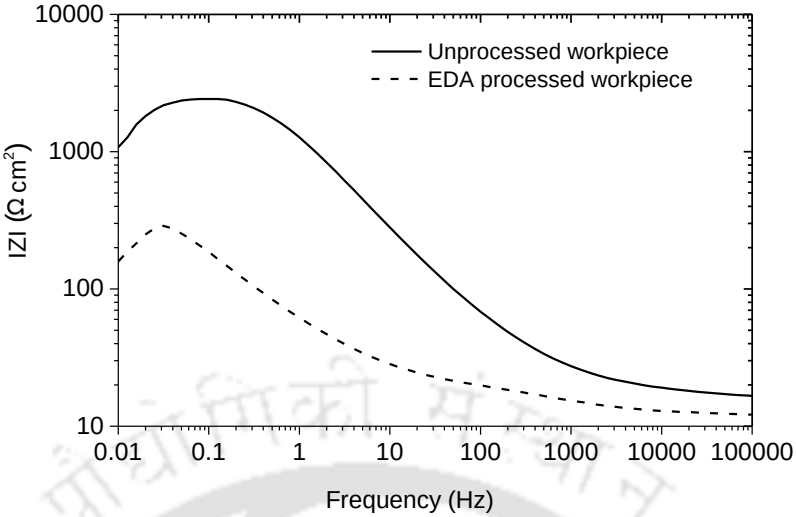

Figure 6.19 Bode diagram lZl for the unprocessed workpiece and EDA workpiece processed at t_{on} of 546 µs and I_d of 10 A in deionized water

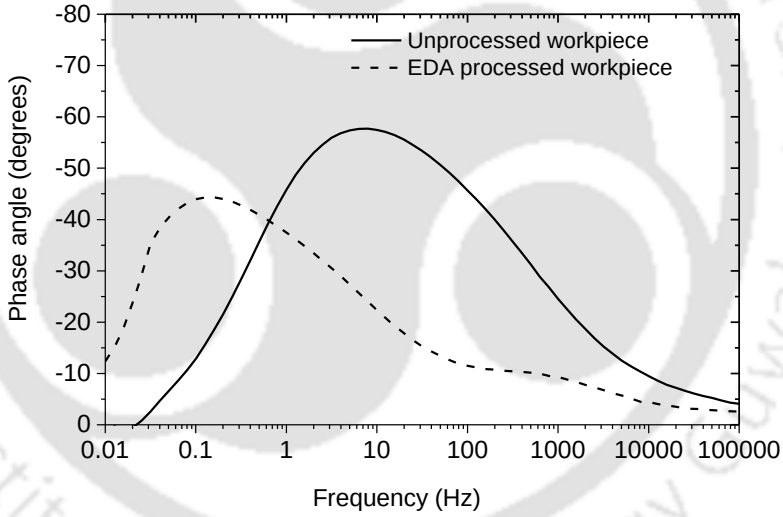

Figure 6.20 Bode diagram phase angle for the unprocessed workpiece and EDA workpiece processed at t_{on} of 546 µs and I_d of 10 A in deionized water

Table 6.3 Equivalent circuit parameters obtained from EIS data for workpiece processed in DI water

Sl. No.	Parameter	EDA workpiece in DI water
1.	Corrosion resistance, R_C (Ω cm^2)	1.27×10^{3}
2.	Porous layer resistance, R_{PL} (Ω cm^2)	14.7
3.	Corrosion capacitance, C_C (F cm^{-2})	3.51×10^{-3}
4.	Porous layer capacitance, C_{PL} (F cm^{-2})	1.76×10^{-3}

TH-2735_136103036

6.3.3 Corrosion behavior of workpieces processed in urea mixed deionized water

Similar to the above-mentioned procedures, the corrosion resistance value of the workpieces processed in urea mixed deionized water was compared with that of the unprocessed workpiece. The Bode diagrams of the comparison are shown in Figure 6.21 and Figure 6.22. In this case, the impedance modulus for the alloyed workpiece was noted to be 0.84 × $10^{3,}$ while that for the unprocessed workpiece was 1.08 × 10^3 Ωcm^2 as indicated in Figure 6.21.

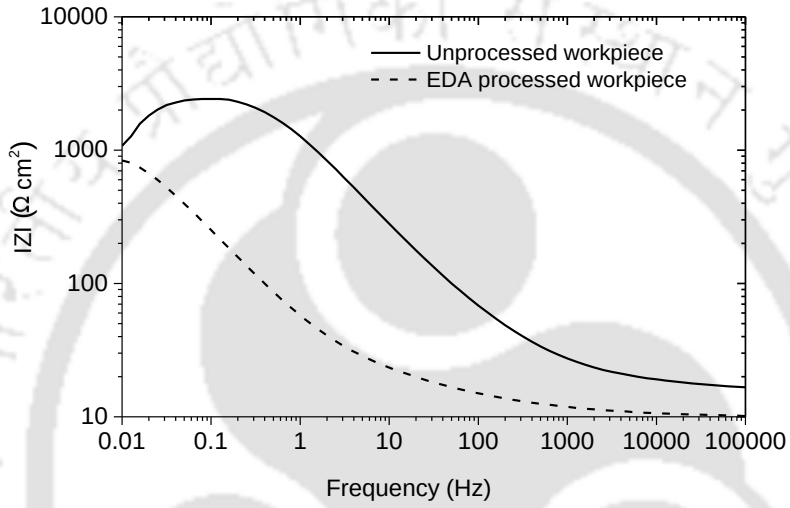

Figure 6.21 Bode diagram lZl for the unprocessed workpiece and EDA workpiece processed at t_{on} of 546 µs and I_d of 10 A in urea mixed deionized water

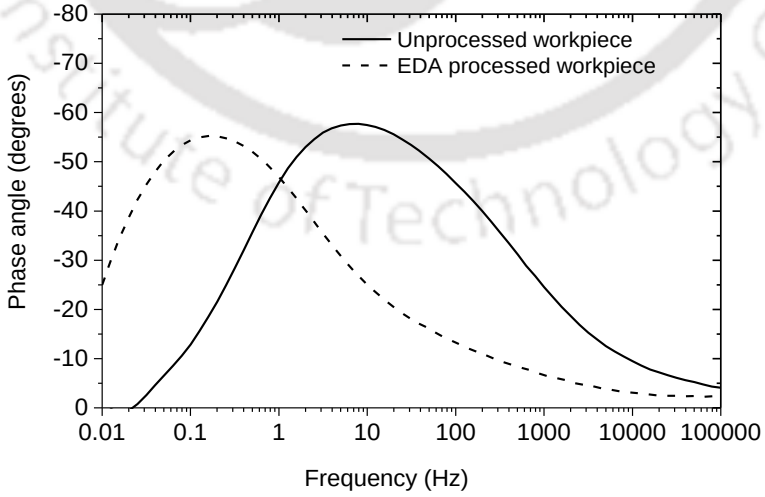

Figure 6.22 Bode diagram phase angle for the unprocessed workpiece and EDA workpiece processed at t_{on} of 546 µs, and I_d of 10 A in urea mixed deionized water

TH-2735_136103036

The maximum phase angle for the workpiece alloyed in urea mixed deionized water was −55°, and that for the unprocessed workpiece was −57° (refer to Figure 6.22). From this, it can be inferred that the polarization resistance is lesser for the alloyed workpieces in comparison with that of the unprocessed workpiece. This is due to the formation of the oxide layer and micropores (see Figure 6.10) over the surface of the alloyed region. The formation of the oxide layer is due to the breakdown of the water molecules during the electric discharge. This is supported by the XRD analysis reported in Chapter 5, Section 5.2.2, Page No. 90. Further, the presence of micropores acts as a source of corrosion initiation, thereby resulting in poor polarization resistance.

Table 6.4 Equivalent circuit parameters obtained from EIS data for workpiece processed in urea mixed DI water

Sl. No.	Parameter	EDA workpiece in urea mixed DI water
1.	Corrosion resistance, R_C (Ω cm^2)	1.34×10^3
2.	Porous layer resistance, R_{PL} (Ω cm^2)	14.41
3.	Corrosion capacitance, C_C (F cm^{-2})	4.17×10^{-3}
4.	Porous layer capacitance, C_{PL} (F cm^{-2})	2.79×10^{-3}

The values of resistances and capacitances for the alloyed surface were obtained by fitting the EIS data in the electrochemical circuit shown in Figure 6.18, and the data are listed in Table 6.4. The corrosion resistance for the workpiece alloyed in urea mixed deionized water was found to be 1.34×10^3 Ω cm^2, which is lesser than that of the unprocessed workpiece (1.865×10^3 Ωcm^2) as listed in Table 6.2. This is due to the formation of oxide layer as the dielectric medium is water based.

6.3.4 Comparison in corrosion behavior of the EDA workpieces

A study on corrosion behavior for the workpieces processed in three different dielectric media has been made. The EIS spectra in the form of Bode diagram for workpieces processed in the different dielectric media are shown in Figures 6.23 and 6.24. It is observed that the workpiece processed in hydrocarbon oil possesses the highest value of impedance modulus (lZl), followed by the parent material and the workpieces processed in deionized water and urea mixed deionized water (Figure 6.23). This indicates that the highest polarization resistance is given by the alloyed workpiece processed using hydrocarbon oil. Regarding the phase angle value (Figure 6.24), the workpieces processed

TH-2735_136103036

using hydrocarbon dielectric exhibited the highest value approaching to -70°. A similar phase angle curve is also observed for the workpieces processed using deionized water and urea mixed deionized water as dielectric; however, they have a lower value of phase angle than that with hydrocarbon dielectric workpiece.

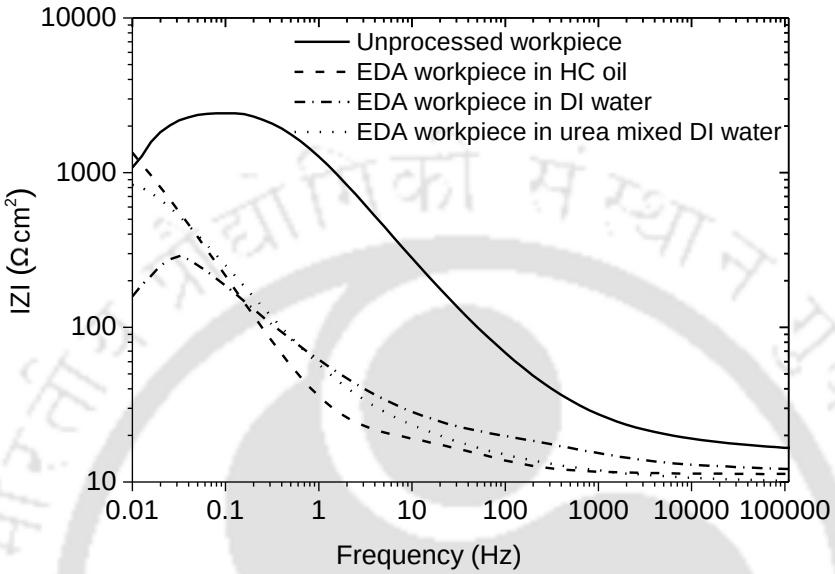

Figure 6.23 Comparison of EIS spectra in the form of Bode diagram |Z|

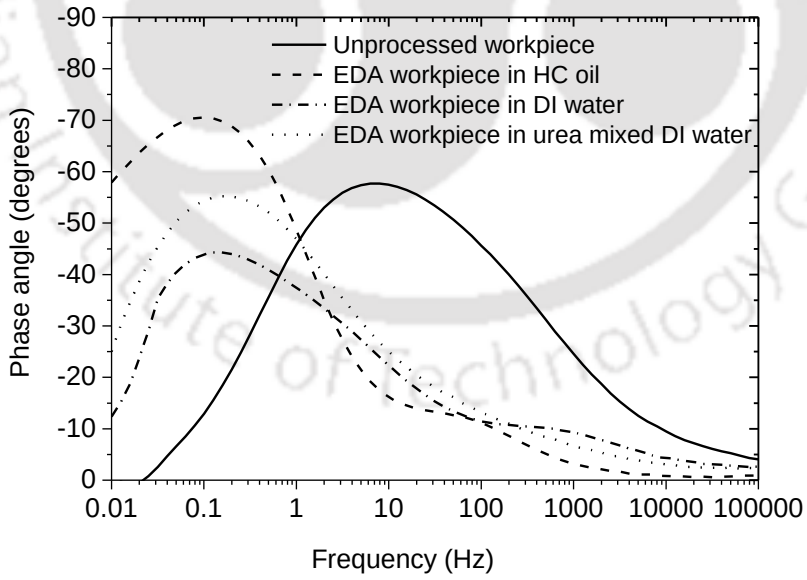

Figure 6.24 Comparison of EIS spectra in the form of Bode diagram phase angle

The corrosion resistance values for the alloyed workpieces and the unprocessed workpiece as tabulated in Tables 6.2, 6.3, and 6.4 have been compared. The bar graph based comparative analysis is shown in Figure 6.25. From the figure, it is observed that

TH-2735_136103036

the corrosion resistance for the workpiece processed in hydrocarbon oil is approximately double that of the unprocessed workpiece, i.e., the corrosion resistance was enhanced by 110 % from that of the unprocessed workpiece. In the present study, powder metallurgy tool of 50 % titanium and 50 % aluminium was used for all the experiments. However, the composition of dielectric media was varied. With the use of hydrocarbon oil, carbon gets decomposed from the dielectric, and it combines with the tool and the workpiece material, thereby forming Fe_3C and TiAl in the alloyed region. Further, with the use of DI water, the compounds formed are TiAl and Fe_3O_4. In the case of urea mixed DI water, the formation of Ti_4AlN_3 was observed along with TiAl and Fe_3O_4. The use of water-based deionized water resulted in the formation of iron oxide in the alloyed region, and this has resulted in the deterioration of the corrosion resistance property. Therefore, high corrosion resistance for workpieces processed using hydrocarbon dielectric is due to the formation of a carbide layer at the surface, which is highly resistant to acidic and alkaline solutions. On further comparing the corrosion resistance values for the workpieces processed in deionized water and urea mixed deionized water, it is observed that the resistance is slightly higher for the workpieces processed in urea mixed deionized water. This is due to the formation of the nitride layer reported in Chapter 5, Section 5.2.2, Page No. 90.

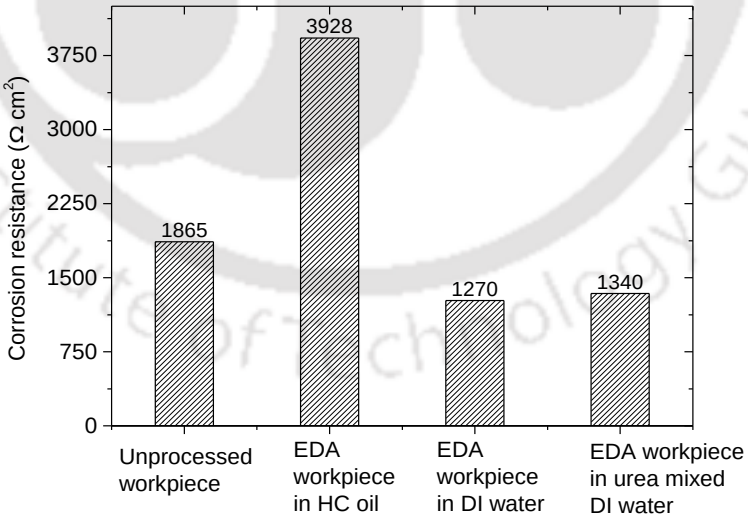

Figure 6.25 Comparison of corrosion resistance for EDA workpieces alloyed using different dielectric media

6.4 Summary

This chapter presents a systematic study on the tribological characteristics such as friction and wear resistance of the EDA workpieces processed with three different dielectric

TH-2735_136103036

media. The investigation of the wear behavior has been made by analyzing the real-time wear data, friction coefficient, and mass loss during the wear test. Further, the corrosion behavior for the alloyed workpieces was studied by studying the EIS spectrum. The polarization resistance was compared by analyzing the impedance modulus and the phase angle curve. Also, the values of corrosion resistance were determined from the EEC circuit. From the present chapter, the following important conclusions can be made.

- The real-time wear data acquired during the test indicated that the wear of the workpieces processed in hydrocarbon oil was the least followed by workpieces processed in urea mixed deionized water, unprocessed workpiece, and workpiece processed in deionized water.
- The low slope in the trend of the wear after a depth of about 10 µm signifies that there was a formation of a uniform hard alloyed region after a depth of 10 µm from the alloyed surface for the workpiece processed in hydrocarbon oil.
- The friction coefficient trend for the workpiece processed using hydrocarbon oil was decreasing. For the unprocessed workpiece and the workpieces processed in deionized water and urea mixed deionized water, the friction behavior was noted to be increasing.
- The mass loss during the wear test result showed that the workpiece processed in hydrocarbon oil was the least followed by workpieces processed in urea mixed deionized water, deionized water, and the unprocessed workpiece. The mass loss for the workpiece processed in hydrocarbon oil was significantly reduced by 46 % from that of the unprocessed workpiece. The change in mass loss is quite marginal for the unprocessed workpiece and the workpieces processed in the water-based dielectric.
- From the Bode diagrams, it was observed that the impedance modulus and the maximum phase angle were the highest for the workpiece processed in hydrocarbon oil, indicating the highest polarization resistance.
- The corrosion resistance value for the workpiece processed using hydrocarbon oil was almost double the corrosion resistance of the workpieces processed using deionized water and urea mixed deionized water and unprocessed workpiece. There was 110 % enhancement in the corrosion resistance for the workpiece processed in hydrocarbon oil from that of the unprocessed workpiece.

TH-2735_136103036

CHAPTER 7

Computation of Alloyed Layer Thickness in Electric Discharge Alloying by Inverse Estimation of Energy Distribution

7.0 Scope

This chapter presents an integrated finite element method (FEM) and artificial neural network (ANN) approach for accurate and quick computation of alloyed layer thickness through inverse estimation of energy distribution factor. Initially, a nonlinear transient numerical model is developed, and the alloyed layer thickness is computed for a wide range of values of the fraction of energy delivered to the workpiece (F_A). Then, the optimal F_A was computed for all the processing conditions by employing the bi-section method. Based on the validated FEM-based model, an ANN-based model is developed for the accurate prediction of F_A for the chosen input process parameters. The FEM-based model is integrated with the ANN-based model, and then the alloyed layer thickness is computed.

7.1 Motivation

The main objective of EDA process is to attain a uniform alloyed layer of desired thickness. In previous chapters, comprehensive experimental studies on electric discharge alloying of Ti, Al and nitrogen on AISI P20 mold steel were reported. From the experimental studies, it was observed that the alloyed layer thickness depends on various processing conditions such as discharge current, pulse on-time, and type of dielectric media. To gain insight of the process mechanism of the alloyed layer formation and also to predict the alloyed layer thickness, there is a need to develop a physics based predictive numerical model. Prediction of alloyed layer thickness is important for prior analysis of the process. It will help to establish the process in the industry. In this regard, neural networks are known to have great function mapping capabilities even from incomplete and noisy data. The advantages of ANN-based process modeling methodology are:

- It has a high potential to approximate nonlinear and complex relationships between input process parameters and performance measures.
- It has the capability to learn and generalize the input data patterns.
- It can tolerate noise in an input dataset or pattern.

TH-2735_136103036

- It has a relatively faster speed of training and execution owing to simple mathematical computations.

Therefore, a comprehensive ANN-based EDA model can find as a promising tool for the modeling of a complex problem.

7.2 Overview

The methodology followed to develop an integrated finite element method and artificial neural network (FEM – ANN) model for computation of alloyed layer thickness consists of the following stages.

- Development of a thermo-physical model for computation of alloyed layer thickness
- Development of methodology for inverse estimation of spark energy distribution factor (F_A)
- Development of an intelligent prediction model based on the estimated F_A
- Computation of the alloyed layer thickness
- Experimental validation of the developed model

The FEM - ANN integrated model has been developed for EDA to predict the energy distribution factor, and then it is used to compute the alloyed layer thickness accurately. The steps involved in the computation of alloyed layer thickness are presented in Figure 7.1.

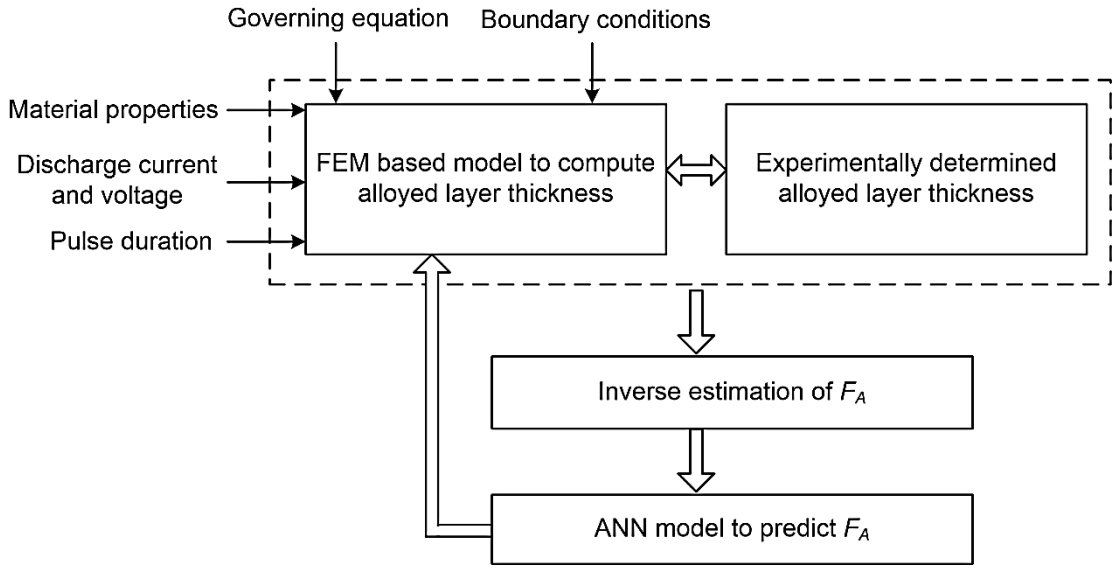

Figure 7.1 Methodology to develop integrated FEM-ANN model for computation of alloyed layer thickness

TH-2735_136103036

Initially, a FEM model was developed for EDA by considering the material properties of AISI P20 mold steel, boundary conditions, initial conditions, and EDA process parameters, namely discharge current (I_d), voltage (V), and pulse on-time (t_{on}). The model was used to compute the alloyed layer thickness for all the possible combinations of discharge current and pulse on-time.

The numerical results were compared with that of the experimental results, and the deviations were recorded. These deviations were minimized by optimizing the energy distribution factor F_A by using the Bisection Method. For quicker prediction of F_A, an ANN-based model was developed. For this, the input data considered were the type of dielectric medium, pulse on-time, and discharge current, while the target was F_A.

After extensive trials, the optimum values of ANN parameters such as an optimal number of hidden layers and the number of neurons in the hidden layer were obtained. The final ANN configuration was experimentally verified. This ANN model was used to predict the F_A accurately, which further helped in the computation of alloyed layer thickness.

7.3 Development of a thermo-physical model of EDA

A thermo-physical model of electrical discharge alloying is developed to compute the alloyed layer thickness by optimizing the fraction of energy delivered to the workpiece for various levels of process parameters. The primary mechanism of EDA is the melting and re-solidification of the melted or eroded tool and workpiece material at the surface of the workpiece. This melting is resulted due to the intense heat generated by the plasma and thereby increasing the temperature of both tool and workpiece material above the melting point temperature. For the present study, conduction is considered to be the main mode of heat transfer in the workpiece. Following assumptions have been considered for the development of the present model:

- The material is homogeneous and isotropic.
- During the EDA process, heat is transferred from the plasma to the electrode material by conduction and radiation, while from plasma to dielectric by convection and radiation (Eubank et al. 1993). In this study, the modes of heat transfer considered were conduction and convection.
- The material properties were considered to be temperature-dependent.
- The EDA spark radius was considered as a function of I_d and t_{on} (Joshi and Pande 2010).

TH-2735_136103036

- Gaussian distribution heat flux was considered (Joshi and Pande 2010).
- Only a fraction of energy was considered to be dissipated as heat into the workpiece, and remaining portions were lost into the dielectric and the tool electrode (Joshi and Pande 2010).
- Flushing efficiency was considered to be 100 %.

The thermal properties of AISI P20 mold steel are listed in Table 7.1 and Table 7.2. The schematic diagram showing the process continuum considered for the single spark EDA model is shown in Figure 7.2.

Table 7.1 Thermal properties of AISI P20 mold steel (Joshi 2009)

Material property	**Value**
Heat capacity	460 J/kg K
Density	7800 kg/m^3
Melting point	1700 K
Latent heat of fusion	250 kJ/kg

Table 7.2 Temperature-dependent thermal conductivity of AISI P20 mold steel (Joshi 2009)

Temperature (K)	Thermal conductivity (W/mK)
293	29
473	29.5
673	31
773	31
873	31

TH-2735_136103036

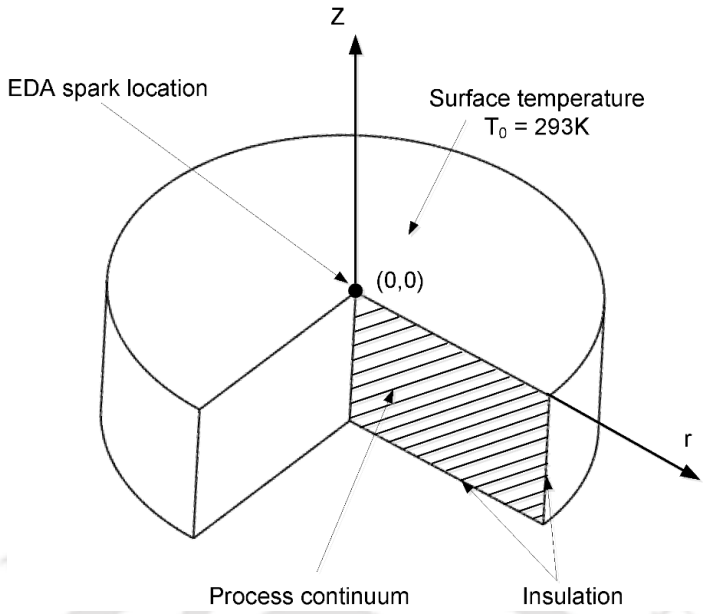

Figure 7.2 Process continuum for 2-D axisymmetric thermo-physical model

7.3.1 Governing equation and boundary conditions

EDA uses an electric discharge machine to generate spark between the tool and the workpieces which are submerged in a dielectric medium. In general, the thermal model has been widely accepted to model the electric spark, wherein the heat generation is considered due to the formation of plasma (Izquierdo et al. 2009; Singh and Ghosh 1999). During the electric discharge, both the electrodes (tool and workpiece) are melted due to the high-intensity heat produced at the spark location. Therefore, the primary mode of heat transfer has been considered as conduction.

A. Governing equation

In the present study, unsteady-state transient heat conduction with no heat generation is considered. The governing equation considered for the study is

$$\frac{1}{r}\frac{\partial}{\partial r}\left(kr\frac{\partial T}{\partial r}\right)+\frac{\partial}{\partial z}\left(k\frac{\partial T}{\partial z}\right)=\rho C_p\frac{\partial T}{\partial t} \tag{7.1}$$

where T represents the surface temperature, r and z are cylindrical coordinates used to represent radial distance and distance below the workpiece surface respectively, t represents time (i.e., pulse on-time in μs), k is the thermal conductivity of the workpiece (W/mK), ρ is the density of the workpiece (kg/m^3), and C_p is the specific heat of the workpiece (J/kg K).

TH-2735_136103036

During EDA, the latent heat of melting has been considered in the thermal analysis. The effective heat capacity (C_{peff}) by considering the latent heat of melting of the workpiece is (Joshi and Pande 2010),

$$C_{peff} = C_p + \frac{L_H}{\Delta T} \tag{7.2}$$

where L_H is the latent heat of melting of the workpiece in kJ/kg and ΔT is the difference in melting temperature of the workpiece and the room temperature in K.

B. Boundary conditions

A two-dimensional axisymmetric transient, nonlinear heat transfer model is developed to simulate the electro-thermal heating of the workpiece by the single spark. A two-dimensional transverse section of 1000 × 1000 µm was considered as the process continuum for the present study. The continuum was fixed after calculating the thermal diffusion length, L_d , which is given by (Stafe 2012)

$$L_d = \sqrt{4 D_t t_{on}} \tag{7.3}$$

where D_t is the thermal diffusivity and t_{on} is the pulse duration

The value of thermal diffusivity length, L_d is found to be 180 µm for pulse on-time (t_{on}) of 1006 µs and the dimension of the continuum was considered about 5 times of L_d which was approximately considered to be 1000 µm. Figure 7.3 shows the Gaussian heat distribution at spark plasma and other boundary conditions used for the analysis. In the present study, the time increment is set at $\Delta t = 10^{-6}$ s.

TH-2735_136103036

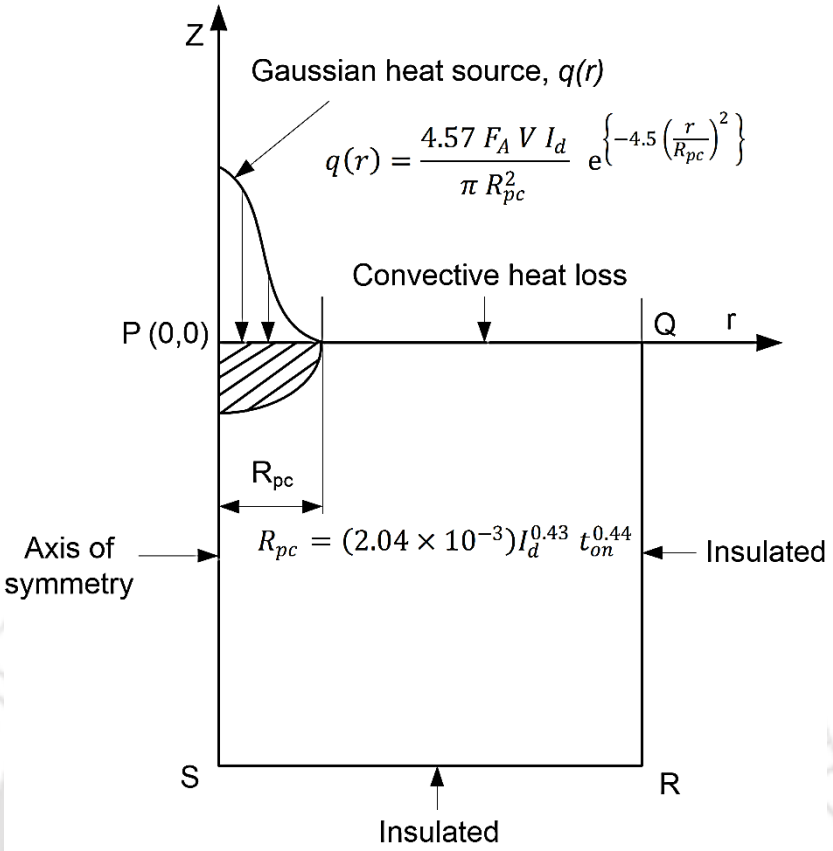

Figure 7.3 Boundary conditions

The initial temperature of the workpiece is considered as ambient temperature (T_a) at a value of 293 K.

$$T(r, z, t = 0) = T_a \tag{7.4}$$

At the region away from the spark location, i.e., as $r = \infty$, the temperature is

$$T(r = \infty, z, t) = T_a \tag{7.5}$$

Due to the symmetry of the heat source about the z-axis, the model was considered axisymmetric, and hence the boundary along the axis of symmetry was considered as insulated and represented mathematically as

$$\left.\frac{\partial T(r, z, t)}{\partial r}\right|_{r=0} = 0 \tag{7.6}$$

TH-2735_136103036

The region of the continuum, which is far away from the spark location, is considered to be insulated in both the axial and radial directions, i.e., the boundaries RS and QR, respectively. It can be written mathematically as

$$\left.\frac{\partial T(r,z,t)}{\partial z}\right|_{z=\infty} = 0 \tag{7.7}$$

$$\left.\frac{\partial T(r,z,t)}{\partial r}\right|_{r=\infty} = 0 \tag{7.8}$$

The heat flux, $q(r)$ is applied on the boundary PQ, i.e., the top surface wherein the value of r is less than or equal to R_{pc}, where R_{pc} is the spark radius. It is represented as

$$\left.\frac{\partial T(r,z,t)}{\partial r}\right|_{r\le R_{pc}} = q(r) \tag{7.9}$$

In the present study, the Gaussian distribution of heat flux has been considered to have a realistic representation of heat generated in the plasma. The amount of heat source applied to the workpiece is given by

$$q(r) = q_0 e^{\left\{-4.5\left(\frac{r}{R_{pc}}\right)^2\right\}} \tag{7.10}$$

where q_0 is the maximum heat flux in W/μm^2, R_{pc} is the radius of the plasma channel in μm.

The maximum heat flux q_0 is given by (Joshi and Pande 2010)

$$q_0 = \frac{4.57 F_A V I_d}{\pi R_{pc}^2} \tag{7.11}$$

where F_A is the fraction of energy going to the workpiece, V is the discharge voltage in V and I_d is the discharge current in A.

In this work, the plasma channel radius suggested as in the work of Joshi and Pande (2010) has been considered. It is a function of discharge current and pulse on time and given by

$$R_{pc} = (2.04\times10^{-3}) I_d^{0.43} t_{on}^{0.44} \tag{7.12}$$

where I_d is discharge current in A and t_{on} is pulse on-time in s.

TH-2735_136103036

For the boundary PQ, which is in contact with the dielectric, the region which is exposed to dielectric ($r > R_{pc}$) experiences convective heat loss. It is represented mathematically as

$$\left.\frac{\partial T(r,z,t)}{\partial r}\right|_{r>R_{pc}} = h(T - T_a) \tag{7.13}$$

where h is the convective heat transfer coefficient in W/m^2 K.

The value of convective heat transfer coefficient, h is given by (Cengel and Ghajar 2016)

$$h = \frac{Nu_x k_d}{x} \tag{7.14}$$

where Nu_x is the Nusselt number, k_d is the thermal conductivity of the dielectric medium (W/mK) and x is the characteristic length in m.

The value of Nusselt number for a fluid flowing over a flat plate is calculated by

$$Nu_x = 0.332\,\mathrm{Re}^{0.5}\,\mathrm{Pr}^{0.33} \tag{7.15}$$

where Re is the Reynolds number and Pr is the Prandtl number and it is given by

$$\mathrm{Re} = \frac{\rho_d v x}{\mu} \tag{7.16}$$

where ρ_d is the density of the dielectric medium (kg/m^3), v is the flow velocity of the dielectric which is considered 1 m/s, x is the characteristic length (m), and μ is the dynamic viscosity of the dielectric medium(kg/ms).

Prandtl number is given by

$$\mathrm{Pr} = \frac{\mu C_{pd}}{k_d} \tag{7.17}$$

where μ is the dynamic viscosity of the dielectric medium (kg/ms), C_{pd} is the specific heat of the dielectric medium in (J/kgK), k_d is the thermal conductivity of the dielectric medium (W/mK).

TH-2735_136103036

Considering the properties of the dielectric medium, the values of the Nusselt number were calculated using equation (7.15). For a characteristic length of 1000 µm and fluid velocity of 1 m/s (Jithin et al. 2020), the values of Nusselt number are 20.81, 19.93, and 20.005 for hydrocarbon (HC) oil, deionized (DI) water, and urea mixed DI water, respectively. Further, the respective convective heat transfer coefficient, h has been calculated using equation (7.14) by considering the thermal conductivity, k_d values to be 0.145 W/m K for HC oil and 0.62 W/m K for DI water and urea mixed DI water. Finally, the values of h were obtained as 3.02×10^3 W/m^2 K, 11.96×10^3 W/m^2 K, and 12.003×10^3 W/m^2 K for HC oil, DI water, and urea mixed DI water, respectively, and these values have been considered in the further utilization of the developed numerical model.

C. Fraction of energy

The fraction of energy transferred to the workpiece plays a very important role in the numerical modeling of the EDA process. It is learned that in the electric discharge alloying process, reverse polarity is generally preferred, i.e., the tool is made cathode while the workpiece is made anode (Mohri et al. 1993) to achieve higher erosion from the tool. Higher erosion from the cathode accounts to the deposition of carbon at the anode (Xia et al. 1996). As such, the exact fraction of energy transferred to the workpiece is not known till date. In such a condition, the concept of using inverse estimation for determining an unknown parameter is widely practiced. Klocke et al. (2017) have worked in determining the fraction of energy transferred to the electrodes during the electric discharge machining process by inverse estimation method. In their work, the simulated temperature was compared with that of the experimentally measured temperature with the aid of a thermocouple. On a similar front, Algodi et al. (2018) also computed the fraction of energy value by comparing the simulated crater radii and experimentally determined crater radii for the electric discharge coating process. In the present study, inverse estimation of F_A has been carried out by comparing the simulated and experimentally determined alloyed layer thickness. Attaining a certain desirable alloyed layer thickness is the prime objective for the EDA process. It is reported from the literature that the alloyed layer thickness depends on various processing conditions such as discharge current, pulse on-time, and tool properties such as compaction pressure and composition. In this work, the effect of discharge current, pulse on-time, and dielectric medium onto the alloyed layer thickness have been considered.

TH-2735_136103036

7.3.2 Solution Methodology

After the formulation of the problem in terms of governing equation and boundary conditions, the FEM was used for solving the transient thermal conduction problem for the determination of the temperature field. To perform the numerical analysis, Multiphysics COMSOL 4.4, a FEM-based software, was used to obtain the thermal distribution by applying all boundary conditions. The transient conduction equation was solved using the optimal mesh size. The temperature of discretized elements was examined, and if the temperature of an element is noted to be above the melting temperature of the material, then that element is considered to be melted. A computer system of 3.9 GHz with a 4 GB RAM processor was used to perform the numerical simulations. A typical numerical simulation in our work consumed about 5 mins. Direct solver PARDISO was used for solving the nonlinear thermal equation in the present study.

A. Finite element formulation

In finite element method, the process continuum considered for analysis is first discretized into a finite number of elements. The governing equation and boundary conditions are expressed in the form of a set of algebraic equations. In the present study, thermal based FEM model was considered with temperature as field variable. The temperature field variable with the element is interpolated by

$$T = [N]\{T_e\} \tag{7.18}$$

$$T = [B]\{T_e\} = \left[\frac{\partial}{\partial x} N\right][T_e] \tag{7.19}$$

where $[N]$ is the interpolation or shape function matrix, $\{T_e\}$ is the element nodal temperature matrix and $[B]$ is the general geometric matrix.

$$[C]\{T\} + [K_T]\{T\} = \{Q\} \tag{7.20}$$

where $[C]$ and $[K_T]$ are the global heat capacity matrix and global conductivity matrices, respectively, and are given as

$$[C] = \int_V^0 \rho c [N][N]^T \, dV \tag{7.21}$$

$$[K_T] = \int_V^0 k [B][B]^T \, dV \tag{7.22}$$

TH-2735_136103036

where $[Q]$ is the heat flux vector.

B. Mesh sensitivity analysis

Free triangular mesh type was used to discretize the process continuum. The mesh sensitivity analysis was carried out by varying pulse on-time and discharge current values. Table 7.3 gives the detailed information of the mesh sensitivity analysis that was carried out for process condition of 546 µs pulse on-time and 6 A discharge current. Initially, the complete domain was discretized with uniform mesh. Extensive numerical simulations were carried out by varying the mesh size from extremely coarse to extremely fine. It is observed from Sl. No. 1 to 9 in Table 7.3 that the maximum temperature obtained during simulation varied with the change in element size. For this, there is a need to determine the optimal mesh size of the element. In the present work, the domain has been meshed with two different types of mesh size. This difference in the mesh distribution has been made to save computation time. The region of spark location or area of our interest was meshed with fine mesh while the region far from spark location was meshed with normal to extremely fine, as shown in Sl. No. 10 to 14 of Table 7.3. It was observed that as the size of the mesh at the finer region was reduced to 1 µm, the maximum temperature attained was constant. Considering the computation time and stability in maximum temperature attained, mesh size of 1 µm at the top surface and 53 µm at the remaining continuum was considered as the optimal mesh distribution. These sizes of mesh elements were considered for all the simulations thereafter. Figure 7.4 shows the mesh distribution over the work domain wherein a finer mesh is used at the top surface and the remaining domain with a larger mesh size.

TH-2735_136103036

Table 7.3 Mesh sensitivity analysis results for 546 µs pulse on-time and 6 A discharge current

Sl. No.	Mesh distribution	Size of element (µm)		Degrees of freedom (internal nodes)	Min temperature (K)	Max temperature (K)	Comp-utation time (s)
		Max	Min				
1.	Extremely coarse	330	330	65(28)	220	2802	4
2.	Extra coarse	200	200	157(44)	293	3247	4
3.	Coarser	130	130	365(68)	293	3641	4
4.	Coarse	100	100	577(84)	293	3695	4
5.	Normal	67	67	1217(124)	293	3679	5
6.	Fine	53	53	1933(156)	293	3658	5
7.	Finer	37	37	3821(220)	293	3637	6
8.	Extra fine	20	20	12765(404)	293	3599	14
9.	Extremely fine	10	10	50225(804)	293	3600	98
10	Normal	67	1	30628(2158)	293	3620	52
11.	Fine	53	1	36550(2210)	293	3620	64
12.	Extra fine	20	1	50693(2348)	293	3620	115
13.	Extremely fine	10	1	117079(2664)	293	3620	460
14.	Extremely fine	10	0.5	189455(4688)	293	3620	1117

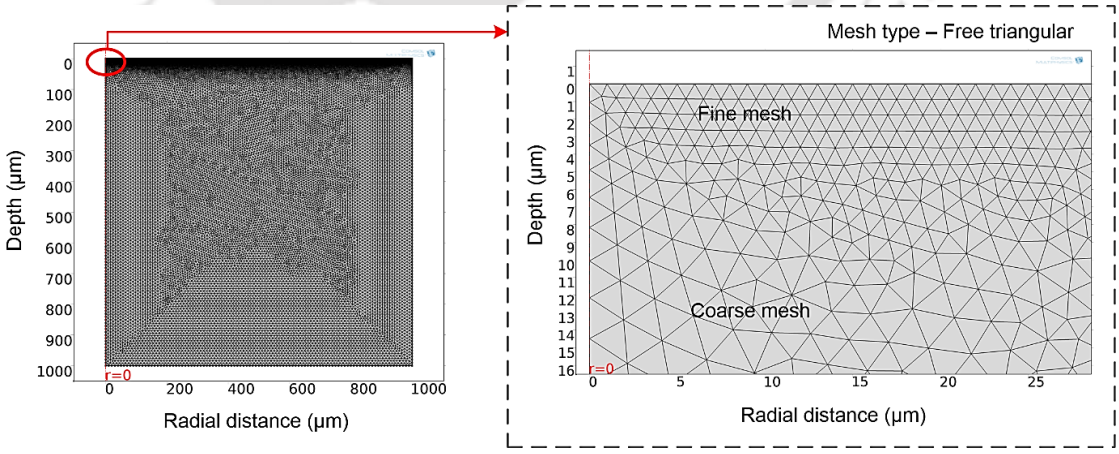

Figure 7.4 Mesh distribution over the process continuum

TH-2735_136103036

7.3.3 Numerical simulation results

The 3D temperature distribution at the top surface and the depth of the workpiece for a typical process condition of 546 µs pulse on-time and 6 A discharge current for the case of hydrocarbon oil is shown in Figure 7.5. A maximum temperature of 3688 K and a minimum temperature of 293 K can be noted at the mentioned processing conditions.

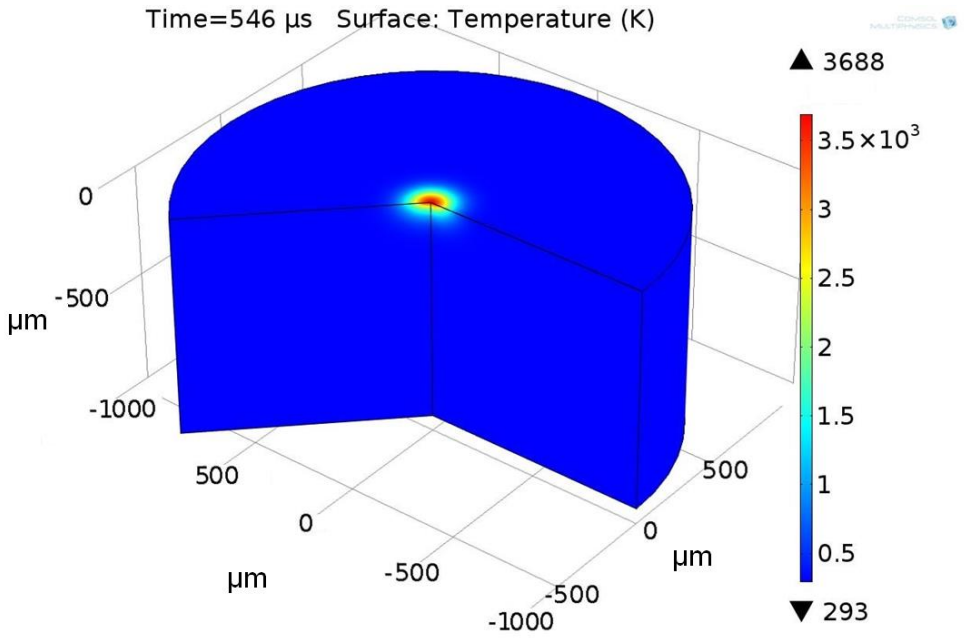

Figure 7.5 Temperature distribution with processing condition of 546 µs pulse on-time and 6 A discharge current

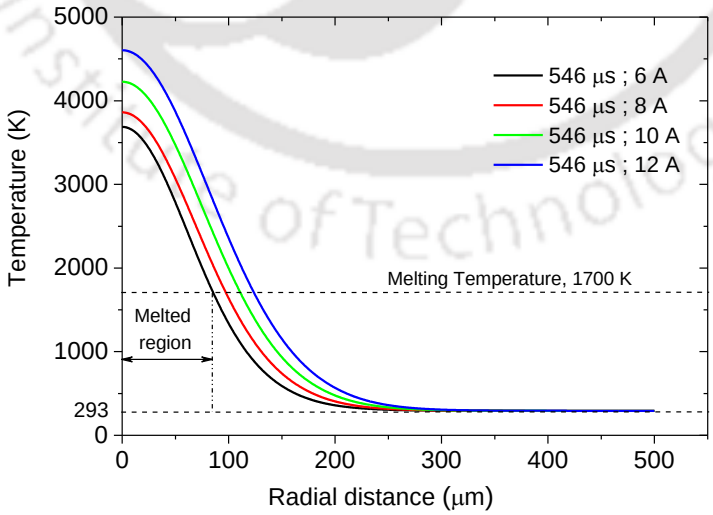

Figure 7.6 Temperature distribution along with the radial distance for fixed pulse on-time with varying discharge current

TH-2735_136103036

The temperature distribution along the radial distance for varying current and pulse on-time are plotted, and comparisons have been made by plotting line graphs. Figure 7.6 shows the line graph for the distribution of temperature at varying current and fixed pulse duration of 546 µs. From the graph, it is observed that with an increase in current, the maximum temperature attained at fixed pulse on-time of 546 µs is increased, which is due to higher heat flux. The radial distance corresponding to the melting temperature of AISI P20 mold steel, i.e., 1700 K is indicated in the figure. Further, it is observed that the radial distance of the melted region is greater for a higher discharge current.

To analyze the heat penetration along the depth of the work domain, a temperature distribution plot has been made. Figure 7.7 shows the distribution of temperature along with the depth of the work domain, i.e., distance from the top surface for fixed pulse on-time and varying discharge current. It is indicated in the figure that with an increase in discharge current, the depth of the melted region from the top surface is increased. Also, with an increase in discharge current, the maximum temperature attained is also increased.

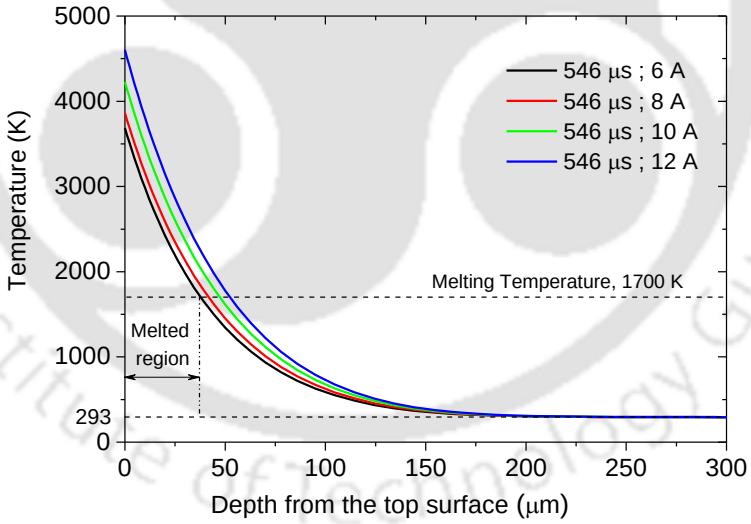

Figure 7.7 Temperature distribution along with the depth for fixed pulse on-time with varying discharge current

To compute the alloyed layer thickness, isotherm contours of melting temperature of the workpiece, i.e., 1700 K were plotted. Figure 7.8 shows the schematic diagram depicting the alloyed layer region and the heat diffused region. The heat diffused region is bounded by the isotherm contours of 1000 K and 1700 K. Figure 7.9 shows the 2D temperature plot for varying discharge current at fixed pulse on-time of 546 µs. The region above 1700

TH-2735_136103036

K isothermal contour is considered to be the alloyed region, and the corresponding maximum depth is considered to be the alloyed layer thickness. It was observed that with the increase in I_d for a fixed value of t_{on}, the maximum depth of the melted region increases which are attributed to higher energy input.

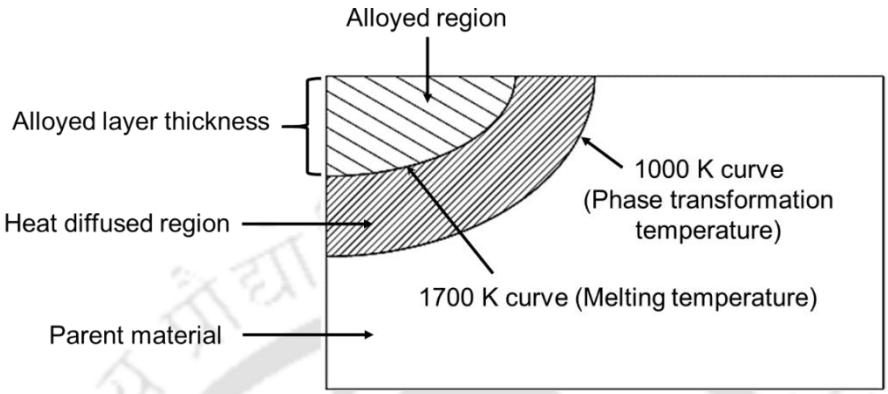

Figure 7.8 Schematic diagram showing the alloyed region

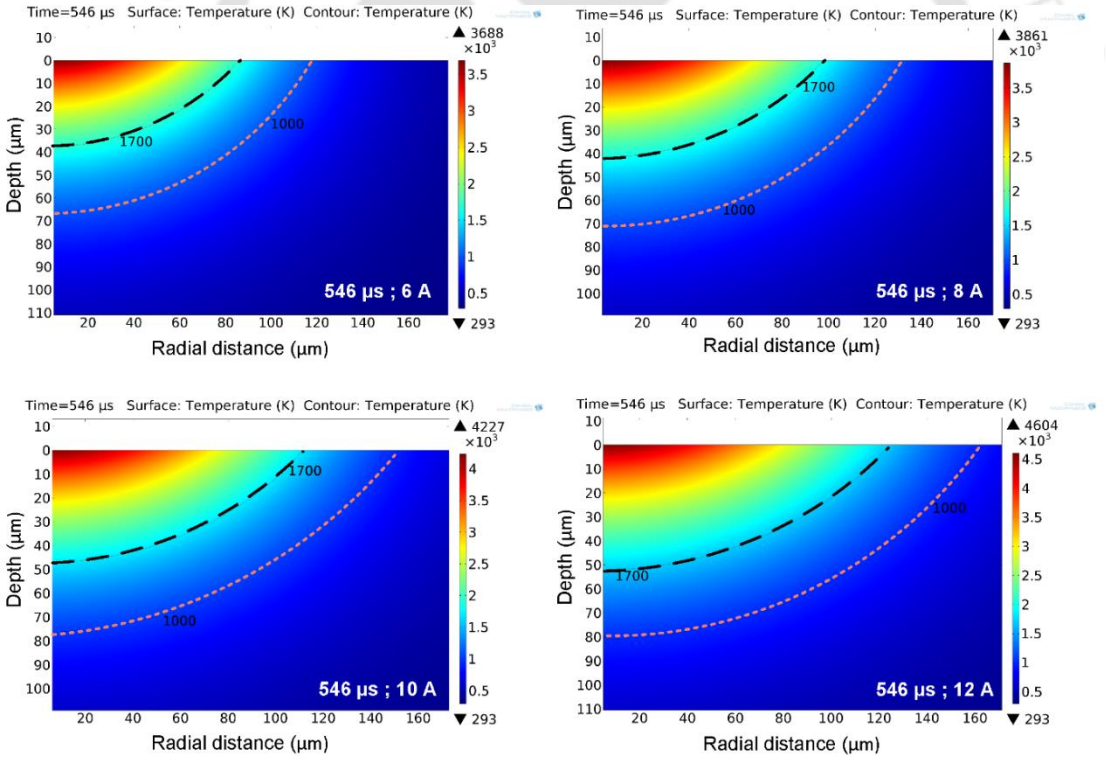

Figure 7.9 2D temperature distribution plot with processing condition of 546 µs pulse on-time and varying discharge current

7.3.4 Experimental validation of numerical results

The numerical results were validated with the experimentally determined alloyed layer thickness discussed in Chapter 4, Section 4.2.3, Table 4.1, Page No. 69 for the workpieces

TH-2735_136103036

processed in hydrocarbon oil and Chapter 5, Section 5.2.3, Table 5.1, Page No. 94, and Table 5.2, Page No. 99 for the workpieces processed in deionized water and urea mixed deionized water, respectively. Figure 7.10 shows the micrograph of the cross-section image of the alloyed workpiece processed at 546 µs t_{on} and I_d of 12 A with the use of HC oil as the dielectric medium. The numerical result was compared with that of the experimental alloyed layer thickness by plotting the melt isotherm on the micrograph. It can be noted that the melt isotherm is bowl-shaped, which is similar to the shape of the experimental deposition region. The maximum temperature is noted at the center and it then decreases radially. This is due to the Gaussian nature of the heat flux, which is considered in the developed model. In the numerical study, the melted region is considered to be the alloyed region which is represented by the isotherm contour of the melting temperature of the workpiece (1700 K) shown in the black dash curve. In addition to this, the region bounded by the melt isotherm and the phase transformation temperature (1000 K) as indicated by the red dash curve in the 2D temperature distribution is considered as the heat diffused region.

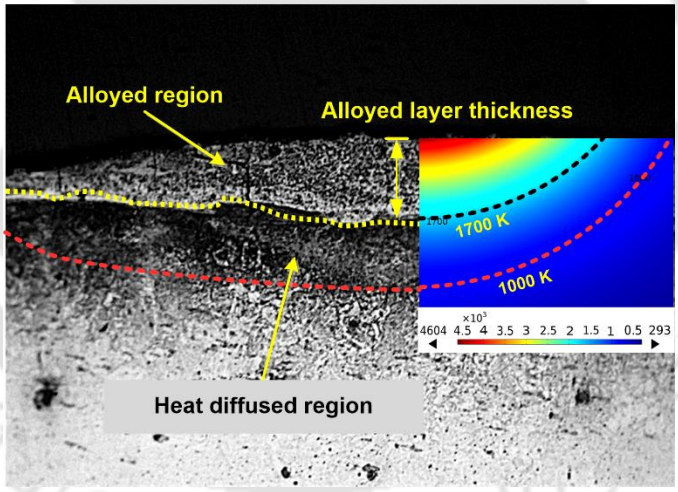

Figure 7.10 Optical micrograph at 25× showing a distinct layer of the alloyed region (t_{on} of 546 µs and I_d of 12 A) with an inset representing the alloyed layer computed numerically

To compute the alloyed layer thickness numerically, the maximum depth of the melted region is considered. Numerical simulations have been carried out for various levels of processing conditions, and corresponding alloyed layer thickness values were recorded. Apart from the processing conditions, the energy distribution factor is the most influential parameter that governs the heat energy applied on the work and tool surface, which in turn controls the depth of crater in the electric discharge machining and alloyed layer

TH-2735_136103036

thickness in electric discharge alloying. There are various studies reported on the computation of energy distribution factors. Among these, certain notable works reported that the energy distribution factor for the anode could be considered 8 % (Patel et al. 1989), 21.7 % (Joshi 2009), and 39 % (Yeo et al. 2007). Therefore, in the present work, numerical simulations were initially carried out by using these three values of energy distribution factor, and accordingly, the alloyed layer thickness values were computed. The obtained numerical results were then compared with that of the experimental results, the comparison chart is presented in Table 7.4. It can be observed that the average deviation is more than 50 % for F_A of 0.08 and 0.39. However, for F_A of 0.217, it was observed that the average deviation is 17.53 % which is quite significant.

Table 7.4. Deviations in the computation of layer thickness for energy distribution factor F_A of 0.08, 0.217 and 0.39

Data No.	Pulse on-time (µm)	Discharge current (A)	Layer thickness (µm)				Absolute deviation % $\left[\frac{(A-B)\times 100}{A}\right]$		
			A (Experimental)	B (Numerical)					
				F_A 0.08	F_A 0.217	F_A 0.39	F_A 0.08	F_A 0.217	F_A 0.39
1	546	6	37.87	2.01	44.55	68.5	94.69	17.64	80.88
2	546	8	41.34	6.84	50.94	75.08	83.45	23.22	81.62
3	546	10	47.64	10.71	55.64	79.81	77.53	16.79	67.53
4	546	12	52.83	13.91	59.41	83.52	73.67	12.45	58.09
Average deviation %							82.33	17.53	72.03

As the energy distribution factor plays a major role in the accurate prediction of the alloyed layer thickness, it was decided to find out the optimum value of F_A by minimizing the prediction deviations. This has been found out by using the bisection algorithm. The details are presented in the next section.

7.4 Inverse estimation of F_A

The procedure adopted to obtain the optimal value of F_A is presented in Figure 7.11. To compute the value of F_A for a set of process conditions, numerical simulations were carried out by initializing the F_A with a lower limit of 0.01 and an upper limit of 1. The numerically computed alloyed layer thickness was compared with that of the experimental results. Extensive trials were carried out by varying the F_A till the deviation in the prediction of alloyed layer thickness is less than 1 %. The value of F_A was obtained by employing the bisection method.

TH-2735_136103036

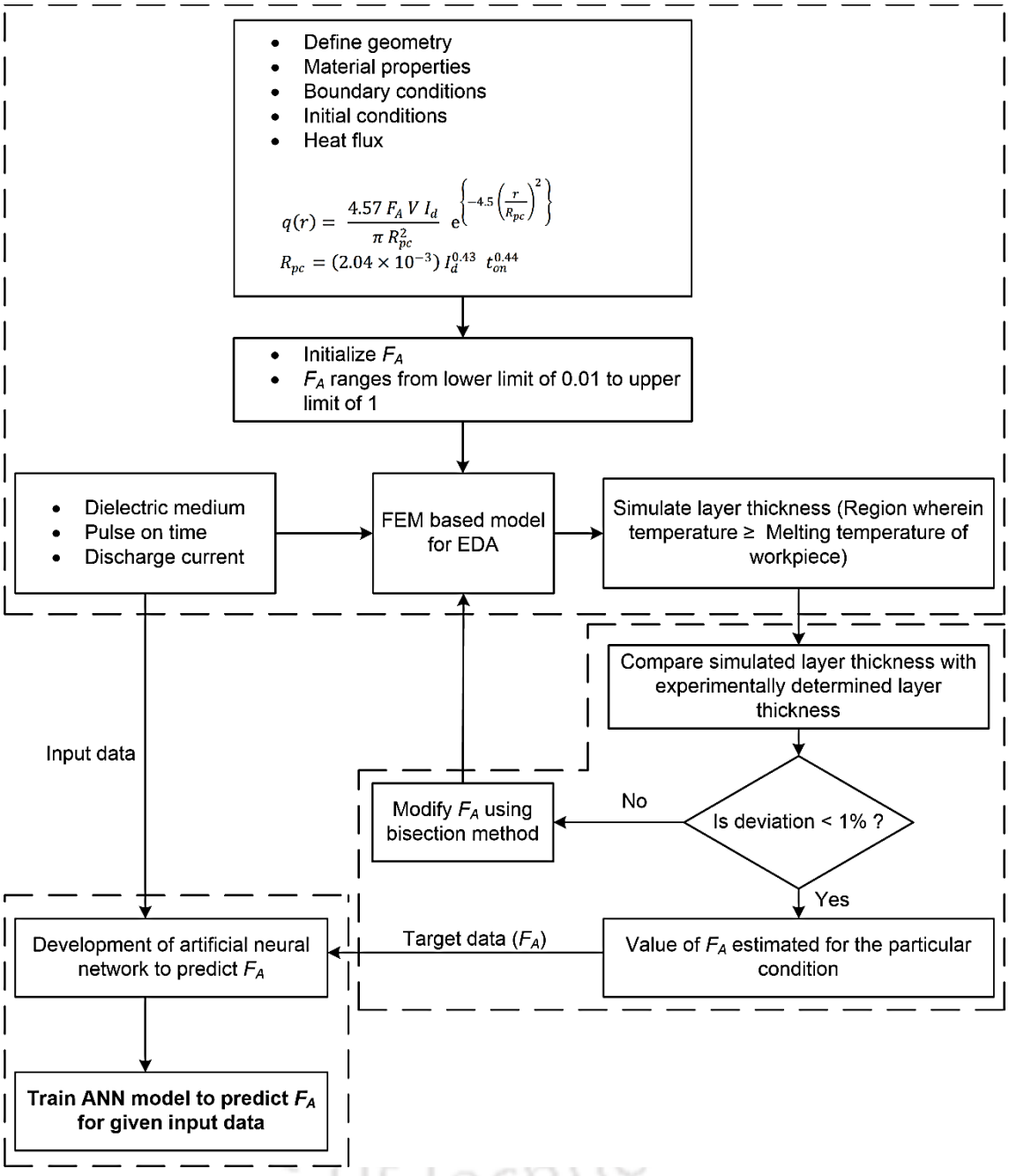

Figure7.11 Approach for predicting the value of F_A

Determination of F_A using bisection methodology for pulse on-time of 546 µs, current of 6 A, and hydrocarbon oil as the dielectric medium is listed in Table 7.5. The F_A was first assigned 0.01 (Sl. No. 1), and it was observed that with this F_A value, the simulated temperature could not reach the melting temperature of the workpiece, and hence the predicted layer thickness is noted to be insignificant. Further, upon taking the F_A to be 0.1, the deviation percentage is noted as −174.69 % (Sl. No. 2). The negative sign

TH-2735_136103036

indicates that the predicted value is larger than the experimental value. Further, the mean value of 0.01 and 0.1, which is 0.505, was considered, and the result is simulated and compared with the experimental result. These steps were followed till the deviation % is less than 1 %. After following this methodology, for the set of processing conditions, t_{on} of 546 µs, I_d of 6 A, and hydrocarbon oil dielectric, the F_A obtained was noted to be 0.184, and the deviation was found out as 0.12 % (Sl. No. 10.). In a similar approach, the values of F_A were computed for all sets of process conditions, and the results are listed in Table 7.6. From the table, it is observed that the computed F_A varies from 0.129 to 0.215. It was noted that the values are dependent on the process conditions viz. type of dielectric medium, discharge current, and pulse on-time.

Table 7.5 Determination of F_A using bisection methodology for pulse on-time of 546 µs, current of 6 A and hydrocarbon oil as dielectric medium

Sl. No.	F_A	Alloyed layer thickness (µm)		Deviation % $\frac{(X-Y)\times 100}{X}$
		X (Experimental)	Y (Numerical)	
1.	0.010	37.87	Insignificant	---
2.	0.100	37.87	104.03	−174.69
3.	0.505	37.87	78.70	−107.82
4.	0.258	37.87	51.84	−36.89
5.	0.134	37.87	24.31	35.79
6.	0.196	37.87	40.40	−6.69
7.	0.165	37.87	33.11	12.56
8.	0.180	37.87	36.81	2.79
9.	0.188	37.87	38.66	−2.09
10.	0.184	37.87	37.82	0.12

TH-2735_136103036

Table 7.6 Alloyed layer thickness and F_A for various processing conditions

Data No.	Dielectric medium *	Pulse on-time (µm)	Discharge current (A)	Alloyed layer thickness (µm)		Absolute deviation % $\left\|\frac{(X-Y)\times 100}{X}\right\|$	F_A
				X (Experimental)	Y (Numerical)		
1	1	546	6	37.87	37.83	0.116	0.184
2	1	546	8	41.34	41.27	0.157	0.172
3	1	546	10	47.64	47.37	0.562	0.178
4	1	546	12	52.83	52.45	0.708	0.184
5	1	706	6	38.54	38.58	0.101	0.188
6	1	706	8	41.55	41.39	0.363	0.172
7	1	706	10	49.98	49.81	0.347	0.184
8	1	706	12	52.46	52.03	0.825	0.176
9	1	856	6	35.18	35.16	0.053	0.177
10	1	856	8	37.83	37.82	0.025	0.162
11	1	856	10	47.11	47.08	0.111	0.173
12	1	856	12	51.81	51.85	0.087	0.173
13	1	1006	6	32.33	32.23	0.319	0.172
14	1	1006	8	34.98	34.69	0.802	0.157
15	1	1006	10	45.88	45.67	0.461	0.171
16	1	1006	12	65.01	64.99	0.026	0.215
17	2	546	6	36.18	36.12	0.176	0.176
18	2	546	8	41.26	41.27	0.037	0.172
19	2	546	10	44.35	44.36	0.042	0.167
20	2	546	12	48.12	48.04	0.161	0.167
21	2	706	6	33.42	33.23	0.573	0.168
22	2	706	8	38.54	38.4	0.36	0.163
23	2	706	10	46.42	46.421	0.002	0.171
24	2	706	12	60.19	60.09	0.156	0.207
25	2	856	6	27.05	26.96	0.313	0.152
26	2	856	8	37.32	37.19	0.339	0.160
27	2	856	10	45.73	45.72	0.013	0.169
28	2	856	12	48.03	48.01	0.041	0.162
29	2	1006	6	26.05	26.04	0.04	0.154

TH-2735_136103036

30	2	1006	8	35.81	35.77	0.091	0.159
31	2	1006	10	43.26	43.43	0.394	0.163
32	2	1006	12	53.11	53.04	0.136	0.176
33	3	546	6	23.07	23.01	0.269	0.129
34	3	546	8	33.28	33.16	0.348	0.143
35	3	546	10	39.77	39.8	0.085	0.150
36	3	546	12	53.25	53.21	0.067	0.187
37	3	706	6	21.07	21.02	0.232	0.130
38	3	706	8	34.85	34.74	0.308	0.150
39	3	706	10	37.87	37.68	0.478	0.144
40	3	706	12	46.88	46.73	0.325	0.159
41	3	856	6	19.38	19.36	0.113	0.132
42	3	856	8	33.46	33.52	0.899	0.150
43	3	856	10	44.72	44.65	0.137	0.166
44	3	856	12	51.39	51.24	0.282	0.172
45	3	1006	6	21.03	21.1	0.349	0.141
46	3	1006	8	28.52	28.46	0.211	0.141
47	3	1006	10	41.08	41.02	0.135	0.157
48	3	1006	12	46.86	46.78	0.166	0.159

***** 1 signifies hydrocarbon oil, 2 for deionized water and 3 for urea mixed deionized water

7.5 Development of ANN model to predict F_A

During the numerical simulations, it was observed that the determination of F_A was found to be time-consuming and tedious as it required multiple simulations for each set of process conditions. In the present work, to predict the F_A accurately and quickly, an artificial neural network (ANN) based model was developed. Feed-forward back propagation neural network (BPNN) was used for training the dataset.

TH-2735_136103036

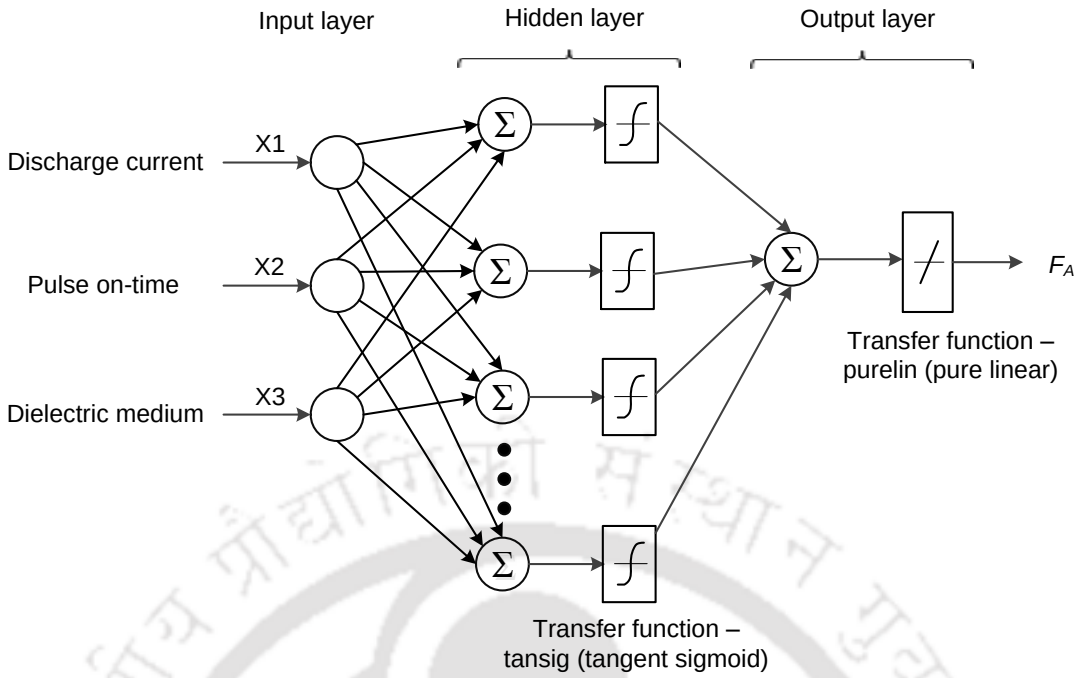

Figure 7.12 ANN architecture

Figure 7.12 shows the developed ANN architecture. The network comprises an input layer, a hidden layer whose number of neurons can be varied, and an output layer. The input layer is comprised of three nodes viz. dielectric medium, pulse on-time, and discharge current. For the dielectric medium, numeric 1 was chosen for HC oil, 2 for DI water, and 3 for urea mixed DI water. In the output layer, the F_A was set as the target. The number of neurons in the hidden layer was varied, and the optimum number was obtained. The training has been done using MATLAB 2017a.

A total of 48 data sets (refer to Table 7.6) were used for the training, validation, testing, and assessment of the network. Out of these, 8 data sets were chosen randomly for the assessment of the network (Kohli and Dixit 2005). The mathematical equation to compute the required number of the datasets is given by

$$X_0 = \left(1 - \frac{X}{100}\right)^n \tag{7.23}$$

where X_0 is the low predictive index, X is the percentage of data having an error greater than the prescribed value, and n is the size of the testing dataset.

In the present work, X is considered as 27, which means that 27 % of the time, the prediction error will be greater than the prescribed value. Further, considering the probability that the network will give the poor predictive capability (X_0) is 0.15, the value

TH-2735_136103036

of *n* is evaluated to be 6 using equation (7.23). This indicates that a minimum of 6 datasets should be used for testing the network, and this developed network will give 85 % confidence.

Out of 48 datasets, 40 were divided into training, validation, and testing data sets, while the remaining 8 were used for assessment. The division of data for training, validation, and testing data sets was set as 70 %, 15 %, and 15 %, respectively. In order to select the dataset for training, validation, and testing, regression plots for training, validation, and testing dataset were checked for different combinations. The procedure followed for the selection of the dataset and the network architecture is as shown in Figure 7.13. The dataset combination which gives the regression value greater than 0.9 for all the datasets was therefore chosen. After the selection of the dataset, the network was trained by varying the number of neurons in the hidden layer from 2 to 30 to determine the optimal network architecture. The network and training parameters are given in Table 7.7. The training, validation, and testing data used are tabulated in Table 7.8, Table 7.9, and Table 7.10, respectively.

TH-2735_136103036

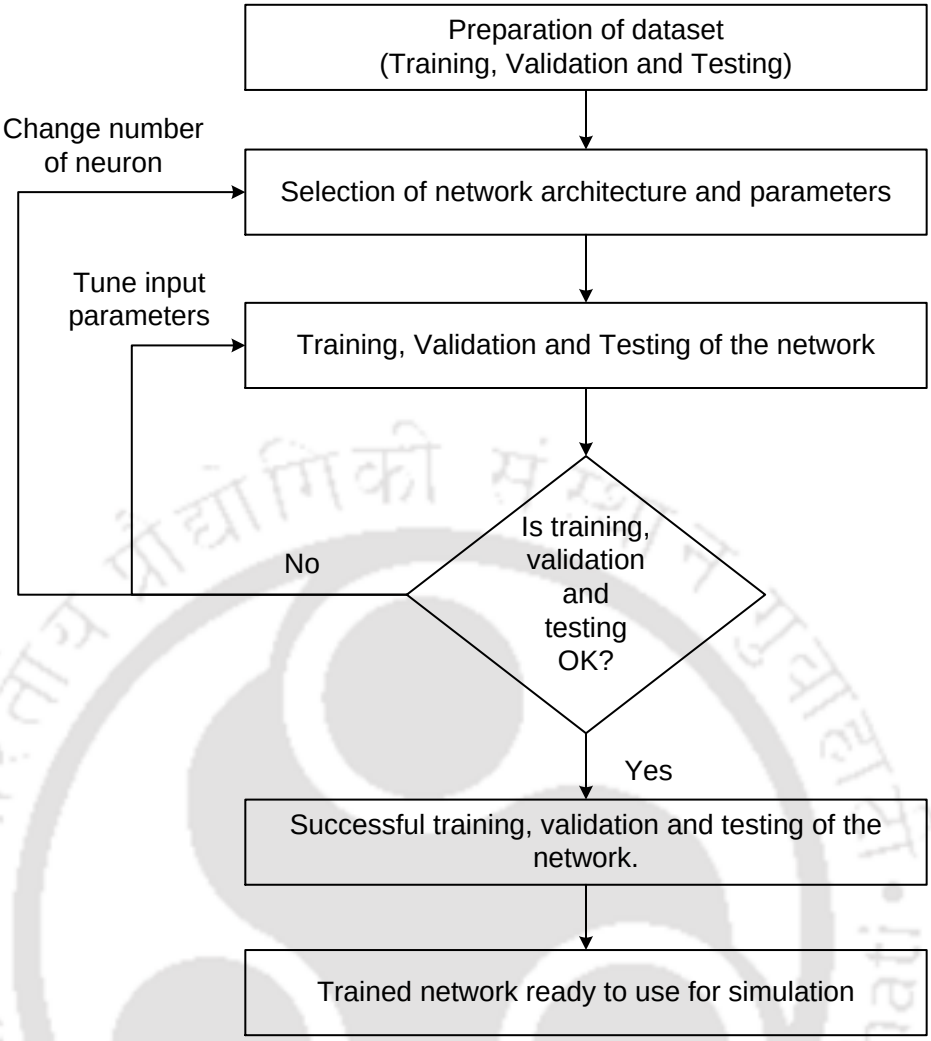

Figure 7.13 Selection of dataset

Table 7.7 Network and training parameters

Parameter	Description / Value
Number of hidden layer	1
Number of neurons in the hidden layer	2 to 30
Transfer function	Tangent sigmoid for hidden layer
	Pure linear for output layer
Training algorithm	Scaled conjugate gradient (SCG)
Performance function	Mean square error (MSE)
MSE threshold (Goal)	1×10^{-5}

TH-2735_136103036

Table 7.8 Training data sets

Data set No.	Dielectric medium	Pulse on-time (µs)	Discharge current (A)	F_A
1	1	546	6	0.184
3	1	546	10	0.178
4	1	546	12	0.184
9	1	856	6	0.177
10	1	856	8	0.162
11	1	856	10	0.173
13	1	1006	6	0.172
15	1	1006	10	0.171
16	1	1006	12	0.215
17	2	546	6	0.176
18	2	546	8	0.172
20	2	546	12	0.167
21	2	706	6	0.168
22	2	706	8	0.163
24	2	706	12	0.207
25	2	856	6	0.152
26	2	856	8	0.16
29	2	1006	6	0.154
30	2	1006	8	0.159
31	2	1006	10	0.163
35	3	546	10	0.15
36	3	546	12	0.187
37	3	706	6	0.13
43	3	856	10	0.166
44	3	856	12	0.172
46	3	1006	8	0.141
47	3	1006	10	0.157
48	3	1006	12	0.159

TH-2735_136103036

Table 7.9 Validation data sets

Data set No.	Dielectric medium	Pulse on-time (µs)	Discharge current (A)	F_A	Prediction error	% Error
7	1	706	10	0.184	0.001	0.871
8	1	706	12	0.176	−0.006	3.528
38	3	706	8	0.15	0.004	3.020
39	3	706	10	0.144	−0.002	1.497
41	3	856	6	0.132	−0.015	12.015
42	3	856	8	0.15	0.002	1.867
					Average deviation	3.80 %

Table 7.10 Testing data sets

Data set No.	Dielectric medium	Pulse on-time (µs)	Discharge current (A)	F_A	Prediction error	% Error
2	1	546	8	0.172	−0.001	0.529
19	2	546	10	0.167	−0.001	0.244
28	2	856	12	0.162	−0.018	11.561
33	3	546	6	0.129	−0.014	10.563
40	3	706	12	0.159	−0.001	0.791
45	3	1006	6	0.141	−0.007	5.156
					Average deviation	4.81 %

To select the optimal network configuration, the average deviation (%) of the testing results have been examined. Figure 7.14 shows the plot of the average deviation (%) of the test results with varying neurons from 2 to 30. The network with a minimum average deviation % is considered to be the best network and it is further used. In the present study, the average deviation (%) is attained at neuron 10. Therefore, the 3-10-1 network architecture is considered to be the best network to predict the value of F_A accurately.

TH-2735_136103036

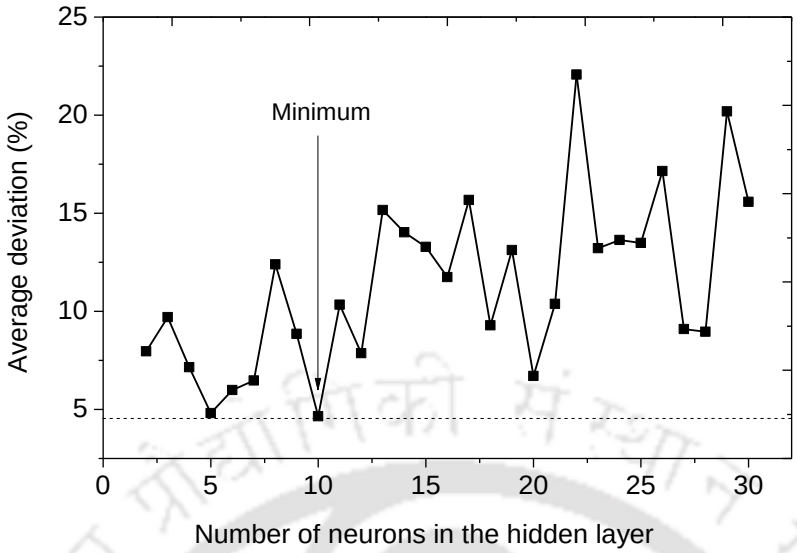

Figure 7.14 Selection of optimal number of neuron in the hidden layer

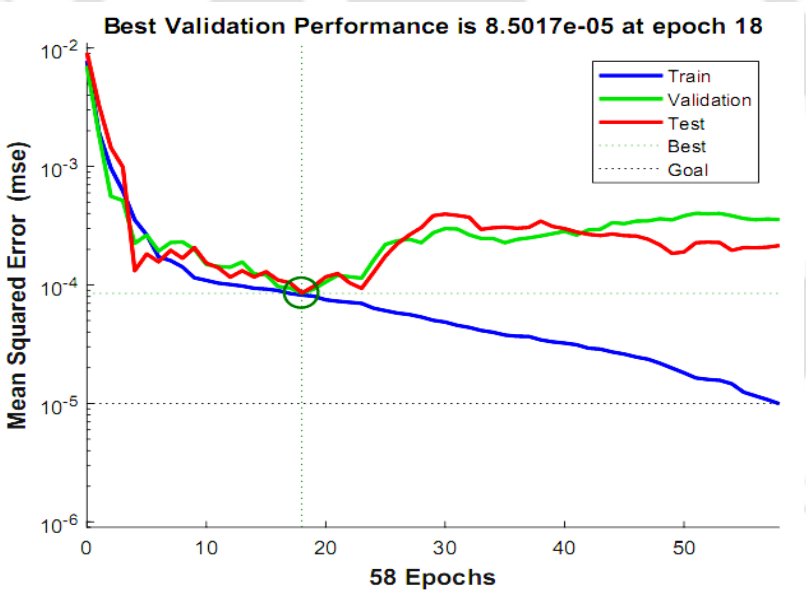

Figure 7.15 Performance plot for 3-10-1 network

Figure 7.15 shows the performance plot for 3-10-1 backpropagation neural network architecture. From the figure, it is observed that the values of the MSE reduce for training, validation, and the testing dataset at the beginning of the simulation, and the best performance was noted to be attained at epoch 18. After epoch 18, the MSE curve for the validation and testing dataset noted to be increased, and this indicated overtraining of the network. Therefore, it can be said that the network is best trained at epoch 18. The regression plots for the training, validation and testing datasets at 3-10-1 network

TH-2735_136103036

architecture are shown in Figure 7.16. It can be noted that in all the cases, the R-value is above 0.85, which is acceptable. Therefore, the 3-10-1 network architecture was considered as the optimal network configuration for accurate prediction of F_A. The performance of this network was verified by using a set of processing conditions that were not used in the training.

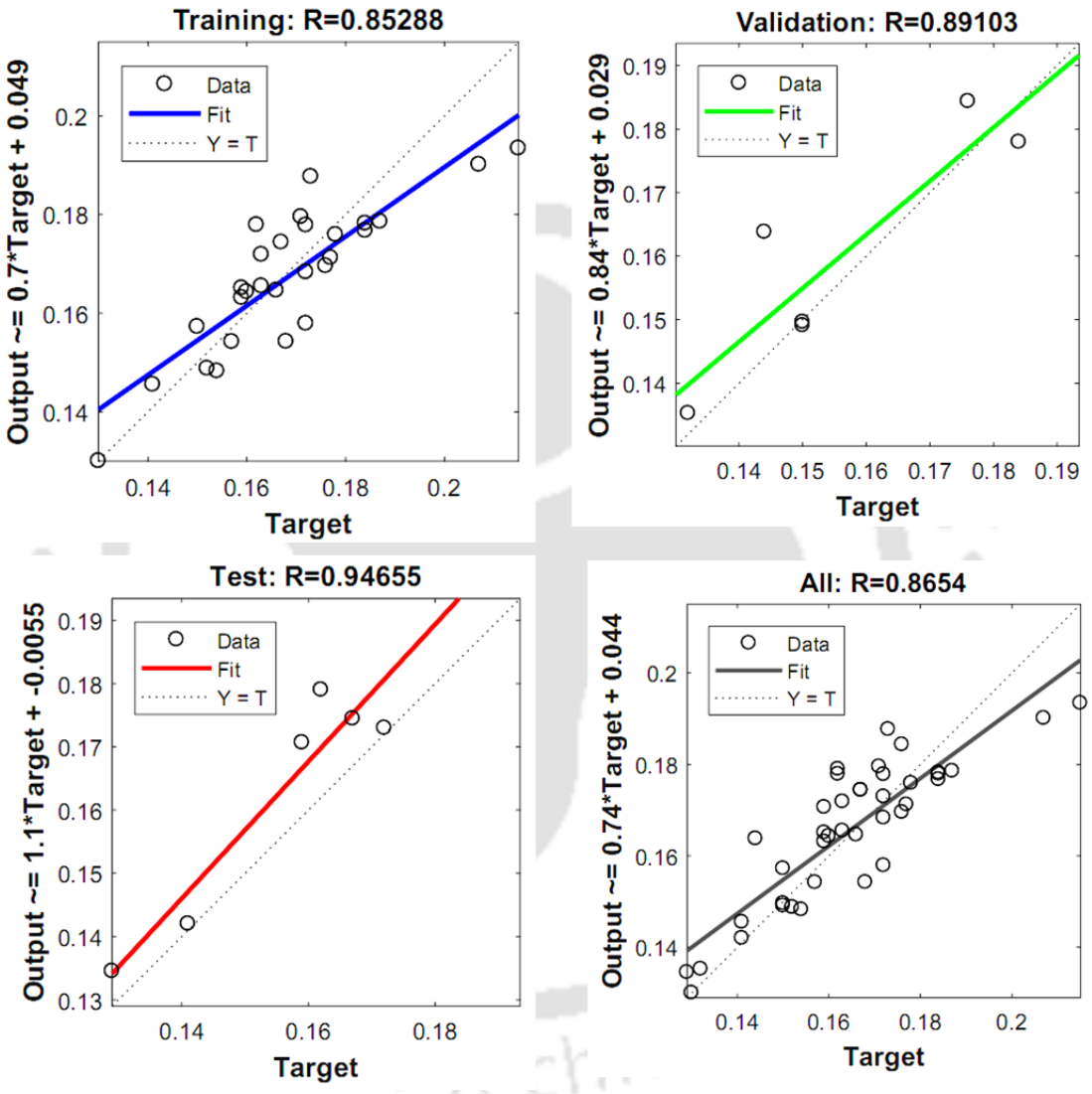

Figure 7.16 Regression plots for training, validation, testing, and all the dataset for 3-10-1 network architecture

7.6 Assessment of the developed integrated FEM-ANN model

The performance of developed FEM-ANN methodology was assessed by predicting the alloyed layer thickness. To compute the F_A, the optimal network 3-10-1 configuration was used. For the assessment, 8 unseen datasets that were not part of the training of the

TH-2735_136103036

network were employed. Computed alloyed layer thickness values and corresponding process conditions are listed in Table 7.11. Initially, by using the optimal network, the F_A values have been computed for the chosen 8 datasets. Then, by employing these F_A values and the respective processing conditions as input to the developed FEM model, the corresponding values of alloyed layer thickness were computed. The computed alloyed layer thickness using the FEM-ANN model was then compared with the experimentally determined alloyed layer thickness for similar process conditions. The absolute % deviations were computed and tabulated (Table 7.11). It was observed that the average percentage deviation was 6.55 %, and the range of the average deviation ranges from 1 % to 14 %, which is considered to be acceptable. Thus it was noted that the developed FEM-ANN could be adopted to accurately and quickly compute the alloyed layer thickness. A similar methodology can further be employed for any tool-work material combination. Therefore, the developed FEM-ANN integrated model was found to be effective and robust as the developed model could successfully compute the expected alloyed layer thickness for the considered process parameters. Further, the present study added more insight in the mechanism of electric discharge alloying process.

Table 7.11 Assessment results using 3-10-1 network

Sl. No.	Dielectric medium	Pulse on-time (µs)	Discharge current (A)	ANN predicted F_A	Alloyed layer thickness (µm)		% Deviation
					Numeri-cal	Experimen-tal	
1	1	706	6	0.185	37.89	38.54	1.68
2	1	706	8	0.178	42.94	41.55	3.34
3	1	856	12	0.198	59.13	51.81	14.13
4	1	1006	8	0.165	37.88	34.98	8.29
5	2	706	10	0.185	50.25	46.42	8.25
6	2	856	10	0.172	47.05	45.73	2.88
7	2	1006	12	0.158	46.35	53.11	12.73
8	3	546	8	0.142	32.90	33.28	1.14
						Average deviation	6.55 %

7.7 Summary

In the present work, an integrated FEM-ANN model has been successfully developed to accurately predict the alloyed layer thickness in electric discharge alloying of AISI P20

TH-2735_136103036

mold steel using powder metallurgy electrode of titanium and aluminium at different processing conditions such as varying discharge current, pulse on-time, and dielectric medium. The total time required to predict the fraction of energy and the alloyed layer thickness is approximately 5 mins. Very scant work is reported on the prediction of alloyed layer thickness using artificial neural networks and hard computing methods together. Literature reports prediction of material transfer rate and average alloyed layer thickness in the EDA process using ANN. However, it needs large input data as the developed model was solely dependent on the empirical relation resulting in high experimental cost. In the present work, the developed model has achieved the accurate computation of the alloyed layer thickness with fewer data. This has been possible by incorporating the optimal fraction of energy distribution value in the developed FEM model. The fraction of energy distributed to the workpiece is one of the important process parameters in modeling the electric discharge phenomenon. Works have been reported in the inverse computation of energy distribution factor F_A by determining the surface temperature or the crater radii. However, in the present work, F_A was computed from experimentally determined alloyed layer thickness. The alloyed layer thickness was computed by considering accurate values of fraction of energy distribution to the workpiece, F_A. These values were computed by using the inverse estimation method and the ANN-based model. Following important conclusions were drawn from the study.

- The neural network of 3-10-1 architecture was found to be the optimum network.
- The developed methodology suggests that the fraction of energy F_A varies from 0.129 to 0.215. This can be employed in the thermal analysis of the electric discharge-based manufacturing processes.
- The performance of the developed FEM-ANN was verified by carrying out the experiments. It was found acceptable with an average prediction deviation of 6.55 %.
- The present work facilitates a simple and quick methodology for accurate prediction of the alloyed layer thickness for complex manufacturing processes such as EDA. This provides an efficient and economical alternative to the costly, tedious, and time-consuming experimental work.

TH-2735_136103036

TH-2735_136103036

CHAPTER 8

Conclusions and Future Scope

The main objective of the present work was to enhance the surface characteristics of AISI P20 mold steel in terms of its hardness, corrosion, and wear resistance by electrical Discharge Alloying. In view of this, the work was planned to investigate the alloying of titanium, aluminium, and nitrogen over AISI P20 mold steel. For this, a powder metallurgy tool of titanium and aluminium was used, and three different dielectric media viz. hydrocarbon oil, deionized water, and urea mixed deionized water were used. Further, to study the underlying process mechanism of EDA, a physics-based numerical model has been developed to predict the alloyed layer thickness. The alloyed layer thickness was computed by considering accurate values of the fraction of energy distributed to the workpiece. This fraction of energy distribution was computed by the inverse estimation method. Thereafter, the developed model has been integrated with ANN to develop a robust predictive model. The overall research work has been carried out in the following major stages.

- Experimental investigations into electrical discharge alloying of titanium and aluminium with AISI P20 mold steel in the presence of hydrocarbon oil dielectric medium
- Experimental investigations into electric discharge alloying of Ti and Al on P20 mold steel with a water-based dielectric medium
- Characterization and assessment of the alloyed workpieces in terms of its wear and corrosion resistance behavior.
- Computation of alloyed layer thickness in electric discharge alloying by inverse estimation of energy distribution.

8.1 Conclusions and research contributions

Important conclusions and specific research contributions are listed in the following sub-section.

8.1.1 Experimental investigations into EDA of titanium and aluminium in hydrocarbon oil dielectric medium

In this work, electrical discharge-based alloying of AISI P20 mold steel has been successfully carried out by using a powder metallurgy tool of titanium and aluminum in

TH-2735_136103036

hydrocarbon oil dielectric medium. A systematic experimental work has been carried out to study the elemental transfer of the tool material and decomposed dielectric, alloyed layer thickness, and hardness of the alloyed layer at varying discharge current and pulse on-time. The discharge current was varied in four levels viz. 6, 8, 10, and 12A, while the pulse on-time values considered were 546, 706, 856, and 1006 µs. Further, the type of alloy formed has been characterized and presented in detail. Following conclusions can be drawn from this study.

- The transfer of the tool elements over the workpiece surface has been successfully confirmed from the EDS result. Elemental mapping of the alloyed surface over the top surface, as well as the cross-sectioned region, indicated that the tool elements present are uniformly distributed in the alloyed region. Elemental composition up to a maximum of 18 % Ti and 18.7 % Al was observed over the alloyed workpiece surface.
- X-ray diffraction pattern indicated the formation of Fe_3C and TiAl at the alloyed region. Therefore, it can be concluded that the electric discharge surface alloying of Ti and Al with AISI P20 mold steel has been successfully achieved.
- A uniform layer of 70 µm thickness can easily be alloyed on the substrate material using powder metallurgy-based green compact tool electrodes with the composition of 50 % Ti and 50 % Al.
- The hardness of the alloyed region was found to be four times more than that of the parent material, i.e., 300 $HV_{0.3}$ to 1125 $HV_{0.3}$. That ascertains the usefulness of the EDA process in improving the surface characteristics of the parent material.
- The material deposition rate was affected by the change in discharge current and pulse on-time. Increase in the discharge current and pulse on-time results in a higher material deposition rate.
- The surface roughness of the alloyed workpieces exhibited a roughness value in the range of 4.5 to 8.5 µm.

8.1.2 Experimental investigations into electric discharge alloying of Ti and Al with water-based dielectric medium

The effects of urea mixed deionized water on the electric discharge alloying of AISI P20 mold steel using powder metallurgy electrodes of titanium and aluminium have been investigated. A comparative study was carried out between the alloyed surfaces obtained with deionized water and that with the urea mixed deionized water. Detailed

TH-2735_136103036

investigations have also been carried out to study the effect of pulse on-time discharge current and dielectric medium on the material transfer rate and alloyed layer thickness. The hardness of the alloyed layer has also been characterized. Following conclusions have been drawn.

- EDS examination confirms successful transfer of tool material along with decomposed elements from the dielectric on the workpiece. A uniform distribution was noticed from the elemental mapping. An elemental composition up to a maximum of 16.5 % Ti with 12 % Al, 35.02 % oxygen, and 4 % nitrogen was observed for the workpiece processed in urea mixed deionized water. For the workpiece processed in deionized water, a maximum of 27.2 % titanium with 7.6 % aluminum and 40.3 % oxygen was observed.
- Formation of an alloyed layer composed of TiAl, Fe_3O_4, and Ti_4AlN_3 was observed from the XRD analysis for the workpiece processed using urea mixed DI water, while for the workpiece processed in deionized water, the alloyed layer was noted to be composed of TiAl and Fe_3O_4.
- The analysis of the alloyed layer thickness indicated that the thickness was more for the workpieces processed using DI water as compared to that with the urea mixed. An alloyed layer of 60.19 µm thickness was noted for the workpiece processed using DI water, while that for urea mixed deionized water was 53.25 µm.
- In case of hardness study, the hardness of the alloyed layer was observed 579.83 $HV_{0.3}$ while using deionized water. For the workpiece processed with mixed deionized water, the hardness was noted to be 604.35 $HV_{0.3}$. The percentage increase in the hardness of the alloyed region for the workpiece processed in DI water was found to be enhanced by 87.04 % as compared to that of the parent material, while that for the workpiece processed in urea mixed deionized water was 101.45 %.
- The material deposition rate was mainly affected by the discharge current. Increase in discharge current resulted in higher deposition rate for both the type of dielectric medium.
- During surface roughness study, the surface roughness of the processed workpieces was found to be dependent on the discharge current and pulse on-time; however, the addition of urea did not find any significant influence on the surface roughness value. The surface roughness extends a range of 5.94 to 12.45 µm for the workpiece

TH-2735_136103036

processed in deionized water while that of urea mixed deionized water, the range was found to be 5.98 to 12.54 µm

8.1.3 Wear and corrosion resistance behavior of electric discharge alloyed workpieces

An investigation of the wear behavior has been made by analyzing the real-time wear data, friction coefficient, and mass loss during the wear test. Further, the corrosion behavior for the alloyed workpieces was studied by studying the electrochemical impedance spectrum. A comparative study has been made for the wear and corrosion resistance of the workpieces processed in three types of dielectric media. From the present work, the following conclusions have been drawn.

- The real-time wear data acquired during the test indicated that the wear of the workpieces processed in hydrocarbon oil was the least followed by workpieces processed in urea mixed deionized water, unprocessed workpiece, and workpiece processed in deionized water.
- The low slope in the trend of the wear after a depth of about 10 µm signifies that there was a formation of a uniform hard alloyed region after a depth of 10 µm from the alloyed surface for the workpiece processed in hydrocarbon oil.
- The friction coefficient trend for the workpiece processed using hydrocarbon oil was decreasing. For the unprocessed workpiece and the workpieces processed in deionized water and urea mixed deionized water, the friction behavior was noted to be increasing.
- The mass loss during the wear test result showed that the workpiece processed in hydrocarbon oil was the least followed by workpieces processed in urea mixed deionized water, deionized water, and the unprocessed workpiece. The mass loss for the workpiece processed in hydrocarbon oil was significantly reduced by 46 % from that of the unprocessed workpiece. The change in mass loss is quite marginal for the unprocessed workpiece and the workpieces processed in the water-based dielectric.
- From the Bode diagrams, it was observed that the impedance modulus and the maximum phase angle were the highest for the workpiece processed in hydrocarbon oil, indicating the highest polarization resistance.
- The corrosion resistance value for the workpiece processed using hydrocarbon oil was almost double the corrosion resistance of the workpieces processed using deionized

TH-2735_136103036

water and urea mixed deionized water and unprocessed workpiece. There was 110 % enhancement in the corrosion resistance for the workpiece processed in hydrocarbon oil from that of the unprocessed workpiece.

8.1.4 Computation of alloyed layer thickness in electric discharge alloying by inverse estimation of energy distribution

An integrated FEM-ANN model has been successfully developed to accurately predict the alloyed layer thickness in electric discharge alloying of AISI P20 mold steel using powder metallurgy electrodes of titanium and aluminium at different processing conditions such as varying discharge current, pulse on-time, and various dielectric media. The alloyed layer thickness was computed by considering the accurate values of fraction of energy distribution to the workpiece, F_A. These values were computed by using the inverse estimation method and the ANN-based model. Following important conclusions were drawn from the study.

- The neural network of 3-10-1 architecture was found to be the optimum network.
- The developed methodology suggests that the fraction of energy F_A varies from 0.129 to 0.215. This can be employed in the thermal analysis of the electric discharge-based manufacturing processes.
- The performance of the developed FEM-ANN was verified by carrying out the experiments. It was found acceptable with an average prediction deviation of 6.55 %.
- The present work facilitates a simple and quick methodology for accurate prediction of the alloyed layer thickness for complex manufacturing processes such as EDA. This provides an efficient and economical alternative to the costly, tedious, and time-consuming experimental work.

8.2 Future scope

The present work can be further extended in the following direction.

- Electric discharge alloying can be explored in the field of biomedical applications to form a biocompatible alloyed surface over metallic biomaterials such as Ti alloy, magnesium alloy, cobalt-based alloy, etc.
- Electric discharge surface alloying studies focusing on the effect of tool and workpiece materials combinations onto the characteristics of alloyed surface can be explored. In this, the effect of different ways of electric discharge alloying such as use

TH-2735_136103036

of solid tool electrode, powder metallurgy electrode, and powder mixed dielectric can be carried out.

- Experimental and theoretical investigations onto the electro-thermal induced hydrodynamic melt flow in the electric discharge alloying process can be carried out. The study can incorporate both the cathode and anode model during EDA. It is expected that the study can give a more realistic approach in computing the thickness of the alloyed layer formed.
- The limitations of the developed thermo-physical model lie in the fact that the developed model is for a single spark, and also, the effect of vaporization of the workpiece due to intense heating during the sparking phenomenon was not considered. Also, the heat capacity and the density are considered to be constant in the present study. These limitations can be an extension of the present work for developing a more realistic model.

TH-2735_136103036

REFERENCES

Aihua, L., Jianxin, D., Haibing, C., Yangyang, C., & Jun, Z. (2012). Friction and wear properties of TiN , TiAlN , AlTiN and CrAlN PVD nitride coatings. *Iternational Journal of Refractory Metals and Hard Materials*, *31*, 82–88.

Algodi, S. J., Clare, A. T., & Brown, P. D. (2018). Modelling of single spark interactions during electrical discharge coating. *Journal of Materials Processing Technology*, *252*, 760–772.

Bai, C.Y., & Koo C.H. (2006). Effects of kerosene or distilled water as dielectric on electrical discharge alloying of superalloy Haynes 230 with Al-Mo composite electrode, *Surface and Coatings Technology*, 200, 4127–4135.

Barash, M. M., & Kahlon, C. S. (1964). Experiments with electric spark toughening. *International Journal of Machine Tool Design and Research*, *4*(1), 1–8.

Beck, J. V. (1981). Transient temperatures in a semi-infinite cylinder heated by a disk heat source. *International Journal of Heat and Mass Transfer*, *24*(10), 1631–1640.

Berg, M., Budtz-jørgensen, C. V, Reitz, H., Schweitz, K. O., Chevallier, J., Kringhøj, P., & Bøttiger, J. (2000). On plasma nitriding of steels. *Surface and Coatings Technology*, *124*, 25–31.

Borrego, L. P., Pires, J. T. B., Costa, J. M., & Ferreira, J. M. (2009). Mould steels repaired by laser welding. *Engineering Failure Analysis*, *16*(2), 596–607.

Boztepe, E., Alves, A. C., Ariza, E., Rocha, L. A., Cansever, N., & Toptan, F. (2018). A comparative investigation of the corrosion and tribocorrosion behaviour of nitrocarburized, gas nitrided, fluidized-bed nitrided, and plasma nitrided plastic mould steel. *Surface and Coatings Technology*, *334*, 116–123.

Cengel, Y. A., & Ghajar, A. J. (2016). Heat and mass transfer fundamentals and applications. *Mc. Graw Hill Education, Fifth edition*, 377-405.

Chang-Bin, T., Dao-Xin, L., Zhan, W., & Yang, G. (2011). Electro-spark alloying using graphite electrode on titanium alloy surface for biomedical applications. *Applied Surface Science*, *257*(15), 6364–6371.

Chen, Y. F., Chow, H.-M., Lin, Y. C., & Lin, C. T. (2008). Surface modification using semi-sintered electrodes on electrical discharge machining. *The International Journal*

TH-2735_136103036

of Advanced Manufacturing Technology, *36*, 490–500.

Chen, Y. F., & Lin, Y. C. (2009). Surface modifications of Al-Zn-Mg alloy using combined EDM with ultrasonic machining and addition of TiC particles into the dielectric. *Journal of Materials Processing Technology*, *209*(9), 4343–4350.

Chiou, W. Y., Chen, C. I., & Lu, W. S. (2011). The inverse numerical solutions of the nonlinear heat transfer problem in electrical discharge machining. *Numerical Heat Transfer; Part A*, *59*(4), 247–266.

Chow, H. M., Yan, B. H., Huang, F. Y., & Hung, J. C. (2000). Study of added powder in kerosene for the micro-slit machining of titanium alloy using electro-discharge machining. *Journal of Materials Processing Technology*, *101*(1), 95–103.

da Silva, S. P., Abrão, A. M., Weidler, P. G., da Silva, E. R., & Câmara, M. A. (2020). Investigation of nitride layers deposited on annealed AISI H13 steel by die-sinking electrical discharge machining. *International Journal of Advanced Manufacturing Technology*, *109*(7–8), 2325–2336.

Das, S., Klotz, M., & Klocke, F. (2003). EDM simulation: Finite element-based calculation of deformation, microstructure and residual stresses. *Journal of Materials Processing Technology*, *142*(2), 434–451.

Deng, Y., Chen, W., Li, B., Wang, C., Kuang, T., & Li, Y. (2020). Physical vapor deposition technology for coated cutting tools : A review. *Ceramics International*, *46*(11), 18373–18390.

Dibitonto, D. D., Eubank, P. T., Patel, M. R., Barrufet, M. A., & Diitonto, D. D. (1989). Theoretical models of the electrical discharge machining process . I . A simple cathode erosion model. *Journal of Applied Physics*, *66*(9), 4095–4103.

Ekmekci, B., Elkoca, O., & Erden, A. (2005). A comparative study on the surface integrity of plastic mold steel due to electric discharge machining. *Metallurgical and Materials Transactions B: Process Metallurgy and Materials Processing Science*, *36*(1), 117–124.

Eubank, P. T., Patel, M. R., Barrufet, M. A., & Bozkurt, B. (1993). Theoretical models of the electrical discharge machining process . III . The variable mass , cylindrical plasma model. *Journal of Applied Physics*, *73(11)*, 7900–7909.

Gangadhar, A., Shunmugam, M. S., & Philip, P. K. (1991). Surface modification in

TH-2735_136103036

electrodischarge processing with a powder compact tool electrode. *Wear*, *143*(1), 45–55.

Gostimirovic, M., Kovac, P., Sekulic, M., & Skoric, B. (2012). Influence of discharge energy on machining characteristics in EDM. *Journal of Mechanical Science and Technology*, *26*(1), 173–179.

Ho, K. H., & Newman, S. T. (2003). State of the art electrical discharge machining (EDM). *International Journal of Machine Tools and Manufacture*, *43*(13), 1287–1300.

Ho, S. K., Aspinwall, D. K., & Voice, W. (2007). Use of powder metallurgy (PM) compacted electrodes for electrical discharge surface alloying/modification of Ti-6Al-4V alloy. *Journal of Materials Processing Technology*, *191*(1–3), 123–126.

Horii, T., Kirihara, S., & Miyamoto, Y. (2008). Freeform fabrication of Ti-Al alloys by 3D micro-welding. *Intermetallics*, *16*(11–12), 1245–1249.

Hwang, Y. L., Kuo, C. L., & Hwang, S. F. (2010). The coating of TiC layer on the surface of nickel by electric discharge coating (EDC) with a multi-layer electrode. *Journal of Materials Processing Technology*, *210*(4), 642–652.

Ibrahim, R. N., Rahmat, M. A., Oskouei, R. H., & Singh Raman, R. K. (2015). Monolayer TiAlN and multilayer TiAlN/CrN PVD coatings as surface modifiers to mitigate fretting fatigue of AISI P20 steel. *Engineering Fracture Mechanics*, *137*, 64–78.

Izquierdo, B., Sánchez, J. A., Plaza, S., Pombo, I., & Ortega, N. (2009). A numerical model of the EDM process considering the effect of multiple discharges. *International Journal of Machine Tools and Manufacture*, *49*(3–4), 220–229.

Janmanee, P., & Muttamara, A. (2012). Surface modification of tungsten carbide by electrical discharge coating (EDC) using a titanium powder suspension. *Applied Surface Science*, *258*(19), 7255–7265.

Jeswani, M. L. (1979). Dimensional analysis of tool wear in electrical discharge machining. *Wear*, *55*(1), 153–161.

Jithin, S., Raut, A., Bhandarkar, U. V, & Joshi, S. S. (2020). Finite element model for topography prediction of electrical discharge textured surfaces considering multi-discharge phenomenon. *International Journal of Mechanical Sciences*, *177*, 105604, 1-16.

TH-2735_136103036

Joshi, S. N. (2009). *Intelligent Process Modeling and Optimization of EDM*.

Joshi, S. N., & Pande, S. S. (2010). Thermo-physical modeling of die-sinking EDM process. *Journal of Manufacturing Processes*, *12*, 45–56.

Joshi, S. N., & Pande, S. S. (2011). Intelligent process modeling and optimization of die-sinking electric discharge machining. *Applied Soft Computing Journal*, *11*(2), 2743–2755.

Jhavar, S., Paul, C. P., & Jain, N. K. (2013). Causes of failure and repairing options for dies and molds: A review. *Engineering Failure Analysis*, *34*, 519–535.

Jilani, S. T., & Pandey, P. C. (1982). Analysis and modelling of edm parameters. *Precision Engineering*, *4*(4), 215–221.

Kansal, H. K., & Kumar, P. (2007). Effect of Silicon Powder Mixed EDM on Machining Rate of AISI D2 Die Steel. *Journal of Manufacturing Processes*, *9*, 13–22.

Kansal, H. K., Singh, S., & Kumar, P. (2008). Numerical simulation of powder mixed electric discharge machining (PMEDM) using finite element method. *Mathematical and Computer Modelling*, *47*, 1217–1237.

Klocke, F., Schneider, S., Mohammadnejad, M., Hensgen, L., & Klink, A. (2017). Inverse Simulation of Heat Source in Electrical Discharge Machining (EDM). *Procedia CIRP*, *58*, 1–6.

Kohli, A., & Dixit, U. S. (2005). A neural-network-based methodology for the prediction of surface roughness in a turning process. *International Journal of Advanced Manufacturing Technology*, *25*(1–2), 118–129.

Kumar, S., & Batra, U. (2012). Surface modification of die steel materials by EDM method using tungsten powder-mixed dielectric. *Journal of Manufacturing Processes*, *14*(1), 35–40.

Kunieda, M., & Yoshida, M. (1997). Electrical discharge machining in gas. *CIRP Annals - Manufacturing Technology*, *46*(1), 143–146.

Lee, H. G., Simao, J., Aspinwall, D. K., Dewes, R. C., & Voice, W. (2004). Electrical discharge surface alloying. *Journal of Materials Processing Technology*, *149*, 334–340.

Ming, W., Ma, J., Zhang, Z., Zhang, G., Huang, Y., Huang, H., & Shen, D. (2016). Soft

TH-2735_136103036

computing models and intelligent optimization system in electro-discharge machining of SiC / Al composites. *The International Journal of Advanced Manufacturing Technology*, *87*, 201–217.

Ming, W., Zhang, Z., Wang, S., Huang, H., Zhang, Y., Zhang, Y., & Shen, D. (2017). Investigating the energy distribution of workpiece and optimizing process parameters during the EDM of Al6061, Inconel718, and SKD11. *International Journal of Advanced Manufacturing Technology*, *92*(9–12), 4039–4056.

Mohana, G. K., Rangajanardhaa, G., Rao, D. H., & Rao, M. S. (2009). Development of hybrid model and optimization of surface roughness in electric discharge machining using artificial neural networks and genetic algorithm. *Journal of Materials Processing Technology*, *209*, 1512–1520.

Mohri, N, Saito, N., Tsunekawa, Y., & Kinoshita, N. (1993). Metal Surface Modification by Electrical Discharge Machining with Composite Electrode. *Annals of the CIRP*, *42*(1), 219–222.

Mohri, N., Takezawa, H., Furutani, K., Ito, Y., & Sata, T. (2000). A new process of additive and removal machining by EDM with a thin electrode. *CIRP Annals - Manufacturing Technology*, *49*(1), 123–126.

Mordyuk, B. N., Prokopenko, G. I., Grinkevych, K. E., Piskun, N. A., & Popova, T. V. (2017). Effects of ultrasonic impact treatment combined with the electric discharge surface alloying by molybdenum on the surface related properties of low-carbon steel G21Mn5. *Surface and Coatings Technology*, *309*, 969–979.

Mordyuk, B. N., Prokopenko, G. I., Volosevich, P. Y., Matokhnyuk, L. E., Byalonovich, A. V., & Popova, T. V. (2016). Improved fatigue behavior of low-carbon steel 20GL by applying ultrasonic impact treatment combined with the electric discharge surface alloying. *Materials Science and Engineering A*, *659*, 119–129.

Moro, T., Mohri, N., Otsubo, H., Goto, A., & Saito, N. (2004). Study on the surface modification system with electrical discharge machine in the practical usage. *Journal of Materials Processing Technology*, *149*, 65-70.

Murray, J. W., Algodi, S. J., Fay, M. W., Brown, P. D., & Clare, A. T. (2017). Formation mechanism of electrical discharge TiC-Fe composite coatings. *Journal of Materials Processing Technology*, *243*, 143–151.

TH-2735_136103036

Niamat, M., Sarfraz, S., Shehab, E., Ismail, S. O., & Khalid, Q. S. (2019). Experimental Characterization of Electrical Discharge Machining of Aluminum 6061 T6 Alloy using Different Dielectrics. *Arabian Journal for Science and Engineering*, *44*(9), 8043–8052.

Novák, P., Vojtěch, D., & Šerák, J. (2006). Wear and corrosion resistance of a plasma-nitrided PM tool steel alloyed with niobium. *Surface and Coatings Technology*, *200*, 5229–5236.

Öztürk, O., Onmuş, O., & Williamson, D. L. (2005). Microstructural, mechanical, and corrosion characterization of plasma-nitrided plastic injection mould steel. *Surface and Coatings Technology*, *196*, 341–348.

Panda, D. K., & Bhoi, R. K. (2005). Artificial neural network prediction of material removal rate in electro discharge machining. *Materials and Manufacturing Processes*, *20*(4), 645–672.

Pandey, P. C., & Jilani, S. T. (1986). Plasma channel growth and the resolidified layer in EDM. *Precision Engineering*, *8*(2), 104–110.

Park, C., Sim, A., Ahn, S., Kang, H., & Chun, E. J. (2019). Influence of laser surface engineering of AISI P20-improved mold steel on wear and corrosion behaviors. *Surface and Coatings Technology*, *377*, 124852, 1-15.

Patel, M. R., Barrufet, M. A., Eubank, P. T., & Dibitonto, D. D. (1989). Theoretical models of the electrical discharge machining process. II. The anode erosion model. *Journal of Applied Physics*, *66(9)*(November), 4104-4111.

Patowari, P. K., Saha, P., & Mishra, P. K. (2011). Taguchi analysis of surface modification technique using W-Cu powder metallurgy sintered tools in EDM and characterization of the deposited layer. *International Journal of Advanced Manufacturing Technology*, *54*(5-8), 593-604.

Patowari, P. K., Saha, P., & Mishra, P. K. (2010). Artificial neural network model in surface modification by EDM using tungsten-copper powder metallurgy sintered electrodes. *International Journal of Advanced Manufacturing Technology*, *51*(April 2010), 627–638.

Petropoulos, G., Vaxevanidis, N. M., & Pandazaras, C. (2004). Modeling of surface finish in electro-discharge machining based upon statistical multi-parameter analysis.

TH-2735_136103036

Journal of Materials Processing Technology, *155–156*(1–3), 1247–1251.

Pereloma, E. V., Conn, A. W., & Reynoldson, R. W. (2001). Comparison of ferritic nitrocarburising technologies. *Surface and Coatings Technology*, *145*(1–3), 44–50.

Puri, A. B., & Bhattacharyya, B. (2003). Modelling and analysis of the wire-tool vibration in wire-cut EDM. *Journal of Materials Processing Technology*, *141*(3), 295–301.

Puri, A. B., & Bhattacharyya, B. (2005). Modeling and analysis of white layer depth in a wire-cut EDM process through response surface methodology. *International Journal of Advanced Manufacturing Technology*, *25*(3–4), 301–307.

Rajurkar, K. P., & Wang, W. M. (1993). Thermal modling and On-Line Monitoring of Wire-EDM. *Journal of Materials Processing Technology*, *38*, 417–430.

Rosalbino, F., Scavino, G., & Mortarino, G. (2012). Electrochemical corrosion behaviour of innovative mould steels in a chloride-containing environment. *Materials and Corrosion*, *63*, 105–110.

Sadagopan, P., & Mouliprasanth, B. (2017). Investigation on the influence of different types of dielectrics in electrical discharge machining. *International Journal of Advanced Manufacturing Technology*, *92*(1–4), 277–291.

Salah, N. Ben, Ghanem, F., & Atig, K. B. (2006). Numerical study of thermal aspects of electric discharge machining process. *International Journal of Machine Tools and Manufacture*, *46*(7–8), 908–911.

Salonitis, K., Stournaras, A., Stavropoulos, P., & Chryssolouris, G. (2009). Thermal modeling of the material removal rate and surface roughness for die-sinking EDM. *International Journal of Advanced Manufacturing Technology*, *40*, 316–323.

Samuel, M. P., & Philip, P. K. (1997). Power metallurgy tool electrodes for electrical discharge machining. *International Journal of Machine Tools and Manufacture*, *37*(11), 1625–1633.

Santos, R. F. dos, da Silva, E. R., Sales, W. F., & Raslan, A. A. (2017). Influence of urea content blended with deionized water in the process of nitriding using electrical discharge machining on AISI 4140 steel. *International Journal of Advanced Manufacturing Technology*, *89*(1–4), 1251–1257.

Shabgard, M., Ahmadi, R., Seyedzavvar, M., & Oliaei, S. N. B. (2013). Mathematical and numerical modeling of the effect of input-parameters on the flushing efficiency

TH-2735_136103036

of plasma channel in EDM process. *International Journal of Machine Tools and Manufacture*, *65*, 79–87.

Shah, S. V., & Dahotre, N. B. (2002). Laser surface-engineered vanadium carbide coating for extended die life. *Journal of Materials Processing Technology*, *124*(1–2), 105–112.

Shankar, P., Jain, V. K., & Sundararajan, T. (1997). Analysis of spark profiles during EDM process. *Machining Science and Technology: An International Journal*, *1:2*, 195–217.

Sharma, D., Mohanty, S., & Das, A. K. (2020). Surface modification of titanium alloy using hBN powder mixed dielectric through micro-electric discharge machining. *Surface and Coatings Technology*, *381*, 125157, 1-12.

Shunmugam, M. S., Philip, P. K., & Gangadhar, A. (1994). Improvement electrode of wear resistance by EDM with tungsten carbide P / M. *Wear*, *171*, 1–5.

Simão, J., Aspinwall, D., El-Menshawy, F., & Meadows, K. (2002). Surface alloying using PM composite electrode materials when electrical discharge texturing hardened AISI D2. *Journal of Materials Processing Technology*, *127*(2), 211–216.

Singh, A., & Ghosh, A. (1999). A thermo-electric model of material removal during electric discharge machining. *International Journal of Machine Tools and Manufacture*, *39*, 669–682.

Sirin, S. Y., & Kaluc, E. (2012). Structural surface characterization of ion nitrided AISI 4340 steel. *Materials and Design*, *36*, 741–747.

Soni, J. S., & Chakraverti, G. (1996). Experimental investigation on migration of material during EDM of die steel (T215 Cr12). *Journal of Materials Processing Technology*, *56*(1–4), 439–451.

Stafe, M. (2012). Theoretical photo-thermo-hydrodynamic approach to the laser ablation of metals. *Journal of Applied Physics*, *112*(12), 1–7.

Stambekova, K., Lin, H. M., & Uan, J. Y. (2012). Surface modification of 5083 Al alloy by electrical discharge alloying processing with a 75 mass% Si-Fe alloy electrode. *Applied Surface Science*, *258*(10), 4483–4488.

Su, Y. L., Yao, S. H., Wei, C. S., & Wu, C. T. (1998). Evaluation on the tension and fatigue behavior of various PVD coated materials. *Thin Solid Films*, *322*(1–2), 218–

TH-2735_136103036

224.

Suzuki, T., & Kobayashi, S. (2013). Mechanisms of TiC layer formation on high speed steel by a single pulse in electrical discharge machining. *Electrochimica Acta*, *114*, 844–850.

Syed, K. H., & Palaniyandi, K. (2012). Performance of electrical discharge machining using aluminium powder suspended distilled water. *Turkish Journal of Engineering and Environmental Sciences*, *36*(3), 195–207.

Tsai, H. C., Yan, B. H., & Huang, F. Y. (2003). EDM performance of Cr/Cu-based composite electrodes. *International Journal of Machine Tools and Manufacture*, *43*(3), 245–252.

Tsai, K. M., & Wang, P. J. (2001a). Comparisons of neural network models on material removal rate in electrical discharge machining. *Journal of Materials Processing Technology*, *117*(1–2), 111–124.

Tsai, K. M., & Wang, P. J. (2001b). Predictions on surface finish in electrical discharge machining based upon neural network models. *International Journal of Machine Tools and Manufacture*, *41*(10), 1385–1403.

Tsai, K. M., & Wang, P. J. (2001c). Semi-empirical model of surface finish on electrical discharge machining. *International Journal of Machine Tools and Manufacture*, *41*(10), 1455–1477.

Tsunekawa, Y., Okumiya, M., Mohri, N., & Takahashi, I. (1994). Surface modification of aluminum by electrical discharge alloying. *Materials Science and Engineering A*, *174*, 193–198.

Tyagi, R., Das, A. K., & Mandal, A. (2018). Electrical discharge coating using WS2 and Cu powder mixture for solid lubrication and enhanced tribological performance. *Tribology International*, *120*, 80–92.

Vedani, M., Previtali, B., Vimercati, G. M., Sanvito, A., & Somaschini, G. (2007). Problems in laser repair-welding a surface-treated tool steel. *Surface and Coatings Technology*, *201*(8), 4518–4525.

Wang, P. J., & Tsai, K. M. (2001). Semi-empirical model on work removal and tool wear in electrical discharge machining. *Journal of Materials Processing Technology*, *114*(1), 1–17.

TH-2735_136103036

Wang, Z. L., Fang, Y., Wu, P. N., Zhao, W. S., & Cheng, K. (2002). Surface modification process by electrical discharge machining with a Ti powder green compact electrode. *Journal of Materials Processing Technology*, *129*, 139–142.

Wong, Y. S., Lim, L. C., Rahuman, I., & Tee, W. M. (1998). Near-mirror-finish phenomenon in EDM using powder-mixed dielectric. *Journal of Materials Processing Technology*, *79*(1–3), 30–40.

Xia, H., Kunieda, M., & Aki, N. N. (1996). Removal Amount Difference between Anode and Cathode in EDM Process. *International Journal of Electrical Machining*, (1), 45–52.

Xiao, H., Jie, X., Zeng, Z., & Li, G. (2014). Titanium carbonitride coating by pulsed electrical discharge in an aqueous solution of ethanolamine. *Surface and Coatings Technology*, *258*, 1006–1010.

Yahya, A. & Manning C. D. (2004). Determination of material removal rate of an electro-discahrge machine using dimensional analysis. *Journal of physics D: Applied Physics*, *37*, 1467-1471

Yan, B. H., Tsai, H. C., & Huang, F. Y. (2005). The effect in EDM of a dielectric of a urea solution in water on modifying the surface of titanium. *International Journal of Machine Tools and Manufacture*, *45*, 194–200.

Yan, G., Lu, S., Zhang, M., Wang, J., Yang, X., Zhang, Z., & Li, C. (2020). Wear and corrosion behavior of P20 steel surface modified by gas nitriding with laser surface engineering. *Applied Surface Science*, *530*, 147306, 1-9.

Yeo, S. H., Kurnia, W., & Tan, P. C. (2007). Electro-thermal modelling of anode and cathode in micro-EDM. *Journal of Physics D: Applied Physics*, 2513–2521.

Zhang, Y., Liu, Y., Shen, Y., Ji, R., Li, Z., & Zheng, C. (2014a). Investigation on the influence of the dielectrics on the material removal characteristics of EDM. *Journal of Materials Processing Technology*, *214*(5), 1052–1061.

Zhang, Y., Liu, Y., Shen, Y., Li, Z., Ji, R., & Cai, B. (2014). A novel method of determining energy distribution and plasma diameter of EDM. *International Journal of Heat and Mass Transfer*, *75*, 425–432.

TH-2735_136103036

LIST OF PUBLICATIONS

(a) Journal

1. Devarani N. and Joshi S. N., (2021). Electric discharge alloying of AISI P20 mold steel using titanium and aluminium. *Surface and Coatings Technology*. Vol 405, 126515, pp 1–13.
2. Devarani N. and Joshi S. N., (2022). Determining alloyed layer thickness in electric discharge alloying by inverse estimation of energy distribution. *International Journal of Thermal Sciences.* Vol 177, 107571, pp 1-18.
3. Devarani N. and Joshi S. N., (2018). Surface alloying of Ti-6Al-4V on P20 mold steel using electric discharge processing (EDP). *Materials today proceedings.* Vol 5, pp 8523-8531.
4. Das S., Raman R. K., Devarani N and Joshi S. N., (2019). Surface alloying of titanium di-boride (TiB_2) and silicon carbide (SiC) on aluminium Al 5052 using electric discharge processing. *Structural Integrity Procedia.* Vol 14, pp 119-126.
5. Devarani N. and Joshi S. N., Effect of dielectric medium on tribology and corrosion behavior of electrically discharge alloyed P20 Mold Steel using powder metallurgy tool electrode of Ti and Al. (*Manuscript under preparation*)

(b) International conference

Devarani N. and Joshi S. N., (2017) Surface Alloying of Ti-6Al-4V on P20 Mold Steel using Electric Discharge Processing (EDP). *International conference on emerging trends in materials and manufacturing engineering, IMME 17, NIT Trichy, March 10-12, 2017.*

TH-2735_136103036

TH-2735_136103036